Flow Boiling and Two-Phase Flow Instabilities in Silicon Microchannel Heat Sinks for Microsystems Cooling

Dario Bogojević

A thesis submitted for the degree of Doctor of Philosophy.
The University of Edinburgh.
July 2009

Declaration

"I declare that this Thesis has been composed by me (i.e. Dario Bogojevic), the work is my own, and it has not been submitted for any other degree or professional qualification except as specified."

_____

Abstract

Flow boiling in microchannels, while very promising as a cooling technology in electronics thermal management, is still a subject being explored that requires further investigation. Before applying this technology for high heat flux computer chip cooling, challenging issues such as fully understanding boiling mechanisms in confined spaces, extending and stabilising the nucleate boiling regime, suppressing flow boiling instabilities, maintaining uniform flow distribution among microchannels, have to be addressed. If flow boiling is to be used as a thermal management method for high heat flux electronics it is necessary to understand the behaviour of a non-uniform heat distribution, which is typically the case observed in a real operating computer chip. In this study, flow boiling of deionised water in a silicon microchannel heat sink under uniform and non-uniform heating has been investigated with particular attention to flow boiling instabilities. An experimental system was designed and constructed to carry out the experimental investigations. The experimental heat sink consisting of forty parallel rectangular microchannels with 194 μm hydraulic diameter together with integrated inlet and outlet manifold was fabricated on a silicon wafer using inductive coupled plasma dry etching, in conjunction with photolithographic techniques. A design with integrated temperature sensors made from a thin nickel film allows local temperature measurements with a much faster response time and smaller thermal resistance as compared to temperature measurements using thermocouples. The integrated heater was designed to enable either uniform or non-uniform heating (hotspot investigation) with a low thermal resistance between the heater and the channels. Numerical simulations for single phase flow in adiabatic conditions were used to assist the design of the manifold geometry in the microchannels heat sink. Microfabricated temperature sensors were used together with simultaneous high speed imaging in order to obtain a better insight related to temperature fluctuations caused by two-phase flow instabilities under uniform and non-uniform heating. Two types of two-phase instabilities with flow reversal were identified and classified into flow stability maps. The effect of

inlet water temperature on flow boiling instabilities was experimentally studied, with the influence of different subcooling conditions on the magnitude of temperatures as well as the influence on temperature uniformity over the heat sink being assessed. The effect of various hotspot locations on flow boiling instabilities has been investigated, with hotspots located in different positions along the heat sink. Bubble growth and departure size have been experimentally investigated. The results of this study demonstrate that bubble growth in microchannels is different from that in macroscale channels. Furthermore, the effects of bubble dynamics on flow instabilities and heat transfer coefficient have been investigated and discussed.

Acknowledgments

I gratefully acknowledge the financial support of the UK Engineering and Physical Sciences Research Council through the grant EP/D500109/1.

I would like to thank my supervisor, Dr. Khellil Sefiane for giving me the opportunity to work in his group, supporting me and leading me through my PhD. I would like to thank Dr. Khellil Sefiane for all his understanding and kindness. It has been a great pleasure to work for him, in supportive and encouraging environment of his research group.

Thanks to Professor Anthony J. Walton and his research group at the Scottish Microelectronic Center for fabricating test module devices I used in my research.

I would also like to thank Professor David Kenning for his useful comments and helping me with data analysis.

I would like to acknowledge my friends and students at the Multiphase Flows and Heat Transfer Laboratory for their friendship, assistance and support. In particular, I want to thank Christian Hutter for helping me to design and build the experimental setup.

I would like to express my appreciation to the staff of mechanical and electronic workshops and their support in building the experimental setup.

I would also like to thank Tijana Bugarčić and Anamaria Suknović who helped me in text editing.

I am especially grateful to my family and friends for all their love, support and encouragement that have contributed greatly to the success of this work.

Table of contents

List of tables

List of figures

Nomenclature

A	area, m^2
Bo	boiling number
Ca	capillary number
Co	confinement number
c_p	specific heat capacity, J/kg˚C
D_{ch}	depth of channel, m
D_h	hydraulic diameter, m
Eo	Eotvos (Bond) number
f	frequency, Hz
G	mass flux, kg/m^2s
g	acceleration of gravity, m/s^2
h	enthalpy of fluid, J/kg
h_l	enthalpy of saturated liquid, J/kg
h_g	enthalpy of saturated vapour, J/kg
h_{lg}	latent heat of vaporization, J/kg
h_z	local heat transfer coefficient, $W/m^{2\circ}C$
I	electrical current, A
L	channel length, m
l	axial distance, m
k	thermal conductivity, W/m˚C
m	fin parameter
$\dot{m}$	mass flow rate, kg/s
N	number of microchannels
P	pressure, bar
p	pressure, Pa
p^*	non-dimensional pressure drop
Q	input power, W
Q_{loss}	heat losses, W

Q volumetric flow rate, m^3/s

Q^* dimensionless flow rate

q heat flux, W/m^2

R thermal resistance, $^\circ Cm^2/W$

R resistance, Ω

R^* dimensionless resistance

$r_{c,}$ cavity mouth radius, m

Re Reynolds number

T temperature, $^\circ C$

t time, s

t_w time elapsed until bubble reached the channel width, ms

U superficial velocity, m/s

u velocity, m/s

U_c characteristic velocity, m/s

V voltage, V

W width of microchannel assembly, m

W_{ch} width of channel, m

We Weber number

W_w width of wall between two channels, m

X Lockhart-Martinelli parameter

x mass vapour quality

x distance (chapter 4), m

x_e exit vapour quality

x_{eq} thermodynamic equilibrium quality

greek

α void fraction

ΔP pressure drop, bar

ΔT temperature difference, $^\circ C$

ΔT_{sat} wall superheat necessary to cause nucleation, $^\circ C$

ΔT_{sub} degree of subcooling, $^\circ C$

δ average liquid thickness, m

δ_t	thermal boundary layer thickness, m
η	fin efficiency
θ_r	bubble contact angle, rad
λ	non-circularity coefficient
μ	dynamic viscosity, Pas
v	kinematic viscosity, m^2/s
ρ	density, kg/m^3
σ	surface tension, N/m
σ	standard deviation
τ	period between two successive events, s
φ	portion of the total power transferred to the water

subscripts

ch	channel
f	fluid
g	vapour
in	inlet
l	liquid
out	outlet
sat	saturation fluid
Si	silicon
sub	subcooled
T	total
w	wall

Chapter 1 Introduction

1.1 Overview of cooling technologies for electronics components

Trends towards the miniaturisation and increases in the packaging density of electronics have led to a significant improvement in the performance of electronic systems in the past decades. According to Moore's prediction the number of transistors on an integrated circuit doubles roughly in 18 months [1]. With the rapid increase in the packaging density, there is a steady increase in the power levels resulting in higher heat dissipation from the electronic device with every new design. Increases in power levels combined with the market expectation of reduced package sizes lead to heat problems that, if uncontrolled, can significantly affect the performances of an electronic device. Therefore, thermal management in electronics is one of the major focal points in the development of next generation electronic systems such as central processor units (CPU). Figure 1.1 shows projected CPU heat flux in relation to module cooling technology limits over this decade [2]. CPU heat flux is projected to increase exponentially through the next decade with heat flux doubling approximately every 3 years. The projections also suggest that CPU heat flux will exceed 200 W/cm^2 by the end of the decade. To meet this demand it is necessary to develop novel cooling technologies able to cope with high heat fluxes electronic systems. The principal challenge is to dissipate the high heat fluxes while maintaining the chip temperature at or below a certain temperature specification

(typically referred as the junction temperature) to ensure reliable performance. However, an additional thermal management problem is non-uniform distribution of heat dissipation in the CPU, which results in local hotspots, where heat fluxes < 300 W/cm^2 are possible. The thermal impact of non-uniform dissipation is illustrated in Figure 1.2 [3].

A convenient way of presenting the cooling capability of a heat sink for electronics cooling is the overall thermal resistance which is defined as follows:

$$R = (T_j - T_{in})/q \tag{1.1}$$

where T_j is the junction temperature, T_{in} is the inlet coolant temperature and q is the maximum heat flux the cooling system is required to dissipate. The overall thermal resistance consists of the TIM (thermal interface material between the CPU and the heat sink) resistance R_{TIM} and the heat sink thermal resistance R_{HS}.

$$R = R_{TIM} + R_{HS} \tag{1.2}$$

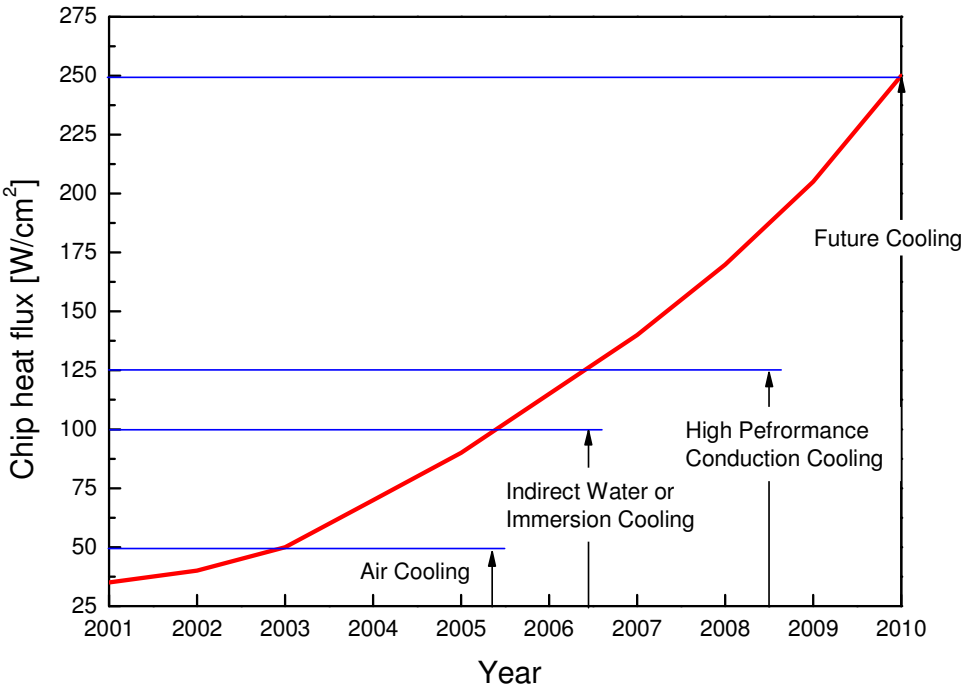

Figure 1.1 *Projected chip heat flux in relation to module cooling technology limits [2].*

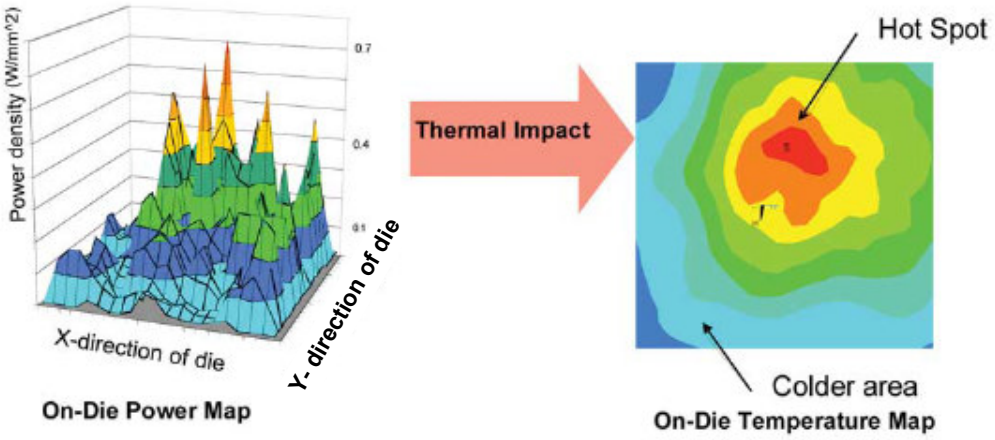

Figure 1.2 *A typical die power map and the resulting hotspots on the corresponding die temperature map. The red region represents the highest temperature region [3].*

A traditionally used cooling technique with forced air convection through the heat sink maintained by a fan is schematically presented in Figure 1.3. Assume the maximum junction temperature for a safe operation of the CPU is 85 ºC, the inlet coolant temperature is 40 ºC (ambient temperature) and the maximum dissipation power of 100 W from the CPU surface with dimensions of 10 × 10 mm^2 (q = 100 W/cm^2). Then, the overall thermal resistance of 0.45 ºC cm^2/W can be calculated from the equation 1.1. With a typical TIM resistance of 0.25 ºC cm^2/W the heat sink thermal resistance is required to be equal or smaller than 0.20 ºC cm^2/W. For comparison, a CPU chip in the early 1990s with an interface thermal resistance as high as 1.5 ºC cm^2/W, because low heat flux dissipation (less than 15 W/cm^2), only requires the heat sink resistance to be 0.8-1.0 ºC cm^2/W. Despite improvements with air cooling, such as the optimized design of the heat sink and thermal consideration in the integrated circuit layout, this cooling technique approaches the limit with CPU heat dissipation fluxes of 100 W/cm^2 [4]. Saini and Webb [5] considered the problem of heat dissipation limits of heat sink-fan cooling a single chip package in a "desktop" computer application. Calculated results were reported based upon a 16 x 16 mm heat source and a temperature difference of 35°C from the heat source to inlet air. The maximum allowable heat load reported was 95.2 W corresponding to a

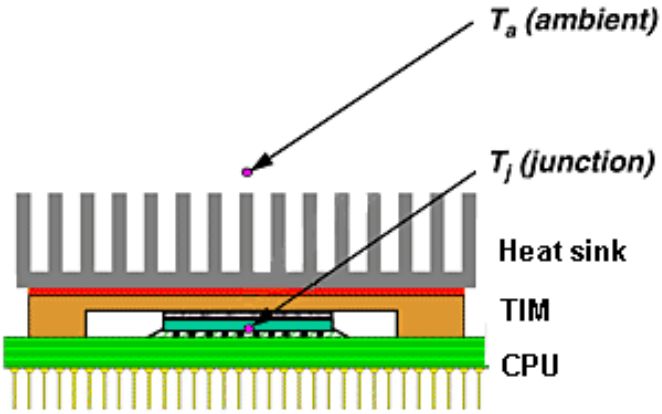

Figure 1.3 *Schematic of the heat sink for traditional cooling of CPU using forced air convection.*

maximum allowable uniform chip heat flux of 37.2 W/cm^2. The predicted minimum convection resistance was 0.211 ˚C/W. Forced air convection is limited as a cooling technique due to the poor thermal transport properties of air and the demand for high flow rates of about 10^6 ml/min. A higher flow rate requires increased fan speed, hence the noise and vibration generated by fans could exceed the limit considered acceptable by humans (45 dB).

Another cooling technology widely used for the thermal management of computers is heat pipe cooling systems. Heat pipes are very reliable in practice as there are no mechanically moving parts. The pipes are embedded in a metal plate which is attached to the computer chip. There are two regions in the heat pipe, the evaporator and condenser regions. The working fluid absorbs heat on the evaporator region where the fluid is vaporized, creating a pressure gradient in the pipe. This pressure gradient forces the vapor to flow along the pipe to a cooler section, where the vapor condenses releasing the heat to the cooling media, as schematically shown in Figure 1.4 [6]. The working fluid is then returned to the evaporator region driven by the capillary force. The main problem with application of heat pipes in electronics cooling is the limited volume of working fluid due to the wick structures, which

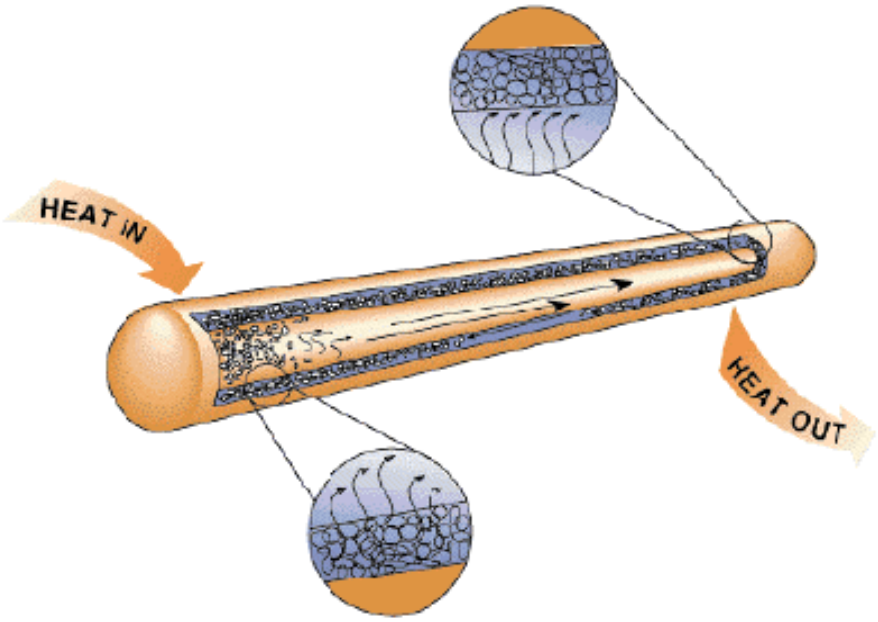

Figure 1.4 *Schematic illustrating the heat pipe operation [6].*

limits the maximum amount of power the heat pipe is capable of carrying. Current heat pipes heat sinks are used for removal heat power about 100 W, with resistances from 0.2 to 0.4°C/W [7].

The need for enhanced cooling technologies in electronics has encouraged a continuous investigation of novel cooling techniques, such as liquid jet impingement, spray cooling, single-phase cooling with microchannels and two-phase flow cooling with microchannels. The main goal of these investigations is to design cooling device with thermal resistance below 0.1 ºC cm^2/W. A review of current cooling techniques and potential alternatives for high flux dissipation in the future has been reported by Lin et al. [8]. The authors point to microchannel flow boiling as the most promising cooling technology that is capable of dissipating high heat fluxes from electronics devices. Ellsworth and Simons [9] compared the performance of air-cooling with liquid cooling options. The authors considered both indirect and direct liquid cooling options. Indirect cooling options, denoted by the presence of distinct physical barriers between the chip and the liquid, include water-cooled cold plates applied at the module level and micro cold plates attached at the chip level. Direct liquid (immersion) cooling brings the dielectric coolant (e.g. fluorocarbon coolants or FCs) in direct contact with the back of the chip. This cooling option includes liquid jet

impingement and spray cooling. The results of the comparison show that indirect liquid cooling offers the capability of heat removal rates two to four times that of air cooling, while direct liquid cooling methods do not approach the performance of indirect liquid cooling. A comprehensive review of the different cooling technologies, currently in development has been provided by Agostini et al. [10]. The authors compared the advantages and drawbacks of four different cooling technologies: single-phase flow in microchannels, single and two-phase flow in porous media, jet impingement cooling and two-phase flow in microchannels. The result of the comparison is shown in Figure 1.5 where the heat sink thermal resistances for all cooling technologies are presented with respect to the ratio between the pumping power and the dissipated thermal power. Cooling technology with a better performance is that nearest the axis intersection point in Figure 1.5 because it represents the lowest thermal resistance at the lowest pumping power. As can be seen in Figure 1.5, jet impingement cooling has the lowest thermal resistance but poor efficiency because high pumping power (high pressure drop).

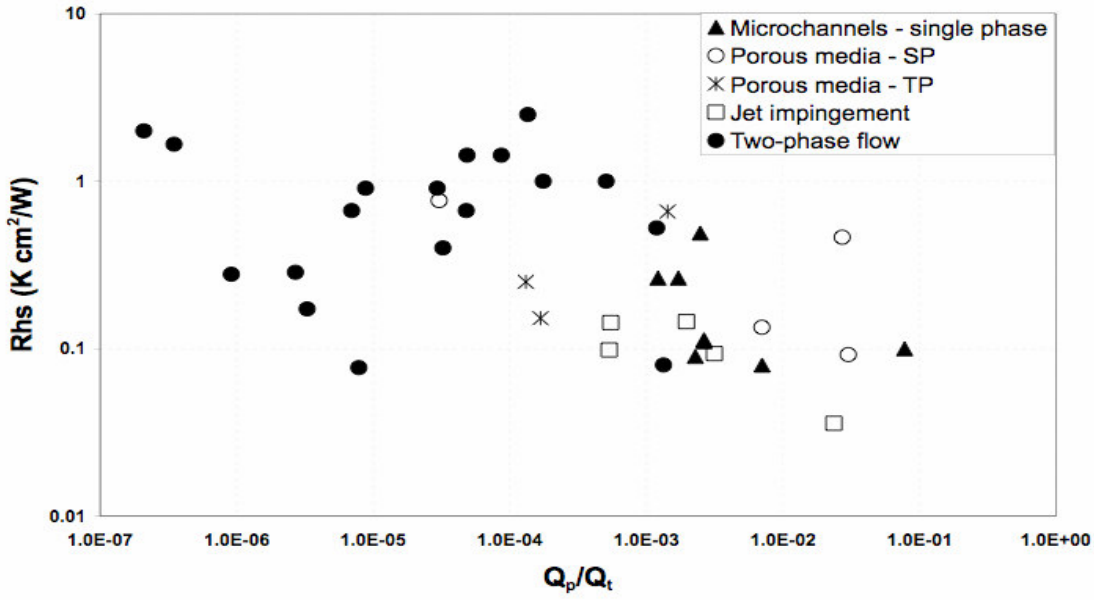

Figure 1.5 *Thermal resistance of heat sinks for all cooling technologies as a function of the pump to the dissipated power ratio, R_{hs} thermal resistance, Q_p pumping power, Q_t dissipated thermal power [10].*

Jet cooling system consists of nozzles (jets) spread in jets arrays. A schematic illustration of a jet cooling system is shown in Figure 1.6. The higher the number of nozzles in the array and the smaller the jet diameter which gives the higher heat transfer rate. The recent development of micromachining techniques has allowed the manufacturing high density arrays of micro jets that provide very high cooling performance. In multi-jet configuration jet cooling is capable of removing over 300 W/cm^2 heat flux with a junction temperature on the chip of 83 ˚C [11]. However, high pumping power requirements, control of the jet velocity, the possibility of surface erosion and nozzle obstruction have prevented this technique from becoming a widely-used cooling technique.

Heat sinks with *single phase flow in microchannels* provide a high heat transfer coefficient, large surface area to volume ratio and small volume cooling devices. Microchannel heat sinks are typically fabricated from a high thermal conductivity material such as silicon or copper containing parallel channels with hydraulic diameters ranging from 10 to 200 μm. With these attributes, single-phase cooling is able to remove high heat flux dissipations. Colgan et al. [12] demonstrated cooling over 500 W/cm^2 using a single-phase silicon microchannel heat sink shown in Figure 1.7. The authors reported a very low heat sink thermal resistance of 0.105 Kcm^2/W

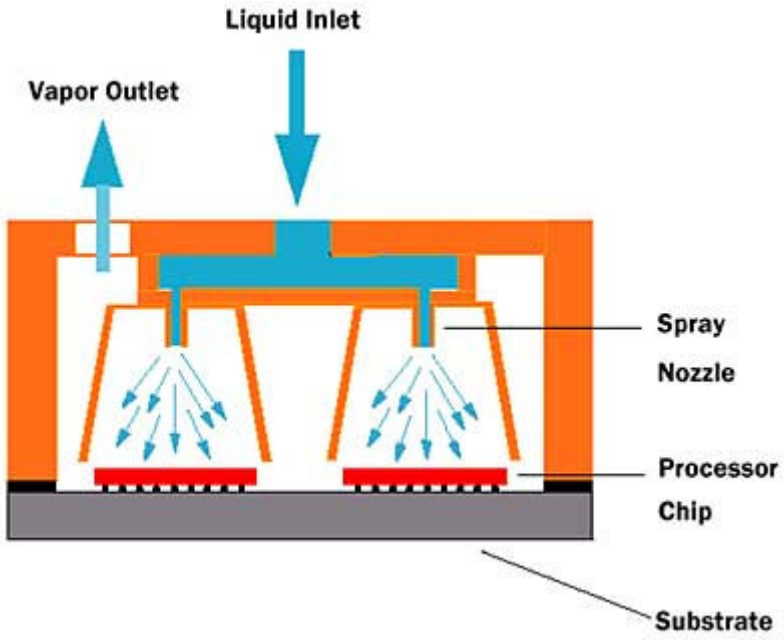

Figure 1.6 *Schematic illustrating the jet cooling operation.*

at a pressure drop of 35 kPa using water as the coolant. Nowadays single phase flow in microchannels technology is used in liquid cold plates to cool high power CPUs. In general, single-phase cooling with microchannels yields low thermal resistance (high cooling performance) but this technology is limited by the high pumping requirements. Another problem with this technique is the temperature gradient along the cooled CPU. However, one advantage of this cooling technique is good physical understanding of the process due to many investigations related to it.

In comparison with single-phase, *two-phase flow in microchannels cooling* provides important advantages such as much higher convective heat transfer coefficients while the requirements for coolant flow are lower. Figure 1.8 presents a comparison of various cooling techniques based on heat transfer mechanisms and coolants utilised [8]. It is noted that highest heat transfer rates can be achieved with phase change processes, hence for high heat flux dissipation, two-phase flow and boiling mechanisms should be considered. The potential of flow boiling in

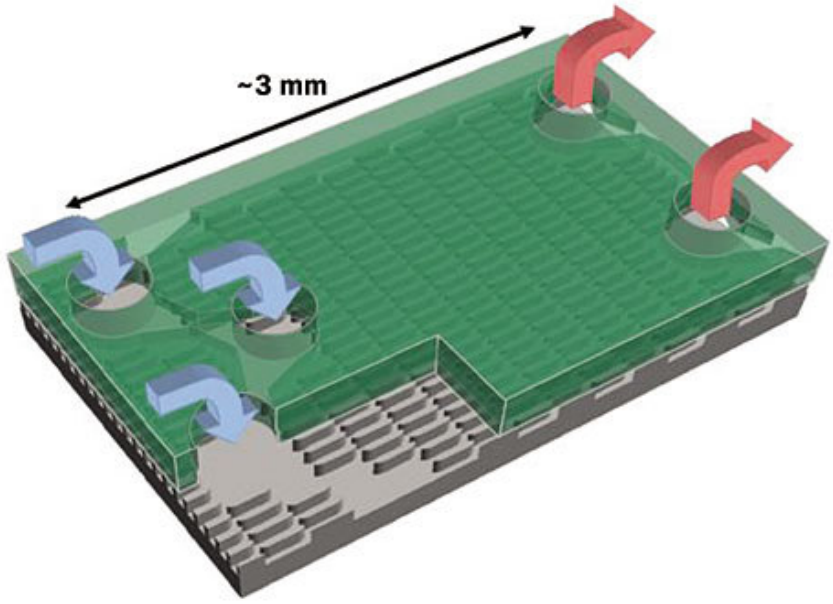

Figure 1.7 *Microchannel heat sink with staggered fin configuration used by Colgan et al. [12].*

microchannels for the thermal management of the next generation of high heat flux computer chips has been demonstrated by a number of researchers. Qu and Mudawar [13] have investigated the flow boiling of water in a copper microchannel heat sink with 21 parallel rectangular channels and 356 µm hydraulic diameter. The maximal heat flux they used in the experiment was 185 W/cm^2 and evaluated boiling heat transfer coefficients were within the range of 20 to 45 kW/m^2°C for five mass velocities (from 135 to 402 kg/m^{2}s). Lee and Mudawar [14, 15] have studied two-phase flow of refrigerant R134 using the aforementioned microchannel heat sink. The heat transfer coefficients were as high as 50 kW/m^{2}K at heat flux of 80 W/cm^2 with a vapour quality of 0.3, while at a vapour quality of 0.8 it decreased down to about 3 kW/m^{2}K. Steinke and Kandlikar [16] have used very high mass fluxes (up to 1782 kg/m^{2}s) at high heat fluxes (up to 90 W/cm^2) in their experimental investigation of flow boiling characteristics of water in 6 parallel 207 µm microchannels. They obtained very high heat transfer (up to 200 kW/m^{2}K). Kosar et al [17] reported average heat transfer coefficient of 50 kW/m^{2}K at a heat flux of 250 W/cm^2 in their experimental investigation of the boiling heat transfer of water in 227 µm hydraulic

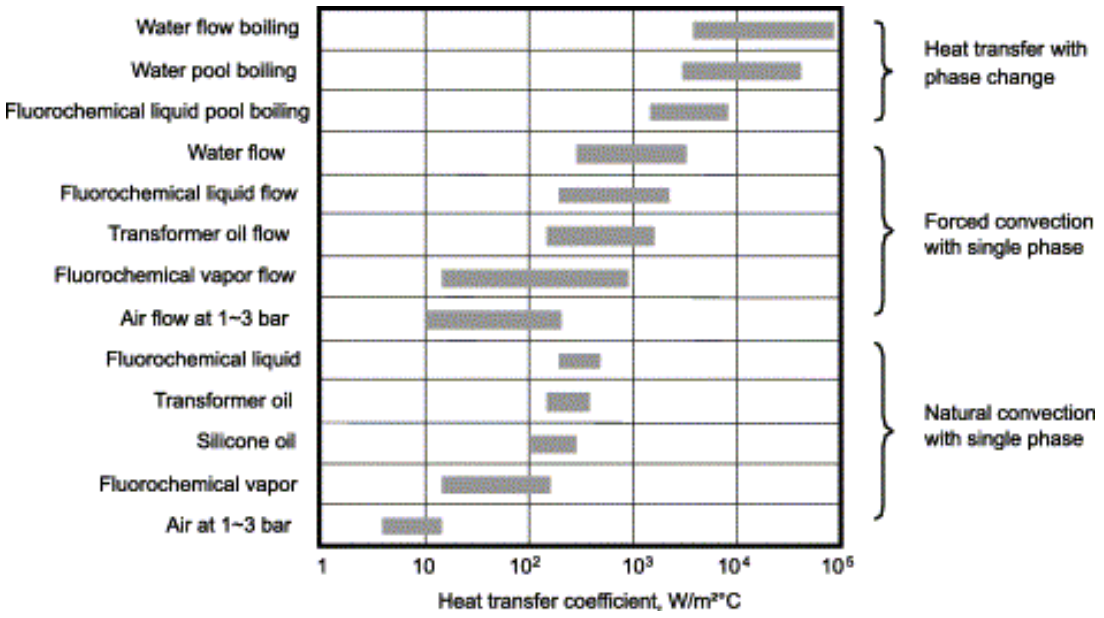

Figure 1.8 *Estimated range of heat transfer coefficients for various coolants and heat transfer modes [8].*

diameter rectangular channels with 7.5 μm wide reentrant cavities on the sidewalls. Agostini et al.[18-20] reported a database of experimentally obtained local heat transfer coefficients along a silicon microchannel heat sink composed of 67 parallel channels. The authors used refrigerants R236fa and R245fa for heat fluxes up to 221 W/cm^2 and mass fluxes between 300 and 1600 kg/m^2s.

Generally, two-phase cooling with microchannels yields a low thermal resistance to the chip-cooling assembly using the small flow rates. That means a smaller pump can be used in comparison with single phase cooling.

1.2 Motivation for study

Previous studies have demonstrated that flow boiling in microchannels may offer a feasible alternative for high flux dissipation in microsystems. The main advantages of two-phase flow boiling in microchannels compared to other cooling techniques are:

- Much higher heat transfer coefficients are possible with flow boiling than with single phase flow;
- A lower coolant flow rate. This is made possible by the latent heat of vaporization which provides high energy absorption;
- A lower coolant flow rate means a lower pressure drop hence a lower pumping power requirements;
- Much better temperature uniformity can be obtained due to constant vaporization temperature.

However, this cooling technology is the least developed and further research and development are required before this concept can migrate into actual products. Before applying this technology for high heat flux computer chip cooling, challenging issues such as fully understanding boiling mechanisms in confined spaces, extending and stabilising the nucleate boiling regime, and using micropumps, have to be addressed. Another big challenge for flow boiling in microchannels cooling technology is local hotspots investigation. It is known that CPUs work with non-uniform thermal dissipation (Figure 1.2) that causes localized hotspots resulting

in an increase in local CPU junction temperature affecting the reliability and performance of the CPU. If flow boiling is to be used as a thermal management method for high heat flux electronics it is necessary to understand the behaviour of a non-uniform heat distribution, which is typically the case observed in a real operating CPU. Thus, flow boiling in microchannels, while very promising cooling technology in electronics thermal management, is still an exploratory subject that requires further investigation.

This work presents results obtained through an experimental investigation of flow boiling in a microchannels based heat sink with particular attention on flow boiling instabilities under uniform and non-uniform heating. Many controversies about flow regimes, flow instabilities and mechanisms of heat transfer in microchannels from the previous studies, discussed in the following chapter, require further investigation in the area. The main objective of the research is to gain further insight into flow boiling in microscale using an experimental set up that allows local temperature measurements and high-speed camera imaging.

References

1. Moore G. E., *Cramming More Components onto Integrated Circuits.* Electronics, 1965. Vol. 38(8) 114-117.
2. Smith, R. *Current Packaging Trends*. in *Proceedings of the Cooling Electronics The Next Decade conference*. 2001. Marlborough, MA, USA.
3. Mahajan R., Chia-pin Chiu, and Chrysler G., *Cooling a Microprocessor Chip.* Proceedings of the IEEE, 2006. 94(8) 1476-1486.
4. Lian Zhang, *PhD thesis "Phase Change Phenomena in Silicon Microchannel Heat Sink for IC Chip Cooling"*, in *Department of Mechanical Engineering*. 2002., Stanford University.
5. Saini, M. and R.L. Webb, *Heat rejection limits of air cooled plane fin heat sinks for computer cooling.* Components and Packaging Technologies, IEEE Transactions on, 2003. 26(1) 71-79.
6. Buffone, C., *An Experimental and Numerical Investigation of Thermocapillary Driven Phenomena for Evaporating Menisci in Capillary Tubes Related to Microelectronics Cooling*. 2004., University of Edinburgh.
7. Scott D. Garner, P., *Heat pipes for electronics cooling applications, .* ElectronicsCooling, 1996. 2(3).
8. Lin, S., K. Sefiane, and J.R.E. Christy, *Prospects of confined flow boiling in thermal management of microsystems.* Applied Thermal Engineering, 2002. 22(7) 825.
9. Ellsworth, M.J., Simons R. E.,, *High Powered Chip Cooling -- Air and Beyond.* ElectronicsCooling 2005. 11(3).
10. Agostini, B., Fabbri, M., Park, J.E., Wojtan, L.,Thome, J.R.,. *State of the art of High Heat Flux Cooling Technologies.* Heat Transfer Engineering 2007. 28(4) 258-281.
11. Brunschwiler, T., Rohuizen, H., Fabbri, M., Kloter, U., Michel, B., Bezama, R.J., Natarajan, G. *Direct Liquid Jet Impingement Cooling with Micron-Sized Nozzle Array and Distributed Return Architecture*. in *ITHERM*. 2006. San Diego, CA, USA.
12. Colgan, E.G., et al., *High Performance and Subambient Silicon Microchannel Cooling.* Journal of Heat Transfer, 2007. 129(8) 1046-1051.
13. Qu, W. and I. Mudawar, *Measurement and correlation of critical heat flux in two-phase micro-channel heat sinks.* International Journal of Heat and Mass Transfer, 2004. 47(10-11) 2045.
14. Lee, J., Mudawar, I.,, *Two-Phase Flow in High-Heat Flux Micro-Channel Heat Sink for Refrigeration Cooling Applications: Part-I - Pressure Drop Characteristics.* International Journal of Heat and Mass Transfer, 2005. Vol. 48 941-955.
15. Lee, J., Mudawar, I.,, *Two-Phase Flow in High-Heat Flux Micro-Channel Heat Sink for Refrigeration Cooling Applications: Part-II - Heat Transfer Characteristics.* International Journal of Heat and Mass Transfer, 2005. Vol. 48 941-955.

16. Steinke, M.E., Kandlikar, S.,, *Control and Effect of Dissolved Air in Water During Flow Boiling in Microchannels.* International Journal of Heat and Mass Transfer, 2004. Vol. 47 1925-1935.
17. Kosar, A., Kuo, C-J, Peles, Y.,, *Boiling Heat Transfer in Rectangular Microchannels with Reentrant Cavities.* International Journal of Heat and Mass Transfer, 2005. Vol. 48 4867-4886.
18. Agostini, B., et al., *High heat flux flow boiling in silicon multi-microchannels - Part I: Heat transfer characteristics of refrigerant R236fa.* International Journal of Heat and Mass Transfer, 2008. 51(21-22) 5400-5414.
19. Agostini, B., et al., *High heat flux flow boiling in silicon multi-microchannels - Part II: Heat transfer characteristics of refrigerant R245fa.* International Journal of Heat and Mass Transfer, 2008. 51(21-22) 5415-5425.
20. Agostini, B., et al., *High heat flux flow boiling in silicon multi-microchannels - Part III: Saturated critical heat flux of R236fa and two-phase pressure drops.* International Journal of Heat and Mass Transfer, 2008. 51(21-22) 5426-5442.

Chapter 2 Overview of flow boiling in microchannels

2.1 Introduction

Boiling is a phase change process in which vapour generation occur either on a heated surface and/or in a superheated liquid layer adjacent to the heated surface. Pool boiling refers to boiling under natural convection, while in flow boiling, liquid flow over heated surfaces is imposed by external means [1]. In flow boiling the two-phase flow patterns change along the heated surface due to vapour production. This is an important difference between pool boiling and flow boiling; i.e., that the forced flow of the liquid-vapour system causes flow pattern transitions at a given wall heat flux (or temperature) as the integral power dissipated in the fluid increases as it flows along the heated surface. Depending on whether liquid-vapour flow occurs over unconfined or confined heated surfaces, forced flow boiling is classified into external or internal flow boiling. Internal flow boiling refers to flow inside tubes. Flow boiling in macroscale tubes is widely used in various heat exchanger systems; hence the heat transfer theories for flow boiling have been well established. However, behaviour of the flow boiling in microchannels can be very different than in macroscale tubes, due to possible change in the dominant force. For example, surface tension forces become more important when the channels dimension scales down, and gravitational forces weaken. Therefore, it is usually not reasonable to extrapolate

macroscale two-phase flow pattern maps, flow boiling heat transfer methods and two-phase pressure drop models to microchannels [2].

2.2 Flow boiling in macroscale tubes

Consider the case of a horizontal tube uniformly heated over its length with a constant heat flux, with subcooled liquid at the inlet and constant system pressure (Figure 2.1). As long as the liquid and the heated wall are below the saturation temperature of the liquid at local pressure, heat transfer to the liquid flowing inside the tube is single-phase convective heat transfer (Region A). At some point along the tube, the wall temperature exceeds the local saturation temperature, while the bulk liquid may still be below the saturation temperature. Depending on the tube surface characteristics bubbles formation can take place at the wall nucleation sites in a presence of subcooled liquid. Boiling under this condition is known as subcooled flow boiling (Region B). Saturated flow boiling occurs when the wall temperature exceeds the local saturation temperature and thermodynamic equilibrium quality is between 0 and 1 (Region C). The void fraction (α) in Figure 2.1 is defined as the ratio of vapour phase flow area to total flow area (eq. 2.1) The vapour mass fraction (quality) is defined as the ratio of vapour mass flow rate to total mass flow rate (eq. 2.2). The thermodynamic equilibrium quality definition is based on thermodynamic properties of liquid and vapour phases in their thermodynamic equilibrium (eq. 2.3).

$$\alpha = \frac{A_g}{A} \qquad (2.1) \qquad x = \frac{\dot{m}_g}{\dot{m}_g + \dot{m}_l} \qquad (2.2) \qquad x_{eq} = \frac{h - h_l}{h_{\mathrm{lg}}} \qquad (2.3)$$

2.2.1 Subcooled flow boiling

In the subcooled flow boiling region the tube surface temperature remains essentially constant, a few degrees above the saturation temperature, while the mean bulk liquid temperature linearly increases to the saturation temperature. The

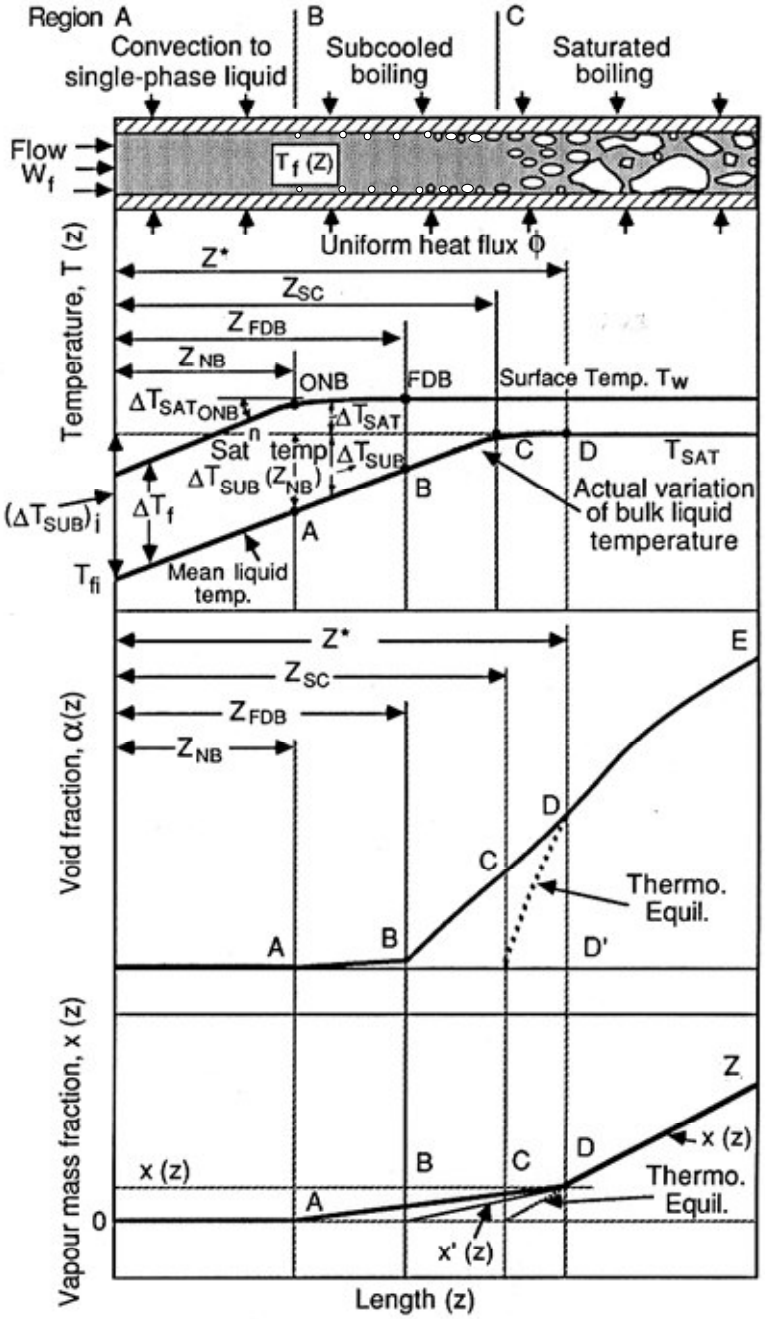

Figure 2.1 *Schematic representation of flow patterns and the variation of the surface and liquid temperatures, void and vapour fractions, in the regions designated by A, B, and C for the case of a uniform wall heat flux [3].*

difference between the wall temperature and the saturation temperature is known as the degree of superheat ΔT_{sat}, and the difference between the mean bulk liquid temperature and the saturation temperature is called degree of subcooling ΔT_{sub}. The point A in Figure 2.1 denotes the place along the tube where the first bubbles appear on the wall surface. This point corresponds to the *onset of nucleate boiling (ONB).* The bubbles nucleation on the heater surface requires a certain amount of wall superheat and presence of cavities on the heated wall. The cavity size that is activated first with increasing wall temperature is called the critical cavity size [1]. Most researchers have proposed the nucleation criteria for the onset of nucleation during flow boiling based on a comparison between the liquid temperature on the vapour bubble interface at the top location from the wall with the saturation temperature inside the bubble. As the initial assumptions, Hsu and Graham [4] used a bubble contact angle of 53.1°, Bergles and Rohsenow [5], and Sato and Matsumura [6] used a hemispherical bubble shape (90° contact angle), while Davis and Anderson [7] left the contact angle as a variable. Kandlikar et al. [8] performed numerical simulations of the flow over a bubble attached to a channel wall at a given contact angle. The authors noted that for nucleation in the presence of liquid flow, flow stagnation occurred at $y_s = 1.1 \cdot r_b$ with y_s representing the distance of the stagnation location from the heated wall, and r_b is the radius of the bubble at nucleation. They modified the bubble nucleation model of Hsu [9] by using the liquid temperature at the stagnation point for the temperature of liquid at the bubble top and derived the following equation for the range of active nucleation cavities:

$$(r_{c,\min}, r_{c,\max}) = \frac{\delta_t \sin\theta_r}{2.2}\left(\frac{\Delta T_{sat}}{\Delta T_{sat} + \Delta T_{sub}}\right)\left[1 \mp \sqrt{1 - \frac{8.8\sigma T_{sat}(\Delta T_{sat} + \Delta T_{sub})}{\rho_g h_{lg} \delta_t \Delta T_{sat}^{\ 2}}}\right]. \quad (2.4)$$

where $r_{c,min}$ and $r_{c,max}$ are the minimum and maximum radii of the nucleating cavities. The critical cavity radius $r_{c,crit}$ that will nucleate first is given by

$$r_{c,crit} = \frac{\delta_t \sin\theta_r}{2.2}\left(\frac{\Delta T_{sat}}{\Delta T_{sat} + \Delta T_{sub}}\right) \quad (2.5)$$

The corresponding local wall superheat is given by

$$\Delta T_{sat,ONB} = \sqrt{\frac{8.8\sigma T_{sat} q}{\rho_g h_{lg} k_l}} \tag{2.6}$$

and the local liquid subcooling is obtained by using the single-phase heat transfer equation prior to nucleation,

$$\Delta T_{sub,ONB} = \frac{q}{h} - \Delta T_{sat,ONB} \ . \tag{2.7}$$

Figure 2.2 shows results of comparison between different ONB models with the experimental results obtained by Kandlikar et al. [8] for subcooled water flowing over a spot heater in a 1 mm × 40 mm rectangular channel. The lines represent the minimum superheat at which a cavity of a given size will nucleate. Hsu's model [9] and the truncated/stagnation model by Kandlikar et al. [8] yield very similar results, while Davis and Anderson's [7] model predicts somewhat higher wall superheat and Bergles and Rohsenow's [5] model predicts somewhat lower wall superheat.

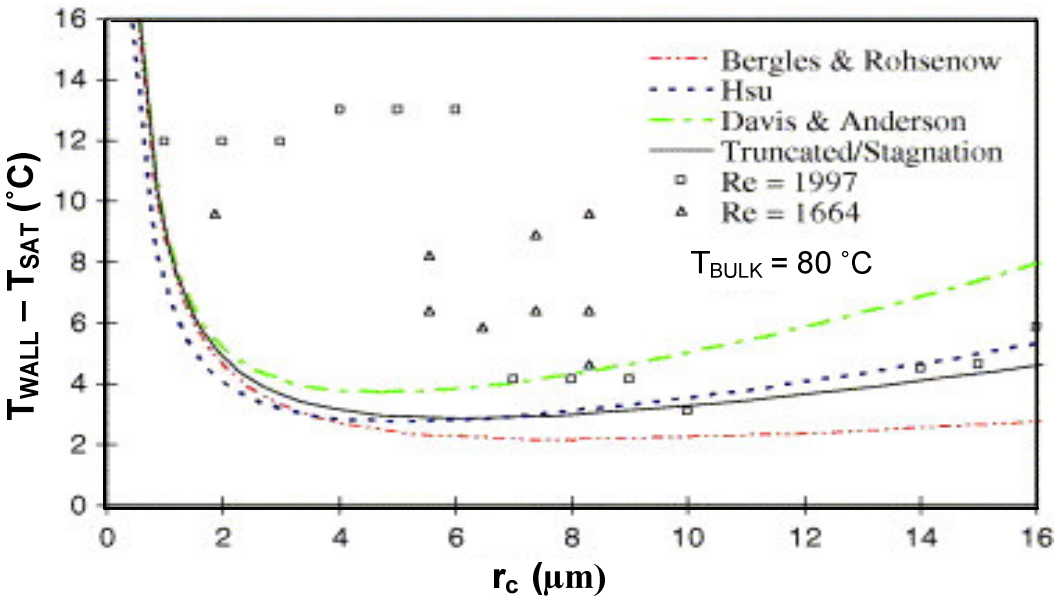

Figure 2.2 *Comparison of experimental data with different ONB models [8]. The lines represent the minimum superheat at which a cavity of a given mouth radius, r_c will nucleate.*

Figure 2.3 (a) shows the experimental results obtained by Kandlikar et al. [8] on the bubble growth rates as a function of Reynolds number with subcooled flow of water. The bubble growth time decreases with increasing Reynolds number. The authors observed also that the bubble frequency increased with Reynolds number. Figure 2.3 (b) shows the effect of increasing the wall temperature on the bubble growth rate.

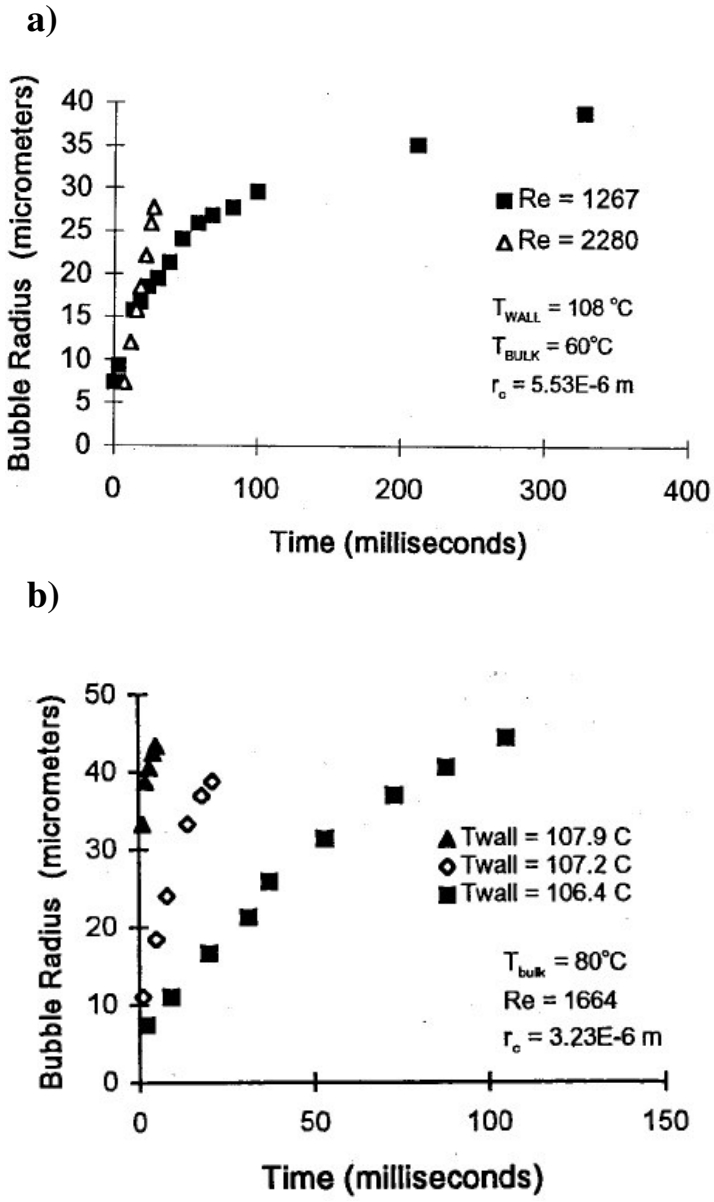

Figure 2.3 *Effect of Reynolds number on bubble growth (a), effect of wall temperature on bubble growth (b) [8].*

Further downstream from point A (Figure 2.1), as more energy is input into the liquid, more nucleation sites are activated and vapour bubbles remain predominantly attached to the wall surface. A thin layer of bubbles is formed on the wall. The contributions to heat transfer from the nucleate boiling continues to rise while the single-phase convective contribution diminishes. This region is called *partial boiling* region (between points A and B). At and beyond point B bubbles departing from the wall can survive condensation and enter the subcooled liquid. Point B is called point of *fully developed boiling* (FDP) or newly defined as the point of *onset of significant void* (OSV) [1, 10]. At and beyond point B the single-phase convective contribution becomes insignificant in comparison with the heat transfer from nucleate boiling. In the FDP region the wall temperature remains almost constant and the bulk liquid temperature is below the saturation temperature. It is a region of inherent non-equilibrium where the flowing mass quality and vapour void fraction are non-zero and positive even though the thermodynamic equilibrium quality and volume fraction would be zero since the bulk temperature is below saturation. The fully developed boiling has been studied extensively for water by earlier investigators in nuclear reactors applications. Saha and Zuber [11] proposed the empirical correlations for the determination of FDP point. The mechanist FDP models based on a force balance on bubbles that have nucleated on wall cavities have been proposed by Levy [12] and more recently by Rogers et al. [13]. Shah [14] has proposed an empirical correlation for transition from partial boiling to fully developed subcooled boiling. Kandlikar [15] proposed correlation for the fully developed boiling based on the nucleate boiling term in the saturated flow boiling correlation by Kandlikar [16].

In general, subcooled flow boiling improves the heat transfer rate significantly over the single-phase value. Therefore, subcooled flow boiling has received considerable attention in many industrial applications where high heat flux cooling is required.

2.2.2 Saturated flow boiling

Consider the case of a horizontal tube uniformly heated over its length with a constant heat flux (Figure 2.1). At some point along the tube, the thermodynamic equilibrium quality becomes positive and the bulk liquid temperature reaches the saturation temperature. The point C in Figure 2.1 denotes the demarcation between the subcooled and saturated flow boiling. Beyond point C along tube the vapour quality increases and the flow pattern changes. The saturated flow boiling refers to the entire region between the point were $x_{eq}=0$ and the *critical heat flux* (CHF). A convenient way to classify saturated flow boiling inside the tube according to the internal phase distribution are flow patterns (flow regimes). Figure 2.4 from Collier and Thome [17] depicts typical flow patterns and cross-sectional views of the flow structure, associated with flow boiling in a horizontal tubes.

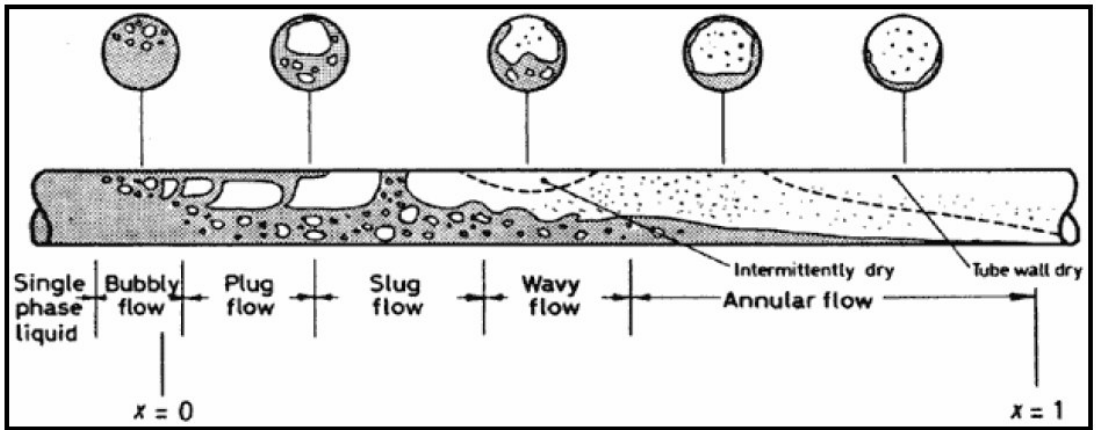

Figure 2.4 *Flow patterns during flow boiling in a horizontal tube [17]*

The patterns shown in Figure 2.4 are defined as follows [1, 17]:

- *Bubbly flow*. The gas bubbles are dispersed in the liquid phase; in horizontal tubes, these bubbles tend to congregate in the upper half of the tube because the buoyancy force. At higher mass flow rates, when shear forces are dominant, the bubbles tend to disperse uniformly in the tube.

- *Plug flow.* Here, the small bubbles coalesce to from elongated bubbles separated by the liquid plugs. The elongated bubbles are smaller than the tube. The bubbles tend to move to the upper half of the tube.
- *Slug flow.* In this flow regime, a higher vapour velocity causes increase in the bubbles diameters, which become similar in size to the channel height.
- *Stratified-wavy flow.* Stratified flow exists at low liquid and vapour velocities, when complete separation between vapour and liquid phase occurs. The liquid flows at the bottom of the tube and the vapour along the top part the tube, separated by undisturbed horizontal interface. At higher vapour velocity, waves are formed on the interface and travel in the direction of flow, giving the stratified-wavy or wavy flow regime.
- *Annular flow.* In this flow regime, the liquid phase flows as a film on the tube wall, and the vapour phase flows in the centre forming vapour core. The liquid film is thicker at the bottom than the top due to the effect of gravity. Usually, there is presence of the liquid droplets in the vapour core.
- *Mist flow.* This flow regime occurs at very high vapour velocities when only continuous vapour phase exists inside the tube.

The determination of the flow pattern has important roll in prediction of the void fraction, flow boiling heat transfer coefficients and two-phase pressure drop. The determination of flow patterns still depends largely on visual observation and it is therefore rather subjective. The usual method of representing data for various flow patterns and the transitions from one pattern to another is in the form of a flow pattern map. Taitel and Dukler [18] and Baker [19] flow regime maps are widely used for horizontal tubes. In the Baker map for air-water flow (Figure 2.5), the axes are defined in terms of G_g/λ and G_l/ψ, where G_g and G_l are mass flux of vapour and liquid phase respectively and

$$\lambda = \left(\frac{\rho_g \rho_l}{\rho_{air} \rho_{water}} \right)^{1/2} \tag{2.8}$$

and

$$\psi = \frac{\sigma_{water}}{\sigma}\left(\frac{\mu_l}{\mu_{water}}\left[\frac{\rho_{water}}{\rho_l}\right]^2\right)^{1/3} . \qquad (2.9)$$

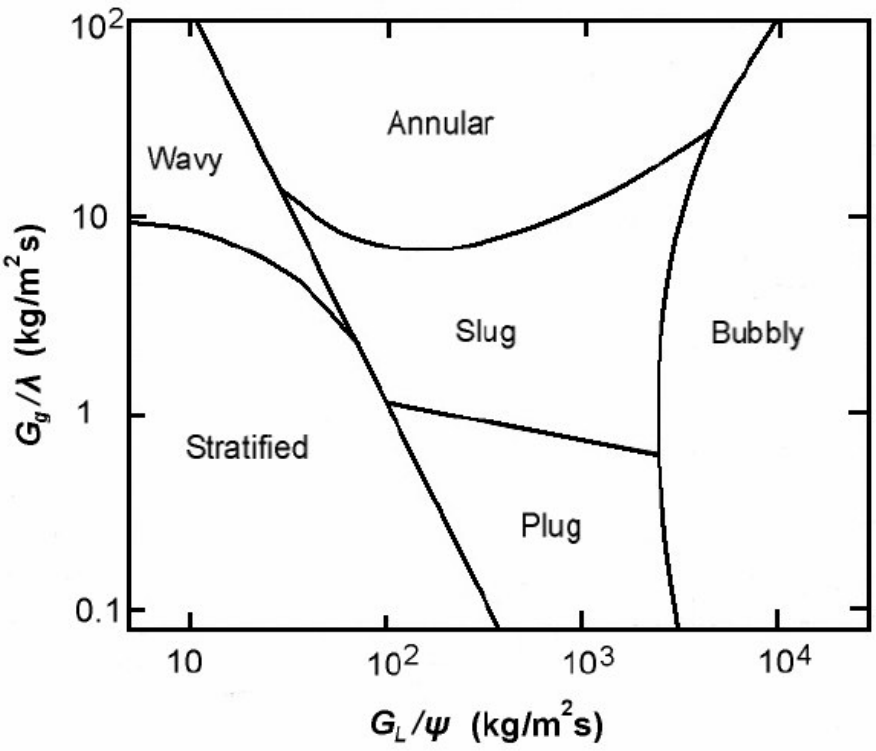

Figure 2.5 *Baker flow pattern map for horizontal tube, G_g is mass flux of vapour phase, G_L is mass flux of liquid phase, λ and ψ are given by equations 2.8 and 2.9 respectively [19].*

Kattan et al. [20] developed a flow pattern map valid for small diameter tubes typical of shell-and-tube heat exchangers for both adiabatic and two-phase boiling flow. This flow pattern map includes the prediction of the onset of dryout at the top of the tube during flow boiling inside horizontal tubes as a function of heat flux and flow parameters.

Heat transfer in the saturated flow boiling is a combination of the nucleate boiling at the wall and the convective heat transfer from the wall to the liquid [17]. At low vapour quality when bubbly flow regime occurs, the nucleate boiling mechanism dominates. The heat transfer coefficient is dependent upon heat flux and by far less sensitive to mass flux and vapour quality. As the vapour quality increases,

the convective heat transfer becomes dominant over the nucleate boiling contribution. Once the annular flow regime is achieved, the convective heat transfer becomes the major mechanism. The heat transfer coefficient becomes dependent upon mass flux and vapour quality, but fairly independent of heat flux. In general, there are two approaches for estimating heat transfer in two-phase flow [1]. In flow regime dependent model, the flow regime is first predicted and the associated model for that flow regime is employed. In the second approach the heat transfer coefficient is directly estimated from the flow parameters without flow regime analysis. The correlation widely used for saturated boiling is the Chen correlation [21], based on the additive model where the total heat transfer coefficient is the sum of the nucleate boiling and convective boiling contributions. Schrock and Grossman [22] proposed an additive model for heat transfer with the boiling number, *Bo*, and the turbulent-turbulent Lockhart-Martinelli parameter X_{tt} as parameters. The boiling number is defined as follows:

$$Bo = \frac{q}{Gh_{\mathrm{lg}}}, \tag{2.10}$$

and the Lockhart-Martinelli parameter:

$$X_{tt} = \left(\frac{\rho_g}{\rho_l}\right)^{0.5}\left(\frac{\mu_l}{\mu_g}\right)^{0.1}\left(\frac{1-x}{x}\right)^{0.9}. \tag{2.11}$$

Kandlikar [16] used a similar concept as Schrock and Grossman and provided the correlation based on 10000 data points covering water, refrigerants and cryogenic fluids. The most commonly used flow regime dependant correlations are Kattan et al. [23], Zurcher et al. [24], and Wojtan et al. [25] correlations. The flow regime map associated with Wojtan et al. correlation for saturated boiling of R-22 in a horizontal pipe is shown in Figure 2.6 [26] .

In general, two-phase flow pressure drop is evaluated by analogy with the evaluation of single-phase pressure drop where a single-phase friction factor is used. Two-phase friction pressure drop is expressed in terms of single-phase pressure drop for the total flow considered as liquid and a suitably defined two-phase friction factor [17]. The two-phase friction factor is known as the two-phase friction multiplier Φ^2

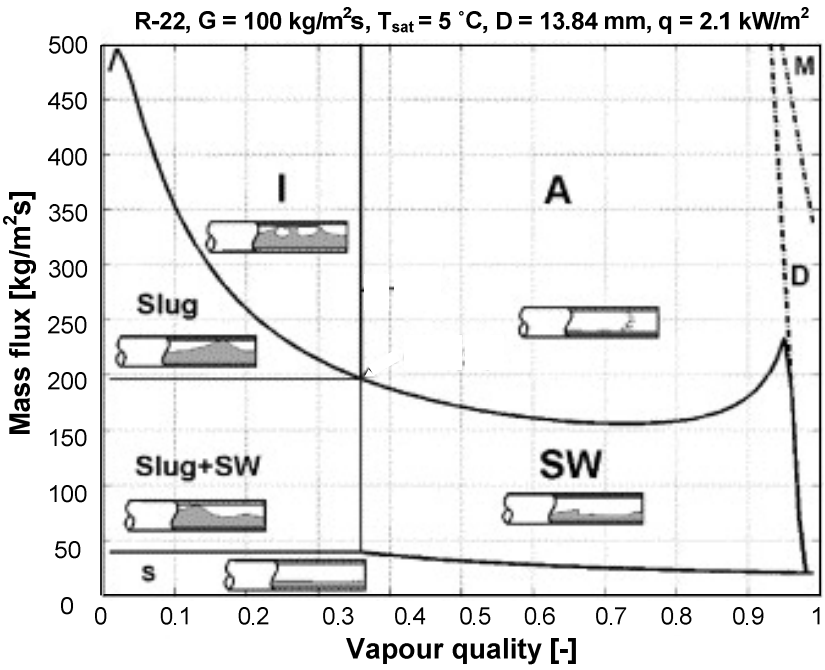

Figure 2.6 *The flow regime map of Wojtan et al. [26] for saturated boiling of R-22 in a horizontal pipe. I denotes intermittent regime, A annular regime, SW stratified wavy regime, M mist regime, D dryout regime.*

and its estimation depends on the two-phase flow model. *The homogenous model* considers the two-phase flow as a homogenous mixture of vapour and liquid with equal vapour and liquid linear velocities. The following relation is obtained for this model by assuming the same viscosity as the liquid phase [1]:

$$\phi^2 = 1 + \left(\frac{\rho_l}{\rho_g} - 1 \right) x \tag{2.12}$$

The separated flow model considers the phases to flow in separate regions of the tube while still interacting at the interface between the regions. Correlation for the two-phase friction multiplier widely used for the separated model is based on the Lockhart-Martinelli parameter *X*. Chisholm [27] correlated the multiplier Φ^2 as a function of the Lockhart-Martinelli parameter X as follows:

$$\phi^2 = 1 + \frac{C}{X} + \frac{1}{X^2}, \tag{2.13}$$

where C is a dimensionless parameter whose value depends on the regime of the phase-alone flows (viscous or turbulent, e.g. 20 for turbulent-turbulent flow).

2.2.3 Critical heat flux (CHF) in flow boiling

Critical heat flux is the most important boundary condition when considering the performance of heat exchangers that utilize flow boiling. CHF generally refers to a condition that causes a sudden, significant decrease in the heat transfer coefficient. For a heat flux controlled system, the sudden decrease in the heat transfer coefficient leads to a sudden large increase in the wall temperature that can lead to heat exchanger failure. Therefore, CHF determination represents the upper limit for the safe operation of the heat sinks that utilize flow boiling heat transfer. CHF can occur under subcooled or saturated flow boiling conditions.

Subcooled CHF refers to the process called the *departure from nucleate boiling* (DNB), when bubbles form a layer covering a significant area of the heated wall. This leads to an appreciable decrease in the heat transfer coefficient from the wall to the liquid and a sharp increase in the wall temperature, even though the bulk flow liquid may still be highly subcooled. A large mass flux, high inlet subcooling, and/or channels with a small length-to-diameter ratio are conditions that often lead to subcooled CHF. Several theories have been proposed to explain the main cause of subcooled CHF [1]: the bubble-liquid layer adjacent to the wall causes the stagnant liquid to evaporate [28]; the liquid flow normal to the wall is blocked by the bubble crowding near the heated wall [29]; and the dryout of a thin liquid sublayer beneath elongated bubble causes the appreciable rise in the local wall temperature [30].

Saturated CHF can occur under saturated flow boiling conditions when the bulk liquid temperature is above the saturation temperature and the thermodynamic equilibrium quality is non-zero and positive. Small mass flux, low inlet subcooling, and/or channels with a large length-to-diameter ratio are conditions that usually lead to saturated CHF. In general, there are two different types of saturated CHF [1]. The DNB type is typically encountered at low quality values when bubbly flow is present. The second type of saturated CHF is the dryout type that occurs in high vapour quality flow associated with annular flow regime. As vapour quality at CHF increases, dryout type dominates over DNB type. When the exit quality is greater

than 10% then most CHF cases are associated with annular flow regime and the dryout type of CHF [1]. The gradual depletion of the liquid film near the outlet is widely regarded as the mechanism for the dryout type of saturated CHF [17, 31].

2.2.4 Two-phase flow instabilities

Two-phase flow instabilities refer to fluctuations of flow rate and system pressure. Such fluctuations are undesirable as they can lead to high amplitude temperature oscillations with premature critical heat flux (CHF) and mechanical vibrations. These vibrations, together with the thermal stress set up in the heat exchanger material, can cause heat exchanger burnout and mechanical breakdown. A two-phase flow system is considered stable, when disturbed, the new operating conditions tend to the original ones. The two-phase system is called unstable when for any applied disturbance a jump from one state to another is observed. Ledinegg [32] pioneered the concept of two-phase flow instabilities in tubes. He studied in particular flow-excursion instability. This instability occurs when the slope of the channel characteristic curve is negative and steeper than the pump characteristic curve (Figure 2.7). Points A and C are stable operating conditions for any applied flow disturbance, while point B is unstable operating conditions and any disturbance leads to operating conditions either A or C.

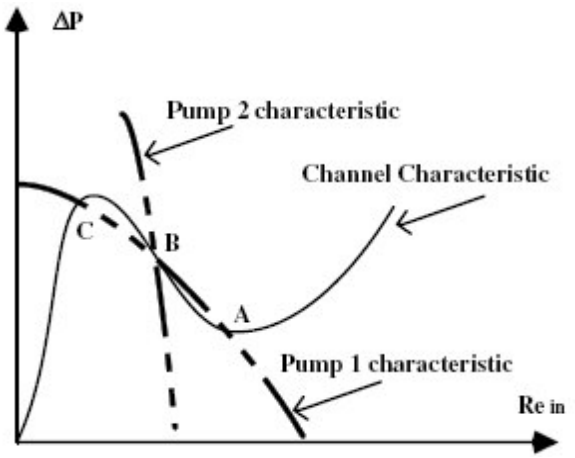

Figure 2.7 *Two-phase pressure characteristic of the pump and a channels versus the inlet Reynolds number [33].*

Flow extrusion instabilities are considered as static instabilities. The instability is considered as static when, for any applied disturbance, the system tends toward the new steady operating conditions that are different from the original ones. The second group of instabilities includes dynamic two-phase flow instabilities and pressure drop instabilities. Dynamic instabilities result from multiple feedbacks between flow rate, pressure drop and change in density due to vapour generation. The most common dynamic inabilities are density wave oscillations. These instabilities occur when a decrease in flow rate brings a rise of the fluid enthalpy and a decrease in the density affecting the channel pressure drop. This leads to self-sustained oscillations of the flow rate and the pressure drop as shown in Figure 2.8a. Pressure drop oscillations are one type of dynamic instabilities commonly related to two-phase boiling flow besides the density wave oscillations. This oscillations result from the interaction between the channel and the compressible volume. Typical recordings of the pressure drop oscillations are shown in Figure 2.8b. The density wave oscillations appear on the positive slope of the pressure drop versus mass flow rate curve, while the pressure drop type oscillations are observed only for those conditions where the pressure drop versus mass flow rate curve has a negative slope [34].

2.3 Flow boiling in microchannels

It has been already pointed out that the behaviour of flow boiling in microscale tubes can differ significantly from macroscale ones. The reasons for such difference are the change in the dominant force when passing from the macroscale to the microscale. Surface tension forces become more important and gravitational forces diminish. While the methods developed for single-phase flow in macroscale tubes are applicable to single-phase in microscale tubes (at least for diameters above 5-10 μm), macroscale flow boiling models usually are not valid in the case of flow boiling in tubes below about 3 mm in diameter [2]. Flow pattern maps, heat transfer methods and pressure-drop models developed for the flow boiling in macroscale usually are not applicable to microscale flow boiling. From a practical point of view,

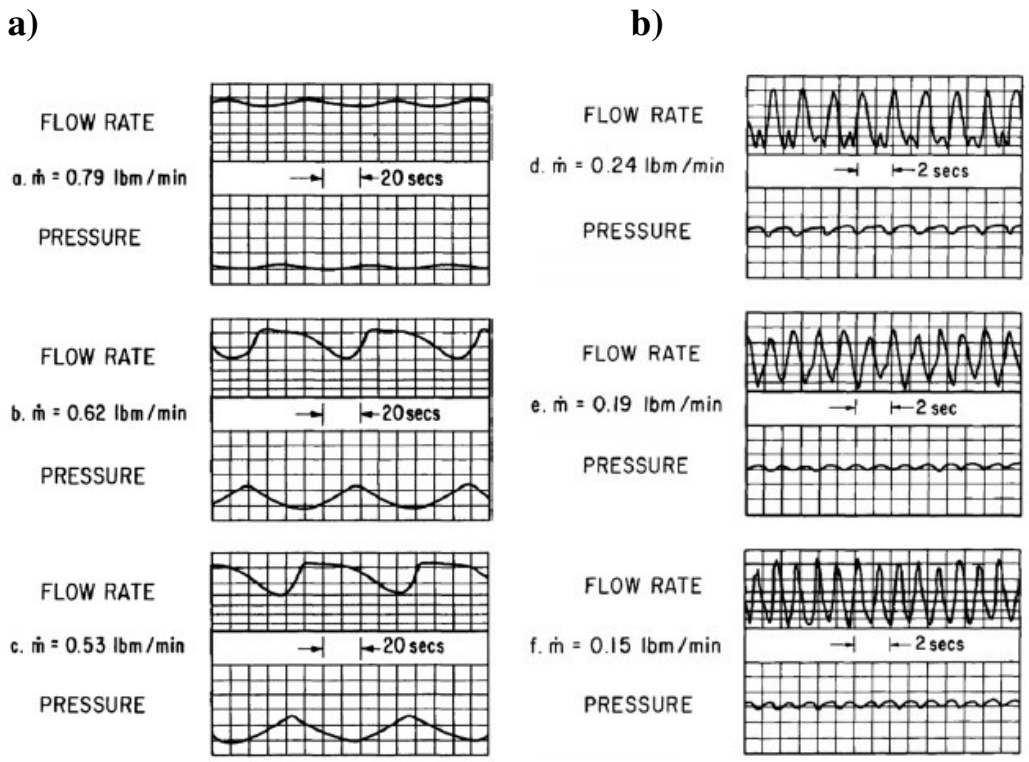

Figure 2.8 *Typical recordings of density wave oscillations (a) and pressure-drop oscillations (b) [34].*

Kandlikar [35] proposed the following classifications based on channel hydraulic diameter:

- Conventional channels, larger than 3 mm;
- Minichannels, from 200 μm to 3 mm;
- Microchannels, from 10 to 200 μm.

As opposed to multiple bubbles in macroscale flow boiling, the bubble growth in microchannels is confined and only one bubble can exist in the channel cross section. Therefore, a macro-to-micro criterion might be related to the point at which the bubble departure diameter reaches that of the channel [36]. Kew and Cornwell [37] suggested using a confinement number *Co* as a criterion of a macro-to-micro scale transition, defined as follows:

$$Co = \left[\frac{\sigma}{g\left(\rho_L - \rho_g\right) D_h^{\,2}} \right]^{1/2}. \tag{2.14}$$

The authors found that the behaviour of flow boiling was significantly different from macrochannels for $Co > 0.5$. The confinement number is similar to the Eotvos (Bond) Eo number that represents the ratio of buoyancy force to surface tension force.

$$Eo = \frac{g\left(\rho_l - \rho_g\right)D_h^{\,2}}{\sigma} \tag{2.15}$$

Kawaji and Chung [38] recommended a criterion for the threshold between the macroscale and microscale two-phase flow based on a set of six dimensionless numbers relevant to two-phase flow (Eotvos number, superficial liquid and vapour Weber numbers, superficial liquid and vapour Reynolds numbers, and Capillary number) and the superficial vapour and liquid velocities.

$$Eo = \frac{g\left(\rho_l - \rho_g\right)D_h^{\,2}}{\sigma} << 4 \tag{2.16a}$$

$$We_{SL} = \frac{\rho_l U_l^{\,2} D_h}{\sigma} << 1 \tag{2.16b}$$

$$We_{SG} = \frac{\rho_g U_g^{\,2} D_h}{\sigma} << 1 \tag{2.16c}$$

$$\mathrm{Re}_{SL} = \frac{\rho_l U_l D_h}{\mu_l} < 2000 \tag{2.16d}$$

$$\mathrm{Re}_{SG} = \frac{\rho_g U_g D_h}{\mu_g} < 2000 \tag{2.16e}$$

$$Ca = \frac{\mu_l U_L}{\sigma} << 1 \tag{2.16f}$$

$$U_G = \frac{Q_g}{A} \tag{2.16g}$$

$$U_L = \frac{Q_l}{A} \tag{2.16h}$$

These five criteria can be applied to further refine the microscale threshold analysis, after applying first the Kew and Cornwell criterion [2].

2.3.1 Flow boiling patterns in microchannels

Although the nucleation criteria based on Hsu's analysis might be applicable to micro-scale flow boiling (Kandlikar [39] proposed the modified bubble nucleation model of Hsu for micro-scale flow boiling), bubble growth following nucleation is restrained by the channel wall. Lee at al. [40] investigated experimentally bubble dynamics during flow boiling inside a single trapezoid microchannel with a hydraulic diameter of 41.3 μm. The authors studied bubble growth rate, bubble departure size and bubble frequency. They reported two bubble growth stages: the isotropic growth stage when the bubble retained a spherical shape, and anisotropic growth shape, when the bubble appeared distorted due to the limitation of channel depth and flow drag. The bubble growth rate was found to be constant, inertia controlled and much smaller than that predicted by the Rayleigh equation. The authors found that the bubble frequency in microchannels is comparable to that in a macro-scale channel. However, they were unable to correlate the bubble departure frequency with corresponding diameter. The evaporation of microlayer underneath the growing bubble has been demonstrated to play a significant role in bubble growth inside macro-scale tubes [41]. However, results obtained by Lee et al. [40] indicate that the microlayer may not be present in microchannels, although the images captured by high speed camera were not clear enough to confirm the presence or absence of the microlayer. Similar to that in a single microchannels Li et al. [42] found linear bubble growth rate in two parallel channels with the bubble departure also governed by surface tension and drag force due to bulk flow. Figure 2.9 shows time evolution of bubble radius for two different heat fluxes measured by Li et al. [42] .

A two-phase flow microchannels heat sink usually operates with a low flow rate due to practical reasons for lower pressure drop across the heat sink. The liquid flow is laminar in most test conditions, with typical range of liquid Reynolds number from 100 to 4000 [36]. Therefore, it is not reasonable to apply flow pattern transition models and flow pattern maps developed for two-phase flow in macro-scale, which is usually in turbulent flow regime. In addition, surface tension forces become

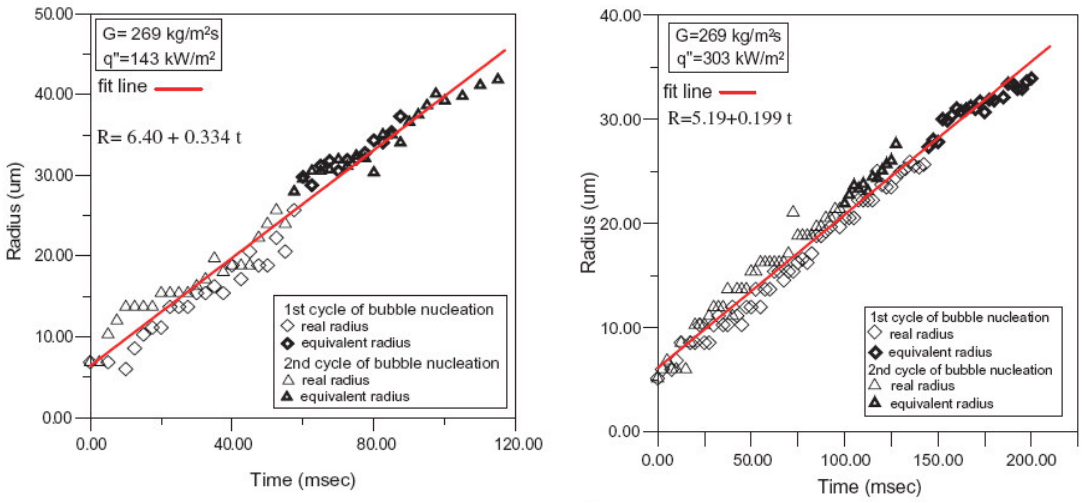

Figure 2.9 *Typical time evolution of bubble radius for G = 269 kg/m^{2}s and two different heat fluxes [42].*

important, eliminating stratified flow regime in microchannels. Earlier investigators of the two-phase flow patterns in channels with small hydraulic diameter observed bubbly, plug, slug and annular flow patterns [43]. Stratified flow was not observed in most of the investigations due to the dominance of surface tension [44]. Kasza et al. [45] observed nucleate boiling in a rectangular flow channel of 2.5 × 6 mm^2 using a high speed video camera. The authors reported the nucleate boiling in thin liquid films that existed in both slug flow and annular flow conditions. This observation indicates that the nucleating bubbles may be present under highly sheared flow conditions in microchannels such as annular and slug flow conditions. The authors observed the stratified flow at a very low mass flux of 21 kg/m^{2}s. Cornwell and Kew [46] carried out experiments with R-113 flowing in 1.2 × 0.9 mm^2 rectangular parallel channels. The authors identified three flow patterns: isolated bubbles, confined bubbles, and slug/annular flow. They observed in the isolated bubble region that the heat transfer was strongly dependent on the heat flux applied, while in the slug/annular region, the heat transfer coefficient dependence on the heat flux diminished. Some authors have identified new flow patterns inside microchannels. Feng and Serizava [47] observed several distinctive flow patterns in microchannel circular glass tubes, namely, dispersed bubbly flow, gas slug flow, liquid ring flow, liquid lump flow, annular flow, frothy or wispy annular flow, rivulet flow, and liquid droplets flow in air–water and steam–water systems. The liquid ring and liquid lump

flows occurred as a transition flow patterns between elongated bubble flow and annular flow. Figure 2.10 shows typical air-water two-phase flow patterns observed

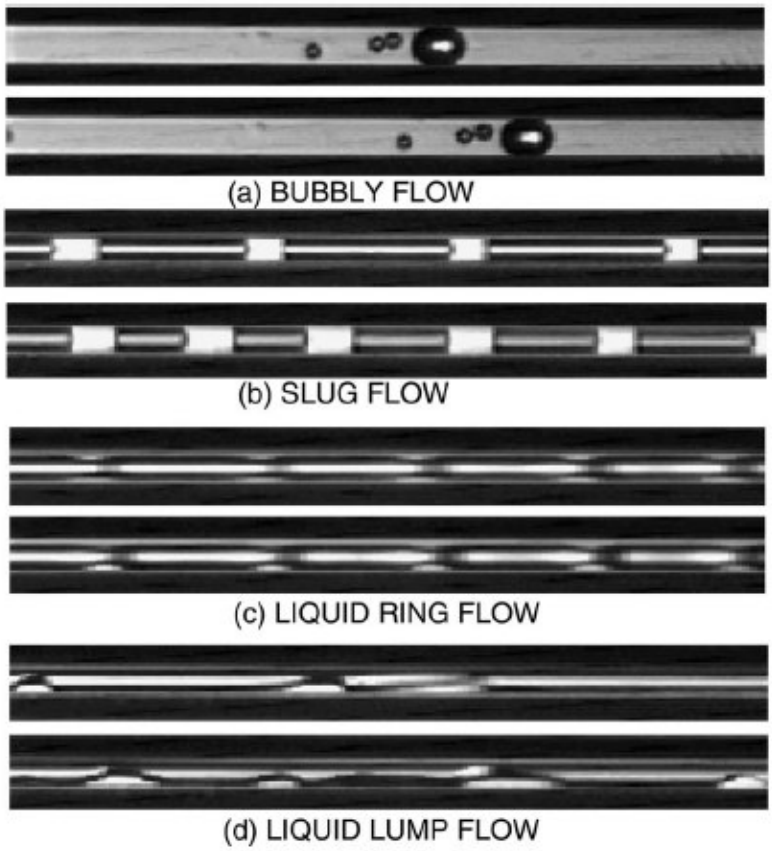

Figure 2.10 *Microchannel flow patterns observed by Feng and Serizava [47].*

by Feng and Serizava in a 25 μm glass tube at nearly atmospheric pressure. Coleman and Garimella [48] classified their observation of two-phase flow in tubes with small hydraulic diameter into bubble, dispersed, elongated bubble, slug, stratified, wavy, annular–wavy, and annular flow patterns. The authors presented adiabatic flow pattern map for two-phase flow in circular and rectangular tubes of small hydraulic diameters. Their channel dimensions ranged from 1 to 4 mm and hence they observed some stratified flows for some test conditions. Revellin et al. [49] used an optical measurements system to characterise diabatic two-phase flow patterns in a

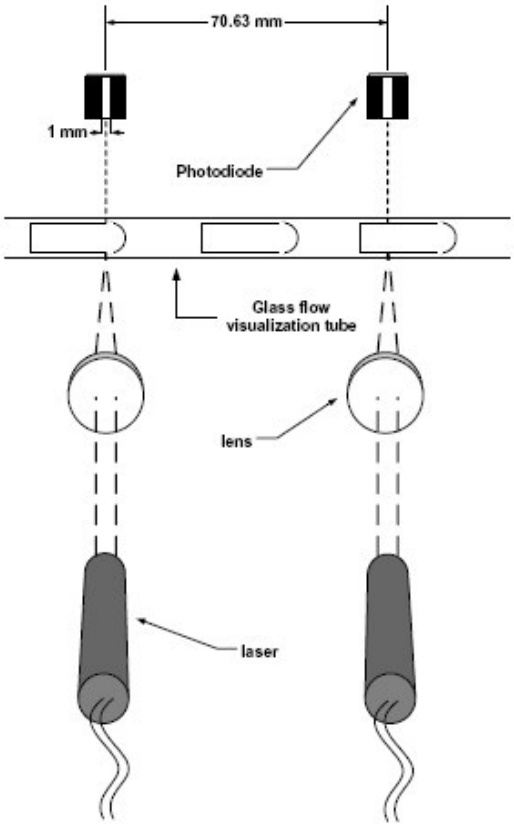

Figure 2.11 *Schematic of the optical measurements system used by Revellin et al. [49].*

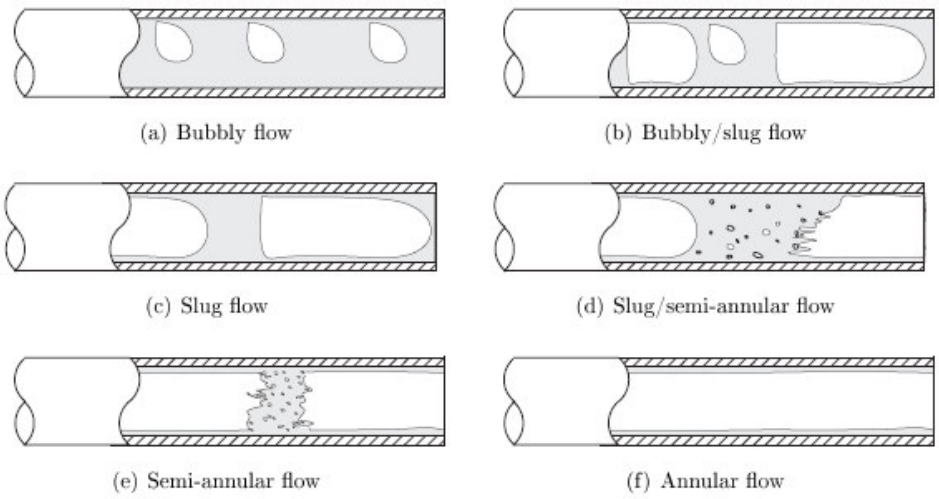

Figure 2.12 *Schematic of flow patterns and transitions [49].*

0.5 mm glass tube with R-134a flow. Using two laser/two diodes technique schematically shown in Figure 2.11, the authors were able to determine bubble frequency, lengths of bubbles and flow pattern transition parameters. Four principal flow patterns (bubbly flow, slug flow, semi- annular flow and annular flow) with their transitions (bubbly/slug flow and slug/semi-annular flow) were observed as shown in Figure 2.12. Revellin and Thome [50] developed a flow pattern map (Figure 2.13) for boiling flows in microchannels based on data for two refrigerants (R-134a and R-245fa), two channel diameters (0.509 and 0.790 mm), various micro-evaporator heater length (20-70 mm), mass fluxes from 210 to 2094 kg/m^{2}s, and uniform heat fluxes from 3.1 to 597 kW/m^2 always at the stable flow conditions. The authors classified flows into four regimes: isolated bubble regime (includes both bubbly or/and slug flow), coalescing bubble regime (slug and churn flow), annular flow regime, and dryout regime.

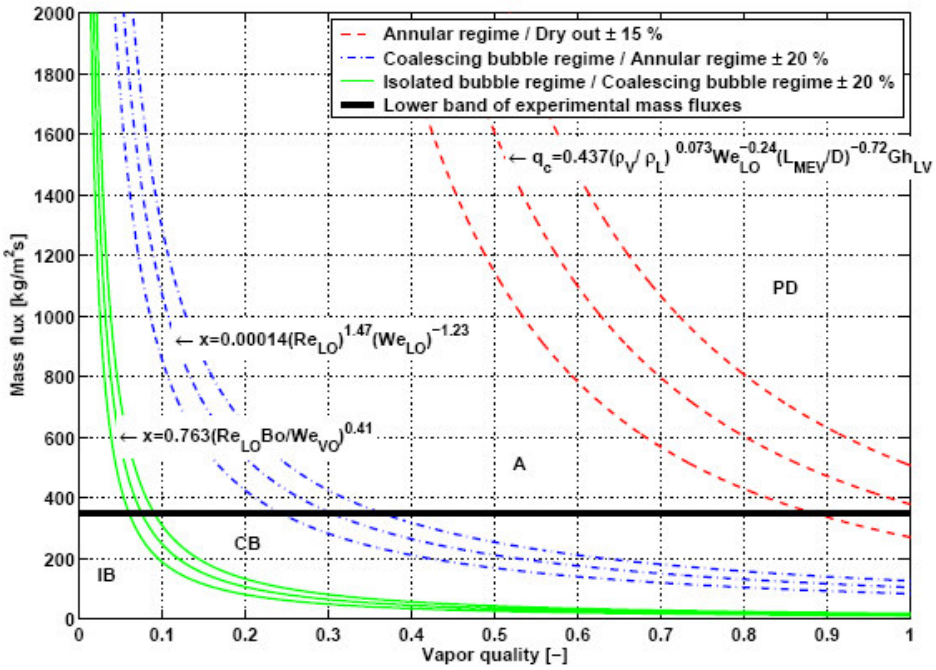

Figure 2.13 *Flow pattern map of Revellin and Thome [50] for evaporating flow in microchannels. IB: Isolated bubble regime, CB: Coalescing bubble regime, A: annular regime, PD: post dryout regime.*

2.3.2 Flow boiling instabilities in microchannels

Two-phase flow instabilities in minichannels and microchannels are more intense than in conventional channels due to the low flow velocities and the confined space available for bubbles growth. These instabilities with characteristic pressure drop and flow rate oscillation are undesirable, as they can lead to high amplitude temperature oscillations with premature critical heat flux (CHF) and heat exchanger burnout. The flow boiling instabilities result in a lower CHF than would be obtained with stable flow in the microchannels based heat sink [51]. Instabilities in microchannels have been reported by many authors, but in many cases with different oscillation amplitude and frequency under similar mass and heat flux conditions.

Qu and Mudawar [52] have investigated hydrodynamic instability and pressure drop in a water-cooled two-phase microchannel heat sink containing 21 parallel 231×713 μm microchannels. Figure 2.14 shows construction of the test module used in their experiments. The authors reported two types of two-phase hydrodynamic instability. The severe pressure drop instabilities were attributed to interaction between the vapour generated within the channels and the compressible volume of the inlet manifold. The second type of instabilities were the mild parallel channel instabilities, observed when the valve installed immediately upstream of the heats sink was throttled. A schematic of the observed two-phase flow instabilities in two neighbouring channels within a short time interval (about 1–5 s) is illustrated in Figures 2.15 (a) and (b). Temporal behaviour of inlet and outlet pressures under the severe pressure drop oscillations and mild parallel channel instability is shown in Figures 2.16 (a) and (b), respectively. Explosive generation of vapour and the temporal behaviour of temperature and pressure in parallel triangular microchannels have been observed by Hetsroni et al. [53-56]. The authors have observed the periodic refilling and rewetting phenomena regarded as explosive boiling. They found that the amplitude and periods of pressure drop oscillations increased with increasing heat flux and vapour quality at constant values of mass flux.

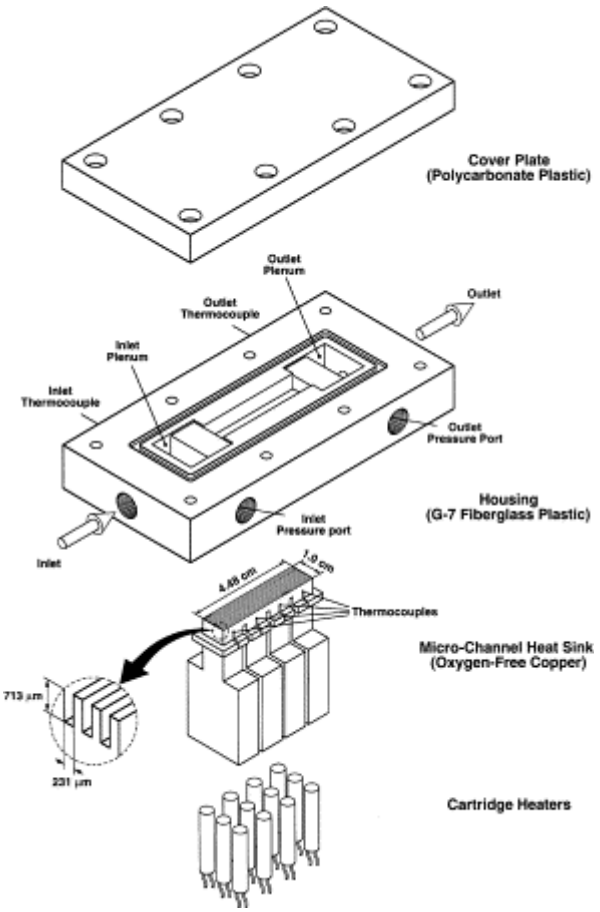

Figure 2.14 *Test module construction used by Qu and Mudawar [52].*

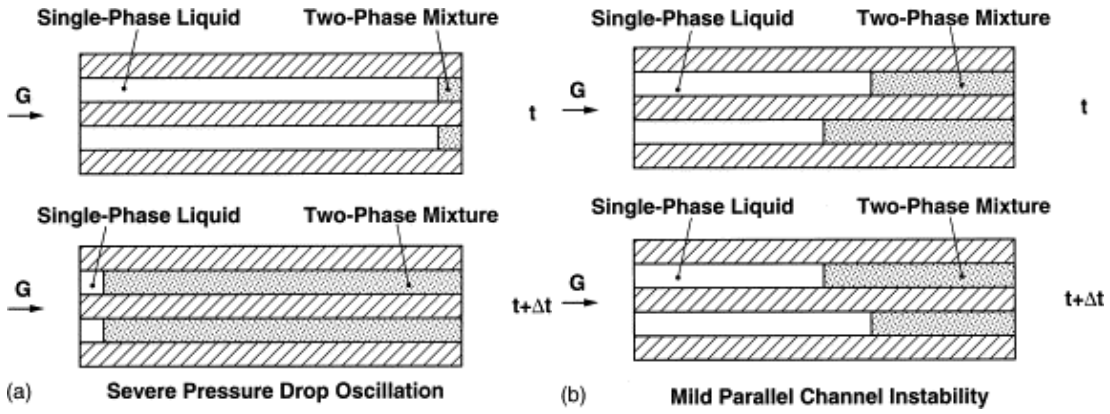

Figure 2.15 *Schematic of neighbouring microchannels illustrating (a) severe pressure drop oscillations and (b) mild parallel channel instability [52].*

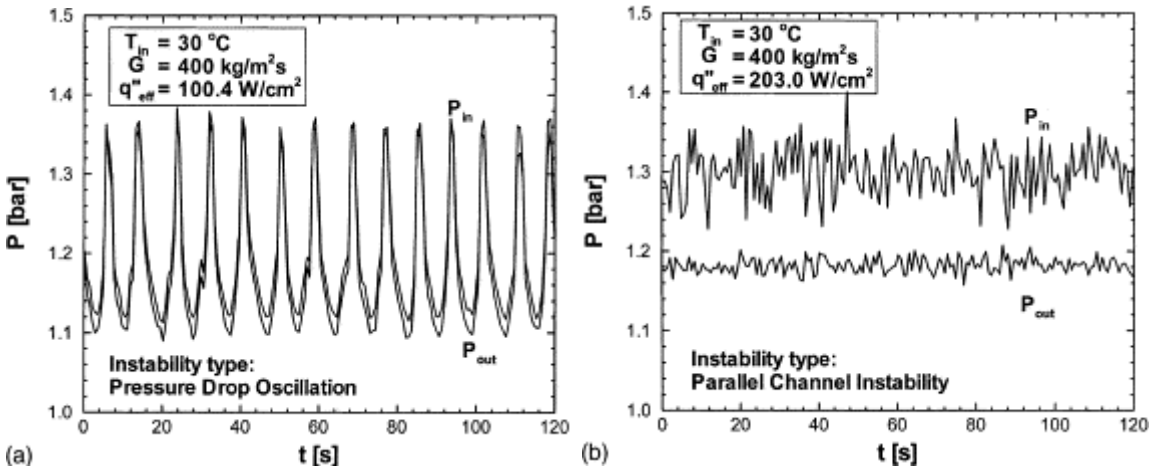

Figure 2.16 *Temporal records of inlet and outlet pressures during (a) pressure drop oscillation and (b) parallel channel instability [52].*

However, time interval between two successive events was found to decrease with an increase in the boiling number. The authors defined initial liquid thickness as the average thickness of the fluid, evenly distributed over the surface of the circular microchannel, after venting of the elongated bubble during the explosive boiling. The initial thickness of the liquid film was found to decrease with increasing heat flux. Kandlikar et al. [57] performed visualisation of the flow boiling inside six parallel channels using high speed camera. The authors noted large amplitude pressure oscillations and flow reversal caused by vapour slug expansion in both upstream and downstream directions. Wu and Cheng [58] reported three oscillatory flow boiling modes in microchannels depending on the heat to mass flux ratio. These were: (1) the liquid/two-phase alternating flow at low heat flux and high mass flux, (2) the continuous two-phase flow at medium heat flux and medium mass flux, and (3) the liquid/two-phase/vapour alternating flow at high heat flux and low mass flux. The authors used a standard pressure transducers and thermocouples for simultaneous measurements of temperatures and inlet/outlet pressure. It was found that mass flux and pressure oscillated out of phase in these three boiling modes, and the large amplitude oscillations of pressure and temperature could be self-sustained. Wang et

al. [59] experimentally investigated dynamic instabilities of flow boiling of water in parallel microchannels as well as in a single microchannel. The authors classified flow boiling regime into stable and unstable, depending on the heat to mass flux ratio. Two types of unstable oscillations were reported, one with long-period oscillations and another with short-period oscillations in temperature and pressure. Wang et al. [60] suggested that the configurations between the inlet and outlet regions with microchannels can significantly influence the type of instabilities observed. The authors investigated effects of different inlet/outlet configurations, schematically shown in Figure 2.17, on two-phase flow instabilities in microchannels. In the microchannel heat sink with Type-A connection (Figure 2.17 (a)) where the inlet/outlet conduits are perpendicular to microchannels, the amplitudes of pressure and temperature fluctuations were the highest among the three types of connections. In the heat sink with Type-C connections and orifices installed at the inlet of each channel, nearly steady flow boiling existed with no oscillation of temperature and pressure. The authors recommended this configuration for high heat flux microchannel applications.

Flow instabilities have been observed during flow boiling inside a single microchannel with periods ranging from hundreds of seconds (indicating interactions with external flow circuit) to milliseconds associated with bubble nucleation and growth. Instabilities inside a single microchannel occur if incompressible volume exists in the upstream external circuit. Kenning et al. [61, 62] and Brutin and Tadrist [63] observed severe pressure drop instabilities in a single channel flow boiling when a large compressible volume existed at upstream location from the channel. The authors found that the high frequency fluctuations in pressure were associated with the upstream compressibility. Zhang et al. [64] have used doped silicon sensors to measure transient pressure fluctuations frequencies during boiling in a single microchannel with water as the working fluid. The authors observed frequencies ranging from 3 to 40 Hz, and recorded up to 138 kPa transient pressure fluctuations. However, the microfabricated sensors were sensitive to both temperature and pressure, causing problems in separating the simultaneous effects of one bubble on pressure and temperature measurements.

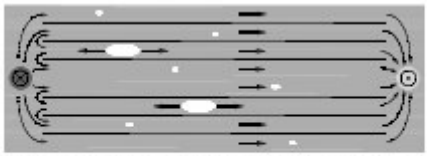

(a) Type-A connections: flow entering and exiting from parall microchannels with restrictions because inlet/outlet conduits perpendicular to microchannels

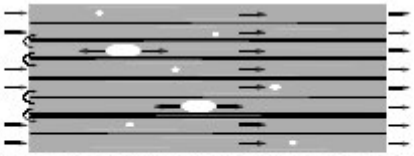

(b) Type-B connection: flow entering to and exiting from microchannels freely without restriction

.

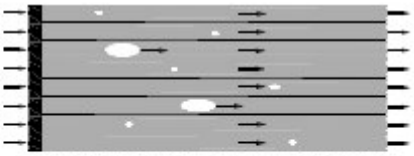

(i) Arrangement of parallel microchannels with restrictive inlet

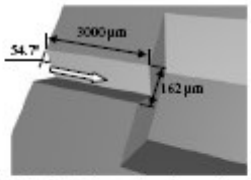

(ii) Sketch of the microchannel with a restrictive inlet

(c) Type-C connection: flow entering with restriction and exiting without restriction in microchannels

Figure 2.17 *Different inlet/outlet configurations investigated by Wang et al. [60].*

Kandlikar et al. [65] have assessed the effects of an inlet pressure restrictor and fabricated nucleation sites as a means of stabilizing the two-phase flow instabilities in microchannels. The authors found that fabricated nucleation sites in conjunction with the pressure restrictor having a flow area of 4% of the channel cross-sectional area completely eliminated the instabilities associated with reverse flow. However, the introduction of nucleation sites alone increased the instabilities, while nucleation sites in conjunction with the only 51 % restriction partially reduced the instabilities. Kosar et al. [66] have experimentally investigated the effects of inlet orifices with various geometries on the suppression of flow boiling instabilities in parallel microchannels. The schematic drawing of their experimental device is shown in Figure 2.18. They have shown that for sufficiently high inlet pressure restriction imposed by the inlet orifices, parallel channels and upstream compressible volume instabilities are eliminated. Kuo and Peles [67] experimentally studied the effects of

pressure on flow boiling instabilities in microchannels. They found that high system pressure moderates instabilities by reducing the void fraction, the superheat needed to activate bubble nucleation and bubble departure diameter. Local transient temperature measurements showed lower magnitudes and higher frequencies of oscillations at high system pressure.

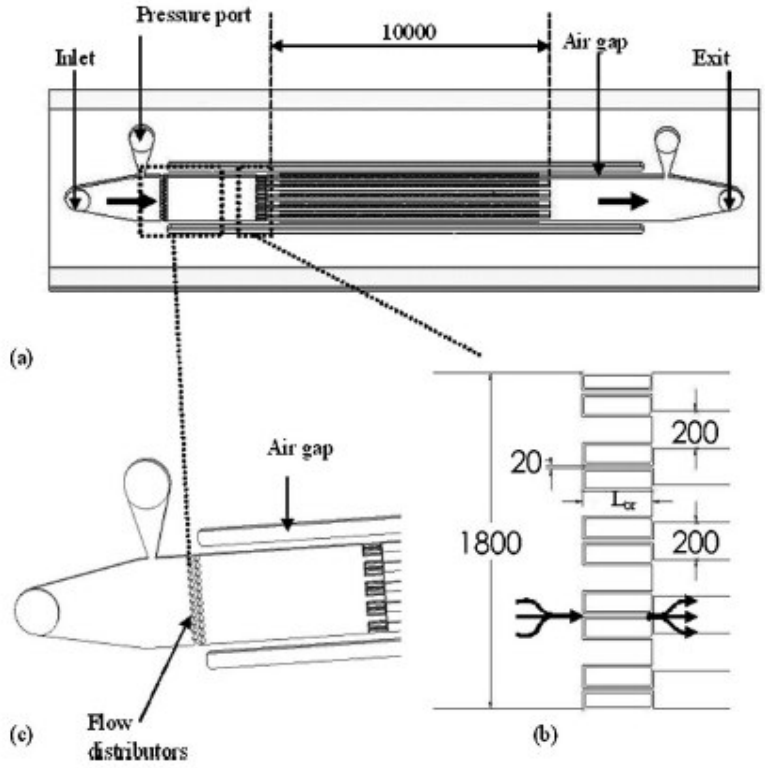

Figure 2.18 *(a) Schematic illustration of the device used by Kosar et al. [66] (b) Geometry of the inlet orifices (c) Flow distributive pillars located at inlet manifold.*

2.3.3 Flow boiling heat transfer in microchannels and models applied in microchannels

Although, numerous experimental studies of flow boiling heat transfer in minichannels and microchannels are available, there is disagreement among authors as to the mechanism of heat transfer. While some authors believe that the nucleate boiling is the dominant mechanism of heat transfer [68-70] other authors point out to the forced convective boiling as the dominant heat transfer mechanism [71-73]. An

additional problem in the investigation of flow boiling heat transfer in microchannels is the oscillatory nature of the flow. The flow pattern during flow instabilities inside microchannels is a combination of different flow patterns rather than a clearly defined one. This implies difficulties in assessment of experimental data as well as in modelling of the heat transfer in microchannels.

Bao et al. [70] investigated local heat transfer coefficients for R-11 and R-123 inside a copper tube with a diameter of 1.95 mm. The authors observed that heat transfer coefficients strongly depended on heat flux and increased with saturation pressure. However, the influence of vapour quality and mass flux were very small. Following an analogy with macroscale flow boiling, the authors concluded that nucleate boiling was the dominant mechanism of the heat transfer process. Figure 2.19 shows the effects of mass flux and heat flux on flow boiling data of Bao et al. Similar to this study, Tran et al. [69] found that nucleate boiling was always the dominant mode of heat transfer for R-12 flow boiling in a 2.46 mm circular channel.

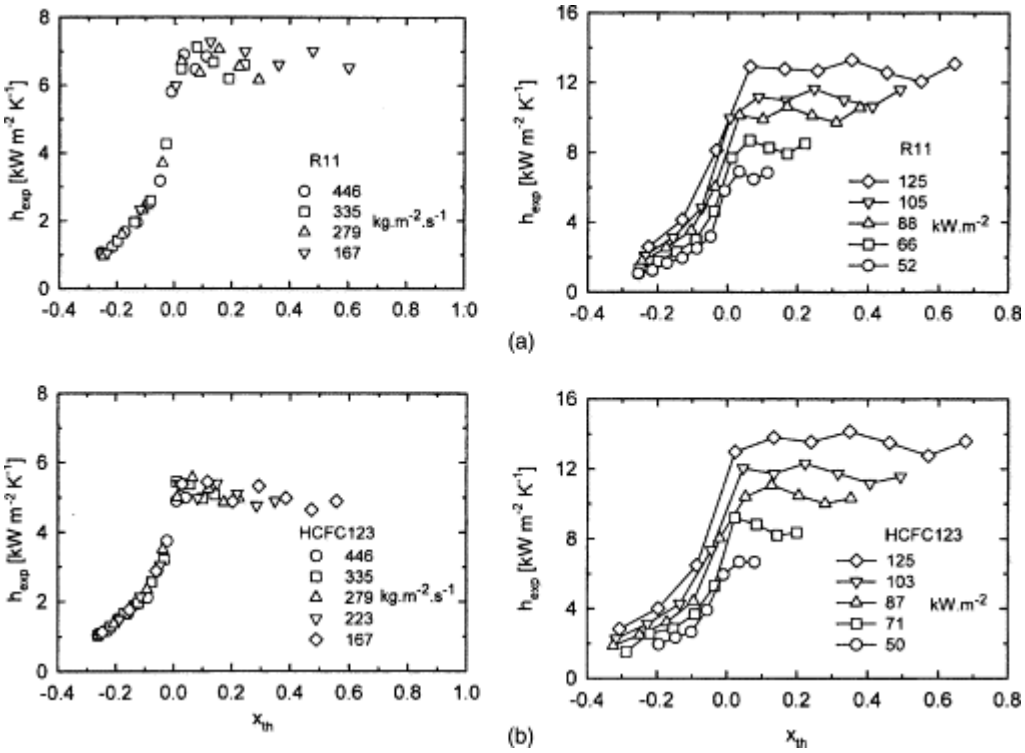

Figure 2.19 *Flow boiling heat transfer coefficients obtained by Bao et al. plotted versus vapour quality [70], (a) influence of mass flux, (b) influence of heat flux.*

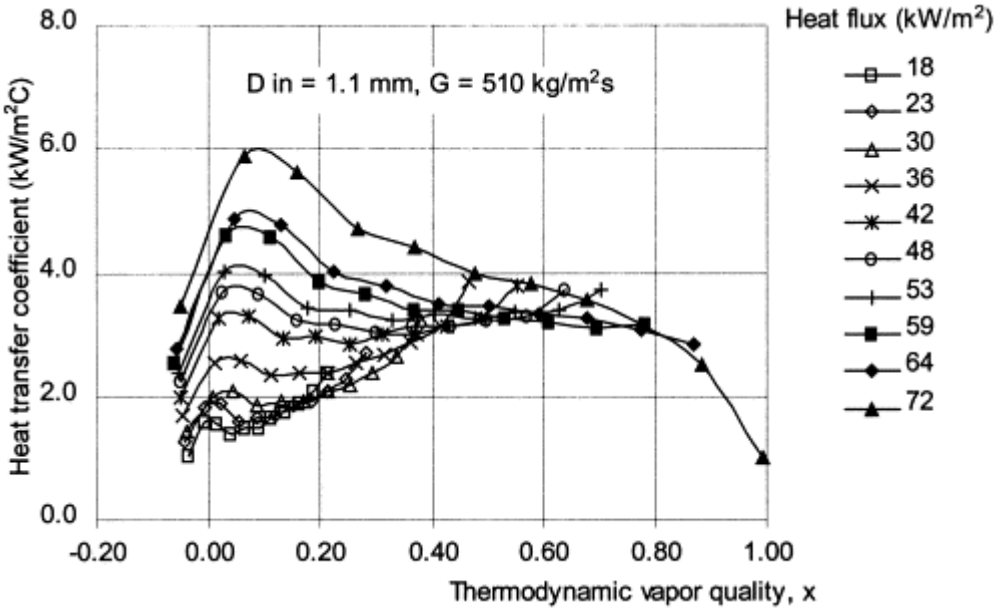

Figure 2.20 *Flow boiling data for R-141b of Lin et al. [71].*

On the other hand, the studies of Lin et al. [71] demonstrate significant effects of vapour quality and mass flux on heat transfer coefficient, implying that forced convective boiling dominates over nucleate boiling. The authors studied flow boiling of R-141b in a vertical 1.1 mm tube over a mass flux range of 300-2000 kg/m^{2}s and heat flux range of 18-72 kW/m^2. Their results for heat transfer coefficient in terms of vapour quality for a mass flux of 510 kg/m^{2}s are shown in Figure 2.20. At high heat fluxes, their data exhibit a sharp peak at low vapour qualities followed by a monotonic decrease. At low heat fluxes, there is a monotonic increase in heat flux up to a value about x = 0.60. For intermediate heat fluxes, heat transfer coefficient is nearly independent of vapour quality. These results indicate that heat transfer coefficient is a complex function of heat flux, mass flux and vapour quality. The authors concluded that nucleate boiling dominated at low vapour qualities and that forced convective boiling was dominant at high vapour qualities. Qu and Mudawar [72] experimentally investigated flow boiling heat transfer in microchannels heat sink shown in Figure 2.14. The authors reported an abrupt transition to annular flow near the point of zero thermodynamic equilibrium quality with the dominant heat transfer mechanism being forced convective boiling and not nucleate boiling. Figure 2.21 shows their results for saturated flow boiling heat transfer coefficients versus

thermodynamic equilibrium quality. As can be seen from Figure 2.21, heat transfer coefficient decreases with increasing thermodynamic equilibrium quality implying that heat transfer coefficient may also decrease with increasing heat flux. This is in contrary to macrochannel trends where heat transfer coefficient increases significantly with q increasing near the point of zero thermodynamic equilibrium quality due to intensification of bubble nucleation along the heated wall. The authors attributed this unique behaviour to the strong influence of liquid droplet entrainment and deposition within the annular flow region. As Figure 2.21 indicates, heat transfer coefficient significantly increases with increasing mass flux for a given x_{eq}. The authors concluded that forced convection boiling is the dominant mechanism for the saturated region in microchannels. Based on their experimental observations Qu and Mudawar [74] developed a model to predict the saturated flow boiling heat transfer coefficient. The model is based on several assumptions such as annular flow regime, laminar liquid and vapour flow, smooth interface, and strong droplet entrainment and deposition phenomena. The authors reported a good agreement between the model predictions and their experimental results for saturated flow boiling heat transfer coefficient over broad ranges of flow rate and heat flux. Steinke and Kandlikar [73]

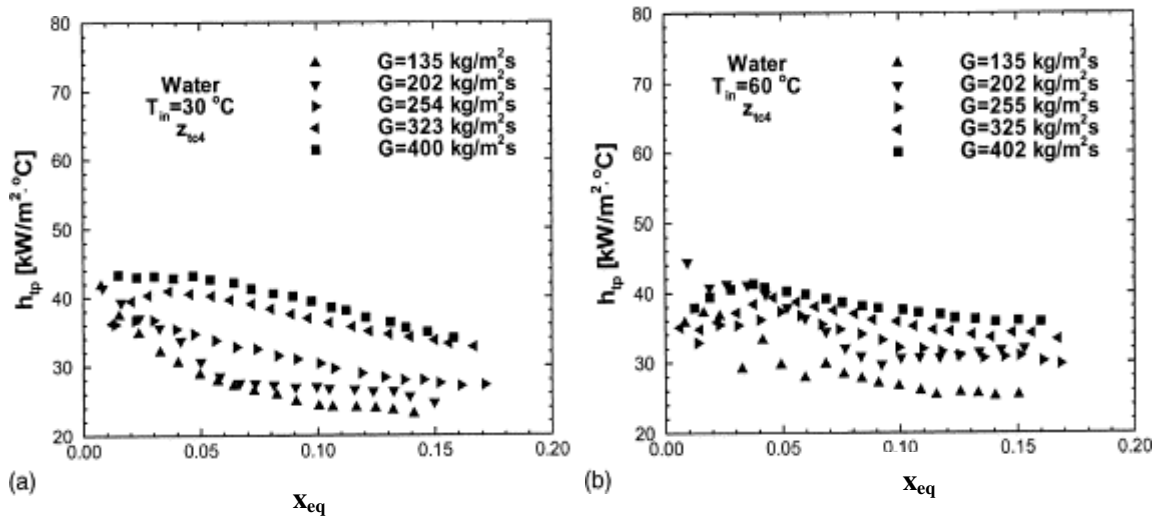

Figure 2.21 *Saturated flow boiling heat transfer coefficient obtained by Qu and Mudawar [72] for (a) T_{in}=30 °C and (b) T_{in}=60 °C.*

also observed the decreasing trends in heat transfer coefficient with quality seen in Qu and Mudawar's data. The authors performed an experimental investigation on flow boiling using water in six parallel microchannels with a hydraulic diameter of 207 μm for the range of mass flux from 157 to 1782 kg/m^{2}s, heat flux from 5 to 930 kW/m^2, and inlet temperature of 22˚C. They found very high heat transfer coefficients in the low quality region and a decreasing trend in heat transfer coefficient for the higher values of the vapour quality. Very high heat transfer coefficients at low quality region were attributed to the rapid growth of bubbles. The authors recommended the modified Kandlikar flow-boiling correlation [16] that includes only the nucleate boiling dominant equation and the laminar single-phase heat transfer coefficient. The correlation showed good agreement with experimental data between qualities of 0.2 to 0.8. However, the correlation was not able to predict the high heat transfer coefficients observed near the point of zero quality.

Agostini et al. [75, 76] have studied flow boiling of refrigerants R-236fa and R-245fa in a silicon heat sink consisting of 67 parallel channels, which are 223 μm wide, 680 μm deep and 20 mm long with 80 μm thick fins between the channels. The authors identified three different heat transfer trends for a range of heat fluxes from 3.6 to 221 W/cm^2, the mass flux from 281 to 1501 kg/m^{2}s and the exit vapour quality from 0.02 to 0.75. In most cases, the heat transfer coefficient increased with the heat flux and was fairly dependent on vapour quality and mass flux. Figure 2.22 shows measurements of Agostini et al. for R-236fa and a mass flux of 811 kg/m^{2}s. The heat transfer coefficient trends are similar to those observed by Lin et al [71]. It can be seen from Figure 2.22 that heat transfer coefficient at low heat fluxes tends to increase. At moderate heat fluxes, heat transfer coefficient first increases with quality and then becomes fairly dependant on vapour quality. The heat transfer coefficient as a function of vapour quality shows a sharp peak at very high heat fluxes and then decreases with further increase of the heat flux.

Agostini and Thome [77] summarized the trends in heat transfer coefficient reported in 13 published microchannels flow boiling studies until 2005. At very low vapour qualities ($x < 0.05$), heat transfer coefficient tends to increase with vapour quality or it is not a function of vapour quality while it increases with heat flux. At

high vapour qualities (x > 0.5) the general trend is that the heat transfer coefficient decreases sharply with vapour quality and does not depend on heat flux and mass flux. This trend was not found for the low to medium vapour quality (0.05 < x < 0.5). The influence of mass flux varies from no effect, an increasing effect, or a decreasing effect, while increasing the heat flux increases the heat transfer coefficient except at high vapour quality where it has an effect. The authors concluded that such contradictory trends, which are different from simple trends typical to macroscale, are a consequence of surface roughness and/or heat transfer mechanism active during flow boiling in microchannels. These mechanisms can be classified in four groups [2]: (1) bubble flow with nucleate boiling mechanism, (2) evaporation of the thin liquid film between trapped bubbles and the wall associated with slug flow, (3) convective evaporation of the liquid film in annular flow, and (5) vapour phase heat transfer associated with mist flow.

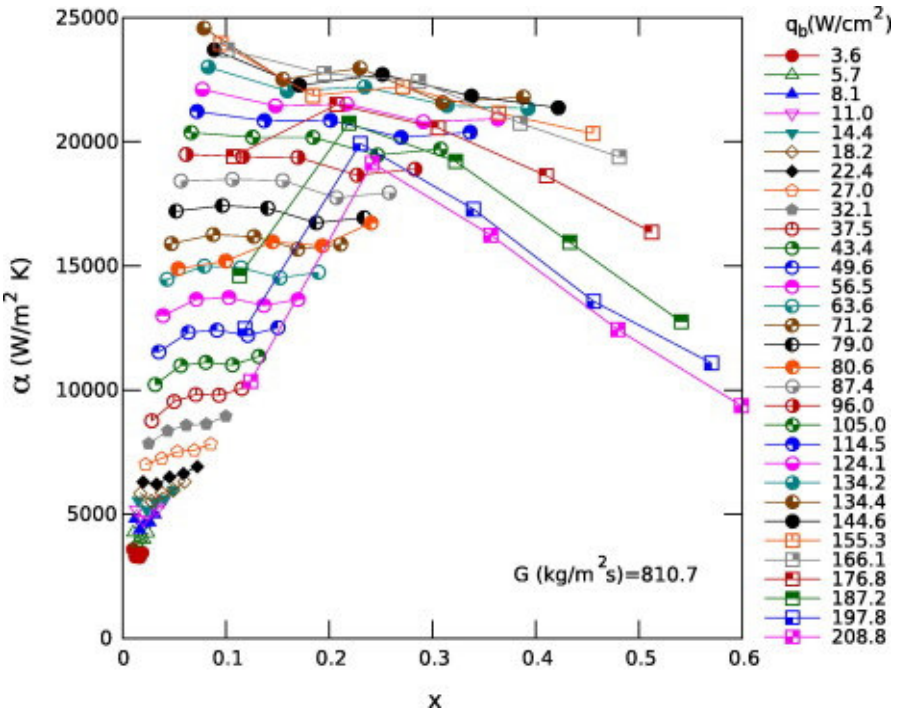

Figure 2.22 *Heat transfer coefficient versus vapour quality data of Agostini et al. [75] for R-236fa at a mass flux of 810.7 kg/m²s.*

Jacobi and Thome [78] have suggested that the dependency of the heat transfer coefficient on the heat flux does not mean necessarily domination of the nucleate boiling mechanism. The authors proposed a new model based on the hypothesis that thin-film evaporation into elongated bubbles is the important heat transfer mechanism in flow boiling inside microchannels. Following this initial work, Thome et al. [79] developed a three-zone model for flow boiling in microchannels to predict the local dynamic heat transfer coefficient and the local time-averaged heat transfer coefficient at a constant, uniform heat flux boundary condition. The model describes the flow boiling in microchannel as a cyclic passage of (1) a liquid slug, (2) an evaporating elongated bubble and (3) a vapour slug. Therefore, the model predicts the cycle variation in local heat transfer coefficient with time. A schematic of the three-zone model is shown in Figure 2.23. The frequency of the successive events is a function of the formation rate of the bubbles upstream. The model predicts strong dependency of the heat transfer on the bubble frequency, the thin liquid film between the bubble and the inner tube wall and the lengths of the bubbles and liquid slugs. The authors compared time-averaged local heat transfer coefficient to flow boiling experimental data covering the following seven fluids: R-11, R-12, R-113, R-123, R-134a, R-141b and CO_2 in tube diameters from 0.77 to 3.1 mm. They found that the model predicted 67% of the database to within ±30% [80].

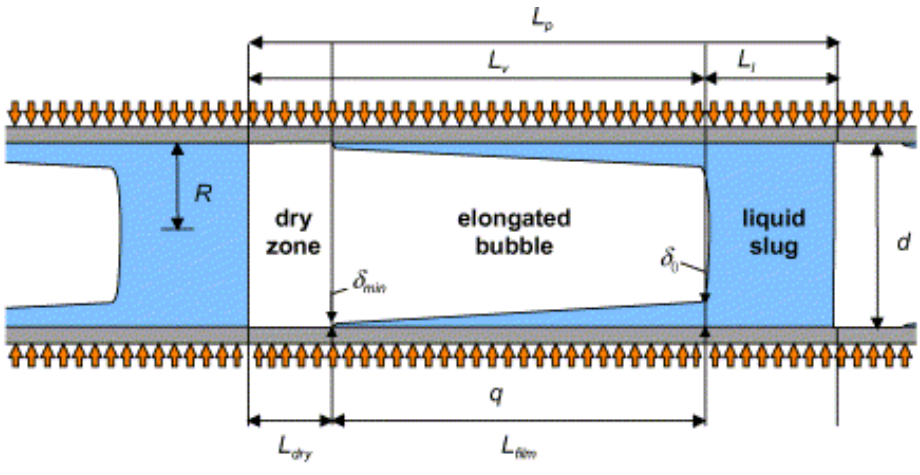

Figure 2.23 *Schematic of three-zone evaporation model [79].*

2.3.4 Effect of non-uniform heating on flow boiling in microchannels

A big challenge for microchannel cooling technology is to fully characterise local hotspots and their effects on the system. It was highlighted in the previous chapter that CPUs work with non-uniform thermal dissipation that causes localized hotspots. This results in an increase in local CPU junction temperature affecting the reliability and performance of the CPU. Whilst the averaged heat flux on CPU can be lower than critical heat flux, local heat fluxes can be very high with damaging consequences [81]. This has not been fully investigated and it is essential that this phenomenon is more fully characterised. Eun Seok et al. [82] have experimentally investigated the impact of liquid distribution within channels on the temperature field in a microchannels heat sink with hotspots. The authors compared the performance of two microchannels heat sinks: a regular microchannel heat sink and a cross-linked microchannel heat sink. They found that optimal microchannel heat sink configuration depends on the required flow rate and hotspot position. Jae-Mo et al. [83] carried out simulations using a theoretical model to examine the effect of hotspot location on the pressure drop in two-phase flow region and maximum wall temperature. They found that a hotspot located downstream showed better performance in terms of the pressure drop and maximum wall temperature than the one located upstream in the microchannel heat sink. Revellin et al. [84] used numerical simulations to investigate the effects of a number of parameters (mass flux, saturation temperature, microchannel diameter, heated length, size, location and number of hotspots as well as the distance between two consecutive hotspots) on the maximum dissipation rates during flow boiling in a microchannel with non-uniform heating. The authors proposed that, for hotspots situated in the mid-point along the length of the microchannel element, the fluid inlet would be better located at the mid-point with an exit at both ends. It is clear that despite numerous attempts, the investigation of the effect of hotspots (magnitude and location) remains a crucial question for the design of microchannels based heat sinks.

2.4 Scope of the research

The aforementioned studies on flow boiling in microchannels indicate that still many controversies about flow regimes, flow instabilities and mechanisms of heat transfer exist. An additional problem in investigation of flow boiling in microchannels is the oscillatory nature of the flow. It is crucial for the assessment of the mechanisms and modelling of the heat transfer in microchannels to understand the nature and behaviour of flow boiling instabilities. The understanding of heat transfer mechanisms, flow instabilities and development of reliable models require synchronised local measurements with high-speed imaging.

The present investigation focuses on flow boiling in a silicon heat sink with parallel, rectangular microchannels with a hydraulic diameter of 194 μm. The objective is to provide further insight into two-phase regimes, flow boiling instabilities, bubble dynamics and heat transfer mechanisms. An experimental system with an integrated heater for uniform or non-uniform heating and integrated temperature sensors that allow local measurements has been developed. The experimental setup has been designed to enable synchronised local measurements with high-speed imaging.

The outline of the following chapters is given below:

- *Chapter 3* describes the experimental setup, including flow loop, test module, and measurement uncertainties;
- *Chapter 4* presents the results obtained using an approximate model and CFD simulations that assisted in the design of the heat sink with microchannels;
- *Chapter 5* presents an investigation of two-phase flow instabilities under uniform heating;
- *Chapter 6* presents an investigation of bubble dynamics and the effect of the bubble dynamics on flow instabilities and heat transfer coefficient;
- *Chapter 7* presents an investigation of two-phase flow instabilities under non-uniform heating (“hotspot” investigation);
- *Chapter 8* presents general conclusions and future work.

References

1. Kandlikar, S.G., Shoji M., Dhir V.K.,, *Handbook of Phase Change*. 1999, Taylor & Francis London
2. Thome, J.R., *Engineering Data Book III*. 2008, Wolverine Tube, http://www.wlv.com/products/databook/db3/DataBookIII.pdf
3. Corradini, M.L., *Fundamentals of Multiphase Flow* 1997, Univesity of Wisconsin, Madison, USA, http://wins.engr.wisc.edu/teaching/mpfBook/main.html.
4. Hsu, Y.Y., Graham, R.W., *An Analytical and Experimental Study of the Thermal Boundary Layer and Ebullition Cycle in Nucleate Boiling*. NASA TN-D-594. 1961.
5. Bergles, A.E., Rohsenow, W.M., *The Determination of Forced Convection Surface Boiling Heat Transfer.* Journal of Heat Transfer, 1964. 86 365-372.
6. Sato, T.M., H., *On the Conditions of Incipient Subcooled Boiling With Forced Convection* Bull. JSME, 1964. 7(26) 392-398.
7. Davis, E.J., Anderson, G.H., *The Incipience of Nucleate Boiling in Forced Convection Flow* AIChE J., 1966. 12(4) 774-780.
8. Kandlikar, S.G., Mizo, V.R., Cartwright, M.D, Ikenze, E. *Bubble Nucleation and Growth Characteristics in Subcooled Flow Boiling of Water* in *HTD-Vol. 342, ASME Proceedings of the 32nd National Heat Transfer Conference, vol. 4, pp. 11-18*. 1997.
9. Hsu, Y.Y., *On the Size Range of Ative Nucleation Sites on a Heating Surface.* Journal of Heat Transfer, 1962. 84C 207-216.
10. Ghiaasiaan, S.M., *Two-Phase Flow, Boiling, and Condensation in Conventional and Miniature Systems*. 2008, New York, USA: Cambridge University Press.
11. Saha, P., Zuber, N., *Point of net vapour generation and vapour void fraction in subcooled boiling* Proc., Int. Heat Transfer Conf., 5th, 1974. 4 175-179.
12. Levy, S., *Forced convection subcooled boiling: Prediction of vapour volumetric fraction.* International Journal of Heat and Mass Transfer, 1967. 10 951-965.
13. Rogers, J.T., M. Salcudean, Z. Abdullah, D. McLeod, D. Poirier, *The onset of significant void in up-flow boiling of water at low pressure and velocities.* International Journal of Heat and Mass Transfer, 1987. 30(11) 2247-2260.
14. Shah, M., *A general correlation for heat transfer during subcooled boiling in pipes and annuli* ASHRAE Trans, 1977. 83(Part 1) 205-215.
15. Kandlikar, S.G., *Heat Transfer Characteristics in Partial Boiling, Fully Developed Boiling, and Significant Void Flow Regions of Subcooled Flow Boiling.* Journal of Heat Transfer, 1998. 120(2) 395-401.
16. Kandlikar, S.G., *A General Correlation for Saturated Two-Phase Flow Boiling Heat Transfer Inside Horizontal and Vertical Tubes.* Journal of Heat Transfer, 1990. 112(1) 219-228.

17. Collier, J.G., Thome, J.R., *Convective Boiling and Condensation* 3rd ed. 1994, Oxford: University Press, .
18. Taitel, Y., Dukler, A.E., *A model for predicting flow regime transitions in horizontal and near horizontal gas-liquid flow* AIChE J., 1976. 22 47-55.
19. Baker, O., *Design of pipelines for simultaneous flow of oil and gas.* Oil and Gas J., 1954 26.
20. Kattan, N., J.R. Thome, D. Favrat, *Flow Boiling in Horizontal Tubes: Part 1--Development of a Diabatic Two-Phase Flow Pattern Map.* Journal of Heat Transfer, 1998. 120(1) 140-147.
21. Chen, J.C., *A Correlation for Boiling Heat Transfer to Saturated Fluids in Convective Flow* Industrial and Engineering Chemistry, Process Design and Development, 1966. 5(3) 322-329.
22. Schrock, V.E., Grossman, L.M., *Forced Convection Boiling in Tubes,.* Nuclear Science and Engineering, 1962. 12 474-481.
23. Kattan, N., J.R. Thome, D. Favrat, *Flow Boiling in Horizontal Tubes: Part 3--Development of a New Heat Transfer Model Based on Flow Pattern.* Journal of Heat Transfer, 1998. 120(1) 156-165.
24. Zurcher, O., J.R. Thome, D. Favrat, *Evaporation of Ammonia in a Smooth Horizontal Tube: Heat Transfer Measurements and Predictions.* Journal of Heat Transfer, 1999. 121(1) 89-101.
25. Wojtan, L., T. Ursenbacher, J.R. Thome, *Investigation of flow boiling in horizontal tubes: Part II--Development of a new heat transfer model for stratified-wavy, dryout and mist flow regimes.* International Journal of Heat and Mass Transfer, 2005. 48(14) 2970-2985.
26. Wojtan, L., T. Ursenbacher, J.R. Thome, *Investigation of flow boiling in horizontal tubes: Part I--A new diabatic two-phase flow pattern map.* International Journal of Heat and Mass Transfer, 2005. 48(14) 2955-2969.
27. Chisholm, D., *A theoretical basis for the Lockhart-Martinelli correlation for two-phase flow.* International Journal of Heat and Mass Transfer, 1967. 10(12) 1767-1778.
28. Kutateladze, S.S., Leontiev, A.I., *Some aplication of teh asymptotic theory of the turbulent boundary layer* Proc. 3rd International heat trasfer conference, , Chigago,1966. 3 1-6.
29. Weisman, J., Pei, B.S., *Prediction of critical heat flux in flow boiling at low qualities.* International Journal of Heat and Mass Transfer, 1983. 26 1463-1477.
30. Celata, G.P., M. Cumo, A. Mariani, *Assessment of correlations and models for the prediction of CHF in water subcooled flow boiling.* International Journal of Heat and Mass Transfer, 1994. 37(2) 237-255.
31. Hall, D.D. and I. Mudawar, *Critical heat flux (CHF) for water flow in tubes--I. Compilation and assessment of world CHF data.* International Journal of Heat and Mass Transfer, 2000. 43(14) 2573-2604.
32. Ledinegg, M., *Instability of flow during natural and forced circulation.* Die Waerme, 1938. 61(8) 891-898.
33. Tadrist, L., *Review on two-phase flow instabilities in narrow spaces.* International Journal of Heat and Fluid Flow, 2007. 28(1) 54-62.

34. Kakac, S. and B. Bon, *A Review of two-phase flow dynamic instabilities in tube boiling systems.* International Journal of Heat and Mass Transfer, 2008. 51(3-4) 399-433.
35. Kandlikar, S.G., *Fundamental issues related to flow boiling in minichannels and microchannels.* Experimental Thermal and Fluid Science, 2002. 26(2-4) 389-407.
36. Thome, J.R., *Boiling in microchannels: a review of experiment and theory.* International Journal of Heat and Fluid Flow, 2004. 25(2) 128-139.
37. Kew, P.A. and K. Cornwell, *Correlations for the prediction of boiling heat transfer in small-diameter channels.* Applied Thermal Engineering, 1997. 17(8-10) 705-715.
38. Kawaji, M. and P.M.Y. Chung, *Adiabatic gas-liquid flow in microchannels.* Nanoscale and Microscale Thermophysical Engineering, 2004. 8(3) 239-257.
39. Kandlikar, S.G., *Nucleation characteristics and stability considerations during flow boiling in microchannels.* Experimental Thermal and Fluid Science, 2006. 30(5) 441-447.
40. Lee, P.C., F.G. Tseng, C. Pan, *Bubble dynamics in microchannels. Part I: single microchannel.* International Journal of Heat and Mass Transfer, 2004. 47(25) 5575-5589.
41. Moore, F.D., Mesler, R.B., *The measurements of rapid surface temperature fluctuations during nucleate boiling of water.* AIChE J., 1961. 7 620-624.
42. Li, H.Y., F.G. Tseng, C. Pan, *Bubble dynamics in microchannels. Part II: two parallel microchannels.* International Journal of Heat and Mass Transfer, 2004. 47(25) 5591-5601.
43. Fukano, T., Kariyasaki, A., Kagawa, M., *Flow patterns and pressure drop in isothermal gas-liquid flow in a horizontal capillary tube.* ANS Proc. 1989 National heat trasfer conference,, 1989. 4 153-161.
44. Triplett, K.A., S.M. Ghiaasiaan, S.I. Abdel-Khalik, A. LeMouel, B.N. McCord, *Gas-liquid two-phase flow in microchannels: Part II: void fraction and pressure drop.* International Journal of Multiphase Flow, 1999. 25(3) 395-410.
45. Kasza, K.E., Didascalou, T., Wambsganss, M.W. *Microscale flow visualization of nucelate boiling in small channels: mechanisms influencing heat transfer* in *Proc. of International Conference on Compact Heat Exchanger for the Process Industries, New York*. 1997.
46. Cornwell, K., Kew, P.A., *Boiling in small parallel channels,* . Proc. of CEC Conference on Energy Efficiency in Process Technology, 1992 624-638.
47. Serizawa, A., Z. Feng, Z. Kawara, *Two-phase flow in microchannels.* Experimental Thermal and Fluid Science, 2002. 26(6-7) 703-714.
48. Coleman, J.W. and S. Garimella, *Characterization of two-phase flow patterns in small diameter round and rectangular tubes.* International Journal of Heat and Mass Transfer, 1999. 42(15) 2869-2881.
49. Revellin, R., V. Dupont, T. Ursenbacher, J.R. Thome, I. Zun, *Characterization of diabatic two-phase flows in microchannels: Flow parameter results for R-134a in a 0.5 mm channel.* International Journal of Multiphase Flow, 2006. 32(7) 755-774.

50. Revellin, R. and J.R. Thome, *A new type of diabatic flow pattern map for boiling heat transfer in microchannels.* Journal of Micromechanics and Microengineering, 2007. 17(4) 788-796.
51. Bergles, A.E. and S.G. Kandlikar, *On the Nature of Critical Heat Flux in Microchannels.* Journal of Heat Transfer, 2005. 127(1) 101-107.
52. Qu, W. and I. Mudawar, *Measurement and prediction of pressure drop in two-phase micro-channel heat sinks.* International Journal of Heat and Mass Transfer, 2003. 46(15) 2737-2753.
53. Hetsroni, G., A. Mosyak, Z. Segal, G. Ziskind, *A uniform temperature heat sink for cooling of electronic devices.* International Journal of Heat and Mass Transfer, 2002. 45(16) 3275-3286.
54. Hetsroni, G., A. Mosyak, Z. Segal, E. Pogrebnyak, *Two-phase flow patterns in parallel micro-channels.* International Journal of Multiphase Flow, 2003. 29(3) 341-360.
55. Hetsroni, G., A. Mosyak, E. Pogrebnyak, Z. Segal, *Explosive boiling of water in parallel micro-channels.* International Journal of Multiphase Flow, 2005. 31(4) 371-392.
56. Hetsroni, G., A. Mosyak, E. Pogrebnyak, Z. Segal, *Periodic boiling in parallel micro-channels at low vapor quality.* International Journal of Multiphase Flow, 2006. 32(10-11) 1141-1159.
57. Kandlikar, S.G., Steinke, M.E., Tian, S., Campbell, L.A., *High-speed photographic observation of flow boiling of water in parallel minichannels* Paper presented at the ASME National Heat Transfer Conference 2001.
58. Wu, H.Y. and P. Cheng, *Boiling instability in parallel silicon microchannels at different heat flux.* International Journal of Heat and Mass Transfer, 2004. 47(17-18) 3631-3641.
59. Wang, G., P. Cheng, H. Wu, *Unstable and stable flow boiling in parallel microchannels and in a single microchannel.* International Journal of Heat and Mass Transfer, 2007. 50(21-22) 4297-4310.
60. Wang, G., P. Cheng, A.E. Bergles, *Effects of inlet/outlet configurations on flow boiling instability in parallel microchannels.* International Journal of Heat and Mass Transfer, 2008. 51(9-10) 2267-2281.
61. Kenning, D.B.R., Yan, Y., *Saturated flow boiling of water in a narrow channel: experimental investigation of local phenomena, IChemE Trans. A, .* Chem. Eng. Research and Design 2001. 79 425-436.
62. Wen D.S., Kenning D.B.,Yan, Y., *Flow boiling of water in a narrow vertical channel at low mass flux: observation of local phenomena* Proc. of 12th Int. Heat Transfer Conf. Grenoble 2001. 3 773-778.
63. Brutin, D. and L. Tadrist, *Pressure drop and heat transfer analysis of flow boiling in a minichannel: influence of the inlet condition on two-phase flow stability.* International Journal of Heat and Mass Transfer, 2004. 47(10-11) 2365-2377.
64. Zhang, L., E.N. Wang, K.E. Goodson, T.W. Kenny, *Phase change phenomena in silicon microchannels.* International Journal of Heat and Mass Transfer, 2005. 48(8) 1572-1582.

65. Kandlikar, S.G., W.K. Kuan, D.A. Willistein, J. Borrelli, *Stabilization of Flow Boiling in Microchannels Using Pressure Drop Elements and Fabricated Nucleation Sites.* Journal of Heat Transfer, 2006. 128(4) 389-396.
66. Kosar, A., C.-J. Kuo, Y. Peles, *Suppression of Boiling Flow Oscillations in Parallel Microchannels by Inlet Restrictors.* Journal of Heat Transfer, 2006. 128(3) 251-260.
67. Kuo, C.J. and Y. Peles, *Pressure effects on flow boiling instabilities in parallel microchannels.* International Journal of Heat and Mass Transfer, 2008. In Press, Corrected Proof.
68. Wambsganss, M.W., D.M. France, J.A. Jendrzejczyk, T.N. Tran, *Boiling Heat Transfer in a Horizontal Small-Diameter Tube.* Journal of Heat Transfer, 1993. 115(4) 963-972.
69. Tran, T.N., M.W. Wambsganss, D.M. France, *Small circular- and rectangular-channel boiling with two refrigerants.* International Journal of Multiphase Flow, 1996. 22(3) 485-498.
70. Bao, Z.Y., D.F. Fletcher, B.S. Haynes, *Flow boiling heat transfer of Freon R11 and HCFC123 in narrow passages.* International Journal of Heat and Mass Transfer, 2000. 43(18) 3347-3358.
71. Lin, S., P.A. Kew, K. Cornwell, *Two-phase heat transfer to a refrigerant in a 1 mm diameter tube.* International Journal of Refrigeration, 2001. 24(1) 51-56.
72. Qu, W. and I. Mudawar, *Flow boiling heat transfer in two-phase micro-channel heat sinks--I. Experimental investigation and assessment of correlation methods.* International Journal of Heat and Mass Transfer, 2003. 46(15) 2755-2771.
73. Steinke, M.E. and S.G. Kandlikar, *An Experimental Investigation of Flow Boiling Characteristics of Water in Parallel Microchannels.* Journal of Heat Transfer, 2004. 126(4) 518-526.
74. Qu, W. and I. Mudawar, *Flow boiling heat transfer in two-phase micro-channel heat sinks--II. Annular two-phase flow model.* International Journal of Heat and Mass Transfer, 2003. 46(15) 2773-2784.
75. Agostini, B., J.R. Thome, M. Fabbri, B. Michel, D. Calmi, U. Kloter, *High heat flux flow boiling in silicon multi-microchannels - Part I: Heat transfer characteristics of refrigerant R236fa.* International Journal of Heat and Mass Transfer, 2008. 51(21-22) 5400-5414.
76. Agostini, B., J.R. Thome, M. Fabbri, B. Michel, D. Calmi, U. Kloter, *High heat flux flow boiling in silicon multi-microchannels - Part II: Heat transfer characteristics of refrigerant R245fa.* International Journal of Heat and Mass Transfer, 2008. 51(21-22) 5415-5425.
77. Agostini, B., Thome, J.R.,. *Comparison of an extended database for flow boiling heat transfer coefficinets in multi-microchannels elements with the three-zone model.* ECI Heat Transfer and Fluid Flow in Microscale, Italy, Sept 25-30, 2005.
78. Jacobi, A.M. and J.R. Thome, *Heat Transfer Model for Evaporation of Elongated Bubble Flows in Microchannels.* Journal of Heat Transfer, 2002. 124(6) 1131-1136.

79. Thome, J.R., V. Dupont, A.M. Jacobi, *Heat transfer model for evaporation in microchannels. Part I: presentation of the model.* International Journal of Heat and Mass Transfer, 2004. 47(14-16) 3375-3385.
80. Dupont, V., J.R. Thome, A.M. Jacobi, *Heat transfer model for evaporation in microchannels. Part II: comparison with the database.* International Journal of Heat and Mass Transfer, 2004. 47(14-16) 3387-3401.
81. Smith, R. *Current Packaging Trends*. in *Proceedings of the Cooling Electronics The Next Decade conference*. 2001. Marlborough, MA, USA.
82. Eun Seok, C., K. Jae-Mo, J. Linan, R.S. Prasher, K. Min Soo, J.G. Santiago, T.W. Kenny, K.E. Goodson. *Experimental study on two-phase heat transfer in microchannel heat sinks with hotspots*. in *Semiconductor Thermal Measurement and Management Symposium, 2003. Ninteenth Annual IEEE*. 2003.
83. Jae-Mo, K., J. Linan, A. Bari, L. Zhang, E. Wang, T.W. Kenny, J.G. Santiago, K.E. Goodson. *Convective boiling in microchannel heat sinks with spatially-varying heat generation*. in *Thermal and Thermomechanical Phenomena in Electronic Systems, 2002. ITHERM 2002. The Eighth Intersociety Conference on*. 2002.
84. Revellin, R., J.M. Quiben, J. Bonjour, J.R. Thome, *Effect of Local Hot Spots on the Maximum Dissipation Rates During Flow Boiling in a Microchannel.* Components and Packaging Technologies, IEEE Transactions on, 2008. 31(2) 407-416.

Chapter 3 Experimental facility

3.1 Introduction

An experimental system was designed and constructed to carry out an experimental study of flow boiling in microchannel heat sinks. The experimental set up consists of a flow loop and a test module. Details of the experimental system, including the flow loop, the test module, and measurement uncertainties are presented in this chapter. A drawing of the assembly of the experimental setup is given in appendix A.

3.2 Flow loop

The flow loop was designed to supply cooling liquid (deionised water) to the test module at the desired subcooling conditions, flow rates and system pressures. Figure 3.1 shows a schematic of the flow loop. A reservoir serves as both a degassing and condensation chamber during flow boiling experiments. Three immersion heaters with total power of 1500 W were installed inside the reservoir to preheat and degas the water. The heaters were controlled using a PI controller with a K-type thermocouple. Water level inside the reservoir was monitored using a LED level

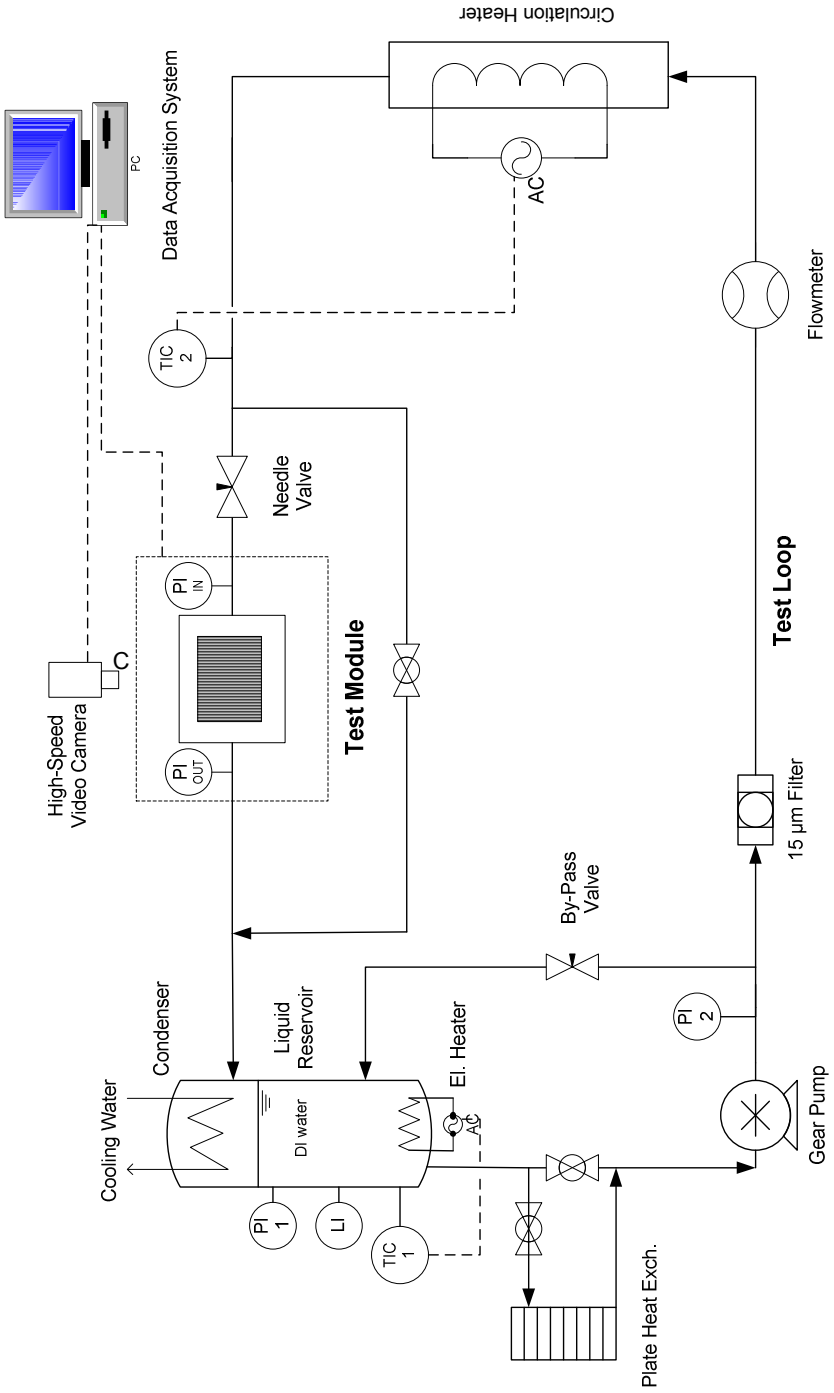

Figure 3.1 *Schematic of the flow loop.*

indicator installed on a tube with a floating magnet connected to the bottom and the top side of the reservoir. A copper coil with cooling water supply, positioned inside the reservoir, serves both as a condenser for vapour generated in the test module and a regulator of pressure in the flow loop. The desired pressure was obtained by controlling the flow rate of water through the copper coil. A magnetically coupled gear pump (Micropump GA-T23PFSB) was used to pump the water from the liquid reservoir and circulate it through the flow loop. The pump is capable of generating flow rates from 4.6 to 460 ml/min of water at a maximum differential pressure of 5.2 bar. A plate heat exchanger with water as a coolant was installed between the reservoir and the pump to prevent pump cavitations. The pump's exit was monitored by a pressure gauge situated immediately downstream from the pump. A 15 μm filter was used to prevent any solid particles from entering the test section. Flow rates were measured by a thermal mass flow meter (Bronkhorst L30 Series) calibrated for the range from 1 to 50 g/min based on water. Subcooling conditions for water (test module inlet temperature) were maintained using negative feedback control on a low flow liquid circulation heater (Omega AHPF-122) with a total power of 1200 W. The negative feedback control consisted of a PID regulator with a K-type thermocouple installed at the heater exit. The flow rate through the test module was regulated using a bypass valve and a fine needle valve located upstream of the test module.

3.3 Test module

The test modules were heat sinks with 15 mm long parallel rectangular microchannels together with integrated inlet and outlet manifolds etched into a silicon wafer using a deep reactive ion etching process. The design process of the test module is described in detail in chapter 4. Figure 3.2 shows geometry of the heat sink. The heat sink has forty channels, 273 μm deep, 150 μm wide spaced by 100 μm. The depth of the inlet/outlet manifold is the same as the depth of the microchannels. A 500 μm thick Pyrex glass cover plate was anodically bonded to the silicon wafer to seal and enable visualisation of boiling within channels. On the back

a)

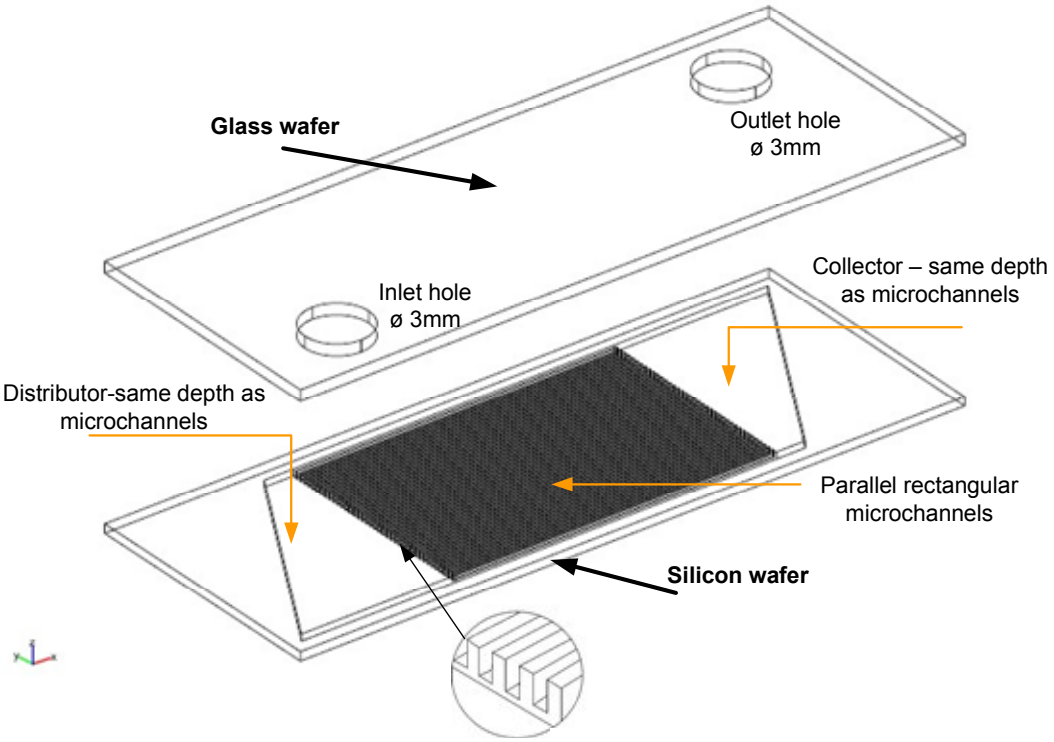

b)

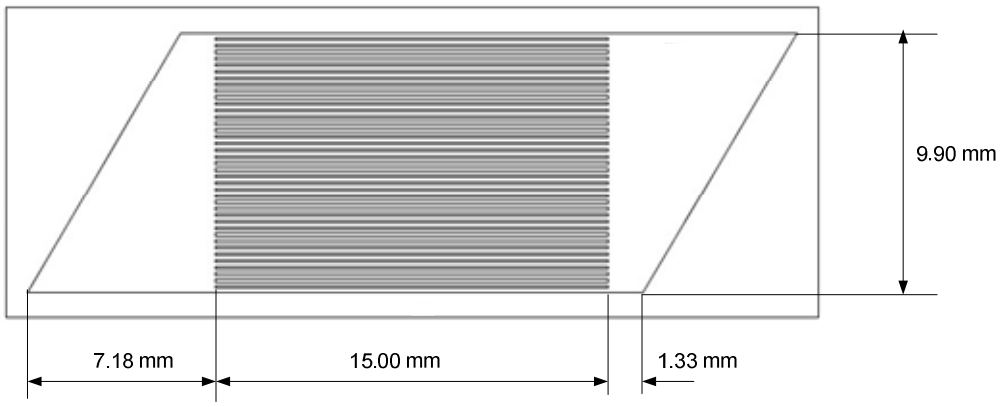

Figure 3.2 *Schematic illustration of the heat sink (a) split view (b) geometry of the inlet/outlet manifold.*

side of the device there are five integrated sensors made from a thin nickel film for temperature measurements and an aluminium heater track. Figure 3.3 shows (a) top view of the silicon chip with microchannels and (b) back side with pads for the sensors and the heater connections. The sensors were integrated between the heater

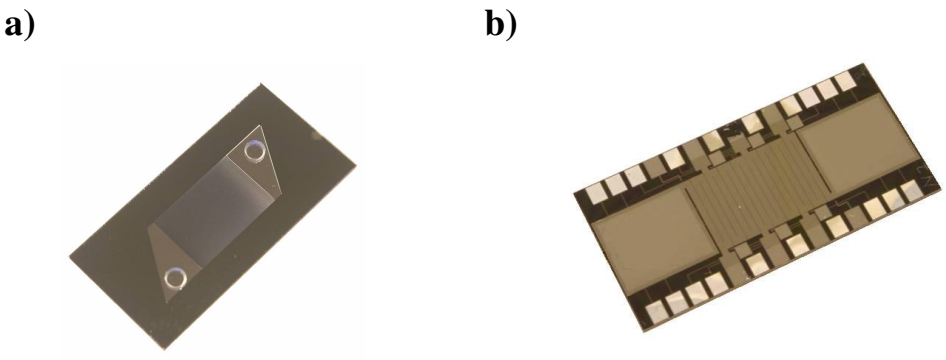

Figure 3.3 *Photographs of (a) top side of the test device and (b) back side.*

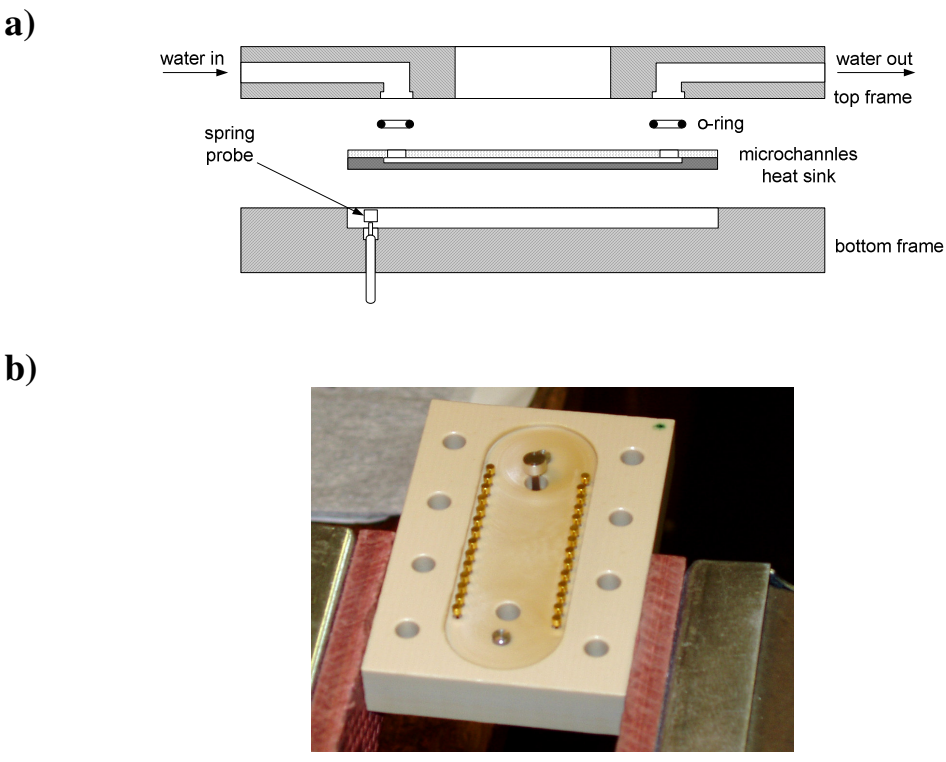

Figure 3.4 *Schematic illustration of the test module construction (a), photo of the bottom frame with spring probes for electrical connections (b).*

and the microchannels. The heater was designed to enable either uniform or non-uniform heating, the later being achieved by the independent operation of the upstream, middle or downstream heating elements.

The silicon heat sink was sandwiched between the top and the bottom frames as shown in Figure 3.4a. A drawing with dimensions of the top and the bottom frames is given in appendix B. The bottom frame is made from PEEK plastic which has a good thermal insulation property (a thermal conductivity of 0.25 W/m K and a maximum service temperature of 260 ˚C). The top frame is a transparent polycarbonate plastic with a thermal conductivity of 0.19 W/m K and a maximum service temperature of 120 °C. Such thermal insulation properties of both the top and the bottom frames ensure that the water flow absorbed most of the heat with a minimal heat dissipated due to conduction. In the top frame, holes for external stainless tubes and a square window for visualisation inside microchannels were machined. Water was supplied through external stainless tubes, connected to the top frame and the inlet/outlet holes drilled in the Pyrex glass cover plate. Two small o-rings were used to seal the connections between the holes in the top frame and those drilled in the Pyrex glass and prevent any leaks from the heat sink. Electrical connections for the heater and the sensors are made via aluminium pads deposited on the backside of the device and spring probes inserted inside the holes drilled in the bottom frame, Figure 3.4b. The spring probes were connected to the measurement instrumentation. Figure 3.5 shows photographs of (a) the experimental system and (b) the test module situated beneath the microscope.

3.4 Microfabrication process

The microchannels were fabricated in the Scottish Microelectronics Centre (SMC) using an Inductive Coupled Plasma (ICP) dry etch in conjunction with photolithographic techniques. The mask pattern is transferred onto the silicon using the contact lithography with an emulsion mask. Figure 3.6 shows the layout of masks used for the microfabrication process. The deep silicon etch process (developed by

a)

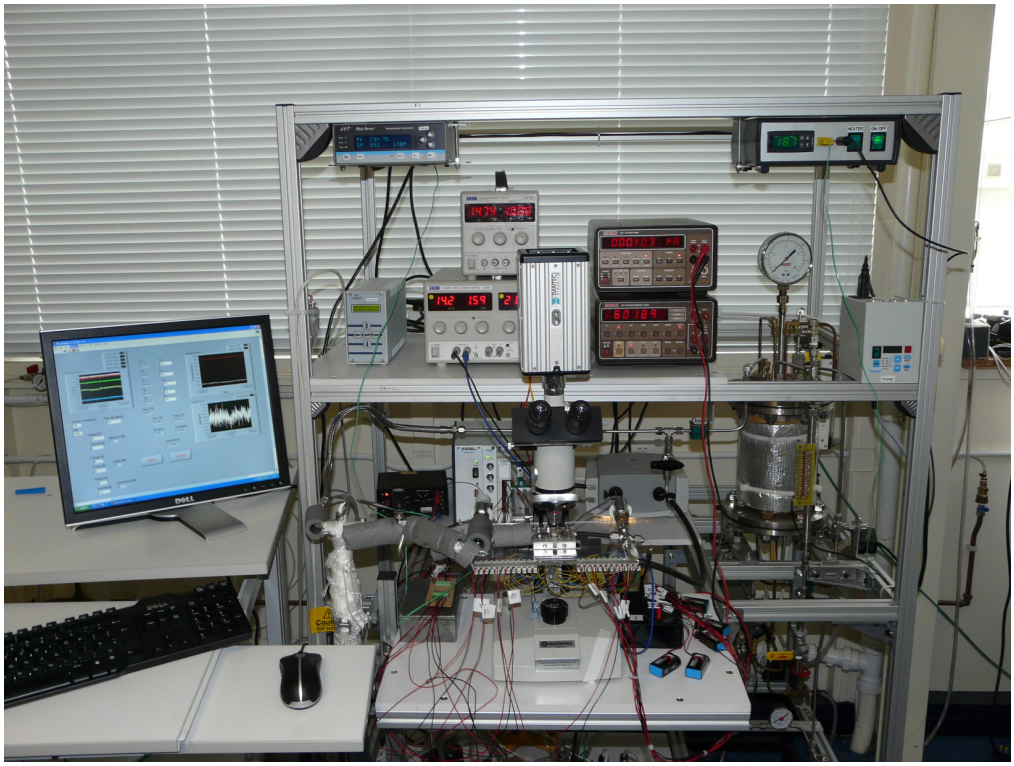

b)

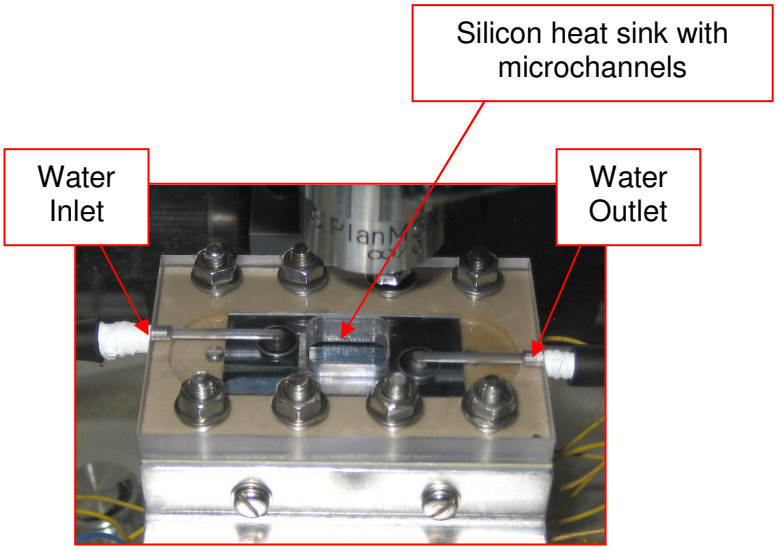

Figure 3.5 *Photographs of (a) experimental system (b) test module.*

workers at Bosch (Bosch process)) was used to make the microchannels, enabling nearly vertical side walls to be achieved. The following is a brief description of the microfabrication process according to the specifications provided by the SMC.

The fabrication started with 3-inch double-side polished n-type (100) single-crystalline silicon wafers (thickness of wafer is 380 µm). A thermal silicon dioxide layer of 0.3 µm was grown on both sides of the wafer to electrically isolate the temperature sensors from the silicon substrate on the back side of the wafer, and to prevent any possible scratches to the front side of the wafer during fabrication, Figure 3.7a. A lift-off process was then used to form temperature sensors on the back side of the wafers. A negative photoresist AZ5124 was used to define sensor tracks, and the patterned photoresist formed a shadow mask for the subsequent Ti/Ni deposition, as shown in Figure 3.7b. A combination of 0.02 µm Ti followed by 0.25 µm Ni was then deposited using a Balzers BAS450M sputterer (Figure 3.7c). The wafers were then immersed in acetone solvent, and followed by a megasonic agitation. The photoresist dissolved in the acetone and the thin metal film on top of

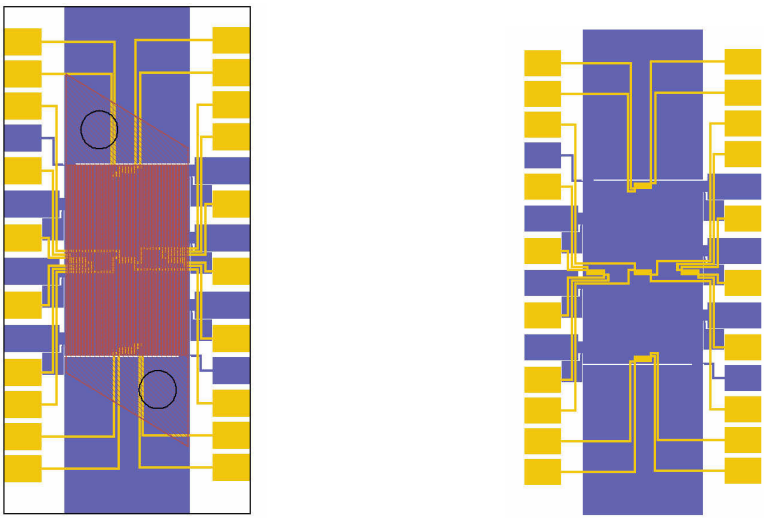

a) **b)**

Figure 3.6 *Layout of masks used in the microfabrication process (a) overall view, (b) layout of the heater and the sensors masks (red – channels with integrated inlet/outlet manifold; blue - heater; yellow - sensors).*

the photoresist lifts off into small pieces and is carried away by acetone, as shown in Figure 3.7d. The lift-off process is finished with a deionised water rinse (15 minutes) and wafer drying. A 3.0 μm PECVD (plasma enhanced chemical vapor deposition) oxide layer was then deposited on Ti/Ni layers using STS PECVD Multiplex, and the surface was then planarised using a CMP (chemical mechanical polishing) process with Presi E460, Figure 3.7e. A 1.0 μm Al deposition using Balzers sputterer, a lithography step using Karl Suss MA8 wafer aligner, and an Al dry etch using STS RIE Metal etcher were then performed to create the Al heater. The heater was then covered by PECVD oxide and the top surface planarised using CMP, Figure 3.7f. The silicon dioxide layer on the front side of the wafer was then dry etched using a Plasmatherm PK 2440 RIE etcher, Figure 3.7g. The micro-channels were then patterned using a thick photoresist SPR220-7 (7.0 μm), and the channels etched using a STS Multiplex ICP Deep etcher. After removing the photoresist on the front side of the silicon wafer, it was anodically bonded to a glass wafer (Pyrex 7740) using a Karl Suss BA8, Figure 3.7i. The test devices were ready to use after the subsequent wafer dicing.

The location of the sensors T1-T5, shown in Figure 3.8a, enables the measurement of temperatures in both the flow stream direction and the transverse direction. Figure 3.8b shows the layout of a single sensor. Each of the sensors has serpentine configuration with 13 turns and total width of 435 μm. The sensor length is 1500 μm covering 6 channels. The sensors are located 112 μm underneath the channel bottom wall. Each sensor has four pads for electrical connection, two for current supply and another two for voltage measurements. Such configuration enables a “four points” resistance measurement for a higher accuracy. The heater also has a serpentine configuration with 17 turns covering an area of 10.15 × 15.00 mm^2. The heater was powered via two large pads for uniform heating. Every three turns forms a small heater which can be powered independently via additional small pads for the case of non-uniform heating.

Figure 3.9a shows image of the microchannels obtained using the Philips Field Emission Gun Scanning Electron Microscope (SEM). The average surface

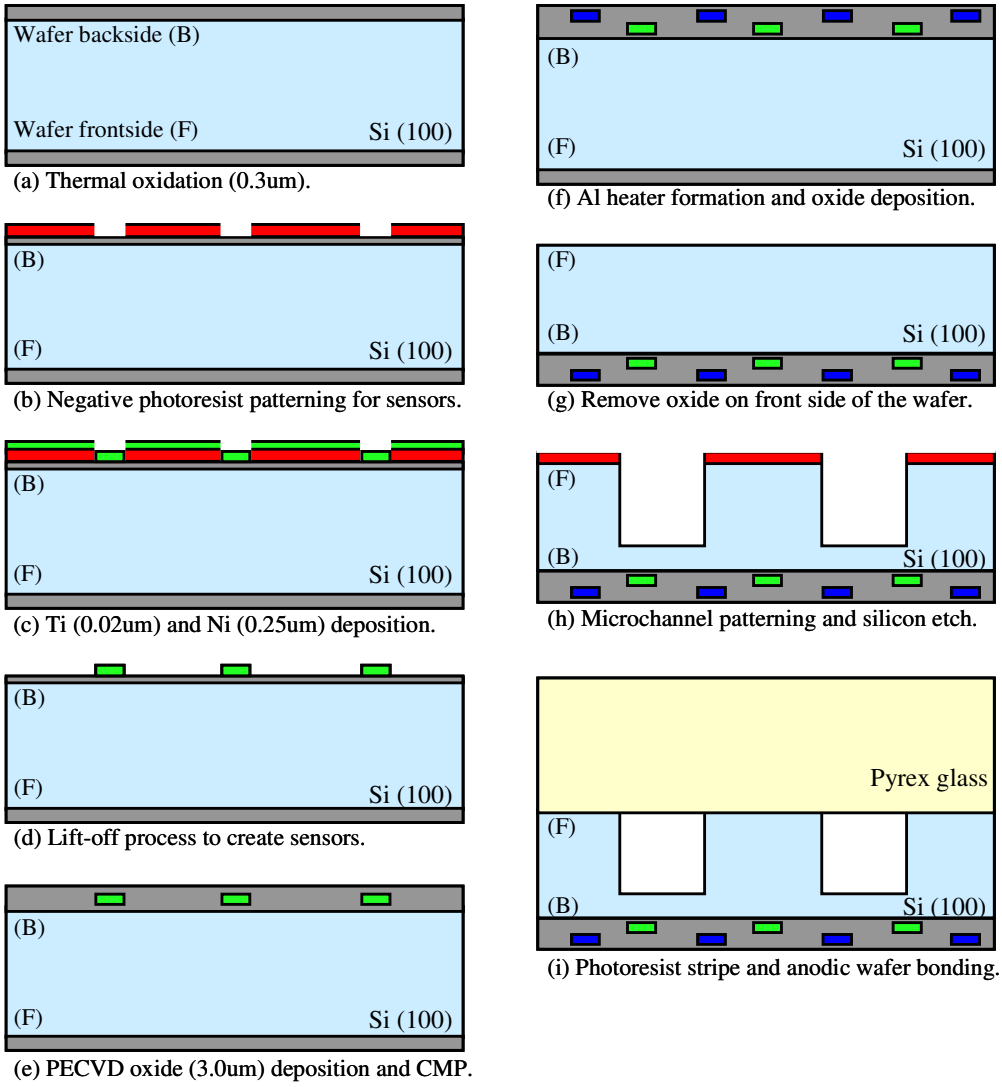

Figure 3.7 *Fabrication sequence of the integrated multi-channel device.*

roughness was measured using the Dektak 8000 Profilometer, values obtained were on the order of hundreds of nanometers. The surface of the bottom of the microchannels can be seen in Figure 3.9b and at the magnification used the various surface features can be observed. It is important to know the average surface roughness as this can affect any microboiling carried out in the channels [1, 2]. The atomic force microscope (AFM) image of the bottom of the channels is shown in Figure 3.10. The channels bottom surface has a root mean square (RMS) roughness of 59.1 nm.

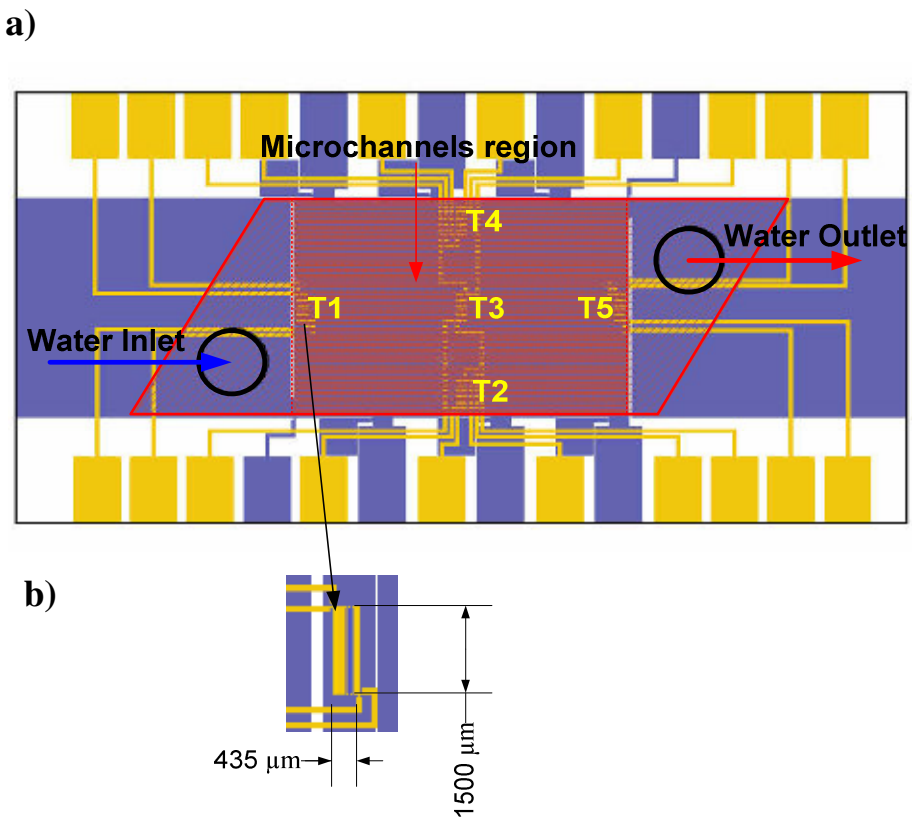

Figure 3.8 *(a) location of the temperature sensors (b) the layout of a single sensor.*

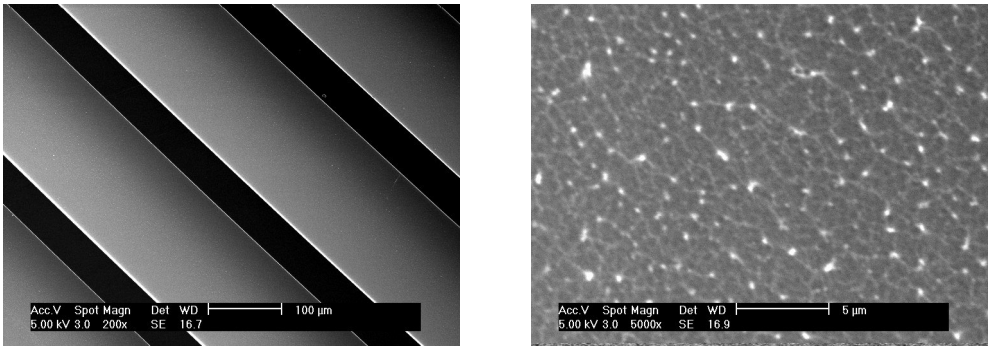

Figure 3.9 *SEM image (a) microchannels (b) bottom surface of microchannel.*

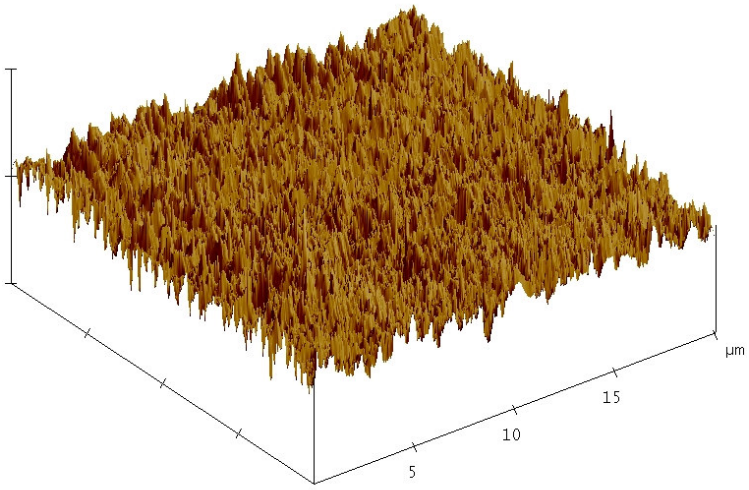

Figure 3.10 *AFM image of bottom surface of microchannel (RMS roughness: 59.1 nm).*

3.5 Data acquisition system and measurements uncertainty

Pressure, temperature and voltage from the microsensors were acquired and recorded using a National Instruments 16-bit SCXI-1600 data acquisition system (DAQ system) in conjunction with SCXI-1100 analog input module and a LabView software interface (appendix C). This configuration enables 166 kS/s maximum sampling rate scanning all 32 channels of SCXI-1100 module with a resolution of 0.15 mV at 0-10 V input range. According the manufactures specification absolute accuracy of this system is ± 8.2469 mV for the signal range from -10 to 10 V [3]. Two absolute pressure transducers and two T-type thermocouples, located immediately upstream and downstream of the test module were used for monitoring the inlet/outlet pressures and temperatures respectively. The pressure transducers and the thermocouples were directly connected to differential channels of the DAQ system.

The pressure transducers used (Omega PXM219 series) have a full scale accuracy of 0.25% (including linearity, hysteresis and repeatability) and a response time of 2 ms. The measurement range is 0-2.5 bar with 0-10 V output and operating

temperature from -54 to 121 ˚C. The pressure transducers were calibrated by the manufacturer and a 5 points calibration certificate was provided.

The Bronkhorst L30 mass flow meter is essentially a straight tube of 316L stainless steel with a thin film thermopile sensor/heater design, fixed to the outside of the tube. The sensor signal is obtained by measuring the power needed to maintain a constant temperature rise of the fluid. The standard accuracy of the thermal mass flow meter (Bronkhorst L30 Series) was ±0.5 g/min with reproducibility of ± 0.2 % of full scale (50 g/min).

The uncertainties related to the thermocouples measurements were ±0.5 ˚C for T-type thermocouples. The thermocouples used for inlet/outlet water temperature measurements and sensors calibration were checked using ASL F250 MKII Precision Thermometer with platinum resistance thermometer probe with an accuracy of ± 0.01 ˚C at the full range. The three T-type thermocouples connected to the DAQ system were placed inside a controllable temperature bath together with the platinum probe connected to the precision thermometer. Water temperature in the bath was varied from 26 to 94 ˚C in steps of approximately 5 or 10 ˚C. Once the steady state was reached, temperatures from the three thermocouples and platinum probe were recorded. Table 3.1 presents data recorded using the DAQ system with thermocouples and the precision thermometer with platinum probe. Differences between the values recorded with thermocouples and values recorded with high precision thermometer were less than 0.45 ˚C.

The heater was connected to a TTi EX354Tv DC power supply having two independent and isolated outputs each with a 0 to 35 V, 0 to 4 A capability. The total power capability is 280 W. The power supply incorporate separate digital voltage and current meters on each main output. The meters use LED displays and have a scanning rate of 4 per second with resolutions of 100 mV and 10 mA. Meter accuracies are 0.3 % for voltage readings and 0.6 % for currents. The total power supplied to the heater was calculated from the product of voltage and current and the uncertainty related to the power measurements is 0.9 % of calculated power.

Table 3.1 *Comparative measurements of temperatures using high precision thermometer (T_{ref}) with platinum resistance probe and DAQ system with thermocouples (T_{cal} for sensors calibration, T_{in}/T_{out} for inlet/outlet water temperature).*

T_{ref}, ˚C	T_{cal}, ˚C	T_{in}, ˚C	T_{out}, ˚C
26.60	26.90	26.90	26.90
35.34	35.60	35.60	35.70
44.93	45.20	45.20	45.20
54.81	55.06	55.05	55.08
64.78	64.91	64.90	64.93
69.70	70.03	70.01	70.07
74.73	75.04	75.04	75.10
79.67	79.96	79.93	79.99
84.61	84.98	84.90	84.95
89.49	89.90	89.85	89.89
94.41	94.86	94.78	94.81

The heat flux transferred to the water was calculated from $q = \varphi VI/A$, where V and I are the input voltage and the current across the film heater, A the area of the heated microchannels region, and φ the portion of the total power transferred to the water. In order to determine φ, a series of single-phase heat transfer experiments were carried out prior to boiling experiments. The portion of the total power transferred to the water was computed from $Q = mc_p(T_{out}-T_{in})$, where the specific heat capacity was calculated based on the mean water temperature (average of the water inlet and outlet temperatures). The total power to the heater was determined from product of the voltage (V) and current (I) with φ being computed from $\varphi = Q/VI$. The values of φ were found to be in the range of 0.83 to 0.95 depending on the heat flux and flow rate. The mean value of 0.89 was used to determine the heat flux transferred to the water. It is worth noting that the procedure of calculating the portion of the total power transferred to the water was similar to that used by Hetsroni et al.[4], Liu et al. [5], and Wang et al. [6].

Temperature measurement using integrated microsensors (T1-T5, Figure 3.8) is based on resistance measurements. The electrical resistance of the microsensors was measured with a four points measurement technique. Two pads of each sensor were used for an independent current source providing 0.5 mA constant current and

another two pads for the measurements of the voltage across the sensor using DAQ system. The resistance was determined from the measurements of the voltage and constant current and converted to corresponding temperature using a temperature vs. electrical resistance function obtained from calibration. The sensors were calibrated using a reference T-type thermocouple to characterise the temperature-resistance relationship. The calibration system is schematically presented in Figure 3.11. High mass flux of preheated water was supplied into the insulated test module to ensure temperature uniformity over the chip. Once the steady state was reached temperature from the reference thermocouple and the resistance from the sensors were recorded simultaneously. The temperature-resistance relationship for 5 integrated sensor is shown in Figure 3.12. The sensors had a typical sensitivity of 3.3 Ω/˚C and an accuracy of ±0.5 ˚C using the present acquisition system. The thermal time constant associated with the nickel sensors was 1.6×10^{-4} s. Temperatures on the sensors and the inlet/outlet pressures were sampled at rates of 100 and 50 Hz. The test module inlet temperature was maintained within ± 1 ˚C.

When building a DAQ system it is important to consider the output range of the sensor in order to apply suitable device gain (the factor by which a signal is amplified in a DAQ system), type of the output signal (single ended or differential, and ground or ungrounded-floating) and the sensor's output impedance. As already mentioned the resistance was determined from the measurements of the voltage and constant current and converted to the corresponding temperature. Current source of 0.5 mA was powered with 9V battery for each sensor therefore, temperature sensor was considered as ungrounded (floating) differential signal with a voltage output from 0 – 1 V. Impedance is a combination of resistance, inductance, and capacitance across the input or output terminals of a circuit. It is important that the input impedance of the DAQ device is much higher relative to the output impedance of the selected transducer. In general, the higher the input impedance of the DAQ device the less the measured signal will be disturbed by the DAQ device. It is also important to select a sensor with as low output impedance as possible to achieve the most accurate analog input (AI) readings by the DAQ device. High source

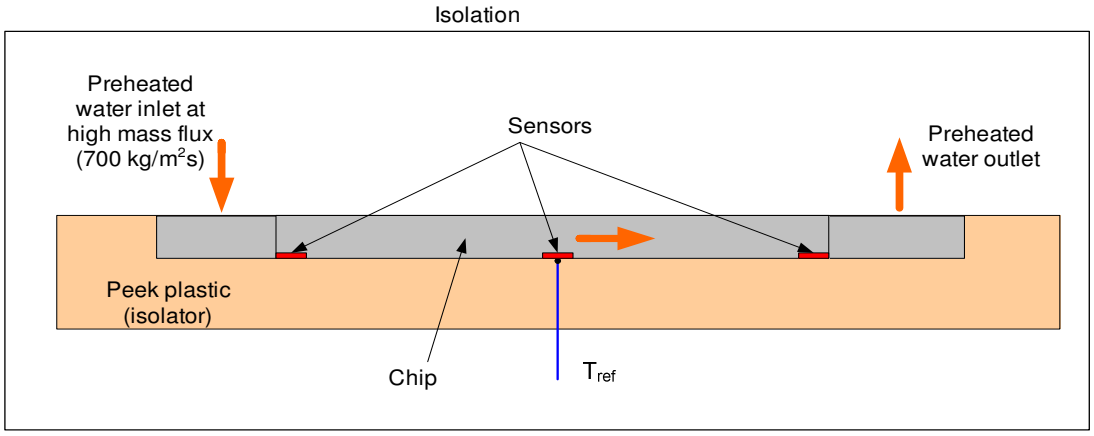

Figure 3.11 *Calibration system for integrated temperature sensors calibration.*

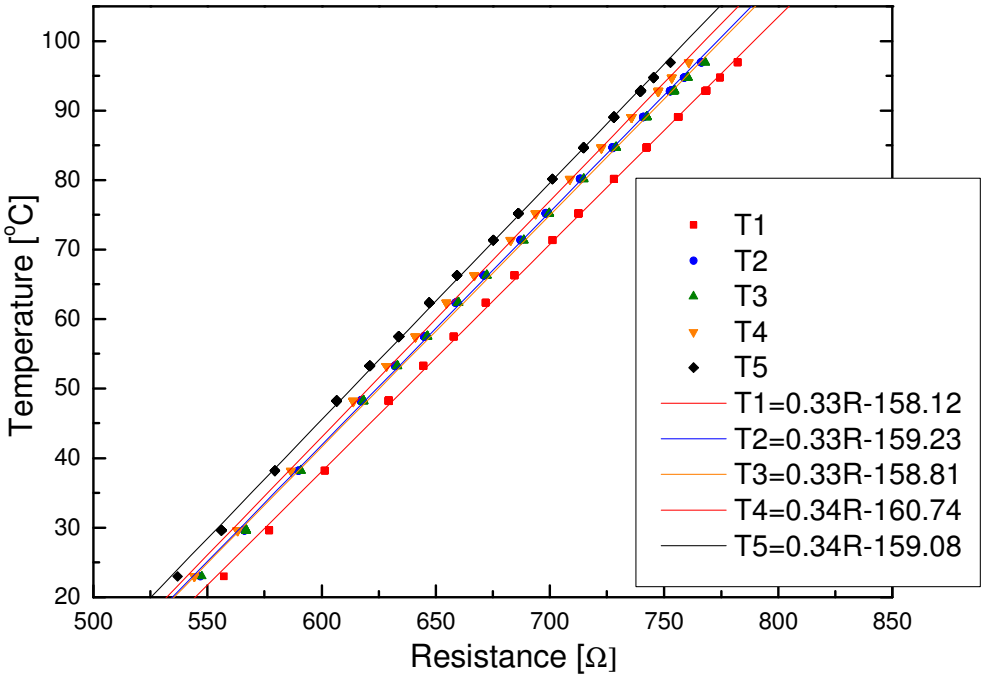

Figure 3.12 *Temperature calibration curves.*

impedance affects a DAQ system by increasing the settling time of the amplifier of the DAQ device amplifier when sampling multiple channels. Settling time is the amount of time that it takes for a measured signal to reach a specified accuracy and to stay within the range tolerance. The settling time increases when sampling high-impedance sources due to the input capacitance of the DAQ device and also due to a phenomenon called charge injection. When the input multiplexer of the DAQ device switches to a given channel, the input capacitance of the DAQ device must be charged through the output impedance of the source. Such output impedance can take a long time if the source impedance is especially high. Ideally, source impedances should be kept low (< 1 kΩ) when sampling multiple analog-input channels. The temperature sensors integrated in microchannels device were considered as a high source impedance preventing the signal from settling to within the specified accuracy of the DAQ device. Therefore, it was necessary to implement a unity gain buffer (voltage follower) between the sensors and the DAQ device to reduce the impedance of the source. Figure 3.13 shows a schematic of the voltage follower used for each of

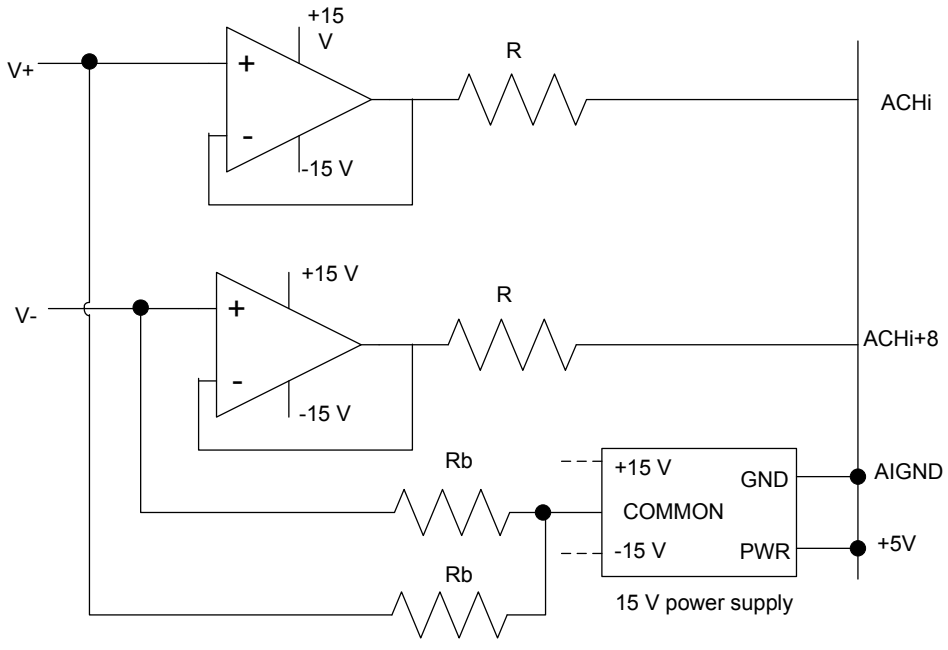

Figure 3.13 *Schematic of voltage follower used for each of temperature sensors.*

the temperature sensors in the device. The positive and negative leads of the sensor (V) were connected to positive input of two op-amplifiers. A power supply was required to provide ± 15 V to the op-amp, with the power supply being referenced to the analog input ground (AIGND) of the DAQ device. The output of the op-amp is then connected to the input of the DAQ device. A bias resistor was connected between the negative input and AIGND to keep the signal within common-mode range and to prevent the amplifier in the DAQ device from saturating.

The use of microfabrication techniques enables more accurate and reproducible channel dimensions. In the x-y plane the dimensions and layout of the channels are largely determined by the mask pattern. The mask pattern is transferred onto the silicon using photolithography and the pitch of the channels is always faithfully reproduced. The width of the channel depends upon both the lithography and etch process biases. The variations of channel width were considerably less than the accuracy of the Vickers CSS microscopic measuring system (resolution of 1 μm and accuracy of ± 8 μm). Channel depths were also measured at several points across the array using the Vickers CSS microscope. These depths varied from 252 to 280 μm, with the average depth being 273 μm. The difference in channel depth across a microchannel array can be attributed to non-uniformities in the plasma density of the deep reactive ion etch system and also the non-uniformity of the density of exposed silicon being etched. It is unclear whether the variation in the channel depth is random or systematic.

Visualisation of boiling within the channels was undertaken using a high speed camera (NanoSense MkIII), mounted on a microscope with a 5× magnification objective and axial illumination. The camera had a maximum frame rate of 1000 fps at full resolution of 1280×1024 pixels.

3.6 Conclusions

An experimental system has been designed and built to conduct an experimental study of flow boiling in microchannels. A silicon heat sink with parallel microchannels and integrated heater and temperature sesnors has been developed.

The advantages of using microfabricated temperature sensors and integrated heater in comparison to using standard temperature measurements technique such as thermocouples and a heater separated from the heat sink are:

1. A much faster response time (1 micron thick nickel film in comparison to standard thermocouples with diameter of e.g. 0.1 mm). The response time is practically instantaneous allowing high frequency sampling.
2. Smaller thermal resistance between the sensors and the channels as the sensors were integrated between the thin metal film heater and the channels etched into silicon wafer. With thermocouples there is inevitable gap between the heater and the silicon heat sink.
3. Better accuracy using the "four point" measurements and temperature measurements based on the resistance measurement method.
4. Using of the integrated heater gives the lower thermal resistance between the heater and the channels.

References

1. Golobič, I. and K. Ferjančič, *The role of enhanced coated surface in pool boiling CHF in FC-72.* Heat and Mass Transfer, 2000. 36(6) 525-531.
2. Honda, H., H. Takamastu, J.J. Wei, *Enhanced Boiling of FC-72 on Silicon Chips With Micro-Pin-Fins and Submicron-Scale Roughness.* Journal of Heat Transfer, 2002. 124(2) 383-390.
3. *http://www.ni.com/advisor/accuracy/.*
4. Hetsroni, G., A. Mosyak, E. Pogrebnyak, Z. Segal, *Explosive boiling of water in parallel micro-channels.* International Journal of Multiphase Flow, 2005. 31(4) 371-392.
5. Liu, D., P.-S. Lee, S.V. Garimella, *Prediction of the onset of nucleate boiling in microchannel flow.* International Journal of Heat and Mass Transfer, 2005. 48(25-26) 5134-5149.
6. Wang, G., P. Cheng, H. Wu, *Unstable and stable flow boiling in parallel microchannels and in a single microchannel.* International Journal of Heat and Mass Transfer, 2007. 50(21-22) 4297-4310.

Chapter 4 Investigation of flow distribution within microchannels

4.1. Introduction

This chapter presents the results obtained using numerical simulations that assisted in the design of the heat sink with microchannels used in the experimental investigations. The thermal efficiency of microchannel-based heat sinks relies on uniform fluid flow distribution between channels. Maldistribution, whether caused by poor manifold design or blockage of individual microchannels, can lead to hot-spots and consequent thermal damage. Proper design of the geometry of microchannel-based heat sinks, including design of inlet/outlet manifolds and channels size, thus ensures good thermal efficiency of microchannel heat exchangers whilst keeping the pressure drop reasonable. Good flow distribution depends not only on achieving a distributor design that will work when all microchannels are operational, but also on consideration of the effect of temporary or permanent blockage of microchannels. Such blockage may occur through manufacturing imperfections, by fouling or through the particle deposition in the microchannels.

Flow distribution is also important in the design of microreactors. Miniaturization of chemical reactors offers many advantages such as high heat and mass transfer rates, high interfacial area between phases in the case of multiphase reaction systems, higher yields and reduced safety risk and environmental impact [1,

2]. Here it is important to design micro-devices able to guarantee the same residence time in all microchannels. Flow maldistribution can affect the performance of microreactors in terms of yield and product selectivity and can cause significant fluctuation of heat and mass transfer coefficients over the reaction time.

Generally, there are three approaches to design of micro-devices to ensure even distribution: analytical, computational fluid dynamics (CFD) modelling and experimental.

An analytical model based on approximation of pressure drop along channels of a microreactor as linear function of inlet velocity was developed by Commenge et al. [3]. The authors compared the results obtained by the analytical model with the finite-volume method and it was found to show good agreement for the geometries studied in all cases. The analytical model was used to assess the influence of various geometric parameters on flow distribution. The authors found that a larger contribution of pressure drop through the channels should result in a more uniform velocity distribution. An increase in channels length or/and decrease in the cross section for fluid flow through the channels results in a higher pressure drop, yielding a more uniform velocity distribution. Since the model neglects the additional pressure losses due to merging and branching effects, the distribution does not depend on the flow rate. This model is valid only for low Reynolds numbers when additional pressure losses are of secondary importance.

Amador et al. [4] have used a similar approach developed by Commenge et al. [3] to investigate flow distribution in two different manifold structures: consecutive and bifurcation using an analogy with electrical resistance networks. The model allows for randomly generated manufacturing variations as well as channel blockage. It was found that bifurcation structure always gives even flow distribution in the absence of manufacturing variations. The authors pointed out disadvantages of bifurcation structures such as high pressure drop and large area occupied by the channels. For the consecutive structure, two different designs have been considered, one with uniform cross section in the distributor and the collector manifolds and another with non-uniform cross-section. The first design is recommended when manufacturing tolerances are large and uncertain and channel blockages are

expected, while the second design is suitable when the manifolds area needs to be minimized and tolerances are small. The model is valid only for low Reynolds number because additional pressure losses were neglected.

Facao and Gruss [5] analyzed flow distribution in an array of parallel minichannels in "Z" configuration using simulation and experiments. The authors developed a model that accounts for the additional pressure losses. The model was compared to both CFD simulations and experimental results. Good agreement between CFD simulation and model was attained. The model was found to predict well the total pressure drop. The authors proposed an experimental technique with a liquid crystal sheet and a CCD camera to evaluate the flow distribution. The technique is based on recording the thermal front position as a function of time. However, the absolute measured velocity had a significant deviation from velocities evaluated by CFD simulations. Another experimental technique was used by Pfeifer et al. [6], who measured the flow distribution in a microchannel reactor using hot-wire anemometry with constant wire temperature.

A CFD-based optimisation method is proposed by Tonomura et al. [7] for the design of microchannel devices. Fluent based code with finite-volume method was used to investigate effects of design parameters such as channel length and manifold area on flow distribution. It was found that longer channels and bigger outlet manifold area enabled the fluid to be more evenly distributed. An optimization method was developed in order to minimize the manifold area. The CFD optimisation method gives rigorous results, but requires much more time for solution than approximate analytical models. Another CFD simulation has been performed by Griffini and Gavriilidis [8] in order to investigate flow distribution in microstructured plates of various geometries. The authors used both 2D and 3D models of microchannel plates in their investigations. It was found that a critical value for Reynolds number exists above which additional pressure losses due to inertial effects started to influence the flow distribution within the microchannels. The results of simulations showed discrepancies in a critical Reynolds number between 2D and 3D models. According to the authors, two-dimensional simulations can be misleading in assessing flow maldistribution, as they give an overestimate of flow maldistribution.

The authors concluded that at low flow rates channel length, manifolds length, plate width, shape of manifolds, and inlet/outlet location are the most important parameters that have to be considered in order to achieve optimal flow distribution over a microstructured plate. Pan et al. [9] studied the flow distribution among microchannels using a numerical analysis method applied to microchannel physical model. Their results indicated that the flow distribution among microchannels with symmetrical manifolds is better than that with asymmetrical ones. According to the authors, the angles of asymmetrical manifolds with right triangle shape have a considerable effect on the flow distribution among microchannels.

Eun Seok et al. [10] compared two configurations of heat sinks consisting of parallel microchannels. One was standard with straight channels, whereas the second contained 5 cross-linked channels. According to the authors, the cross-linked microchannel improved temperature distribution uniformity at low flow rates of 1 ml/min when hotspot type heat fluxes were applied. The authors suggested that cross-linking of microchannels can be promising for achieving better temperature uniformity and more effective cooling due to the lateral fluid transport and mixing. Dang et al. [11] experimentally investigated adiabatic two-phase flow distribution and flow patterns in two test sections with parallel minichannels using water and air as the working fluids. One test section was a standard straight multi-channel configuration, while the second was similar with two cross-linked channels. Their results showed that the straight and cross-linked designs both have unequal flow distributions. The authors observed intermittent flow regime (plug, elongated bubble flows), and annular flow in both test sections investigated. However, more instances of intermittent flow regime were observed in the cross-linked test section, whereas less annular flow pattern was observed compared to the straight test section.

In the present work an approximate model based on the one developed by Amador et al. [4] and 3D simulations with COMSOL modeling software were used to obtain velocity and pressure fields in microchannel heat sinks. Various parameters, which influence the flow distribution such as the shape of distributing and collecting manifolds and position of inlet and outlet holes, have been studied for different inlet flow rates. The effect of channel blockage on flow distribution and pressure drop has

been investigated. Based on the simulation results micro heat-exchangers have been designed and fabricated. In addition, some experiments for single and two-phase flow boiling have been carried out in order to estimate the flow distribution within the channels.

4.2. Approximate model

An approximate model developed by Amador et al. [4] has been used for the design of inlet distributor and outlet collector for the six models with microchannels specified in Table 4.1. Results for flow uniformity through channels obtained by this model were compared with the results of CFD simulations.

Table 4.1 *Dimensions of six devices with microchannels (D_{ch} channel depth, W_{ch} channel width, W_w wall thickness, D_h channel hydraulic diameter).*

Design	D_{ch} [μm]	W_{ch} [μm]	W_w [μm]	D_h [μm]	No. of channels
1	300	50	50	85.7	100
2	300	50	100	85.7	66
3	300	100	50	150	66
4	300	100	100	150	50
5	300	150	50	200	50
6	300	150	100	200	40

A parallel network of microchannels in "Z" configurations and manifolds with constant and non-constant, linear cross sections have been chosen for the models used in this study. Figure 4.1 shows the two structures of manifolds assessed a) with non-constant, linear cross-section and b) with constant cross-section. According to several authors [3-5, 7] Z configuration of a microchannel assembly yields the best results in term of flow distribution within microchannels. A single-phase, adiabatic, laminar water flow with constant density and viscosity along the whole structure was assumed. It was also assumed that the fluid behaved as a continuum with pressure

drop being calculated using equations for macro scale flows. Additional pressure losses due to merging, branching and bend effects were neglected.

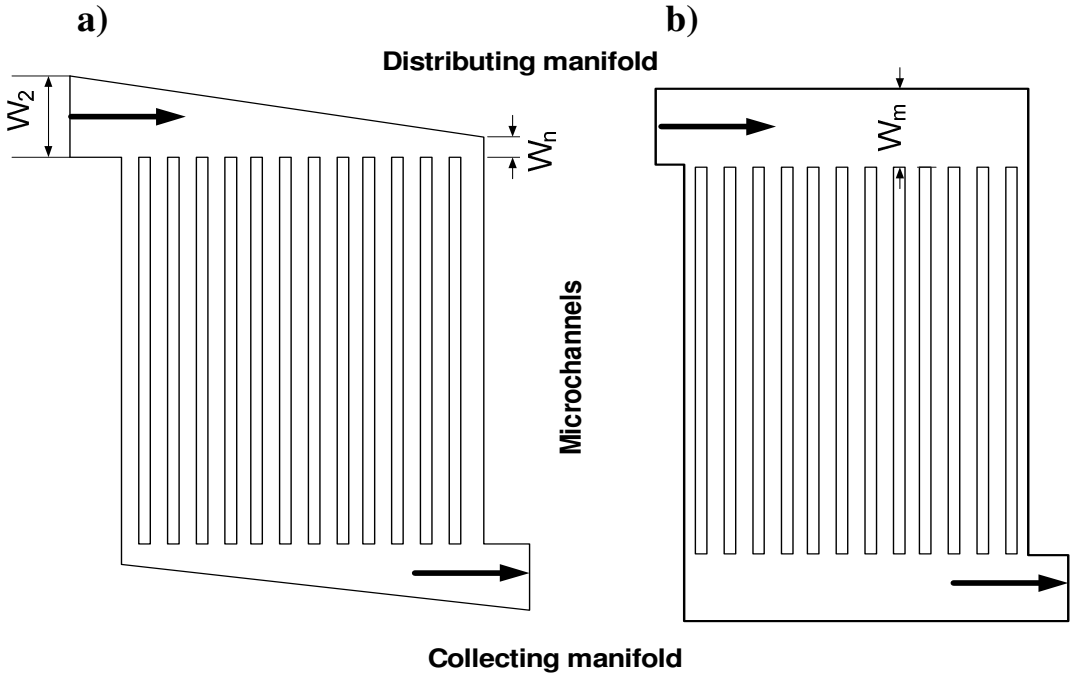

Figure 4.1 *Schematic diagrams of parallel microchannels network in Z configurations with a) non-constant, linear cross-section manifolds and b) constant cross-section manifolds (arrows show direction of the liquid flow, W_2 is width of the first zone and W_n is width of the last zone for non-constant cross-section manifolds, W_m is width of the constant cross-section manifolds).*

Microchannel arrays with distributor and collector are converted to a resistance network as presented in Figure 4.2. An analogy with Ohm's law was used in eq. 4.1 where dimensionless pressure drop is made equivalent to voltage difference with dimensionless flow rate being equivalent to current. All dimensionless values are denoted by asterisks. Dimensionless channel lengths L^*, channels depth D_{ch}^* and channel widths W_{ch}^* were determined with respect to the width of channels W_{ch}, thus $L^*=L/W_{ch}$, $D_{ch}^*=D_{ch}/W_{ch}$ and $W_{ch}^*=1$. The dimensionless flow rate Q^* is defined using characteristic flow rate Q_{eq}, being the flow rate in each channel for uniform flow distribution, so that $Q_{eq}=Q_T/N$ and $Q^*=Q/Q_{eq}$.

$$\Delta P^* = R^* \cdot Q^* \tag{4.1}$$

The equation for the dimensionless resistance, based on the Hagen-Poiseuille flow equation, is given by (Amador et al. [4]):

$$R^* = \frac{128 L^* \lambda}{D_h^{*4} (D_{ch}^* / W_{ch}^* + W_{ch}^* / D_{ch}^* + 2)}, \tag{4.2}$$

where the non-circularity coefficient λ is defined by eq. 4.3.

$$\lambda = 0.5 / ((1 - 0.315 D_{ch} / W_{ch})^2 (1 + D_{ch} / W_{ch})^2) \tag{4.3}$$

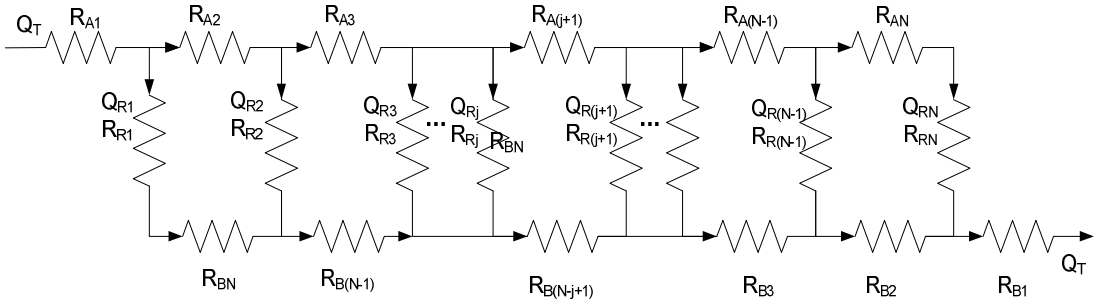

Figure 4.2 *Resistance network for microchannels array.*

Implementing Kirchoff's laws for electrical networks (junction rule as equivalent to mass conservation and loop rule as equivalent to energy conservation), presents a system of linear equations and can be expressed in a matrix form

$$M \cdot Q = S \tag{4.4}$$

$$Q = inv(M) \cdot S \tag{4.5}$$

where M is an N x N matrix with the dimensionless resistances and N is the number of channels. Q is the column vector with N channel dimensionless flow rates and S is an N column vector composed of zeros and dimensionless total flow rate Q_T in the last position. MATLAB code was used to solve the system of linear equation in a matrix form. A uniform distribution through the channels implies equal pressure drop along the channels. Using this condition for uniformity it is possible to find a relation between the width of the inlet zone and the width of the corresponding outlet zone

[3]. Additionally, a linear geometry for optimal distributor layout was used to avoid unrealistic designs for distributing and collecting manifolds. Using these two conditions together with an electrical resistance network, the model can be used for rapidly calculating the flow distribution through the channels and optimal geometry parameters such as the width of inlet/outlet manifolds.

A summary of the results from simulations for the six designs from Table 4.1 with non-constant, linear cross-section manifolds is given in Figure 4.3. This graph presents the dimensionless width of the first zone of the inlet/outlet manifold (W_2, Figure 4.1) and corresponding dimensionless width of the last zone of the inlet/outlet manifold (W_n, Figure 4.1) yielding a uniform flow distribution within microchannels. Simulations gave the same results for optimal widths of inlet/outlet manifold for devices 2 and 3 as well as devices 4 and 5, and therefore lines overlap in the graph. However, the pressure drop results are different. All values are non-dimensional where the characteristic dimension is the width of channels W_{ch}. The pressure drop for different designs has also been calculated. The non-dimensional pressure drop is defined by eq. 4.6 where $U_c = Q_T/(N \cdot W_{ch}^2)$ is a characteristic velocity.

$$p^* = \Delta P \cdot W_{ch} / (\mu \cdot U_c) \tag{4.6}$$

The values for the pressure drop obtained using the approximate model are not reliable since the model does not take into account the additional pressure drops due to inertial forces. The results in Figure 4.3 serve to give an idea as to how pressure drop increases as the size of the inlet/outlet manifolds decreases.

Results of comparison between flow distributions among microchannels with non-constant linear cross-section manifolds and flow distributions with constant cross-section manifolds showed that non-linear cross-section yielded a better distribution. The approximate model was used and the flow rate in each channel is worked out by a numerical analysis method. The flow rates are normalized with respect to the channel flow rate for uniform flow distribution Q_{eq}. The results of comparison are shown in Figure 4.4. It is clear from the Figure 4.4 that non-constant linear manifolds enabled better flow distribution within microchannels than constant cross-section manifolds with the same width as that of the first zone for non-constant

cross-section manifolds. A width of 6.18 mm was used for the first zone of non-constant cross-section manifolds, same as later being used in the process of microfabrication for design 6 (Table 4.1).

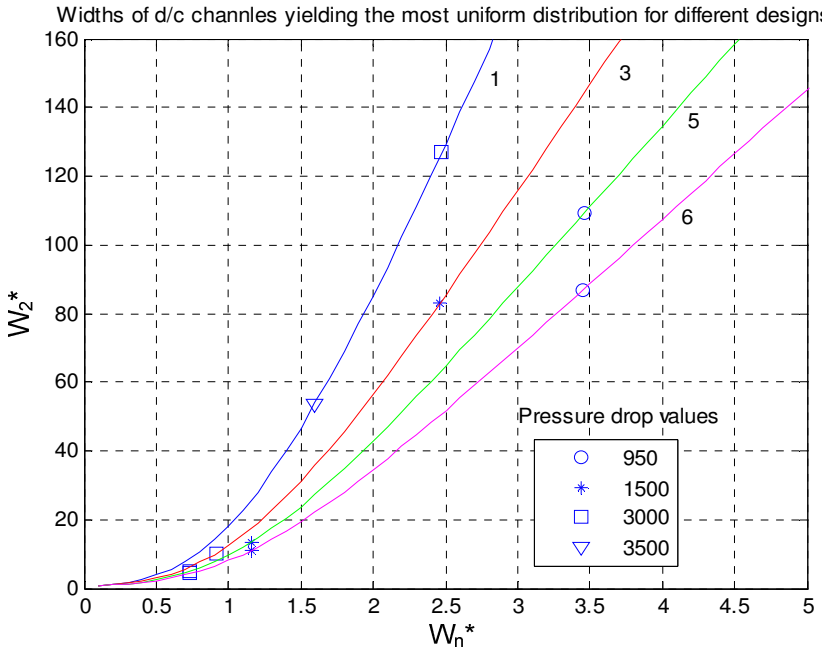

Figure 4.3 *Geometry of manifolds yielding the most uniform distribution for six designs from Table 4.1.*

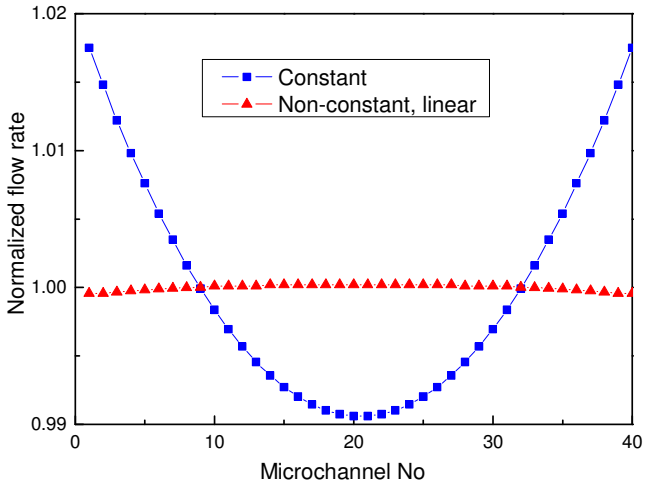

Figure 4.4 *Flow distributions within 40 channels for two manifolds structures, one with constant cross-section manifold (Figure 4.1b) and another with non-constant, linear cross-section manifold (Figure 4.1a).*

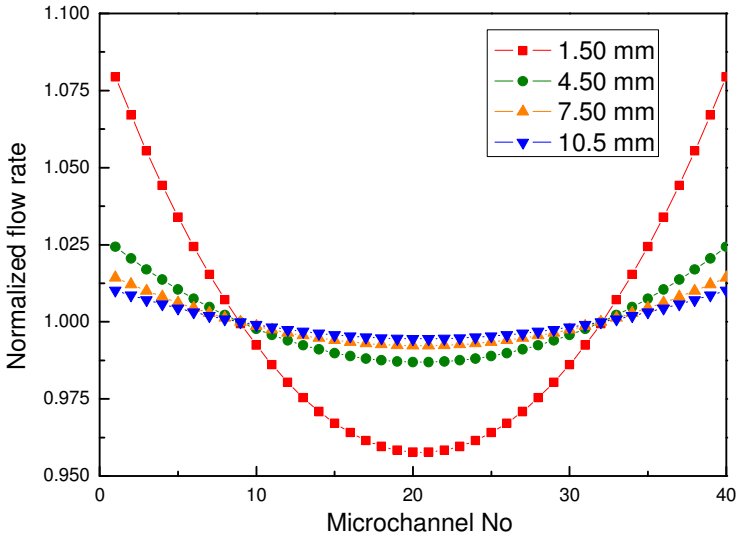

Figure 4.5 *Flow distributions within microchannels with constant cross-section manifold for different widths (W_m, Figure 4.1b) of the inlet/outlet manifold.*

It was found that an increase in width (W_m, Figure 4.1b) of inlet and outlet manifolds with a constant cross-section, resulted in more uniform flow distribution as shown in Figure 4.5 for different widths of inlet/outlet manifold. The latter is in agreement with the general rule that reduction of pressure drop in distributing/collecting manifolds enables fluid to be uniformly distributed within microchannels.

The results obtained by the approximate model for microchannels with both manifold structures were compared with the results obtained by CFD simulations. The results of this comparison are presented in the following section.

4.3 CFD simulations

In this study COMSOL Multiphysics, which implements the finite element method for solving partial differential equations, has been used for CFD simulations [12]. All the simulations were carried out on four dual-core Opteron 275s workstations with 8 GB RAM, and 3D models of parallel rectangular microchannels with integrated inlet/outlet manifolds were generated.

3D incompressible Navier-Stokes application mode was used to solve steady-state models, considering water as a fluid with density of 1000 kg/m^3 and viscosity of 0.001 Pa s. The governing equations are Navier-Stokes with negligible gravity,

$$\rho \frac{\partial u}{\partial t} - \mu \nabla^2 u + \rho (u \cdot \nabla) u + \nabla p = 0 \tag{4.7}$$

with the equation of continuity for incompressible fluids being

$$\nabla \cdot u = 0 \tag{4.8}$$

The Navier-Stokes equation was rewritten in a dimensionless form, introducing the dimensionless variables $u^*=u/u_c$, $x^*=x/x_c$, $t^*=tu_c/x_c$, $p^*=p/(\rho u_c^2)$, where u_c is the characteristic velocity in the microchannels, assuming uniform flow rates through the channels $u_c=Q_T/(N \cdot W_{ch} \cdot D_{ch})$. The dimensionless formulation is convenient in cases where iterations may not converge [13]. This is usually the case when CFD in microchannels is considered. The variables were substituted into the Navier-Stokes equation and introducing Reynolds number the equation becomes

$$\frac{\partial u^*}{\partial t^*} - \frac{1}{\mathrm{Re}} \nabla^{*2} u^* + u^* \nabla^* u^* + \nabla^* p^* = 0 \tag{4.9}$$

Equation 4.9 was implemented together with the dimensionless continuity equation in the fluid sub-domain. Inflow/outflow velocity was selected as the inlet boundary condition, non-slip boundary conditions were set at all walls and a zero outflow/pressure was set as outlet boundary condition. A structured mesh was generated extruding a 2D mesh with triangular elements (Figure 4.6a) into a 3D mesh with prism elements (Figure 4.6b). The stationary nonlinear solver with element type Lagrange p2-p1 was used for solving the incompressible Navier-Stokes equations. An iterative solver (GMRES) with incomplete LU preconditioner for non-symmetric problem was selected to solve the system of linear equations. Results of the generated simulations were the velocity and pressure fields and, by using boundary integrations, the flow rates through each channel were obtained.

The approximate model was used to design two 3D models; one with constant cross-section (design A1) and another with non-constant, linear cross-section of

manifolds (design 6 from Table 4.1). Design A1 consists of 20 channels with the same dimensions of channels as design 6 and channel lengths of 10 mm. The width of inlet and outlet manifolds is 2 mm. Design 6 consists of 40 channels with 15 mm length (Table 4.1) and integrated inlet/outlet manifolds. Widths of inlet/outlet manifolds are 6.18 mm for first zone and 0.33 mm for the last zone of manifolds. Figure 4.7 shows the layout of design A1, while Figure 4.8 the layout of design 6 with the inlet and outlet flow being designed parallel to the plane of the channels. Design A1 has a structured mesh with 20672 elements and 354074 degrees of freedom, while design 6 has a structured mesh with 58968 elements and 1017380 degrees of freedom.

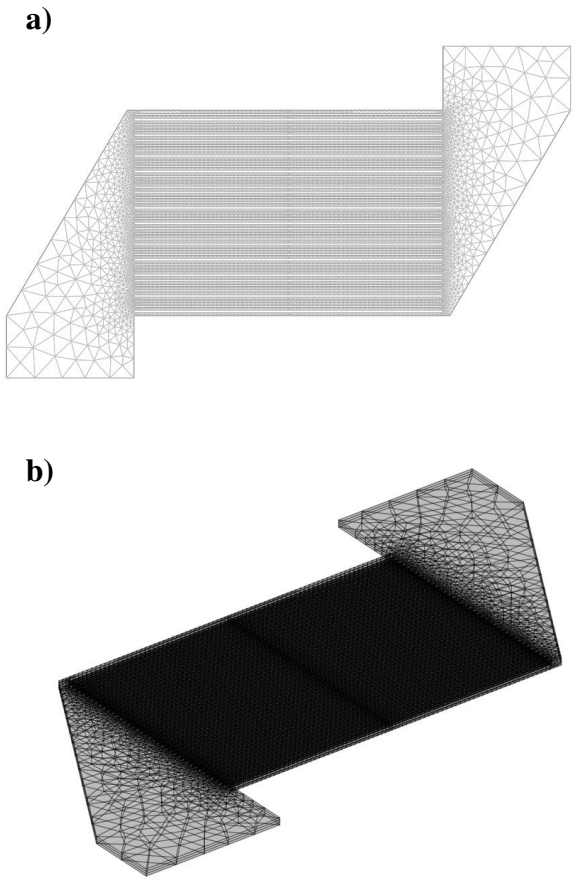

.

Figure 4.6 *2D mesh with triangular elements (a) and 3D mesh with prism elements (b).*

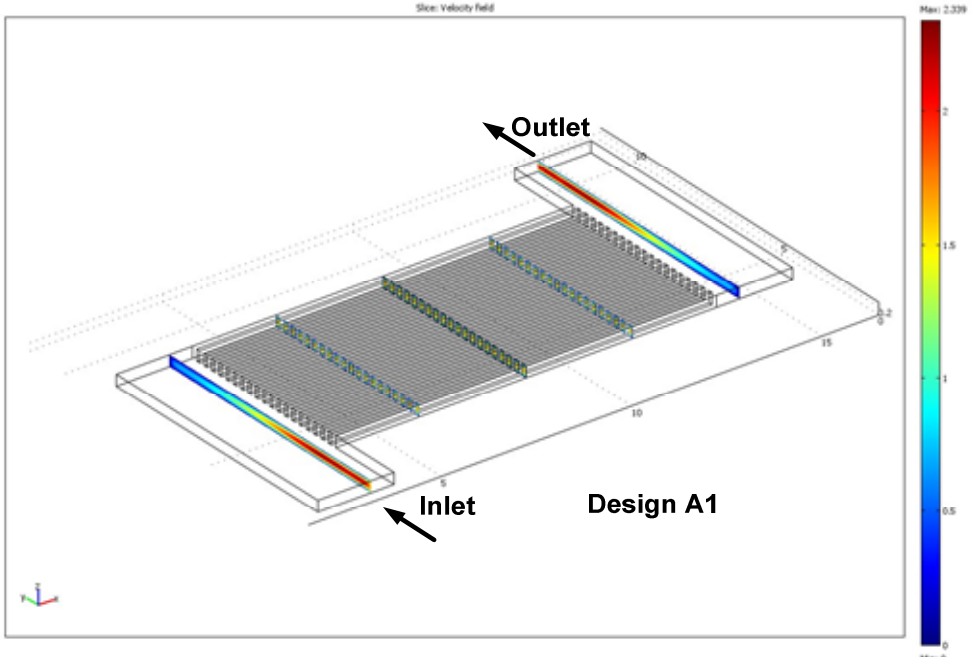

Figure 4.7 *3D model of design A, slice: dimensionless velocity field.*

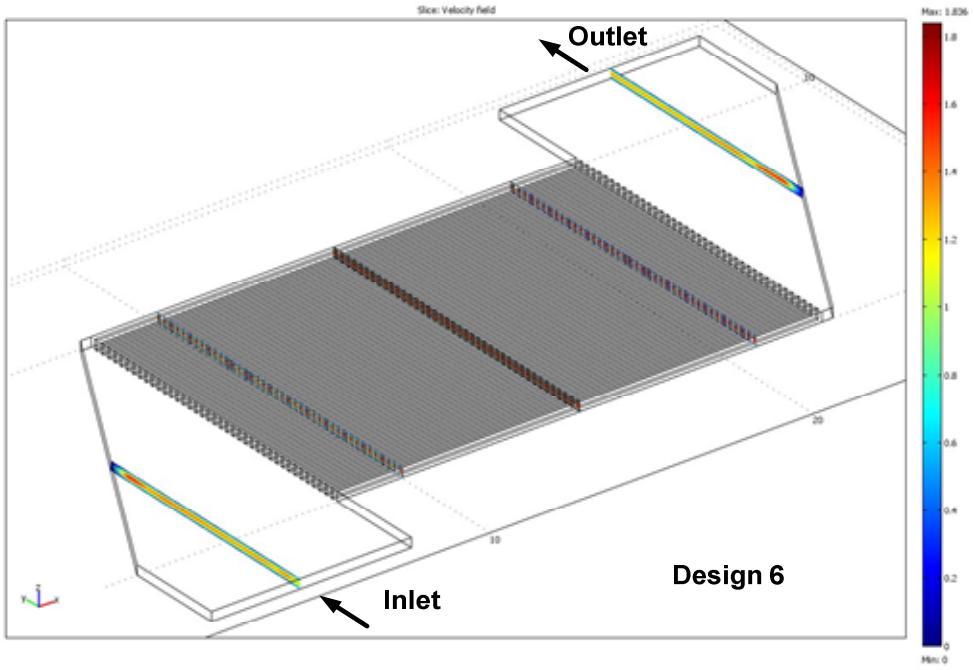

Figure 4.8 *3D model of design 6, slice: dimensionless velocity field.*

CFD simulations were carried out for design A1 using four different Reynolds numbers defined as follows:

$$\mathrm{Re} = \frac{\rho \mathrm{u}_c D_h}{\mu} \tag{4.10}$$

where u_c is the characteristic velocity in the microchannels, assuming uniform flow rates through the channels. Figure 4.9 shows a velocity distribution across the two channels at Reynolds number of 100 for Design A1. The velocity profile indicates developed laminar flow regime inside the channels.

Figure 4.10 presents a plot of normalized flow rate distribution for design A1 evaluated by CFD simulations and by the approximate model. The flow rates are normalized with respect to the channel flow rate for uniform flow distribution Q_{eq}. There is good agreement between the approximate model and CFD simulation for Reynolds values of 0.01 and 10. Small deviations were found for Reynolds number of 30 with the deviation becoming more significant for Reynolds number of 100.

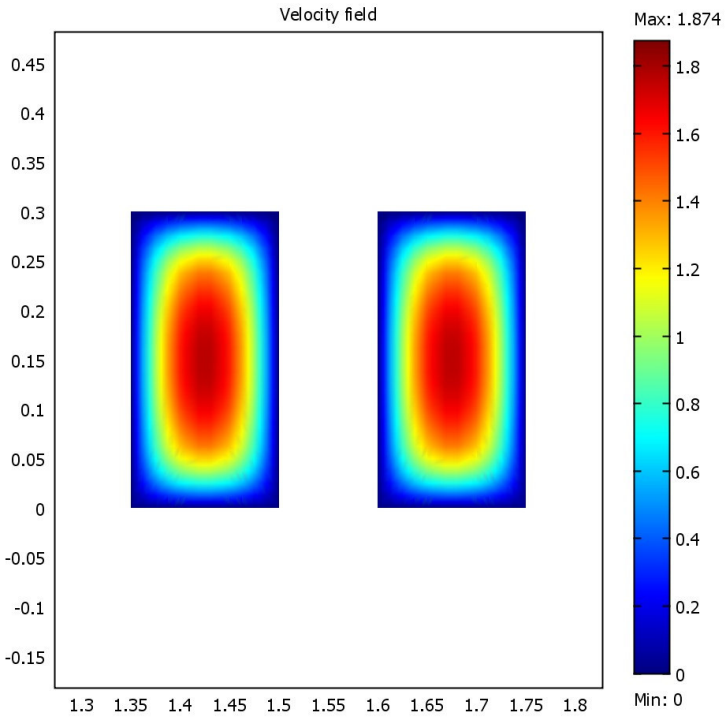

Figure 4.9 *Dimensionless velocity field across two neighboring channels for Re = 100.*

The approximate model always gives symmetric flow distribution while flow distributions evaluated by CFD appear to be slightly asymmetric with the asymmetry increasing with increasing Reynolds number. A reason for this difference between the flow distributions evaluated by the two models might be the effect of additional pressure losses, which are important in inlet and outlet manifolds.

The approximate model does not take into account additional pressure drops caused by inertial forces, and therefore the flow distribution does not depend on Reynolds number. Additional pressure drops become significant for higher Reynolds number especially at the entrance and exit of the microchannels.

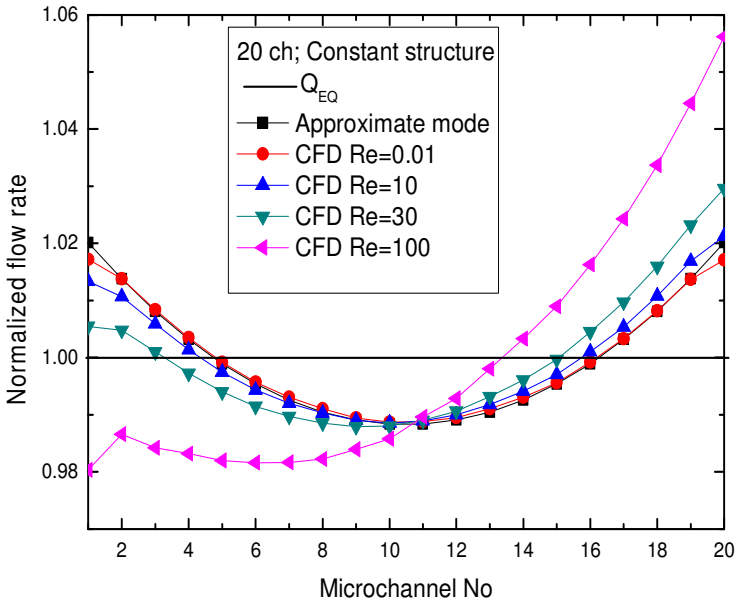

Figure 4.10 *Normalised flow rate distribution within the microchannels for design A1.*

Flow distributions for device 6 were considered for different Reynolds numbers and compared with results evaluated by the approximate model. The results of comparison are shown in Figure 4.11. Both the approximate model and CFD predict good flow distribution for Reynolds numbers 0.01 and 10 but the shape of distribution is different. While the approximate model gives symmetric and slightly convex shape, CFD simulations give an asymmetric and concave shape. As Reynolds number increases, asymmetry is more apparent and becomes significant for Reynolds of 50.

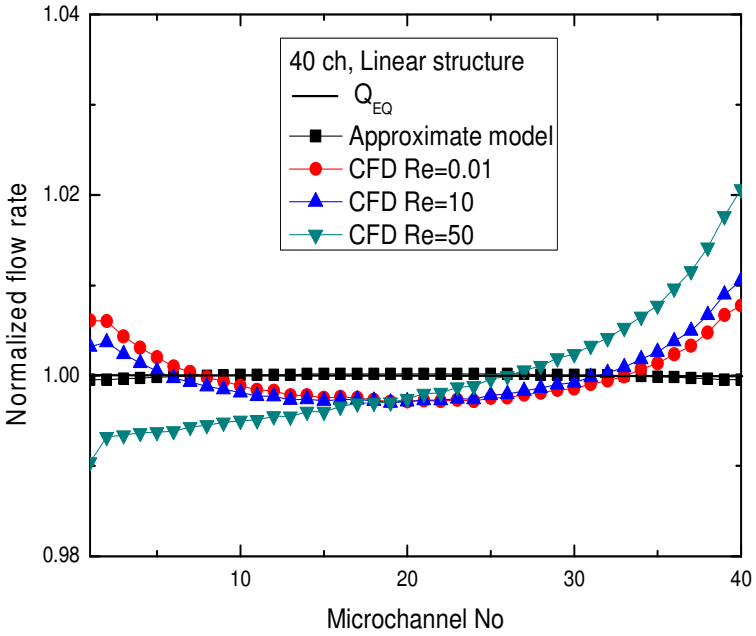

Figure 4.11 *Normalised flow rate distribution within the microchannels for design 6.*

4.3.1 Influence of inlet/outlet holes positions on flow distribution

It is well known that the flow distribution depends on parameters such as channel length, channel width and the shape of inlet and outlet manifolds. Generally, a larger contribution of pressure drop through the channel than that in manifolds and magnification of outlet manifolds area makes the flow distribution more uniform [3, 7]. In this section, the influence of position of inlet/outlet holes on flow distributions is discussed. CFD simulations were carried out in order to determine which position of holes, either inside or outside of manifolds yields better uniformity. The 3D models consist of 40 channels (dimensions of channels as for design 6), with a non-constant, linear structure of manifolds. The diameters of inlet/outlet holes were 2.50 mm with their positions being located inside the manifolds for one model (Figure 4.12) and outside the manifolds for another (Figure 4.13). The inlet and outlet flows were designed perpendicular to the plane of the channels for both models.

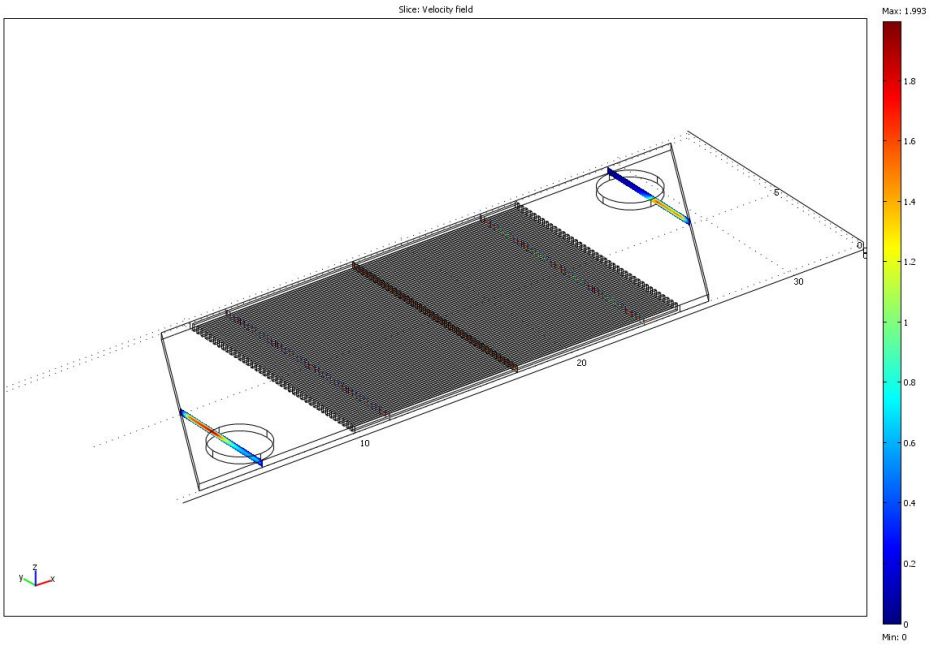

Figure 4.12 *3D model with inside inlet/outlet holes, slice: dimensionless velocity field.*

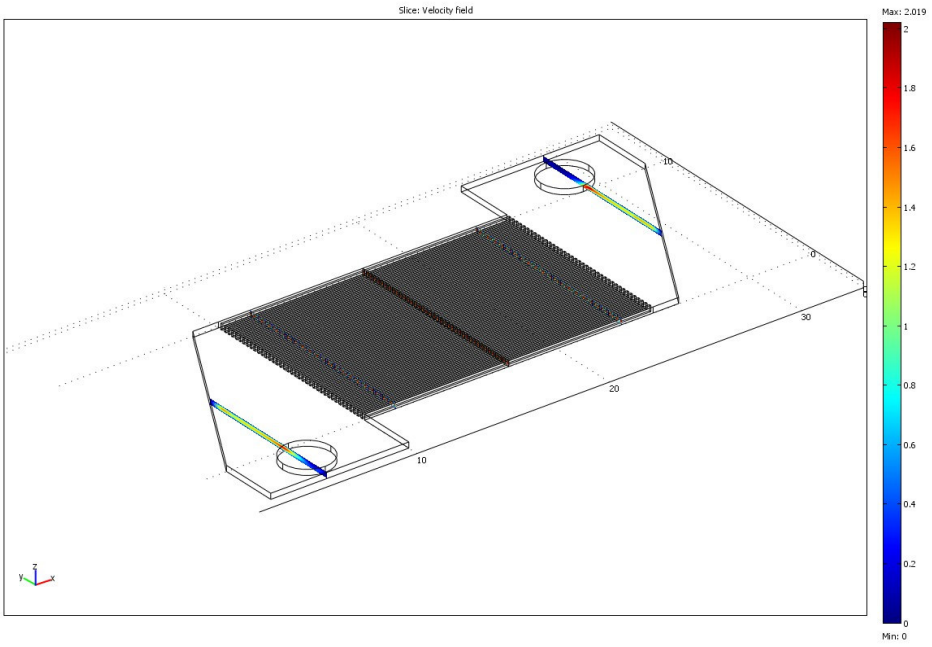

Figure 4.13 *3D model with outside inlet/outlet holes, slice: dimensionless velocity field.*

Results of the flow distribution for the above models with a Reynolds number of 10 are shown in Figure 4.14. In order to compare the quality of flow distribution, a standard deviation σ(%) has been used given by:

$$\sigma(\%) = 100\sqrt{\frac{\sum_{i=1}^{N}(Q_i - Q_{eq})^2}{N}} \tag{4.11}$$

Flow rates in channels, Q_i have been normalised with respect to the Q_{eq}, hence, the value for normalised Q_{eq} is unity. The standard deviation for the model with an inside position for the inlet/outlet holes is 0.28 %, while for the model with the outside position it was 0.53 %. These values indicate that the inside position of inlet/outlet holes enables the fluid to be distributed more uniformly through the microchannels. Another advantage is that inside position minimizes the total area of the device what enables more devices to be placed on a silicon wafer during the microfabrication process.

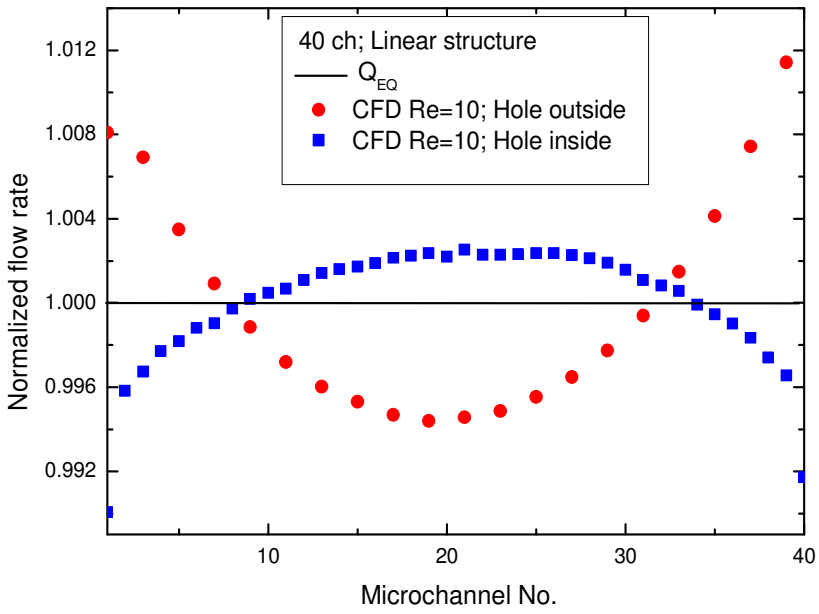

Figure 4.14 *Normalized flow rate distribution for different inlet/outlet holes positions.*

3D model with the holes situated inside the manifolds, shown in Figure 4.12, was used to asses the mesh sensitivity of the numerical results. Two types of mesh were considered for this model: a structured mesh generated extruding a 2D mesh with

triangular elements into a 3D mesh with prism elements (45441 elements and 810717 degrees of freedom) and an unstructured mesh containing tetrahedral elements (26309 elements and 195928 degrees of freedom). Figure 4.15 shows examples of the mesh cases. Influence of the mesh type on the total pressure drop for different inlet flow rates is shown in Table 4.2. All solutions give reasonable results. The number of mesh elements is related to the number of degrees of freedom. However the relation is not the same for structured and unstructured meshes. The same number of mesh elements creates more degrees of freedom for a structured mesh

a)

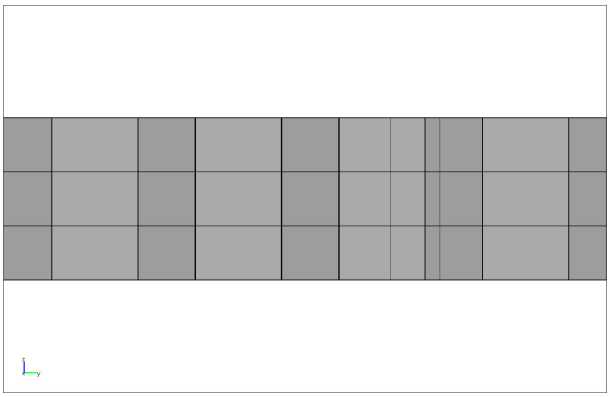

b)

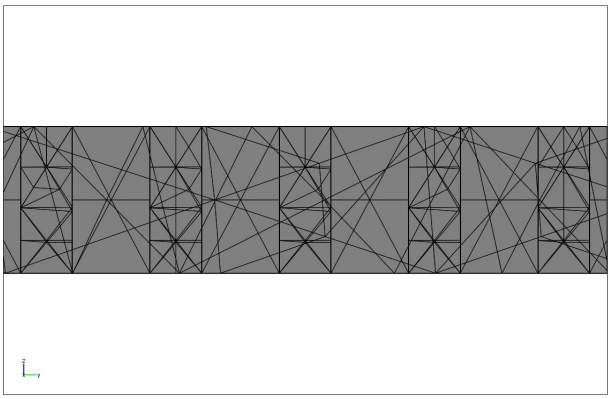

Figure 4.15 *Examples of mesh cases: (a) structured mesh and (b) unstructured mesh.*

Table 4.2 *Influence of the mesh type on the total pressure drop.*

Inlet flow rate [cm^3/min]	Pressure drop obtained with structured mesh [bar]	Pressure drop obtained with unstructured mesh [bar]
3.5	0.021	0.026
5	0.03	0.038
18.3	0.108	0.132
25	0.147	0.19

than for an unstructured mesh, simply because the rectangular shape of the mesh elements. For the same number of degrees of freedom the solution time is longer for a structured mesh than for an unstructured mesh. This is due to the structured mesh having a stronger coupled system, which results in system matrices that are less sparse [14].

4.3.2 Influence of channels blockages on flow distribution

Channel blockages, caused by particle deposition or clogging by manufacturing defects, can be a reason for poor flow distribution and increased pressure drops in micro-reactors and micro-heat exchangers. CFD simulations were carried out in order to systematically assess the influence of channel blockages in different locations of the microchannel array. A model consisting of 20 channels with the inlet/outlet holes located inside the manifolds has been used for a Reynolds number of 10 to assess blockages at the positions shown in Figure 4.16 ((a) middle, (b) bottom, and (c) top). The number of blocked channels was increased successively and the pressure drop and standard deviations analysed. Pressure drops were normalized with respect to the pressure drop for the model without blocked channels and the standard deviations calculated using equation 4.11. Increasing the number of blocked channels caused the pressure drop to significantly increase, with the trend being the same for each of the three blockage positions as shown in Figure 4.17. However, the standard deviation was found to be dependent not only on the number

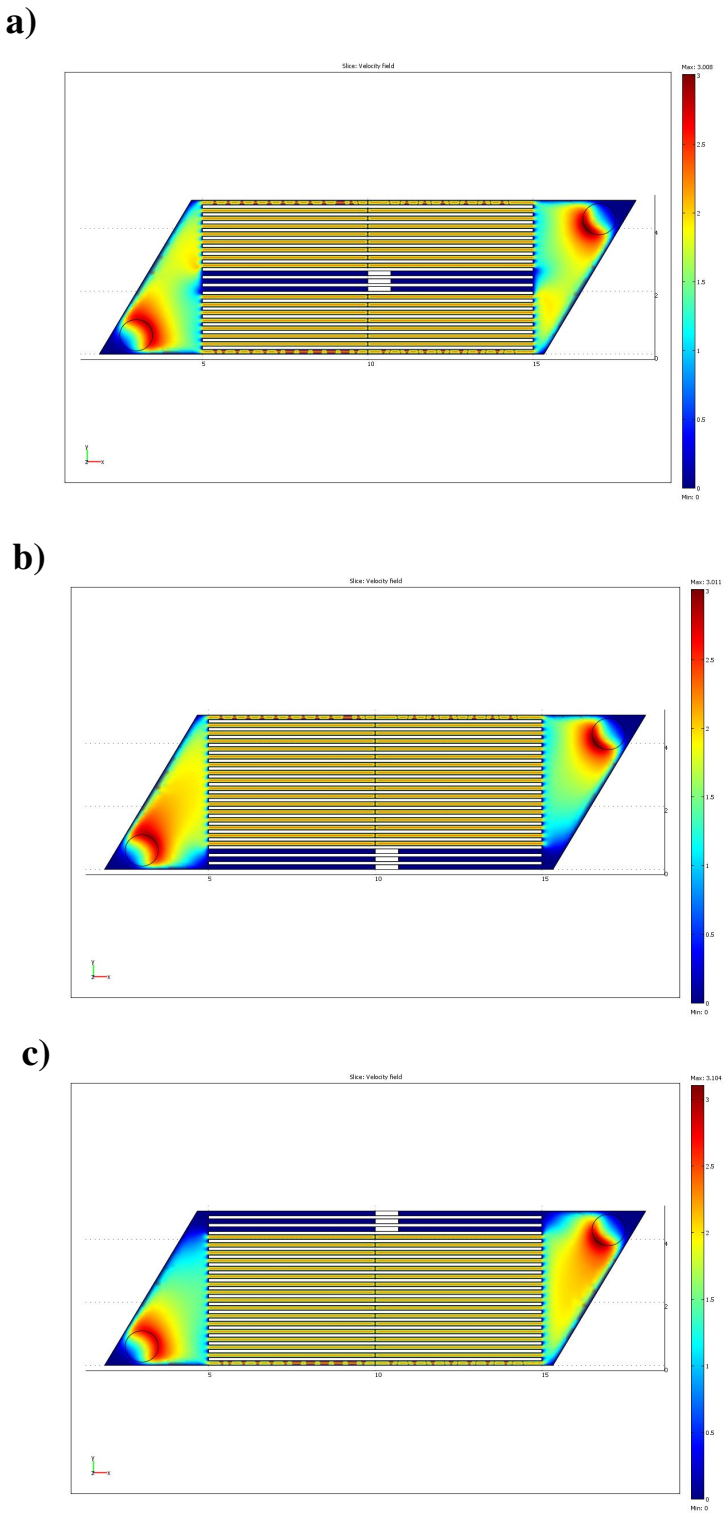

Figure 4.16 *Example of 3 sets of blocked channels: (a) Middle, (b) Bottom and (c) Top location, slice: dimensionless velocity field.*

of blockages but also on their position. Three different trends for standard deviation are shown in Figure 4.18. Blockages in the middle channels have the smallest influence on flow distribution while top channel blockages make flow distribution more uneven. It was found that the seven blocked channels in the assessed design give the non-uniform distribution with the maximum standard deviation. Further blockages of channels made the flow more uniformly distributed.

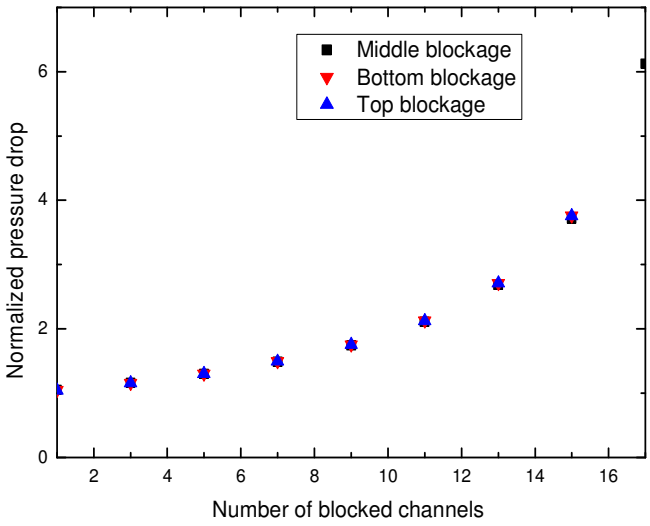

Figure 4.17 *Normalised pressure drop as function of number of blocked channels and their positions.*

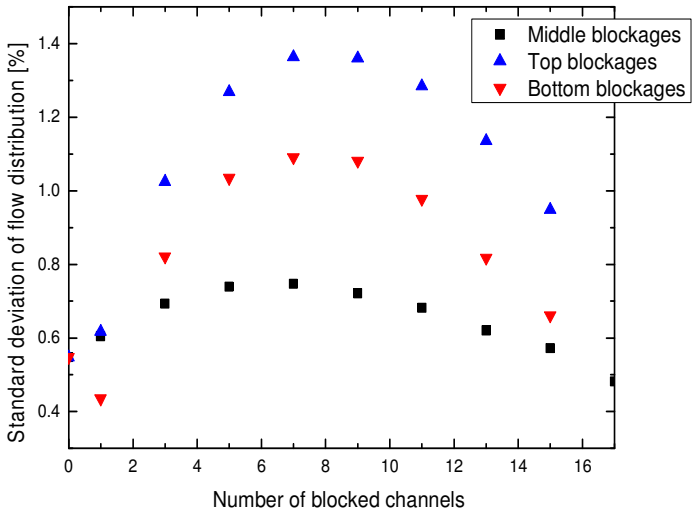

Figure 4.18 *Standard deviation of flow distribution as function of number of blocked channels and their positions.*

4.4 Experimental Work

Based on the results obtained from the simulations presented in the previous sections, manifolds for design 6 from Table 4.1 were designed. Consecutive Z-type structure with non-constant, linear cross sections manifolds was selected in order to make flow distribution even, minimize manifold area and avoid stagnation zones. The approximate model has been used to evaluate the widths of the first zone and the last zone of inlet/outlet manifolds. The first zone of inlet/outlet manifolds was 6.18 mm wide, while the last zone was 0.33 mm wide. An additional one millimeter was added to both manifolds in order to ensure more space for external tubing connection. Inlet and outlet holes are placed inside the manifolds to enable better flow distribution within channels and to minimize the manifold area. The latter enables more devices to be placed on one silicon wafer during the microfabrication process.

In order to estimate the flow distribution within microchannels with single- phase flow and uniform heating, experiments with device 6 (Table 4.1) have been performed. Temperatures from the sensors T2, T4 (Figure 3.8a) and the reference thermocouple located in the center of the device below the heater have been simultaneously recorded for the different mass flow rates and the heat fluxes. Summary of the experimental results is given in Figure 4.19. The inlet temperature of water coming into the device was 54 ˚C. Taking into the account the position of the sensors T2 and T4 (Figure 3.8a) values of the temperatures must be close in the case of uniform flow distribution. According to the results the present design of the microchannel heat sink enables good flow distribution in the case of single-phase flow. However, boiling inside the microchannels affects flow distribution causing the difference between temperatures from the sensors T2 and T4 as it can be seen for the lower flow rates of 7 g/min and 10 g/min.

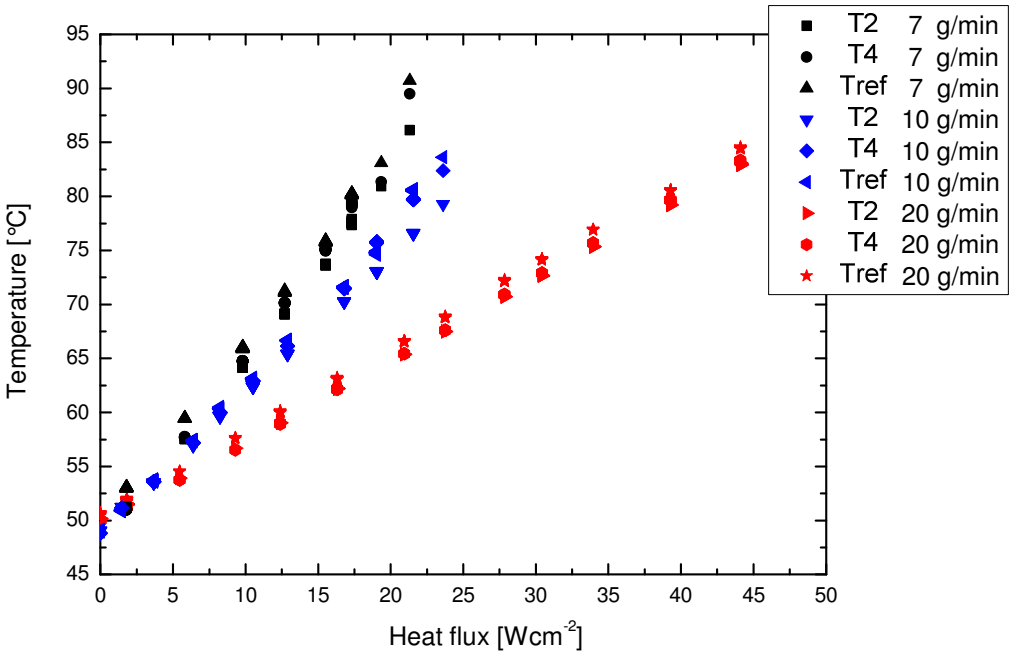

Figure 4.19 *Temperatures from the sensors S2, S4 and reference thermocouple, recorded for different mass flow rates and heat fluxes.*

4.5 Conclusions

Good thermal efficiency of micro heat exchanger relies on uniform flow distribution within microchannels. In this work, simulations were used to assist the design of manifold geometries in microchannel-based heat sinks for the single-phase flow. Both approximate and full 3D models have been used to assess the influence of geometry and Reynolds numbers on flow distribution. For low Reynolds numbers good agreement was found between results of the approximate model and those evaluated by CFD. While the approximate model always predicts a symmetric flow distribution within channels, CFD simulations give asymmetric flow distributions and the asymmetry increases with increasing Reynolds number. The difference between results of the approximate model and CFD becomes more apparent in the case of manifolds with non-constant, linear cross sections. The reason for such deviations is that the approximate model does not take into account additional pressure losses due to inertial forces and the shape of flow distribution does not depend on inlet flow rates. CFD simulations give more rigorous results taking into

account additional pressure losses but this method is time consuming with a single simulation taking up to a couple of hours. On the other hand, the approximate model is very fast and reliable for low Reynolds number.

The influence of inlet/outlet hole positions on flow uniformity was investigated using CFD simulations. Holes inside the manifolds appear to be a better solution for heat sinks with microchannels since they make the fluid more uniformly distributed than holes outside. In addition, holes placed inside manifolds minimise the area of manifolds and enable more devices to be placed on one silicon wafer during the microfabrication process.

Furthermore, the effect of channel blockages and their positions on flow distribution and pressure drop was investigated. Increased number of blocked channels causes the pressure drop to significantly increase and the trend is the same for each of the three sets of blocked channel positions investigated: middle, top and bottom. However, the standard deviation of flow distribution was found to be dependent not only on the number of channels blocked but also on their location.

The above results have been used to design microchannel heat sinks. Experimental investigation performed with the microchannel heat sink indicates good flow distribution within the channels in the case of the single-phase flow. However, it was found that boiling significantly affects the flow distributions in the present heat sink due to bubbles nucleation and bubbles growth, causing the significant temperature difference in transverse direction. The effect of flow boiling on fluid distribution within microchannels and the consequent temperature uniformity in microchannels based heat sink will be discussed in the following chapter

References

1. Jensen, K.F., *Microreaction engineering -- is small better?* Chemical Engineering Science, 2001. 56(2) 293-303.
2. Benson, R.S. and J.W. Ponton, *Process miniaturization - a route to total environmental acceptability?* . Trans. Inst. Chem. Eng. , 1993. 71 160-168.
3. Commenge, J.M., L. Falk, J.P. Corriou, M. Matlosz, *Optimal design for flow uniformity in microchannel reactors.* AIChE Journal, 2002. 48(2) 345-358.
4. Amador, C., Gavriilidis, A., Angeli, P., *Flow Distribution in Different Microreactor Scale-Out Geometries and the Effect of Manufacturing Tolerances and Channel Blockage.* Chemical Engineering Journal, 2004. Vol. 101 379-390.
5. Facao, J. and J. Gruss. *Flow distribution in a network of minichannels: simulation and experiment* in *SHF - Microfluidics* 2006. Toulouse.
6. Pfeifer, P., A. Wenka, K. Schubert, M.A. Liauw, G. Emig, *Characterization of flow distribution in microchannel reactors.* AIChE Journal, 2004. 50(2) 418-425.
7. Tonomura, O., S. Tanaka, M. Noda, M. Kano, S. Hasebe, I. Hashimoto, *CFD-based optimal design of manifold in plate-fin microdevices.* Chemical Engineering Journal, 2004. 101(1-3) 397-402.
8. Griffini, G. and A. Gavriilidis, *Effect of Microchannel Plate Design on Fluid Flow Uniformity at Low Flow Rates.* Chemical Engineering & Technology, 2007. 30(3) 395-406.
9. Pan, M., Y. Tang, W. Zhou, L. Lu. *Flow Distribution among Microchannels with Asymmetrical Manifolds*. in *2007 IEEE International Conference on Control and Automation*. 2007. Guangzhou, China
10. Eun Seok, C., K. Jae-Mo, J. Linan, R.S. Prasher, K. Min Soo, J.G. Santiago, T.W. Kenny, K.E. Goodson. *Experimental study on two-phase heat transfer in microchannel heat sinks with hotspots*. in *Semiconductor Thermal Measurement and Management Symposium, 2003. Ninteenth Annual IEEE*. 2003.
11. Dang, M., I. Hassan, R. Muwanga, *Adiabatic two phase flow distribution and visualization in scaled microchannel heat sinks.* Experiments in Fluids, 2007. 43(6) 873-885.
12. Comsol, *User's guide*. 2005, Stockholm: COMSOL AB.
13. Finlayson, B.A., *Introduction to chemical engineering computing* 2006, New York, USA: John Wiley
14. Comsol, *Modeling Guide*. 2005, Stockholm: COMSOL AB.

Chapter 5 Investigation of two-phase flow boiling instabilities in a uniformly heated silicon microchannels heat sink

5.1 Introduction

Two-phase flow instabilities are highly undesirable in microchannels-based heat sinks as they can lead to temperature oscillations with high amplitudes, premature critical heat flux and mechanical vibrations. This work is an experimental study of boiling instabilities in a microchannel silicon heat sink with 40 parallel rectangular microchannels, having a length of 15 mm and a hydraulic diameter of 194 μm. A series of experiments have been carried out to investigate pressure and temperature oscillations during the flow boiling instabilities under uniform heating, using water as a cooling liquid. Flow stability maps are presented for two inlet water temperatures, showing stable and unstable flow regimes. It was observed that boiling leads to asymmetrical flow distribution within microchannels that results in high temperature non-uniformity and the simultaneously existence of different flow regimes along the transverse direction. Two types of two-phase flow instabilities with appreciable pressure and temperature fluctuations were observed, that depended on the heat to mass flux ratio and inlet water temperature. These were high amplitude/low frequency and low amplitude/high frequency instabilities. High speed camera imaging, performed simultaneously with pressure and temperature measurements, showed that inlet/outlet pressure and the temperature fluctuations

existed due to alternation between liquid/two-phase/vapour flows. It was also determined that the inlet water subcooling condition affects the magnitudes of the temperature oscillations in two-phase flow instabilities and temperature uniformity over the heat sink.

5.2 Experimental setup and procedure

The experimental system described in chapter 3 was utilized in the present study to investigate two-phase flow instabilities of water boiling in the microchannel heat sink. Prior to carrying out the experiment, deionised water in the reservoir was degassed by vigorous boiling in the reservoir for approximately one hour. Afterwards, the flow rate and the inlet water temperature were adjusted to the desired values. Flow boiling conditions inside the microchannels were then set by either increasing the heat flux with constant flow rate or decreasing the flow rate with constant heat flux. The water reservoir-condensing chamber was kept constant at atmospheric pressure with an open vent to atmosphere during the experiments. Table 5.1 shows the used operating conditions for the experiments conducted under constant heat flux and varying mass flux. The adopted operating conditions for the experiments carried out under constant mass flux and varying heat flux are given in Table 5.2. The mass flux, G was determined from measured mass flow rate, $\dot{m}$:

$$G = \frac{\dot{m}}{NA_{ch}} \tag{5.1}$$

Two standard pressure transducers and thin nickel film thermometers, integrated on the back side of a heat sink with microchannels, were used together with simultaneous visualisation in order to obtain a better insight related to temperature fluctuations caused by two-phase flow instabilities. The location of the sensors T1-T5 (Figure 3.8a) enables the measurement of temperatures in both the flow stream direction and the transverse direction. Most authors investigating flow boiling instabilities have used temperature sensors located only along the direction of the flow stream. Two-phase flow instabilities and flow patterns inside the channels were

Table 5.1 *Operating conditions for two-phase flow instabilities experiments conducted under constant heat flux and varying mass flux.*

Coolant	Inlet temperature, T_{in} [˚C]	Heat flux, q [kW/m^2]	Mass flux, G [kg/m^{2}s]
Deionised water	25.0	178	29.2 - 55.6
		267	44.4 - 97.2
		356	73.6 - 145.8
		445	123.6 - 168.1
	71.0	178	52.8 - 180.6
		267	111.1 - 275.0
		356	205.6 - 370.8
		445	191.7 - 433.3

Table 5.2 *Operating conditions for two-phase flow instabilities experiments conducted under constant mass flux and varying heat flux.*

Coolant	Inlet temperature, T_{in} [˚C]	Mass flux, G [kg/m^{2}s]	Heat flux, q [kW/m^2]
Deionised water	25.0	208.0	506 - 590
	71.0	208.0	186 - 400

monitored and recorded with the aid of a high-speed camera, mounted on a microscope with a 5× magnification objective and axial illumination.

The effects of inlet water temperature on flow boiling instabilities were experimentally studied, with the influence of different subcooling conditions on the magnitude of temperatures as well as the influence on the temperature uniformity over the heat sink being assessed. Using a larger number of microchannels entails the risk of a non-uniform distribution during the flow boiling in the microchannels. One of the objectives of this study is to investigate the effect of non-uniform distribution within the channels on both flow instabilities and the temperature distribution. It is much more likely that in real cooling applications (e.g. cooling of CPU's) heat sinks with a large number of channels will be used (to cover an area > 10×10 mm^2) rather than heat sinks with just a few channels. With the main issues related to using flow boiling as potential cooling technology being flow instabilities and non-uniform distribution, these are thoroughly investigated and discussed.

5.3 Results and Discussion

5.3.1 Flow stability map

In the present study, two types of two-phase flow boiling instabilities were identified for the heat sink consisting of 40 parallel rectangular microchannels. These were high amplitude/low frequency (HALF) and low amplitude/high frequency instabilities (LAHF) and were classified for the two inlet water temperatures of 25 ˚C and 71 ˚C. The results are presented using flow stability maps in terms of heat flux and mass flux with the criterion of classification being the frequency of the pressure drop oscillations. The dominant frequencies were identified by the magnitude of the amplitude obtained by Fourier transformation. The pressure drop oscillations include the effects of all microchannels and give a representative fluctuation frequency for the system. It was found that frequencies typical of HALF type instabilities were in the range of 0.9-2.88 Hz. Frequency analysis identified a broad range of frequencies for LAHF type instabilities higher than those typical of HALF type. Experiments were carried out at four different heat fluxes (178 kW/m^2, 267 kW/m^2, 356 kW/m^2 and 445 kW/m^2) and two inlet subcooling conditions (25 ˚C and 71 ˚C). Figure 5.1 shows experimentally obtained flow stability maps in terms of heat flux and mass flux for two different inlet water temperatures. The two inclined straight lines divide the flow stability map into stable flow, unstable flow boiling with HALF instabilities and unstable flow boiling with LAHF instabilities.

The stable flow regime ($q < 2.62 \cdot G$ for $T_{in} = 25$ ˚C and $q < 0.99 \cdot G$ for $T_{in} = 71$ ˚C) includes single phase flow and incipient flow boiling when isolated bubbles grow inside microchannels which are then flushed downstream by the bulk flow. Figure 5.2 shows image sequences from a recording captured using a high speed camera at a frame rate of 100 fps. The arrow in the first image shows the direction of the water flow and the circle marks the nucleation site. Bubble grows from the nucleation

a)

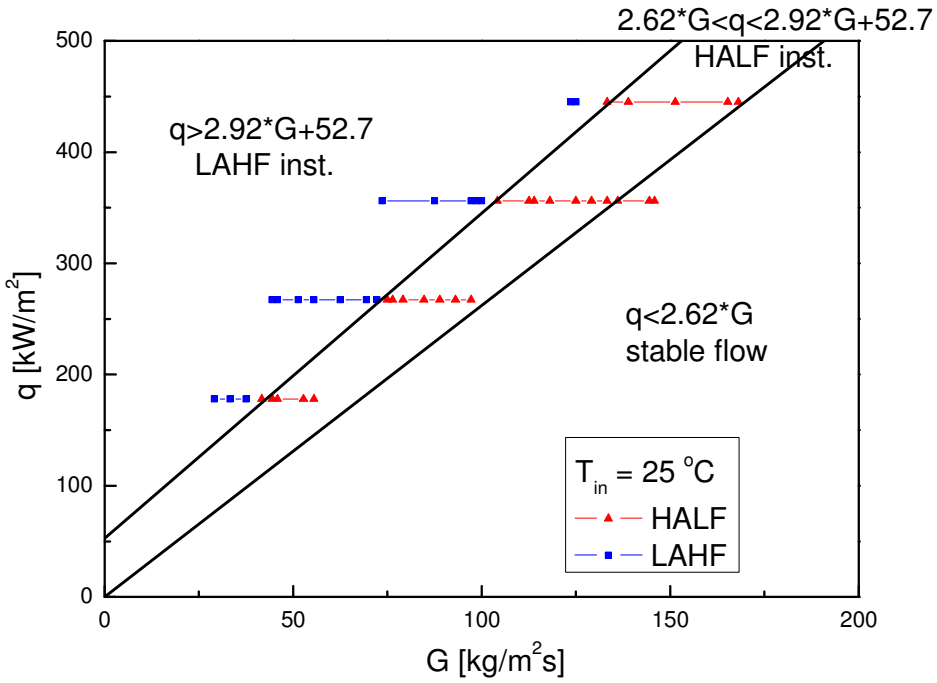

b)

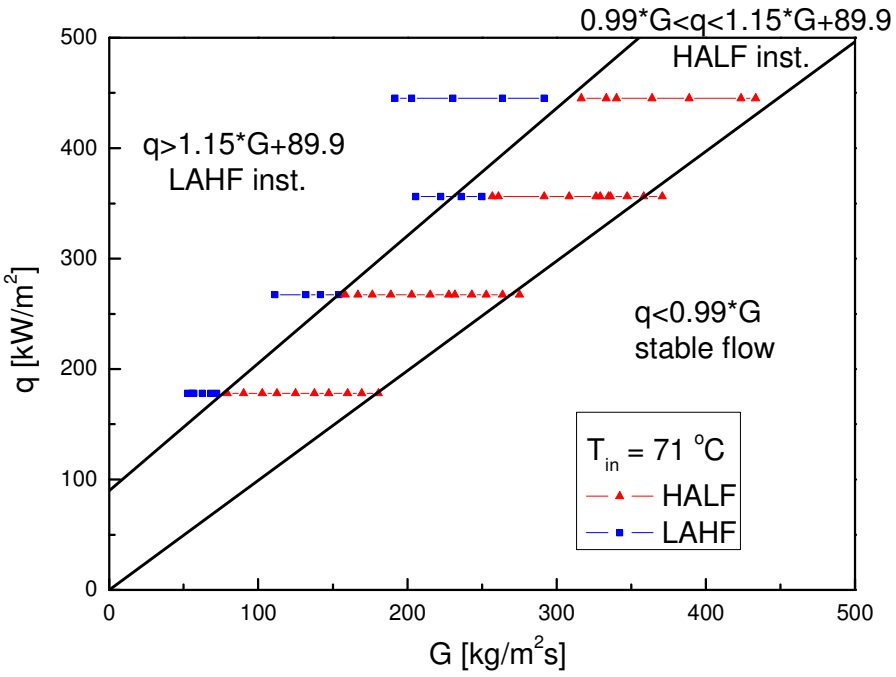

Figure 5.1 *Flow stability maps in parallel microchannels with hydraulic diameter of 194 μm for two different water inlet temperatures (a) 25 ˚C and (b) 71 ˚C.*

site (t = 0 ms), then detaches (t = 510 ms) being swept downstream by the bulk flow (t =730 ms). The reverse flow of vapour, typical for unstable flow boiling, was not observed. Measurements of inlet/outlet pressures and sensor temperatures for the case of stable flow regime with incipient boiling are presented in Figure 5.3. Fluctuations of the inlet/outlet pressure and the sensor's temperature are negligibly small in comparison to those found for unstable flow.

The slopes of the lines in the flow stability maps depend on the inlet water temperature. The flow stability depends on the heat and mass flux as well as inlet subcooling condition. However, the experimental results show that boiling leads to very asymmetrical flow distribution within the 40 microchannels. This results in the simultaneous existence of different flow regimes inside microchannels along the transverse direction. Figure 5.4a shows an image of bubbly flow pattern for a heat flux of 356 kW/m^2, a mass flux of 222.2 kg/m^{2}s and inlet water temperature of 71 ˚C inside microchannels located above the sensor T2. Bubbles grew inside the microchannels, which were then carried downstream by the bulk flow. Figure 5.4b shows an image of simultaneous transient annular flow inside the microchannels located above the sensor T4, at the same conditions of heat flux, mass flux and inlet water temperature (356 kW/m^2, 222.2 kg/m^{2}s and 71 ˚C). Figure 5.5a shows small fluctuations of the temperature T2, while appreciable fluctuations of the temperature T4 and the pressure drop. Frequency analysis of the pressure drop shown in Figure

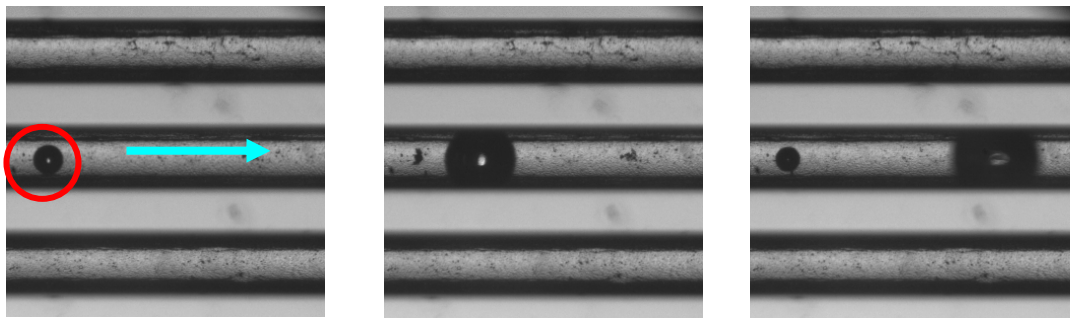

Figure 5.2 *Image sequences of the stable flow regime with incipient boiling inside the parallel microchannels with hydraulic diameter of 194 μm (q = 178 kW/m^2, G = 86.1 kg/m^{2}s, q/G = 2.07 kJ/kg and T_{in} 25 ˚C).*

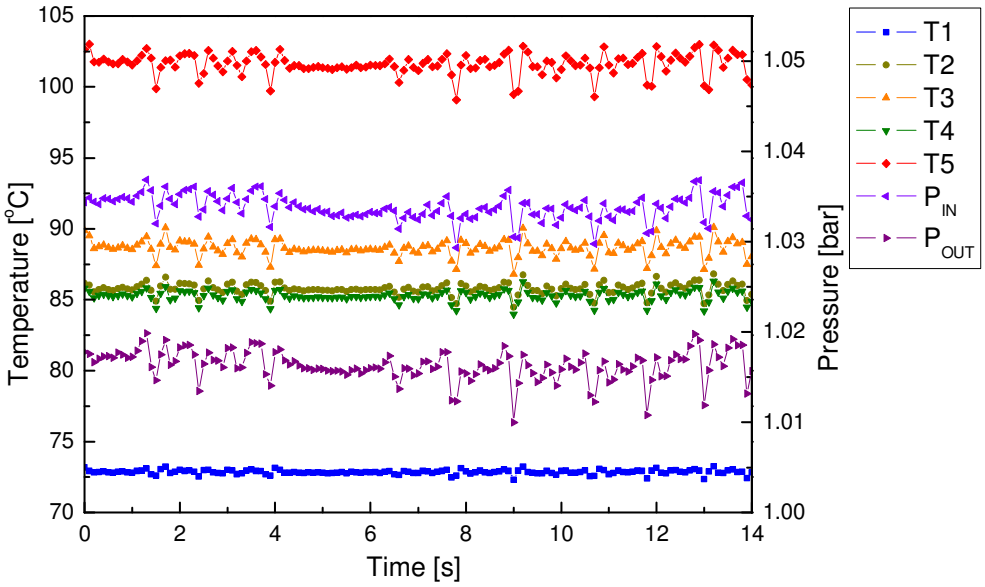

Figure 5.3 *Temporal variation of the sensor temperatures and the inlet/outlet pressures in stable flow regime with incipient boiling (q = 198.6 kW/m^2, G = 208 kg/m^{2}s, q/G = 0.95 kJ/kg and T_{in} = 71 ˚C).*

5.5b indicates LAHF type of instabilities. The pressure drop fluctuations inside the microchannels with transient annular flow dominate the pressure drop fluctuations due to bubbly flow.

In the present investigation when the pressure was set to atmospheric, the boiling flow stability inside the heat sink was found to depend on the heat and mass flux, inlet water temperature and flow distribution within microchannels. Asymmetrical flow distribution within microchannels during flow boiling under constant heat flux might lead to the occurrence of LAHF instabilities at higher value of mass flux than is the case with uniform flow distribution within microchannels under the same heat flux. There are several possible reasons for the asymmetrical flow distribution during flow boiling inside the present heat sink with microchannels such as the shape and geometry of the inlet/outlet manifolds, the position of the inlet/outlet holes and uneven depth of the microchannels.

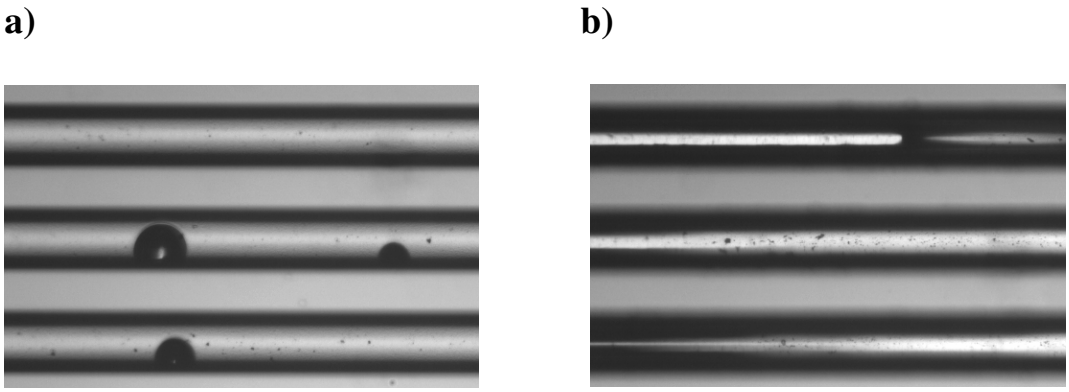

Figure 5.4 *(a) Image of bubbly flow pattern inside the microchannels located above the sensor T2, (b) image of transient annular flow existed simultaneously inside the microchannels located above the sensor T4, q = 356 kW/m^2, G = 222.2 kg/m^{2}s and T_{in} = 71 ˚C.*

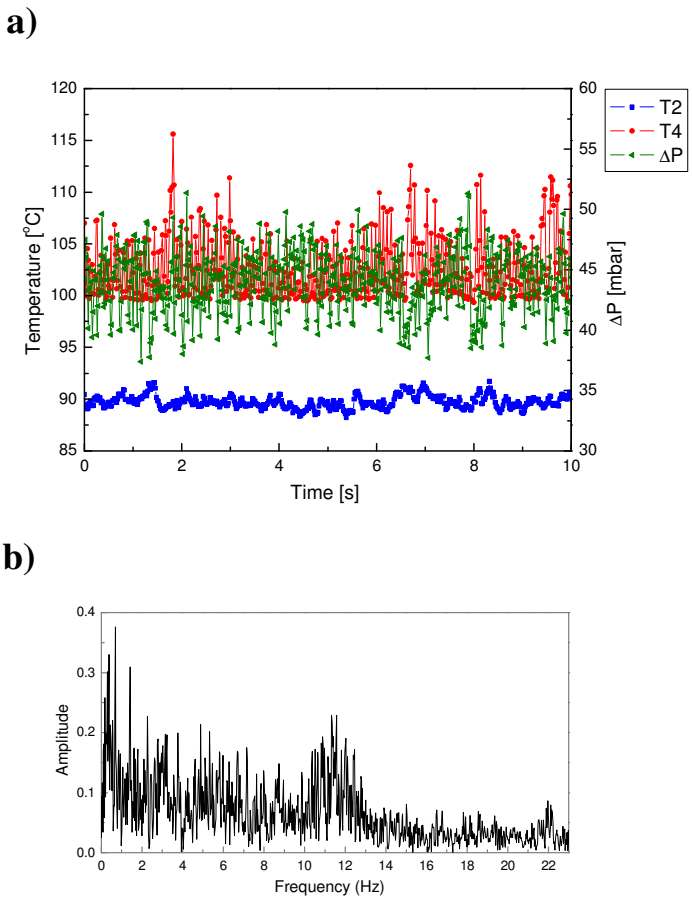

Figure 5.5 *(a) Measurements of temperatures T2, T4 and pressure drop for non-uniform flow distribution within parallel microchannels (q = 356 kW/m^2, G = 222.2 kg/m^{2}s and T_{in} = 71 ˚C, (b) pressure drop frequency analysis.*

5.3.2 High amplitude low frequency (HALF) instabilities

Instabilities occur after the incipience of boiling inside the microchannel heat sink, when increasing heat flux at a constant mass flux or decreasing mass flux with a constant heat flux. HALF instabilities existed for $2.62 \cdot G < q < 2.92 \cdot G + 52.7$ at an inlet water temperature of 25 ˚C and $0.99 \cdot G < q < 1.15 \cdot G + 89.9$ with an inlet water temperature of 71 ˚C. Figure 5.6 shows pressure and temperature oscillations simultaneously recorded at a 50 Hz sampling rate for a constant mass flow rate of 15 g/min (G = 208 kg/m^{2}s), a heat flux of 209.6 kW/m^2 and an inlet water temperature of 71 ˚C. The outlet temperature measured with a thermocouple oscillated between 96.4 ˚C and 101.4 ˚C with a mean value of 99.8 ˚C. The temperature on sensor T1, located at the inlet of microchannels region, oscillated with small amplitudes, while other signals oscillated with appreciable amplitudes.

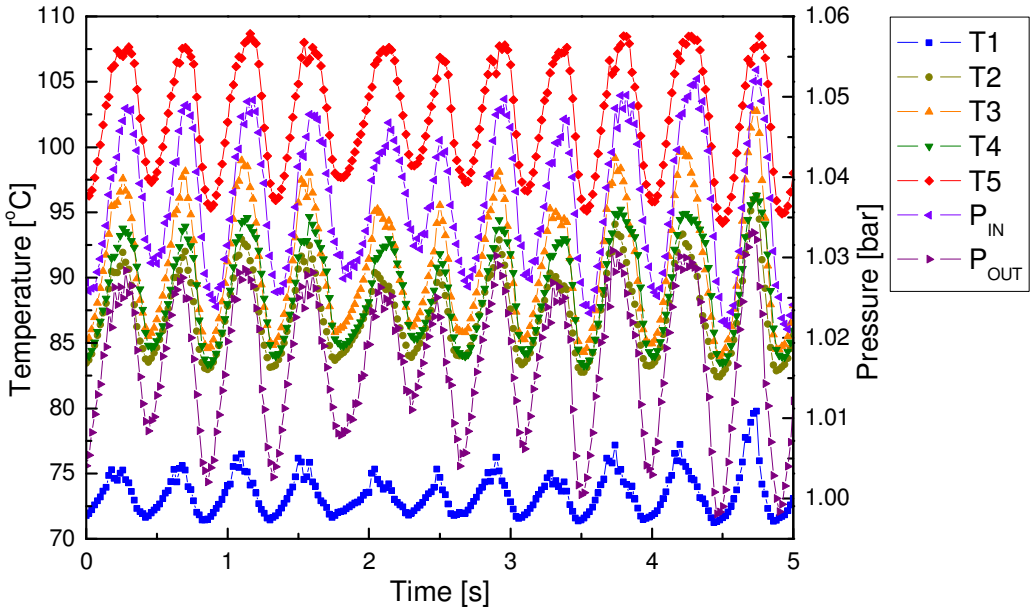

Figure 5.6 *Sensor temperature and inlet/outlet pressure oscillations in unstable flow boiling regime with HALF instabilities (q = 209.6 kW/m^2, G = 208 kg/m^{2}s, and T_{in} = 71 ˚C).*

Figure 5.7 presents the temperature fluctuations recorded for a constant mass flux of 208 kg/m^{2}s, inlet water temperature of 71 ˚C and a range of heat fluxes. As the heat flux increases, the amplitude of temperature oscillations T1 increases as boiling propagates towards the inlet of microchannels. The amplitude of the temperature recorded on sensors T5, located at the outlet of microchannels region, decreases and the signal loses its sinusoidal shape, which was observed at q = 209.6 kW/m^2 and q = 219.6 kW/m^2. Differences between the temperatures T2, T3 and T4, located across the microchannels area, become more pronounced when increasing heat flux. This implies that boiling propagation towards the microchannels inlet leads to asymmetrical flow distribution within the microchannels.

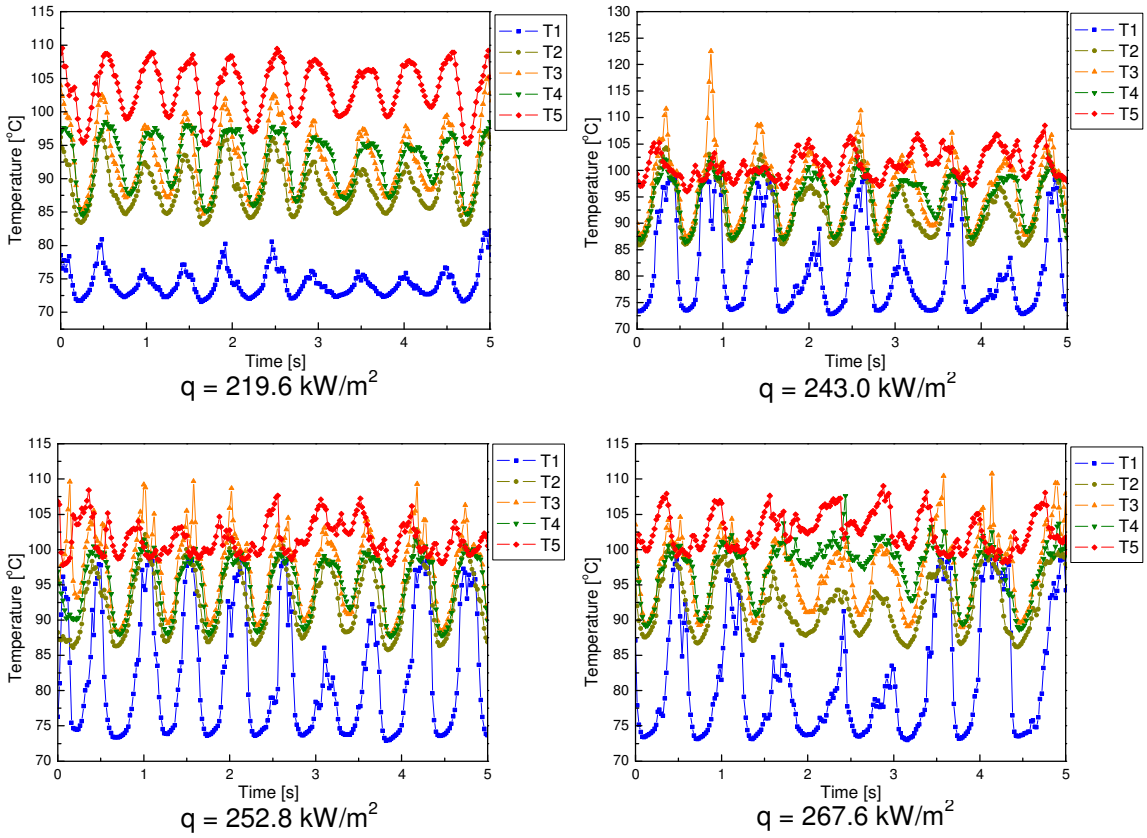

Figure 5.7 *Sensor temperature fluctuations in unstable flow regime with HALF instabilities for a mass flux of 208 kg/m^{2}s, inlet water temperature of 71 ˚C and a range of heat fluxes.*

The temporal behavior of the inlet/outlet pressures and the corresponding pressure drop is shown in Figure 5.8 for different heat fluxes and constant mass flux of 208 kg/m^{2}s. The pressure drop oscillations and the inlet/outlet pressure oscillations are not in phase, implying that the inlet and the outlet pressure oscillations are also not in phase. The outlet pressure reaches the maximum earlier than the inlet pressure as the reverse vapour propagates from the microchannels outlet towards inlet during one cycle of HALF oscillations.

Origin software was used to perform the signal analysis of the pressure drop fluctuations. Fourier analysis was performed using discrete Fourier Transform (DFT). The algorithm used for computing the DFT is Fast Fourier Transform (FFT). FFT transforms the time dependent pressure domain data into frequency domain data. The standard form of transform for engineering application is given by the following equation [1]:

$$X[k] = \sum_{n=0}^{N-1} x[n] \exp\left(\frac{-i2\pi kn}{N}\right) \tag{5.2}$$

where N represents the number of data points, n is the time domain incrementing index (n=0,1,2,…N-1), x[n] is the value of the data point in the time domain, k represents the exponential signals and has the value k=0, 1, 2,…, N-1, i indicates a complex number, and X[k] are the complex values of the Fourier coefficients. In practice, DFT is often performed on data collected at an equal (time) interval τ, with the frequency f_k being computed from:

$$f_k = \frac{k}{N\tau} \tag{5.3}$$

Amplitudes of the frequency domain were derived from the square root of the sum of the squares of the real part and imaginary part of the frequency domain. FFT analyis was performed on pressure drop data in order to obtain the frequency distribution for different heat fluxes and is shown in Figure 5.9. This analysis shows that the frequency of oscillation decreases with increasing heat flux with constant mass flux. The frequencies of the pressure drop oscillations obtained from the experiments with constant heat flux and varied mass flux are presented in Table 5.3 for two different

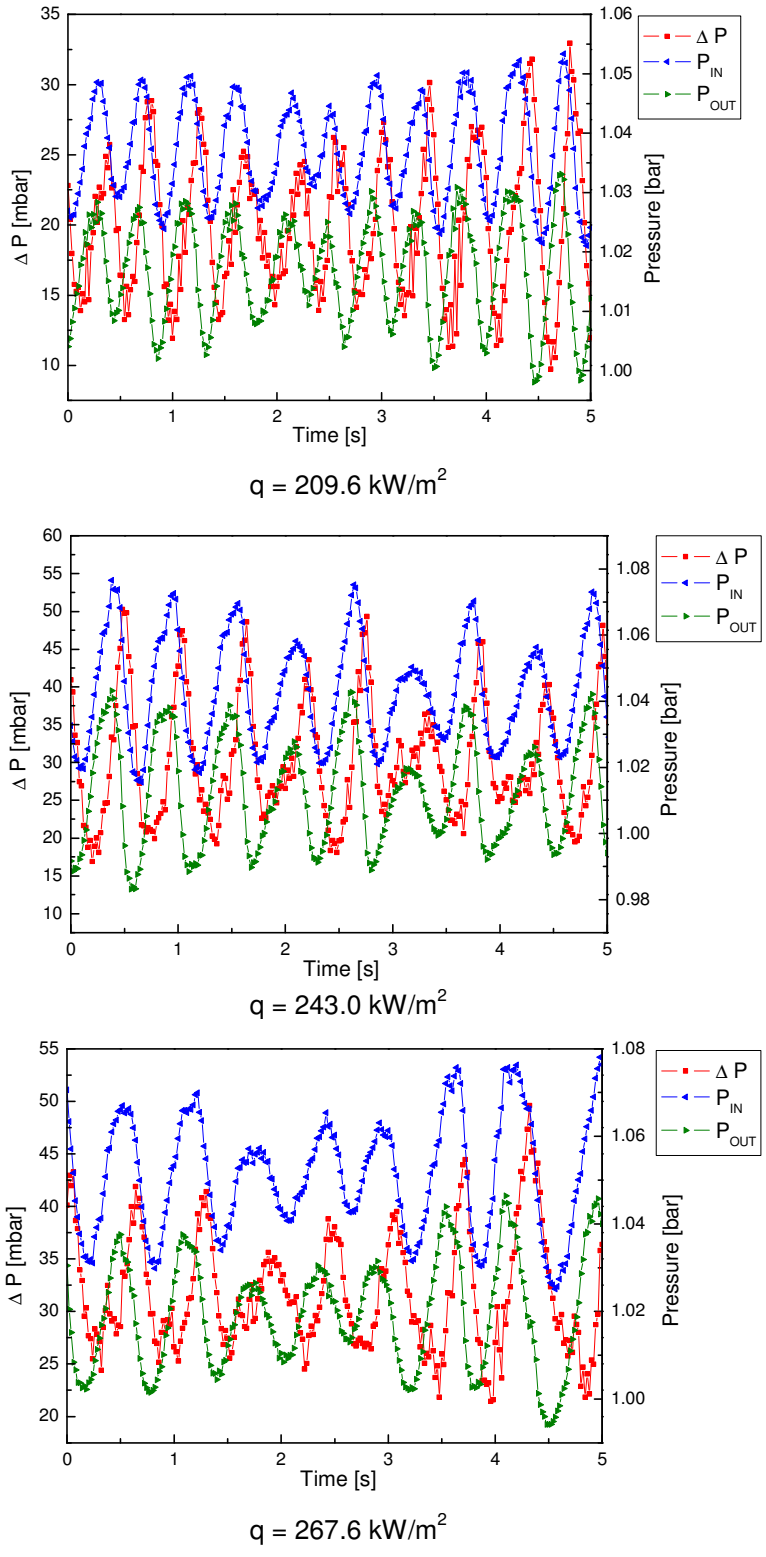

Figure 5.8 *Inlet/outlet pressure and pressure drop fluctuations in unstable flow regime with HALF instabilities for a mass flux of 208 kg/m^{2}s, inlet water temperature of 71 ˚C and a range of heat fluxes presented in time domain.*

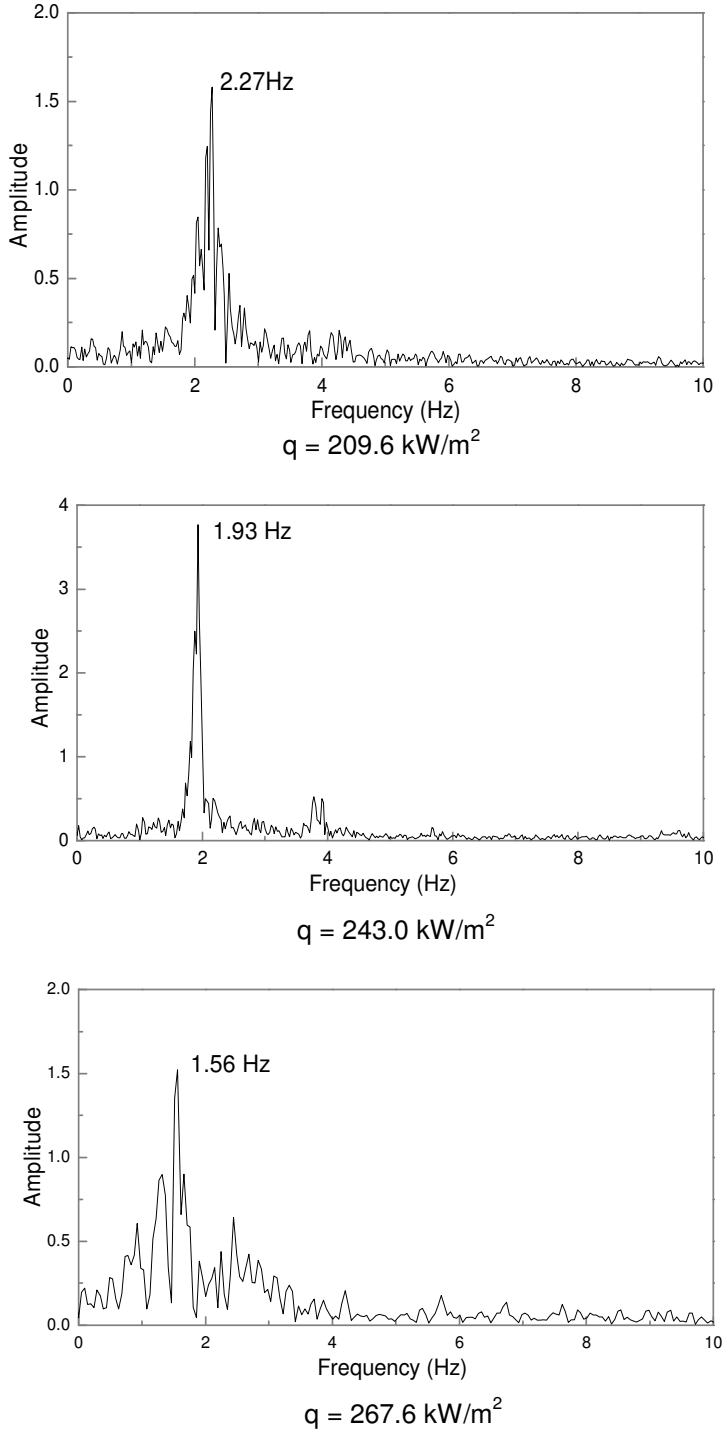

Figure 5.9 *Pressure drop fluctuations in unstable flow regime with HALF instabilities for a mass flux of 208 kg/m^{2}s, inlet water temperature of 71 ˚C and a range of heat fluxes presented in frequency domain.*

Table 5.3 *The frequencies of the pressure drop oscillations obtained from the experiments with constant heat flux and varied mass flux for two inlet water temperatures of 25 ˚C and 71 ˚C.*

Heat flux q [kW/m^2]	T_{in} = 71 ˚C		T_{in} = 25 ˚C	
	Mass flux G [kg/m^{2}s]	Frequency f [Hz]	Mass flux G [kg/m^{2}s]	Frequency f [Hz]
178	72.2	1.07	41.7	1.95
	180.6	2.00	55.6	2.64
267	158.3	1.10	75.0	1.19
	275.0	2.20	97.2	2.59
356	256.9	2.17	104.2	1.32
	370.8	2.34	145.8	2.71
445	316.7	2.10	133.3	0.90
	433.3	2.88	168.1	2.22

inlet water temperatures. The mass flux was varied from high to low values and the frequencies in Table 5.3 are presented for the beginning and the end of the HALF instabilities for each of the four heat fluxes. The pressure drop oscillation frequencies were found to decrease when mass flux decreases at a constant heat flux.

The observed frequencies (periods) are different from those reported by Wang et al. [2]. These authors observed periods ranging from approximately 2.5 to 9.5 s (0.1 to 0.4 Hz), while we observed frequencies ranging between 0.9 and 2.88 Hz for the case of high amplitude/low frequency oscillations. It is suggested that these observed differences are probably due to the fact that during the experiments conducted by Wang et al. the mass flux fluctuated while in our experiments this was kept constant. In an earlier work Wu and Cheng [3] used the same microchannels and experimental test loop as in the study of Wang et al. [2] and reported much longer oscillation periods ranging from 15.4 to 202 s for average values of mass flux from 112 to 146 kg/m^{2}s with a heat flux between 135 and 226 kW/m^2. The authors used compressed nitrogen gas to move the water from the pressure tank to the test section with microchannels and reported that when boiling occurred the pressure drop across the test section suddenly increased due to generation of vapour bubbles. Because pressure drop and mass flux are coupled, this increase in pressure drop caused a decrease in mass flux, which in turn caused the pressure drop to decrease. As a

result, pressure and mass flux oscillations occurred. The period of increase or a decrease of incoming mass flux may be a reason for the long period oscillations in temperatures and pressures, reported by the authors.

Similar frequency values and trends to those observed for HALF instabilities in our experiments have been reported by Hetsroni et al. [4] in their experimental study of flow boiling instabilities in parallel microchannels at low vapour quality. It is interesting to note that the authors used a pump to deliver cooling water into the test section at constant flow rate and reported that the frequencies of the pressure drop and temperature oscillations ranged between 1.6 and 2.8 Hz. In addition, they found that periods of oscillation increased with increasing power. However, they reported only one mode of instability, probably because of using lower values of the heat fluxes for a similar condition of the mass flux used in our experiments. The authors reported an increase in amplitudes of temperatures and pressures with increasing heat flux. We observed that amplitudes increased first then decreased as the system passed from the high amplitude/low frequency towards the low amplitude/high frequency instabilities with heat flux increasing under constant mass flux, or mass flux decreasing under constant heat flux.

Temperature, inlet/outlet pressure and pressure drop fluctuations during the HALF instabilities indicate reverse vapour flow inside the channels. Simultaneous video visualisation confirmed that these fluctuations are caused by the flow alternating between liquid, two-phase and vapour flow. Similar observation have been reported by Hetsroni et al. [4, 5] and Wang et al. [2]. Figure 5.10 shows image sequences from a recording captured using a high speed camera at a frame rate of 500 fps. These images are related to the HALF instabilities for a heat flux of 243.0 kW/m^2, mass flux of 208 kg/m^2s and an inlet water temperature of 71 ˚C. The arrow in the first image shows the direction of the water flow and the circle marks the nucleation site. After the microchannel with the marked nucleation site is filled with water (t = 0 ms), the bubble grows (t = 82 ms) and occupies the entire channel cross section area. Further axial growth causes bubbles to expand (t = 150 ms) forming a transient wispy annular flow as can be observed in the image when t = 180 ms. The vapour generated after the bubble bursts expands both downstream, increasing outlet

pressure, and upstream, pushing the liquid front back leading to reverse flow and an increase of inlet pressure. The image captured at t = 212 ms shows the onset of a temporary "dry out" period inside the channel. This temporary "dry out" period occurs due to thin liquid film evaporation in the transient wispy annular flow. The "dry out" period was found to increase with increasing heat flux for the HALF

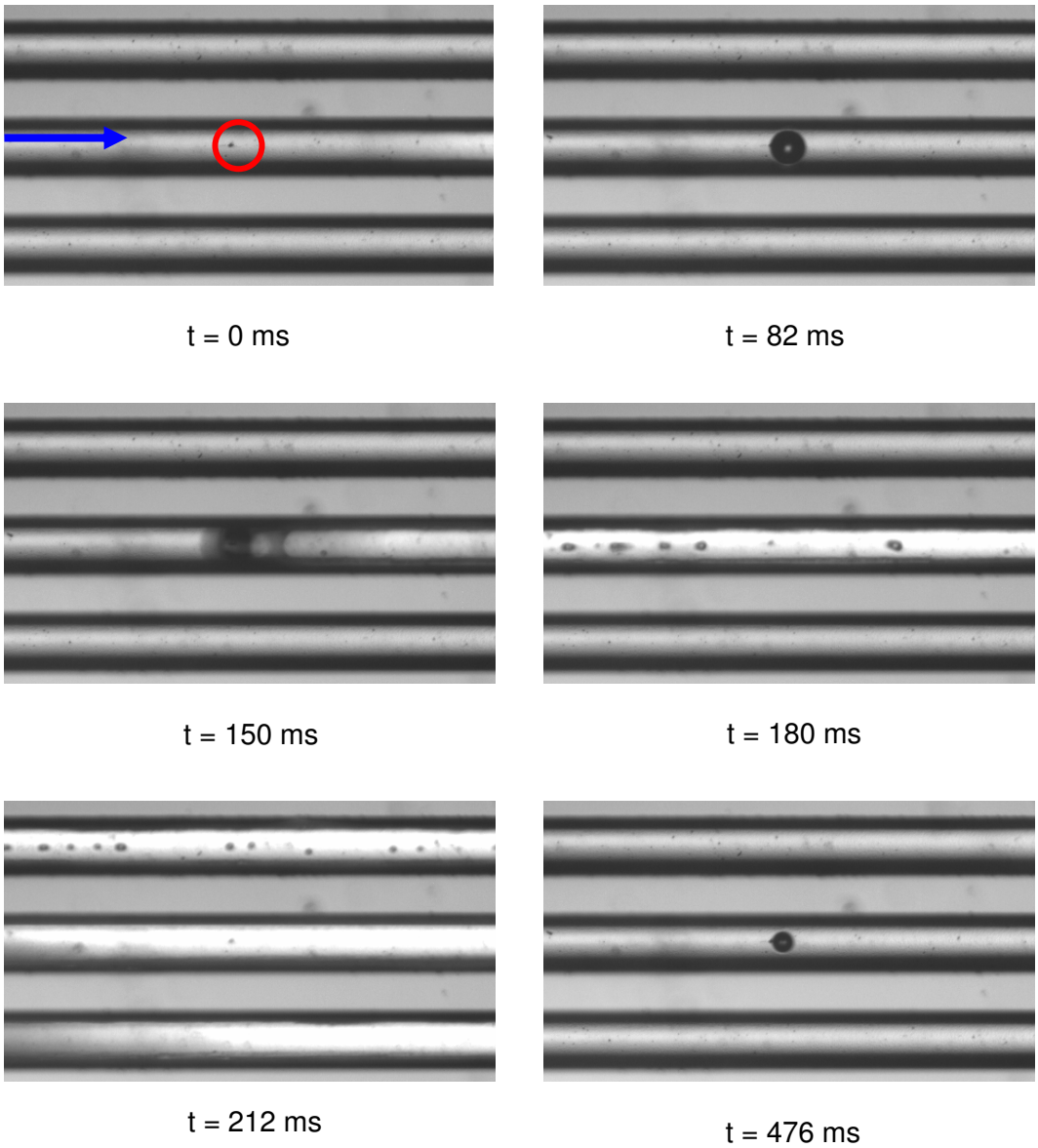

Figure 5.10 *Image sequences of flow boiling with HALF instabilities inside the parallel microchannels with hydraulic diameter of 194 μm (q = 243.0 kW/m^2, G = 208 kg/m^{2}s and T_{in} 71 ˚C).*

instabilities. This leads to a rise in the period for one oscillation, and therefore lower frequencies. The incoming subcooled liquid condenses vapour and a new cycle starts with bubble nucleation when the subcooled liquid refills the channel downstream from the nucleation site (t = 476 ms). It was observed that alternations between liquid, two-phase and vapour flow in adjacent channels are not in phase (e.g. Figure 5.10 t = 180 ms, wispy annular flow present in the middle channel while two adjacent channels are filled with liquid water). However, it was clearly observed that there were short periods when the liquid phase exists inside all microchannels and this was captured using a high speed camera using a 2300 μm diameter field of view, covering about nine channels. This period corresponds to minima in the temperature and the pressure drop measurements during the HALF instabilities. The time elapsed between two successive "refills" measured from the video is 0.476 s for a heat flux of 243.0 kW/m^2, a mass flux of 208 kg/m^{2}s and an inlet temperature of 71 ˚C. The average time between two successive pressure drop minima measured from a simultaneously acquired experimental data set (Figure 5.8, q = 243.0 kW/m^2) is 0.5 s and it is in good agreement with the time measured from the video. At a lower heat flux of 209.6 kW/cm^2 bubbles nucleation and growth was observed only close to the microchannels exit. With an increase of the heat flux, boiling propagates towards the microchannels inlet causing vapour expansion inside the inlet manifold. Figure 5.11 shows backward expansion of the vapour jet into the inlet manifold at a heat flux of 243.0 kW/m^2, mass flux of 208 kg/m^{2}s and inlet water temperature of 71 ˚C. The process of alternation between liquid, two-phase and vapour flow repeats in cycles when both the heat flux and water flow rates are constant inside the channels.

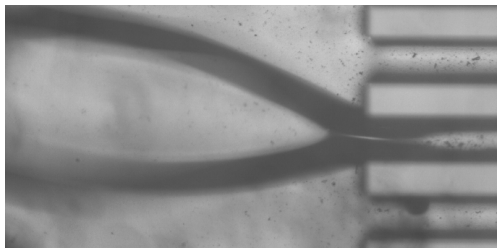

Figure 5.11 *Picture of the vapour jet from the microchannel expanding inside the inlet manifold of the heat sink.*

5.3.3 Low amplitude high frequency (LAHF) instabilities

This type of two-phase flow instabilities inside microchannels was observed after HALF instabilities, when increasing the heat flux at a constant mass flux or decreasing the mass flux at a constant heat flux. LAHF instabilities existed for the cases of $q > 2.92 \cdot G + 52.7$ at an inlet water temperature of 25 ˚C and $q > 1.15 \cdot G + 89.9$ at an inlet water temperature of 71 ˚C. Figure 5.12 shows temperature sensor measurements for LAHF type two-phase instabilities inside the microchannels for two different heat fluxes: 321.7 kW/m^2 and 400.4 kW/m^2, constant mass flux of 208 kg/m^{2}s and inlet water temperature of 71 ˚C. Although, the inlet and outlet pressures oscillated with smaller amplitudes than those found for HALF instabilities, appreciable fluctuations of temperatures, especially those measured by sensor T1 located at channels inlet, were observed. Wang et al. [2] reported nearly constant inlet and outlet temperatures of water as well as wall temperatures for the case of "short-period" oscillation. They reported the thermocouples used for temperature measurements had a response time of 0.1 s, which was too slow to measure any high frequencies associated with "short-period" oscillations.

Temperature oscillations with irregular amplitudes and frequencies higher than those found for the HALF type of instabilities were observed. Temperature measured by sensor T1, located at the inlet of microchannels region, oscillated with high amplitudes, while other signals exhibited smaller amplitudes. With an increase of the heat flux, the amplitude of temperature T1 decreases as the period of the liquid phase becomes shorter inside the microchannels. The increase of the heat flux leads to a rise in magnitudes of temperatures T3, T4 and T5 (Figure 5.12, q = 400.4 kW/m^2). Significant difference between temperatures T2 and T4 indicates asymmetrical flow distributions within the microchannels.

Temporal fluctuations of inlet/outlet pressure and the corresponding pressure drop simultaneously measured with the temperatures in Figure 5.12 are presented in Figure 5.13. Inlet/outlet pressure and pressure drop oscillate with high frequency and irregular low amplitudes. The magnitudes of the inlet/outlet pressure and the pressure

drop oscillations increase with increasing heat flux. FFT analysis was performed on the pressure drop data and the results are presented in Figure 5.14. Frequency analysis shows a wide range of frequencies in the range of 0 – 14 Hz with amplitudes of the frequency domain lower than in the case of high amplitude oscillations.

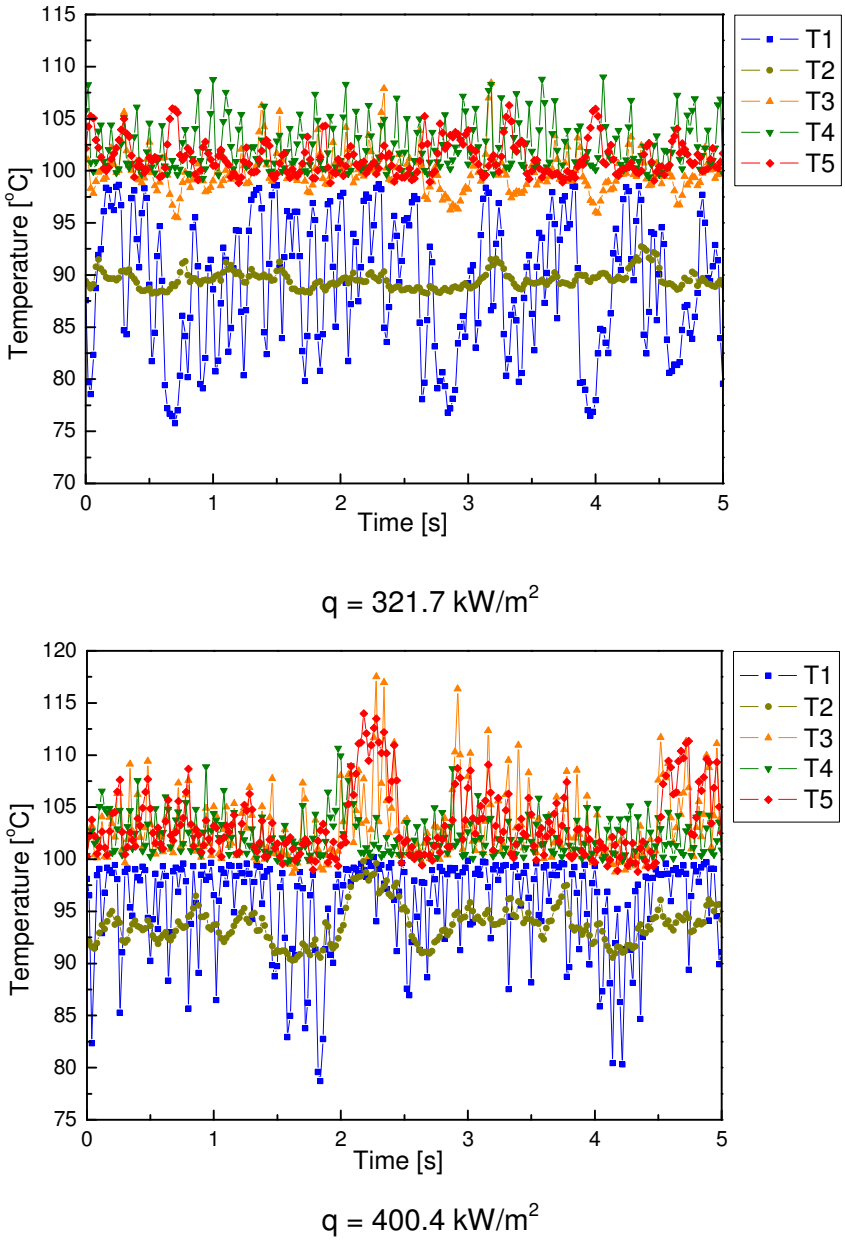

Figure 5.12 *Temperature measurements recorded during the unstable flow with LAHF instabilities for a mass flux of 208 kg/m^{2}s, an inlet temperature of 71 °C and two heat fluxes of 321.7 kW/m^2 and 400.4 kW/m^2.*

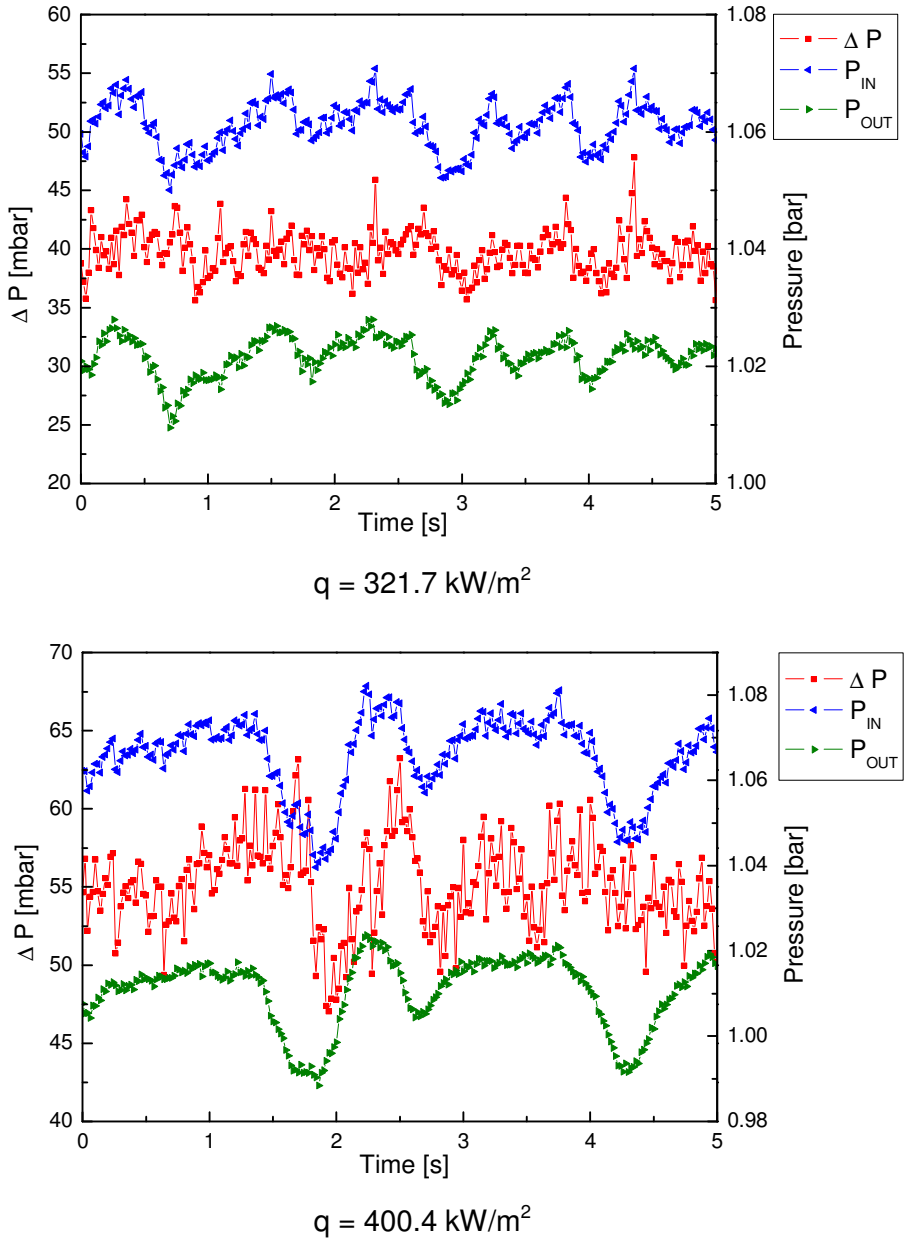

Figure 5.13 *Inlet/outlet pressure and pressure drop measurements recorded during the unstable flow with LAHF instabilities for a mass flux of 208 kg/m^{2}s, an inlet temperature of 71 ˚C and two heat fluxes of 321.7 kW/m^2 and 400.4 kW/m^2 presented in time domain.*

Wang et al. [2] reported a value of 22 Hz for the inlet pressure oscillation under a boiling regime with "short-period" oscillation. The authors concluded that the frequency of pressure fluctuations was independent of the mass flux. The authors reported frequencies of 32 Hz at a heat flux of 740.7 kW/m^2. Such high frequencies have not been observed in this study even at a data acquisition sampling rate of 100

Hz. A possible reason is that smaller heat fluxes were used (the maximum heat flux used in the experiments was 590.4 kW/m^2). Balasubramanian and Kandlikar [6] reported an increase in dominant frequency with increase in surface temperature with a maximum frequency around 13 Hz.

Simultaneous visualisation of boiling inside the channels indicates that these fluctuations are caused by alternation between liquid, two-phase and vapour flow. The liquid phase lasts for a shorter period than in the case of HALF instabilities, turning into droplets and a liquid film, which quickly evaporate. Bubble nucleation

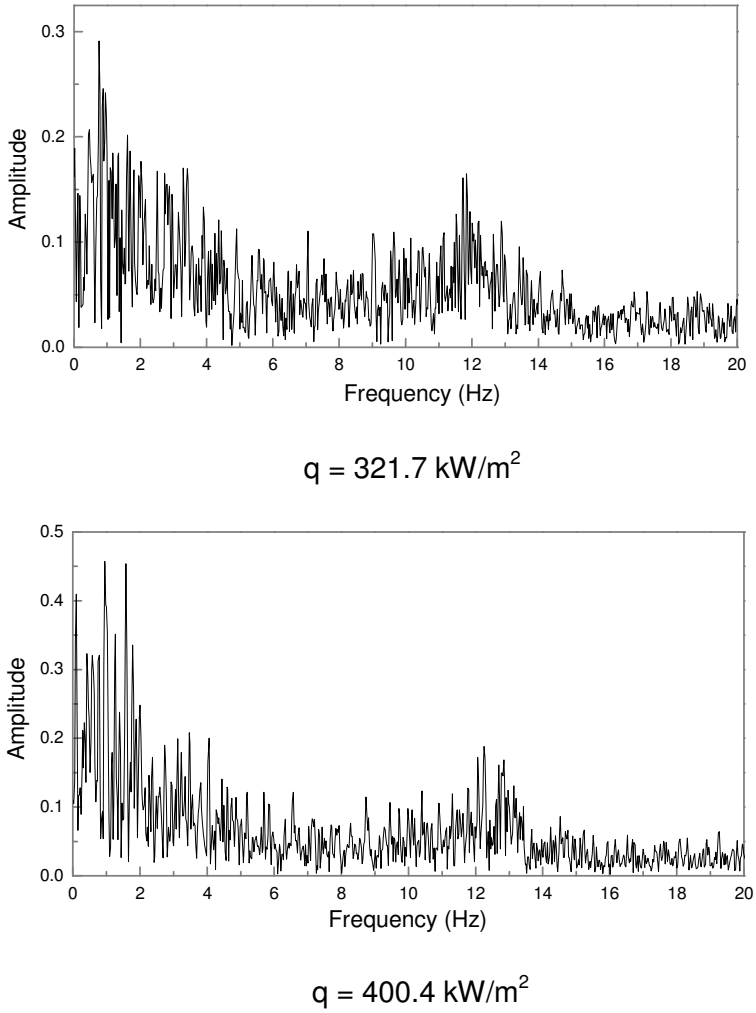

Figure 5.14 *Pressure drop measurements recorded during the unstable flow with LAHF instabilities for a mass flux of 208 kg/m^{2}s, an inlet temperature of 71 ˚C and two heat fluxes of 321.7 kW/m^2 and 400.4 kW/m^2 presented in frequency domain.*

and growth observed inside the bulk flow lasts for a much shorter period than is the case for high amplitude/low frequency instabilities. Figure 5.15 shows image sequences captured using the high speed camera at a frame rate of 500 fps. These images show bubble nucleation, growth and collapse during the LAHF instabilities inside the microchannel with a nucleation site. The nucleation site is marked with the circle and the arrow shows the flow directions (Figure 5.15 image t = 0 ms). It is clear from Figure 5.15 that alternations in adjacent channels were not in phase (non-synchronous alternations within channels). The latter is consequence of the non-uniform distribution of cooling water within 40 channels. The bubble growth time is around 16 ms with the bubble collapsing before occupying the entire channel diameter. The image at t = 16 ms shows transient annular flow formed after the bubble collapsed inside the channel with the nucleation site. The thin liquid film of annular flow rapidly evaporates, causing a temporal "dry out" period inside the observed channel as shown in the image at t = 48 ms. The average period between two successive "refills" measured from the video for the channel with the marked nucleation site is 96 ms. In general, the bubble growth time and the period between two successive "refills" are shorter than in the case of HALF oscillations. Hence, frequencies of LAHF oscillations are higher than those found for the HALF type of instabilities. A large amount of reverse vapour flow was observed inside the inlet manifold during the LAHF instabilities. Figure 5.16 shows image sequences of the alternation inside the inlet manifold between the incoming liquid flow (t = 0 ms) and the reverse vapour flow from the microchannels (t = 78 ms) for a heat flux of 356.0 kW/m^2, a mass flux of 222.2 kg/m^{2}s (q/G = 1.60 kJ/kg) and an inlet temperature of 71˚C.

The LAHF type of instabilities was observed in the experiments with a constant heat flux when decreasing the mass flux for both of the water inlet temperatures used in the experiments (25 ˚C and 71 ˚C). Again, a broad range of frequencies ranging between 0 and 20 Hz was observed. Amplitudes of the frequency domain were lower than in the case of high amplitude oscillations.

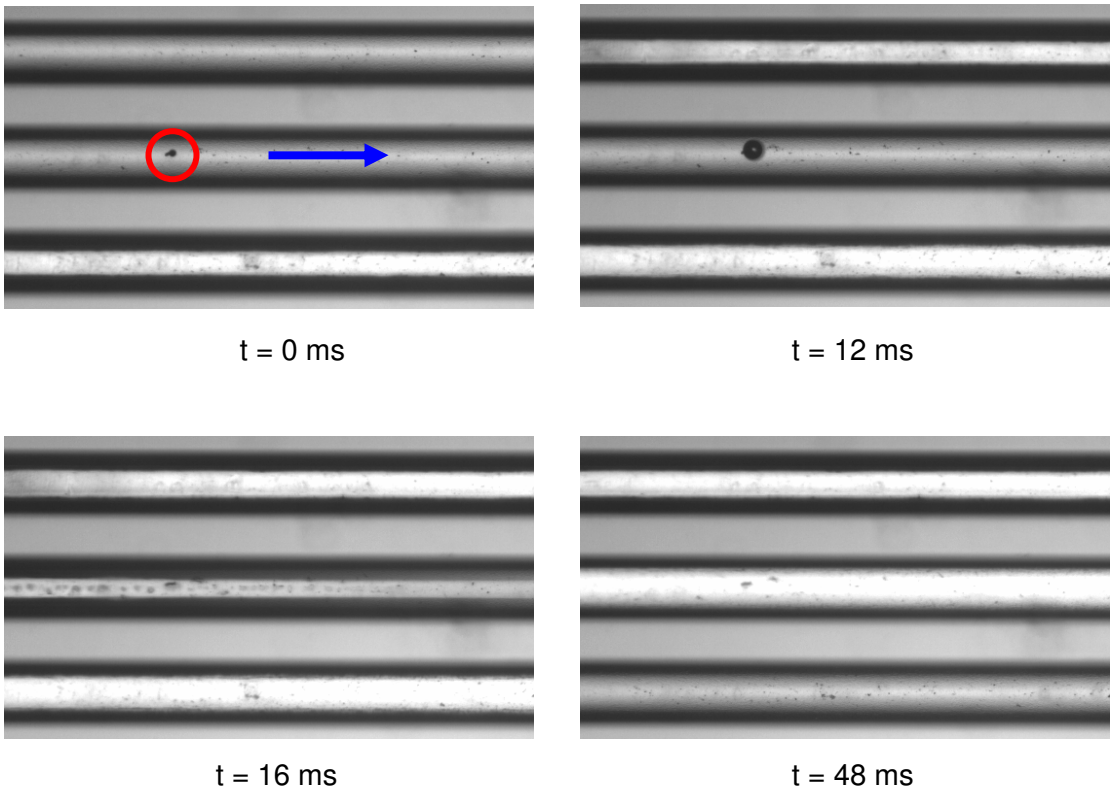

Figure 5.15 *Image sequences of flow boiling with LAHF instabilities inside the parallel microchannels (q = 400.4 kW/m^2, G = 208 kg/m^{2}s and T_{in} 71 ˚C).*

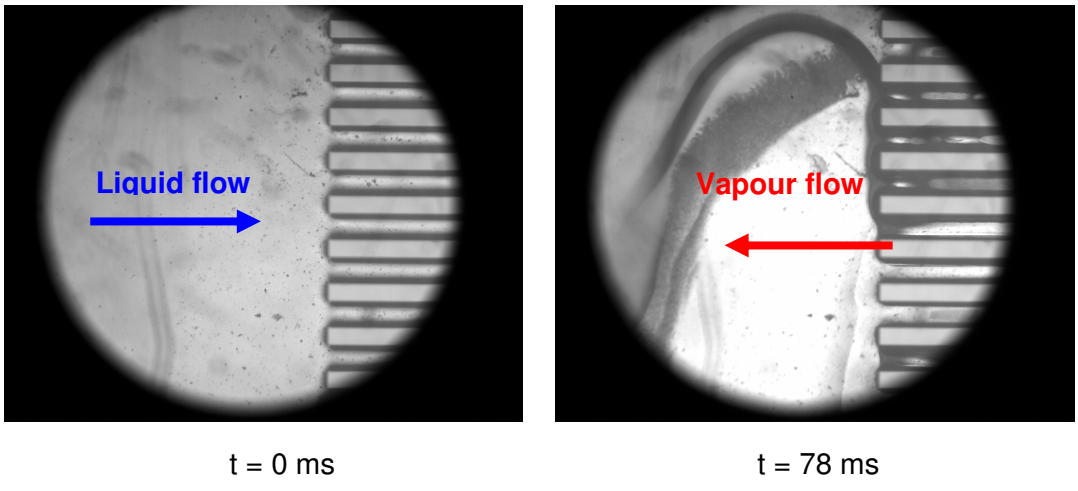

Figure 5.16 *Alternation inside the inlet manifold between the liquid flow (t = 0 ms) and the reverse vapour flow from microchannels at t = 78 ms (q = 356 kW/m^2, G = 222.2 kg/m^{2}s, T_{in} = 71 ˚C).*

5.3.4 Pressure drop characteristic and temperature analysis in microchannels

The determination of the relationship between pressure drop and flow rate (internal characteristic curve) is crucial in the investigation of the two-phase flow instabilities in microchannel heat sinks. A minimum in the curve is the necessary condition for the compressible volume instability and the excursive instabilities (Bergles and Kandlikar [7]). Figure 5.17 shows averaged values of the pressure drop as a function of mass flux curves in the microchannels obtained at different heat fluxes for two inlet water temperatures of 25 ˚C and 71 ˚C. There is a characteristic minimum for each curve corresponding to incipient flow boiling in the stable flow regime. A decrease of the mass flux or increase of the heat flux from the minimum point leads to a higher pressure drop due to vapour generation. The pressure drop characteristic curves exhibit high negative slope for the two-phase flow region indicating two-phase flow instabilities at the both inlet subcooling conditions (25 ˚C and 71 ˚C). High amplitude oscillations were observed for both the inlet and the outlet pressure. For comparison Wang et al. [2] reported only appreciable fluctuations of the inlet pressure. The magnitude of the pressure drop oscillations (difference between maximum and minimum values of the pressure drop) depends on the q/G ratio and T_{in}. In the case of stable flow with incipient boiling the magnitude was found to be in the range of 5 to 10 mbar. Values of the magnitude for the HALF instabilities ranged from 25 mbar to 86 mbar. The maximum value of 85.4 mbar was found for T_{in} = 25 ˚C, mass flux of 208 kg/m^{2}s and heat flux of 530.4 kW/m^2, while for the same mass flux and T_{in} = 71 ˚C the maximum magnitude of the pressure drop oscillation was 42.6 mbar for a heat flux of 243.0 kW/m^2. It was found that the magnitude of pressure drop oscillations for the HALF instabilities first increased and then decreased with heat flux increasing at a constant mass flux or with mass flux decreasing at a constant heat flux. Magnitudes for the LAHF instabilities ranged between 10 and 25 mbar. However, the occurrence of permanent local “dry out” zone observed at the low mass fluxes or the high heat fluxes might lead to a sudden rise in the pressure drop during the LAHF instabilities.

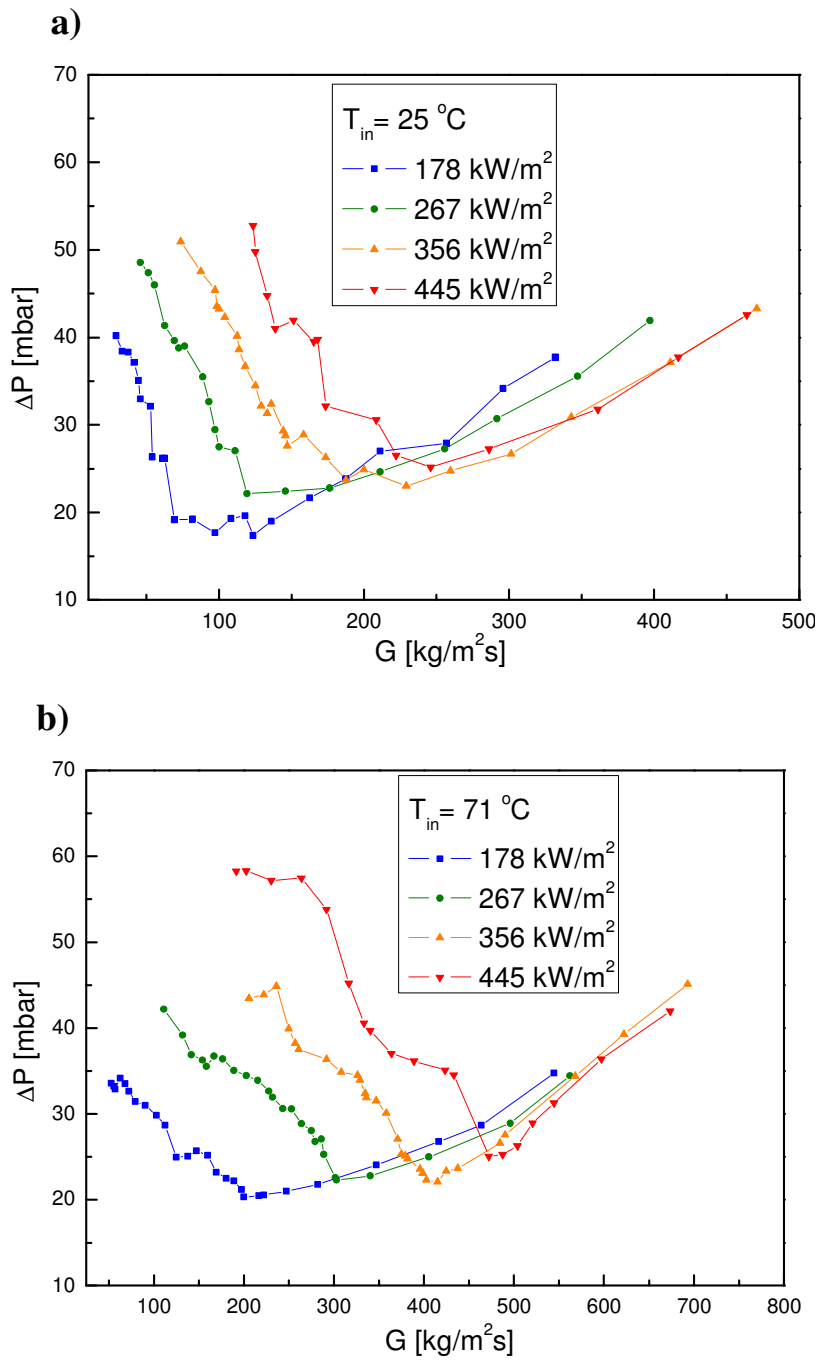

Figure 5.17 *Pressure drop characteristic of the heat sink with parallel microchannels with hydraulic diameter of 194 μm for the different heat fluxes with (a) T_{in} = 25 ˚C and (b) T_{in} = 71 ˚C.*

It has been pointed out that boiling inside microchannels leads to asymmetrical flow distribution and the simultaneous existence of different flow patterns inside microchannels along the transverse direction in the present experimental heat sink. A

significant difference between temperatures measured on the sensors located in the transverse direction (sensors T2, T3 and T4) existed as a consequence of the asymmetrical flow distribution within the microchannels during flow boiling. Figure 5.18 presents the temperature distribution along the flow stream direction and the transverse direction for the mass flux of 208 kg/m^{2}s for two different inlet water temperatures (25 ˚C and 71 ˚C) and a range of heat fluxes. Figure 5.18 shows absolute differences between the average temperatures measured by the sensors. In the single-phase flow regime the differences between the sensors located in the transverse direction T2 and T4 are very small, less then 1˚C, indicating uniform distribution for both inlet water temperatures. However, boiling inside the microchannels affects flow distribution causing an appreciable difference between the values of T3-T2 and T3-T4 (Figure 5.18a and Figure 5.18b). A significant difference exists for both inlet water temperatures indicating asymmetrical flow distribution. However, asymmetrical flow distribution is more transparent for the lower temperature of 25 ˚C. At the heat flux of 584.9 kW/m^2 and T_{in} = 25 ˚C the mean value of the T4 temperature measurement was 110.3 ˚C, while that for the T2 sensor was 69.9 ˚C. Asymmetrical flow distribution at a low inlet temperature of 25 ˚C caused a permanent local “dry out” zone inside the microchannels located above the sensor T4 before the occurrence of LAHF instabilities inside the microchannels. Figure 5.19 shows temperature measurements when the “dry out” zone was observed inside the heat sink for q = 590.4 kW/m^2, G = 208 kg/m^{2}s and T_{in} = 25 ˚C.

With boiling incipience inside the microchannels, differences between the average temperatures on the sensors located along the direction of the flow stream (T3-T1 and T5-T3) become smaller. This implies that boiling leads to a better temperature uniformity in the direction of the flow stream. High inlet temperature (71 ˚C) gives smaller sensors temperature differences and better temperature uniformity along the direction of the flow stream and the transverse direction, indicating better flow distribution than in the case of low inlet water temperature (25 ˚C).

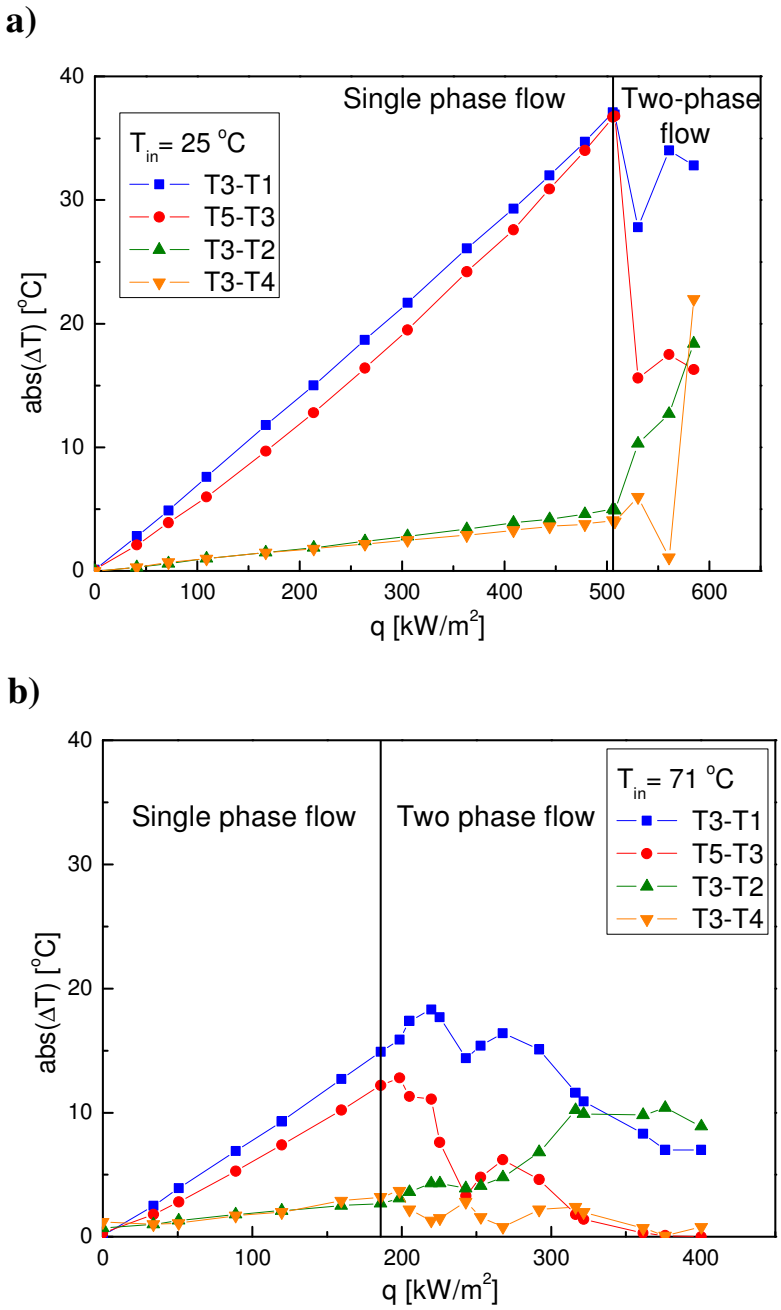

Figure 5.18 *Differences between the average temperatures measured by the sensors vs. heat flux, G = 208 kg/m²s, T_{in} = 25 °C (a) and T_{in} = 71 °C (b).*

It was found that the inlet temperature affects the magnitude of the temperature oscillations during two-phase flow instabilities. Table 5.4 presents the magnitudes (differences between maximum and minimum temperature from one data set) of temperature measurements on sensors T1, T3 and T5 for inlet water temperature of 25 ˚C and 71 ˚C with four different heat fluxes. Each value of magnitude in Table 5.4 is the maximum value measured for a range of mass fluxes at a particular heat flux and inlet water temperature. In general, lower inlet water temperature leads to higher magnitudes of temperature oscillations (the only exception is the magnitude of the temperature T3 for a heat flux of 178.0 kW/m^2 where the magnitude is higher for a higher temperature). Alternation between the incoming liquid at high subcooling condition and reverse flow of vapour causes oscillations of the temperature with significant magnitudes, especially those measured on sensors T1 located at the microchannels inlet and T3 located in the middle of the heat sink.

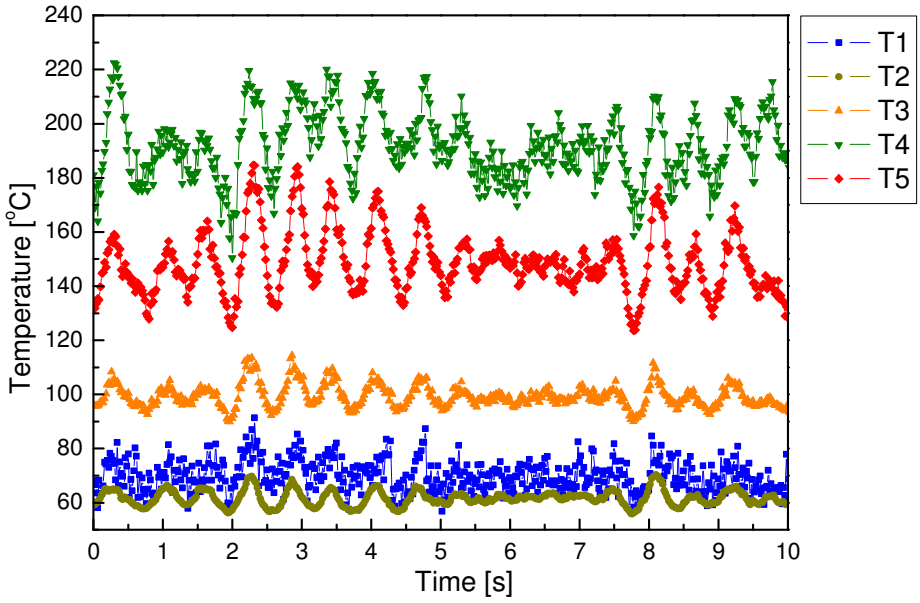

Figure 5.19 *Temperature measurements for q = 590.4 kW/m^2, G = 208 kg/m^{2}s and T_{in} = 25 ˚C. A "dry out" zone existed inside the channels above the sensors T4.*

Table 5.4 *Maximum magnitudes of temperatures T1, T3 and T5 found for the different heat fluxes and inlet water temperatures.*

Heat flux, q [kW/m^2]	Inlet temperature, T_{in} [˚C]	Magnitude, $T1_{max}$-$T1_{min}$ [˚C]	Magnitude, $T3_{max}$-$T3_{min}$ [˚C]	Magnitude, $T5_{max}$-$T5_{min}$ [˚C]
178.0	25	58.2	45.2	38.7
178.0	71	33.8	53.7	37.9
267.0	25.0	58.6	55.6	59.5
267.0	71.0	28.4	28.7	22.7
356.0	25.0	61.5	49.6	35.9
356.0	71.0	27.3	15.9	22.5
445.0	25.0	60.5	69.0	43.8
445.0	71.0	27.8	61.2	41.2

5.4 Conclusions

In the study presented in this chapter, simultaneous measurements and visualisation experiments have been performed in order to examine two-phase flow instabilities in a microchannels based heat sink with 40 parallel rectangular channels having hydraulic diameter of 194 μm, using water at two different inlet temperatures: 25 ˚C and 71 ˚C. In the light of these experiments, two types of two-phase instabilities were identified: one with high amplitude/low frequency oscillations (HALF) and the other with low amplitude/high frequency oscillations (LAHF). The criterion of classification was the frequency and amplitude of the pressure drop oscillations. It was found that the flow regime and type of two-phase flow instabilities depended on the heat flux, mass flux and inlet subcooling condition. However, the experimental results show that two-phase instabilities lead to very asymmetrical flow distribution within the 40 microchannels and result in the simultaneous existence of different flow regimes inside microchannels along the transverse direction.

HALF instabilities existed for $2.62 \cdot G < q < 2.92 \cdot G + 52.7$ at an inlet water temperature of 25 ˚C and $0.99 \cdot G < q < 1.15 \cdot G + 89.9$ at an inlet water temperature of 71 ˚C. It was found that frequencies of the pressure drop oscillations typical for HALF instabilities were in the range of 0.9-2.9 Hz. The frequency of HALF oscillations decreased with increasing heat flux or decreasing mass flow rate. The inlet/outlet pressure oscillations are not in phase as the outlet pressure reaches the maximum earlier than the inlet pressure due to reverse vapour propagation from the microchannels outlet towards inlet during one cycle of HALF oscillations. Simultaneous visualisation and measurement indicate that pressure and temperature fluctuations, characteristic of HALF instabilities are caused by alternation between liquid, two-phase and vapour flow (temporary "dry out" period). The bubble grows occupying the entire channels diameter and its growth time is longer than in the case of LAHF instabilities. The magnitude of pressure drop oscillations (difference between maximum and minimum values of the pressure drop) ranged between 25 mbar and 86 mbar. It was found that the magnitudes of pressure drop oscillations for the HALF instabilities first increased and then decreased with the heat flux increasing at a constant mass flux or with mass flux decreasing at a constant heat flux.

LAHF instabilities existed for the cases when $q > 2.92 \cdot G + 52.7$ at an inlet water temperature of 25 ˚C and $q > 1.15 \cdot G + 89.9$ at an inlet water temperature of 71 ˚C. Frequency analysis for LAHF instabilities showed a broad range of frequencies higher than those found for HALF instabilities with amplitudes of the frequency domain lower than in the case of high amplitude oscillations. The magnitudes of pressure drop measurements for the LAHF instabilities ranged between 10 mbar and 25 mbar. The occurrence of a permanent local "dry out" zone might lead to sudden rise in the pressure drop during the LAHF instabilities. High speed camera imaging shows that bubble growth time and period between two successive "refills" of the microchannels are shorter than in the case of HALF oscillations. This leads to existence of the higher oscillations frequencies during LAHF instabilities than those found for the HALF instabilities.

It was found that inlet water temperature affects the magnitudes of the temperature oscillations during two-phase flow instabilities. Lower inlet water temperature leads to higher magnitudes of temperature oscillations. Higher inlet temperature gives better temperature uniformity along the direction of the flow stream and the transverse direction, indicating better flow distribution than in the case of lower inlet water temperature.

References

1. *Origin (OriginLab, Northampton, MA).*
2. Wang, G., P. Cheng, H. Wu, *Unstable and stable flow boiling in parallel microchannels and in a single microchannel.* International Journal of Heat and Mass Transfer, 2007. 50(21-22) 4297-4310.
3. Wu, H.Y. and P. Cheng, *Boiling instability in parallel silicon microchannels at different heat flux.* International Journal of Heat and Mass Transfer, 2004. 47(17-18) 3631-3641.
4. Hetsroni, G., A. Mosyak, E. Pogrebnyak, Z. Segal, *Periodic boiling in parallel micro-channels at low vapor quality.* International Journal of Multiphase Flow, 2006. 32(10-11) 1141-1159.
5. Hetsroni, G., A. Mosyak, E. Pogrebnyak, Z. Segal, *Explosive boiling of water in parallel micro-channels.* International Journal of Multiphase Flow, 2005. 31(4) 371-392.
6. Balasubramanian, P., Kandlikar, S., *Experimental study of flow patterns, pressure drop, and flow instabilities in parallel rectangular minichannels.* Heat Transfer Engineering, 2005. 26(3) 20-27.
7. Bergles, A.E. and S.G. Kandlikar, *On the Nature of Critical Heat Flux in Microchannels.* Journal of Heat Transfer, 2005. 127(1) 101-107.

Chapter 6 Bubbles dynamics and boiling heat transfer in microchannels

6.1 Introduction

Bubble dynamics is fundamental to the understanding of boiling heat transfer mechanism and prediction of heat transfer coefficient. Qualitative and quantitative description of the vapour bubble growth in superheated liquids is given in the works of Plesset and Zwick [1] and Forster and Zuber [2]. The rate of growth of a vapour bubble, once formed, is controlled by the liquid inertia, the surface tension and the vapour pressure. For flow boiling in macro scale sized channels, the bubble growth and departure diameter are controlled by the inertial force, buoyancy force, surface tension and drag force due to bulk flow in the channel. In the initial stage of the growth when the bubble is small and surrounded by a highly superheated liquid layer near the heated wall, inertia forces are dominant; this results in a rapid bubble growth. Later as the bubble grows, it comes in contact with a liquid at lower superheat. The bubble growth for this stage is controlled by thermal diffusion in the thin liquid film surrounding the bubble. The bubble growth in this stage is slower and thermally controlled.

Kandlikar et al. [3] investigated bubble nucleation and growth under flow conditions. The authors assessed the effects of flow rate, wall temperature, and

subcooling on bubble nucleation and growth characteristics. The authors reported that an increase in flow velocity caused the bubble to grow much faster and to depart at smaller diameters. A higher wall temperature causes bubbles to grow rapidly and reach the departure conditions sooner.

Bubble dynamics in microcscale channels can be very different from that in macroscale tubes, due to change in the dominant forces. In microchannels, dominant forces acting on bubbles are surface tension and drag force, while buoyancy force diminishes. The bubble growth in the confined space of a microchannel causes a large pressure drop through the channel. This results in a significant drag force and shear stress acting on the bubble. The change in the dominant force when passing from the macroscale to the microscale results in different bubble growth characteristics in a microchannel as compared to a macroscale channel.

The objective of the work presented in this chapter is to gain further understanding of bubble growth characteristic in the case of flow boiling in microchannels. The bubble growth and bubble departure size in parallel rectangular microchannels with a hydraulic diameter of 194 μm have been experimentally investigated. The results of this study demonstrate that the bubble growth in microchannels is different from that in macroscale channels. Furthermore, the effects of bubble dynamics on flow instabilities and heat transfer coefficient are investigated and discussed.

6.2 Experimental setup and procedure

The experimental setup described in chapter 3 was used in the present study to investigate bubble dynamics in the case of flow boiling in the microchannel heat sink. Prior to carrying out the experiment, deionised water in the reservoir was degassed by vigorous boiling for approximately one hour. Afterwards, the flow rate and the inlet water temperature were adjusted to the desired values. Table 6.1 shows the used operating conditions for the experiments conducted under constant mass flux and varying heat flux. The experiments were conducted for five different mass

fluxes with uniform heat flux being varied in the given range for each of the mass fluxes used.

High-speed camera images were taken using a high-speed camera (NanoSense MkIII) with a maximum frame rate of 1000 fps at full resolution of 1280×1024 pixels. The high-speed camera was mounted on a microscope with a 5× magnification objective and illuminator modified to accept fiber optic guide. The microchannels heat sink was illuminated with a continuously working 150 W cold light illuminator with a glass fiber optic conductor connected to the microscope. Light was transmitted axially through the microscope objective illuminating the top side of the microchannel heat sink. High-speed camera imaging was performed simultaneously with integrated temperature sensors and inlet/outlet pressure transducers measurements.

A maximum diameter of the bubble projected area from the top view was measured using ImageJ software. A reference distance of the channel width (150 μm) was used to properly calibrate all measurements. The bubble diameter was measured with an accuracy of ± 2 pixels that corresponds to ± 5 μm. Bubble growth and departure diameters were determined only for the bubbles observed in the six channels located above the sensor T3 in the middle zone of the microchannel assembly. Bubble frequency was not possible to determine, as bubbles nucleated and grew from different nucleation sites rather than the same site in two successive cycles during the alternations between liquid/two-phase/vapour flows.

Table 6.1 *Operating conditions for the bubble dynamics experiments conducted under constant mass flux and varying heat flux.*

Coolant	Inlet temperature, Tin [˚C]	Mass flux, G [kg/m^{2}s]	Heat flux, q [kW/m^2]
Deionised water	71.0	71	138 - 259
		112	148 - 366
		153	180 - 469
		178	219 - 473
		204	248 - 537

6.3 Data reduction

The heat flux transferred to the water (effective heat flux) was calculated from the measured input voltage, V and the current, I across the film heater :

$$q = \frac{\varphi VI}{A}, \tag{6.1}$$

where A is the area of the heated microchannels region (10.15 × 15.00 mm^2), and φ the portion of the total power transferred to the water. The method of calculating the portion of the total power transferred to the water is explained in chapter 3. It was found that approximately 89 % of the input power was transferred to water for the range of conditions considered in this study.

The local heat transfer coefficient, h_z is calculated from:

$$h_z = \frac{q_w}{T_w - T_f} \tag{6.2}$$

in which q_w is the wall heat flux, T_w is the local channel bottom wall temperature and T_f is local fluid temperature. The local heat transfer coefficients were calculated along microchannels where integrated temperature sensors T1, T3 and T5 were located.

The wall heat flux was calculated using fin analysis method:

$$q_w = \frac{q(W_{ch} + W_w)}{(W_{ch} + 2\eta D_{ch})}, \tag{6.3}$$

assuming the uniform heat transfer coefficient, averaged along the entire heated perimeter of the microchannel. The fin efficiency is defined as

$$\eta = \frac{\tanh(mD_{ch})}{mD_{ch}}, \tag{6.4}$$

where m is the fin parameter,

$$m = \sqrt{\frac{h_z}{k_{Si} W_w}}. \tag{6.5}$$

Equations (6.2) – (6.5) require an iterative procedure and an initial guess of the heat transfer coefficient was obtained assuming the wall heat flux being equal to the effective heat flux for the first step of the iterative procedure.

The local channel bottom wall temperature, T_w in eq. (6.2) was calculated assuming one-dimensional heat conduction through silicon substrate:

$$T_w = T_s - \frac{q \cdot d}{k_{Si}}, \tag{6.6}$$

where T_s is the local temperature measured by the sensor located at a distance d = 112 μm underneath the channel bottom wall.

The local fluid temperature, T_f was determined depending on the region along the length of microchannels. Cooling water was supplied into microchannels in a subcooled condition (T_{in} = *71 ˚C*) and a subcooling boiling region extended over a certain distance from the microchannels inlet along microchannels length. Therefore, the length of the microchannel can be divided into the subcooled liquid region and saturated region with respect to thermodynamic equilibrium quality. The separating point between the two regions is the location of zero thermodynamic quality. The thermodynamic equilibrium quality for the subcooled liquid region is negative and for the saturated region is positive. The length of the subcooled region can be evaluated from an energy balance as follows:

$$L_{sub} = \frac{\dot{m} c_p (T_{sat} - T_{in})}{qW} \tag{6.7}$$

where T_{sat} is the saturation temperature at the location of zero thermodynamic quality. T_{sat} was evaluated using the measured inlet pressure, assuming the pressure drop over the subcooled liquid region in microchannels is negligible. The length of the saturated region, L_{sat} was calculated subtracting L_{sub} from the total length, L of microchannels:

$$L_{sat} = L - L_{sub} \tag{6.8}$$

The local fluid temperature T_f for subcooled liquid region at a distance l from the channels inlet was calculated using an energy balance:

$$T_f = T_{in} + \frac{qWl}{\dot{m} c_p} \tag{6.9}$$

In the saturated region, the local fluid temperature corresponds to the fluid saturation temperature at the local pressure. The fluid saturation temperature was determined from NIST standard reference database [4] for saturation properties of water. A linear function between saturation temperature and pressure was obtained by fitting the data from NIST database for a range of pressures corresponding to minimum and maximum values measured for inlet and outlet pressures (Figure 6.1). Since the pressure drop across the microchannels is relatively small in the present study (< 0.1 bar), a linear pressure profile over the microchannels was assumed. A linear interpolation between P_{in} and P_{out} with respect to the axial distance from the microchannels inlet was employed to determine the local pressure. Figure 6.2 shows the temperatures of the fluid for the range of heat fluxes and a constant mass flux of 71 kg/m^{2}s. The local fluid temperatures were calculated at locations of sensors T1, T3 and T5 axially positioned at 0.367, 7.500 and 14.632 mm respectively from the channels inlet. The local fluid temperature T_{f1} above the sensor T1 located immediately downstream from the microchannels inlet indicates high subcooled condition at the inlet zone of the microchannels. T_{f1} increased slightly as the heat flux increased. The local fluid temperature T_{f3} above the sensor T3 increased with the heat

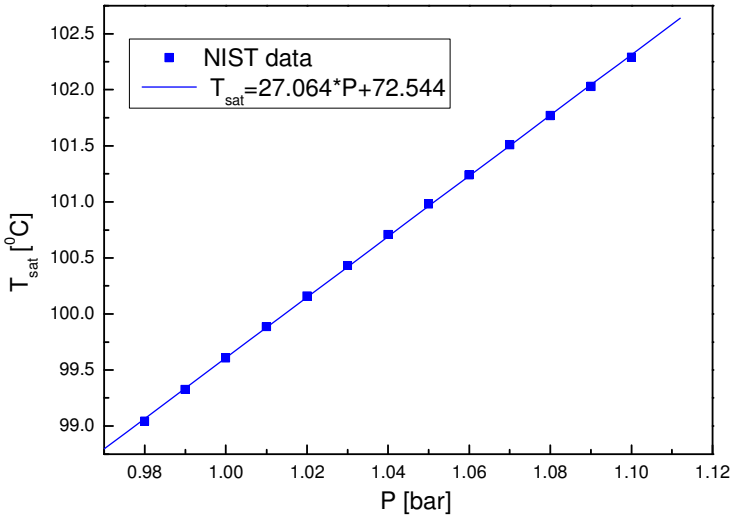

Figure 6.1 *Saturation water temperature as function of pressure.*

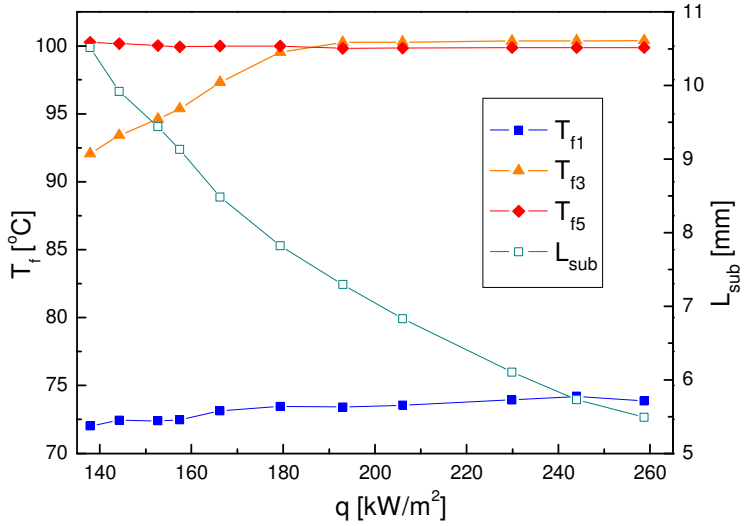

Figure 6.2 *Local fluid temperatures and length of subcooled region in terms of effective heat flux.*

flux increasing in the subcooled liquid region. Once the length of subcooled region, L_{sub} became equal or shorter than 7.5 mm (distance of the sensor T3 from the channels inlet), T_{f3} reached saturation conditions. The local fluid temperature T_{f5} above the sensor T5 located immediately upstream from the microchannels outlet was in saturated conditions and slightly decreased as the outlet pressures decreased.

The exit vapour quality was calculated knowing the mass flow rate, $\dot{m}$ and the net input power, Q as

$$x_e = \frac{Q - \dot{m}c_p(T_{sat} - T_{in})}{\dot{m}h_{lg}}, \tag{6.10}$$

where T_{sat} is saturation temperature corresponding to the outlet pressure.

The uncertainties in the reported two-phase heat transfer coefficients obtained using standard error analysis were in the range of 2.3 – 8.8 %. The larger uncertainties occurred for the subcooled liquid region and at the lower mass fluxes. The uncertainties in the measured signals are given in chapter 3.

6.4 Results and discussion

6.4.1 Bubble growth

Bubble growth characteristics in the present study are for bubbles observed in the six channels located in the middle of the microchannel assembly above sensor T3. Bubbles nucleation in the observed microchannels was preceded by boiling in the outlet zone of the microchannels with intensive flow instabilities and reversed slug/vapour flow. The wall superheat for boiling onset measured at the location of sensor T5 situated immediately before channels exit was in the range from 3.3 to 8.6 ˚C depending on the mass flow rate of water.

The observed bubbles were classified into bottom wall bubbles and sidewall bubbles. Figure 6.3 shows sequential images of a bottom wall bubble growing and

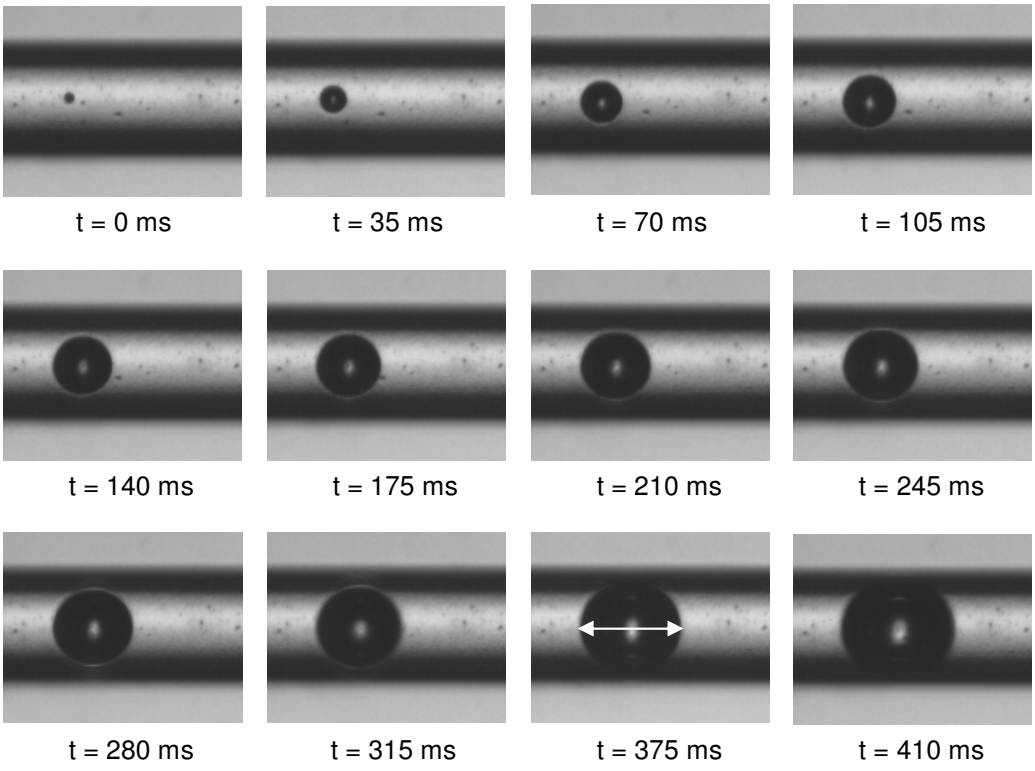

Figure 6.3 *Sequential images of bottom wall bubble growing (G = 153 kg/m^{2}s, q = 271 kW/m^2). Arrows show bubble diameter.*

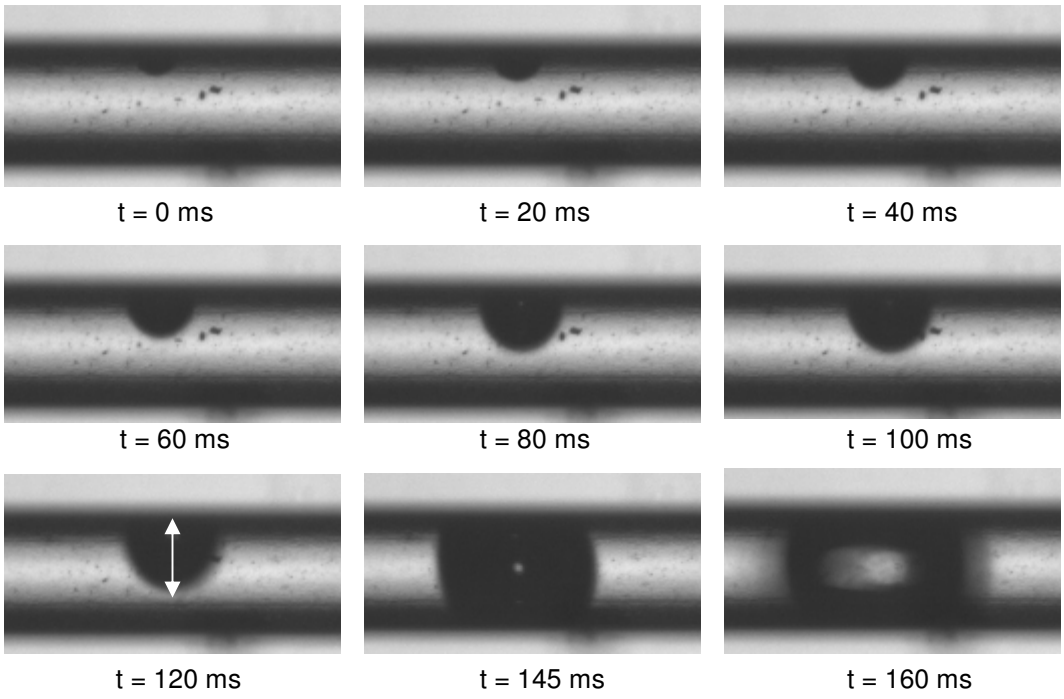

Figure 6.4 *Sequential images of sidewall bubble growing (G = 153 kg/m^{2}s, q = 271 kW/m^2). Arrows show height of bubble.*

Figure 6.4 of a sidewall bubble wall growing captured using the high-speed camera. The projected area of the bottom wall bubbles had a circular shape; hence the diameter of the projected circle was measured to determine the bottom wall bubbles growth. The projected area of the sidewall bubbles had a shape of truncated circle and the height of the bubble was measured to determine the sidewall bubble growth. The bubble growth was measured until the bubble reached the size of the channel width (150 μm). Further bubble growth was only in axial direction due to bubble confinement by the channel walls and it was mainly governed by the evaporation of the thin liquid film around the bubble.

The bubble growth varied between different bubbles in the six microchannels under consideration at the same conditions of heat and mass flux. Figure 6.5 illustrates non-uniform bubble growths observed at constant conditions of the heat and mass flux. The non-uniformity in the growth for the bubbles observed at different nucleation sites was due to differences in the local flow field. The flow instabilities with the reverse vapour slug flow caused the non-uniform fluid

distribution among the channels leading to differences in the local flow field in different channels. A considerable variation in the growth was found for the higher heat flux. The latter was due to intensification in the flow instabilities at higher heat flux leading to high non-uniformity in the flow distribution among the channels.

Figure 6.6 shows the effect of heat flux on (a) the bottom wall bubble growth and (b) the sidewall bubble growth for a mass flux of 153 kg/m^{2}s in subcooled flow boiling condition. The effect of heat flux on the bubble growth in saturated boiling is shown in Figure 6.7 for (a) the bottom wall bubbles and (b) the sidewall

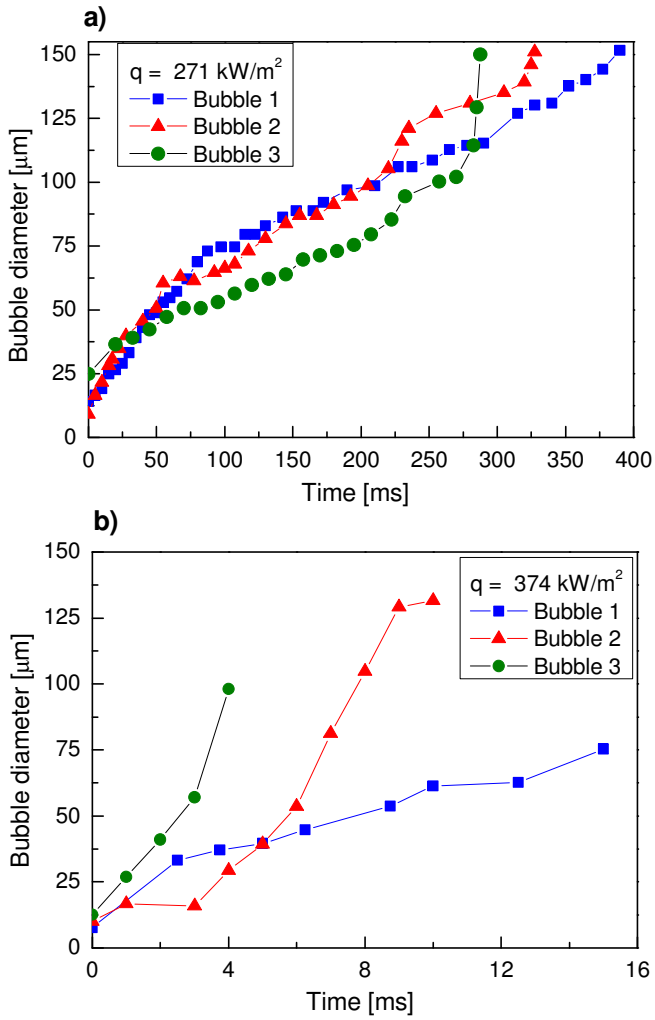

Figure 6.5 *Non-uniform bubble growths for 3 different bubbles for a mass flux of 153 kg/m^{2}s and a heat flux of (a) 271 kW/m^2 and (b) 374 kW/m^2.*

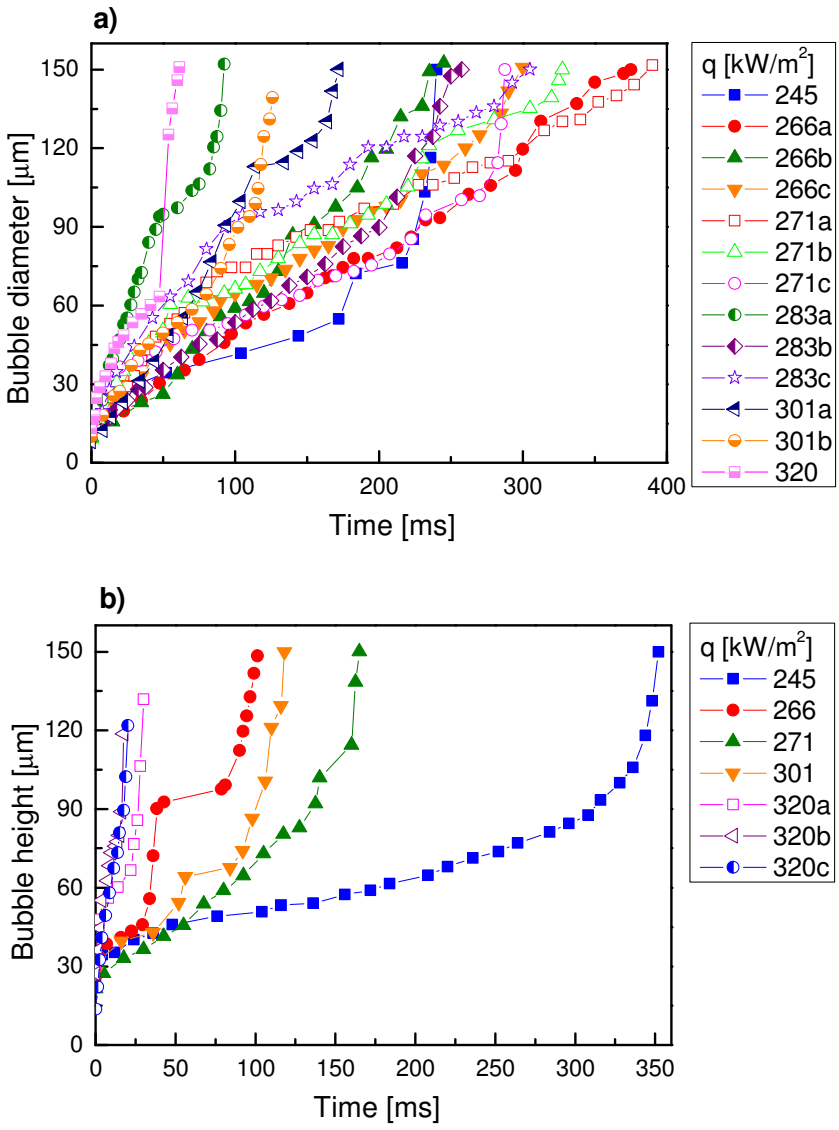

Figure 6.6 *Effect of heat flux on bubble growth in subcooled flow boiling, G = 153 kg/m^{2}s. (a) Bottom wall bubbles growth and (b) side wall bubbles growth.*

bubbles. The bubble growths for other mass fluxes used in the experiments are given in appendix D. Equations 6.7 and 6.8 were used to determine whether flow boiling for a given heat flux was in subcooled or saturated region. In general, the bubble growth rates increased and the growth periods reduced significantly with increasing heat flux.

Figure 6.8 shows the effect of mass flux on the bubble growth for two wall temperatures. For a wall temperature of 100.4 ˚C, as the mass flux increased, the

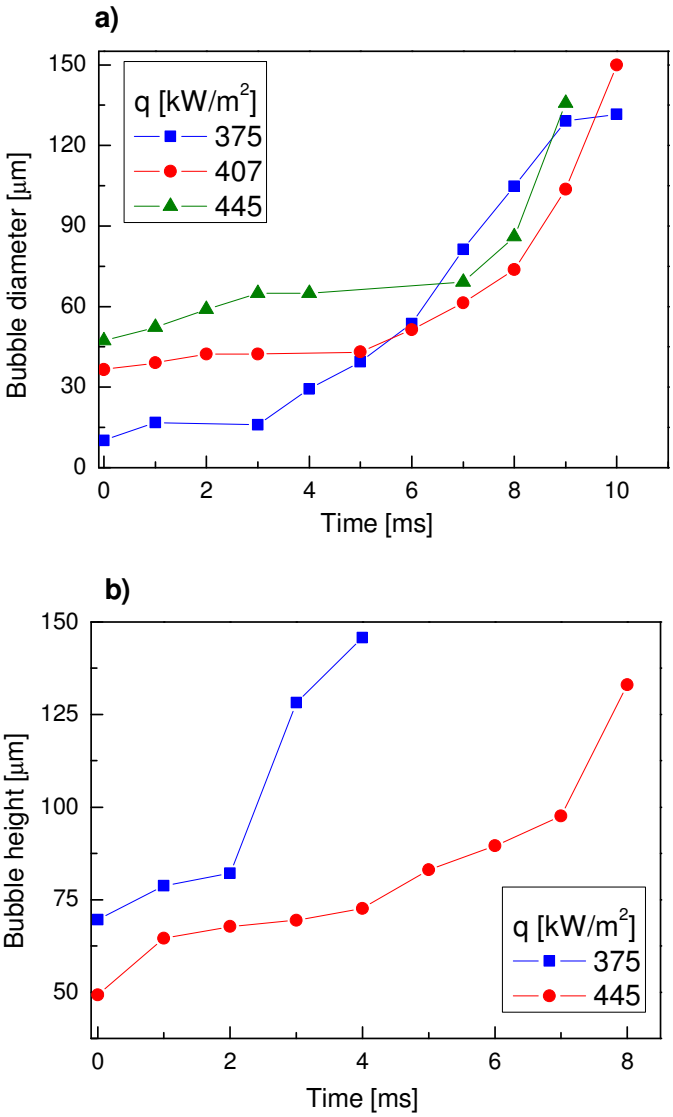

Figure 6.7 *Effect of heat flux on bubble growth in saturated flow boiling, G = 153 kg/m^{2}s. (a) Bottom wall bubbles growth and (b) side wall bubbles growth.*

bubble grew faster and the growth period was shorter. The same effect of flow on bubble growth in subcooled flow boiling of water was reported by Kandlikar et al. [3]. An increase in the single-phase heat transfer coefficient associated with increasing flow velocity caused the bubble to grow much faster in subcooled flow boiling [5]. The growth rates increased significantly and the bubbles growth period was considerably shorter with an increase in the wall temperature for both mass fluxes presented in Figure 6.8b. The effect of flow rate on the bubble growth diminished as compared to lower wall temperature.

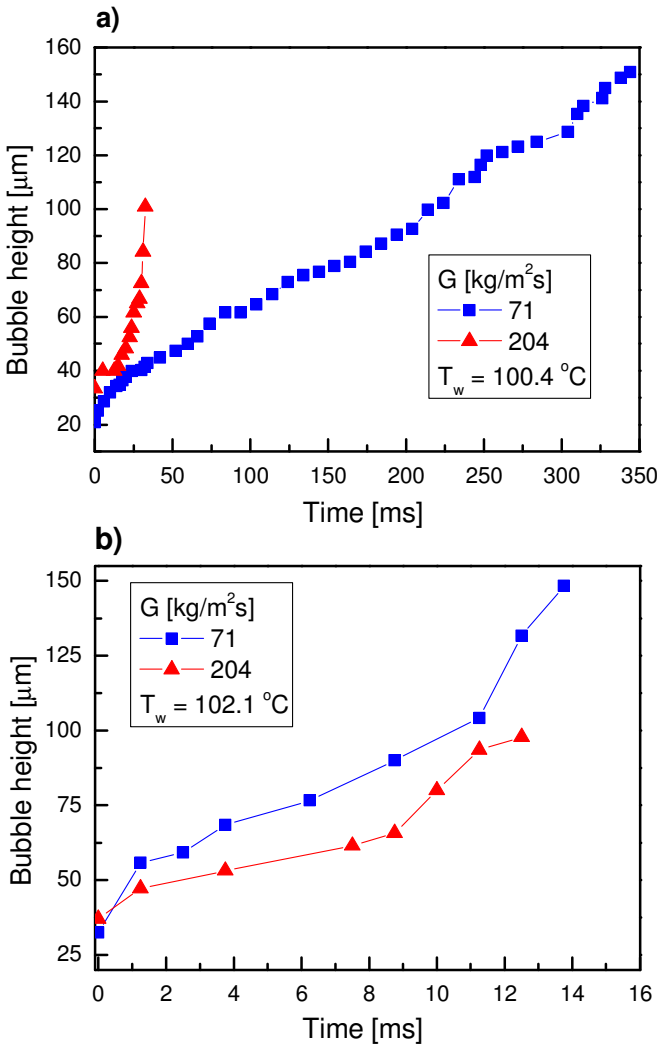

Figure 6.8 *Effect of mass flux on bubble growth for (a) T_w = 100.4 ˚C and (b) T_w = 102.1 ˚C.*

The bubble growth data were normalised in order to generalize a trend in the bubbles growth for all investigated heat fluxes. Normalised time was determined with respect to the time elapsed before the bubble reached the channel width for each of the heat fluxes. For bubbles which exploded before they reached the size of the channel width, normalised time was determined with respect to the bubble growth period. The growth period is defined as the time elapsed from the bubble nucleation until bubble explosion.

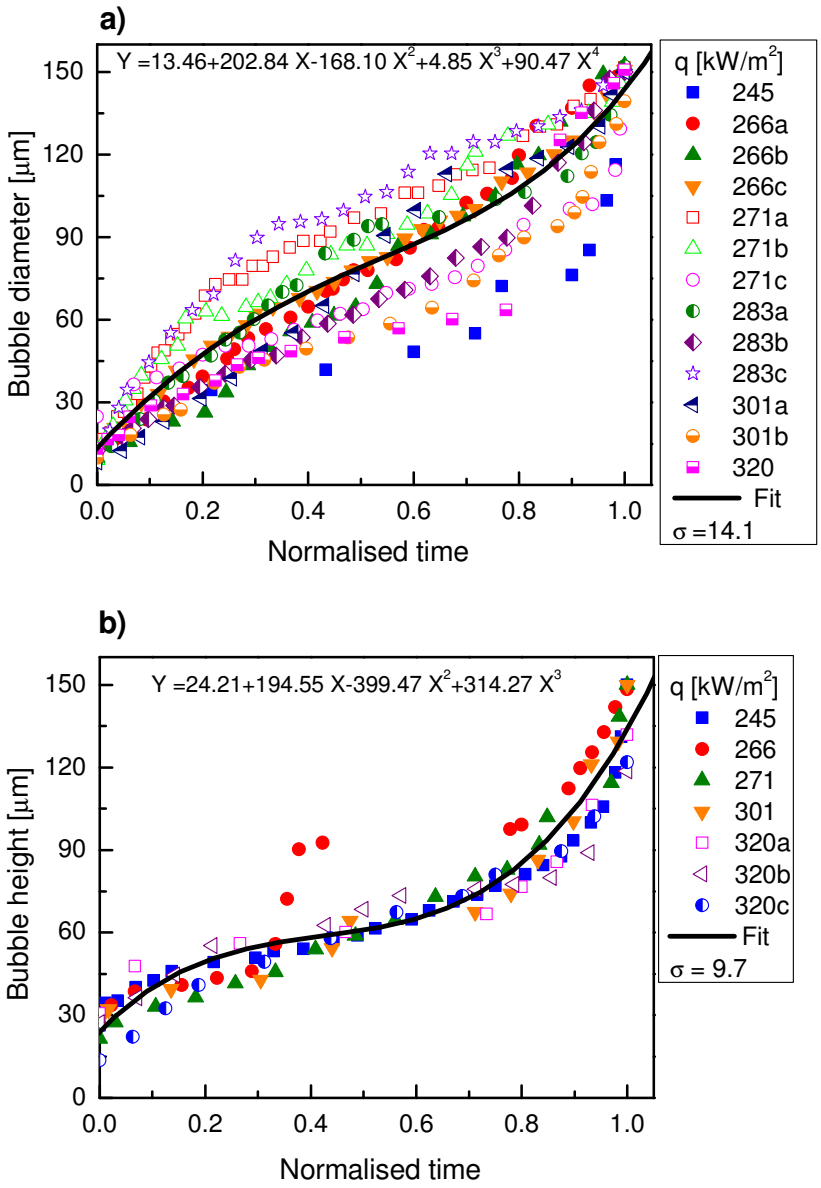

Figure 6.9 *(a) Bottom wall bubbles normalised growth curves and (b) side wall bubbles normalised growth curves in subcooled flow boiling for G = 153 kg/m²s and different heat fluxes.*

Figure 6.9 shows the effect of heat flux on bubble growth in subcooled flow boiling with respect to normalised time for G = 153 kg/m²s. The normalised bubble growth curves for other mass fluxes used in the experiments are given in appendix E. A polynomial fit was applied to obtain the best fit to a series of data points for bubble growth curves at each of the mass fluxes investigated. The results of the fitting showed three stages for the bubble growth in subcooled flow boiling. The first stage

is rapid bubble growth when the small bubble is surrounded by a highly superheated liquid layer. The linear trend of the first stage indicates that inertia forces were dominant. This stage was followed by the stagnation in bubble growth when it came in contact with the liquid with a lower superheat. The rate of evaporation on the bubble contact surface slowed down as the heat transfer was controlled by thermal diffusion through the liquid with a lower superheat. In the third stage the bubble interface comes closer to channel walls due to bubble growth in the confined space of microchannel. A highly superheated liquid layer near the wall enhances the evaporation, increasing bubble growth rate. Although the first two stages are similar to the bubble growth observed in pool boiling or flow boiling in macroscale tubes, the third stage is quite unique to bubble growth in microchannels.

Figure 6.10 shows the effect of heat flux on bubble growth in saturated flow boiling with respect to normalised time for G = 153 kg/m^{2}s. The best fit curve shows an exponential growth of the bubble in saturated flow boiling. It should be noted that bubbles reached up to 47 % of their final diameter/height after nucleation in the first frame captured using the high-speed camera with a time resolution of 1 ms. This suggests that the first stage with a rapid bubble growth may be present in saturated boiling similar to the bubble growth in subcooled boiling. However, it was not possible to capture bubble growth in this stage using the high-speed camera with a maximum frame rate of 1000 fps. The bubble growth period was less than 10 ms as opposed to more than 350 ms in subcooled flow boiling.

An acceleration in the bubble growth as it comes closer to the channel side walls was observed in saturated flow boiling as well. This implies that the superheated liquid layer near channel walls plays a significant role in bubble growth in subcooled and saturated flow boiling in microchannels.

6.4.2 Bubble growth period and departure size

Figure 6.11 presents the effect of heat flux on bubble growth period for a range of mass fluxes. The growth period is defined as the time elapsed from bubble nucleation until bubble explosion. The bubble growth period varied between the

bubbles observed at different nucleation sites at the same conditions of heat and mass flux. For this reason bubbles with the longest growth period were presented in Figure 6.11 for each data point. As the heat flux increased, the bubble growth period shortened for both the bottom wall and the sidewall bubbles. The longest growth periods were found for the sidewall bubbles in subcooled flow boiling. This suggests

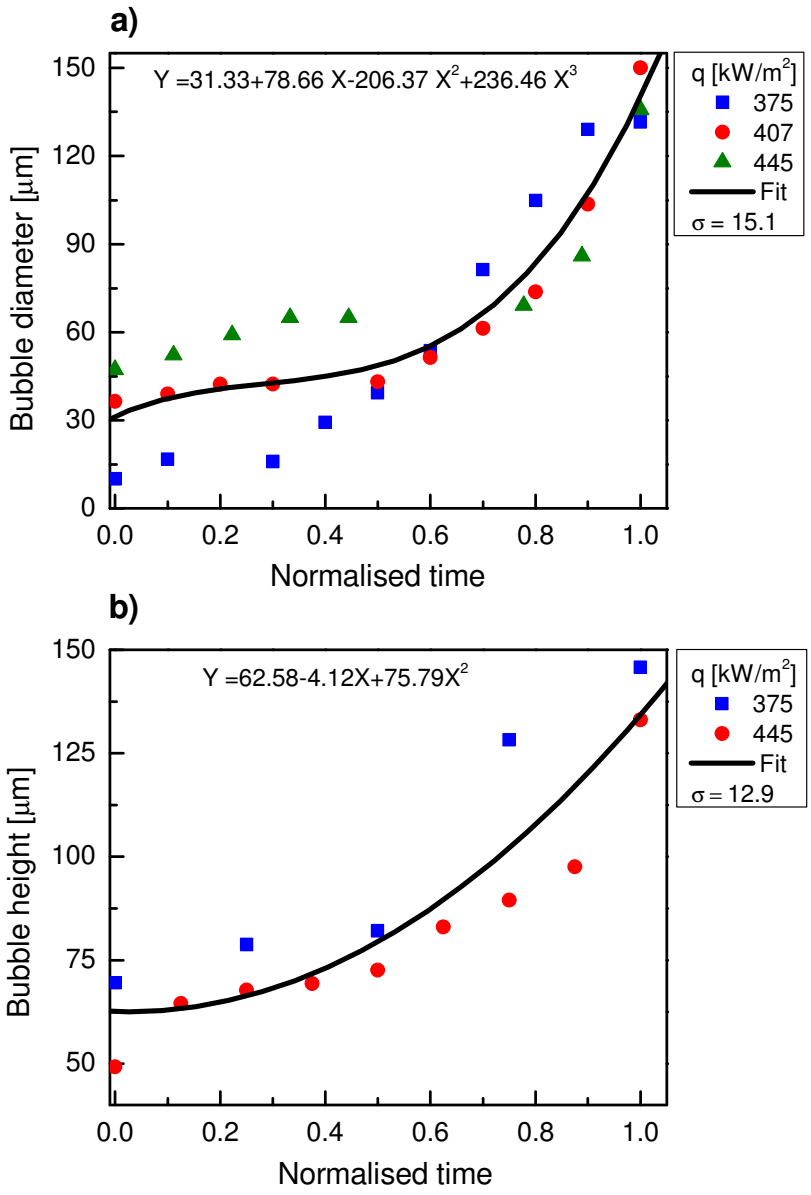

Figure 6.10 *(a) Bottom wall bubbles normalised growth curves and (b) side wall bubbles normalised growth curves in saturated flow boiling for G = 153 kg/m²s and different heat fluxes.*

that a lower superheat of the sidewall may be a reason for longer growth period as compared to bottom wall bubbles. However, this trend was observed only at the lowest heat flux for each of the mass fluxes investigated.

High bubble growth rate associated with saturated flow boiling and high heat fluxes is not the only reason for shorter bubble growth periods as compared to the bubble growth periods in subcooled flow boiling and lower heat fluxes. The

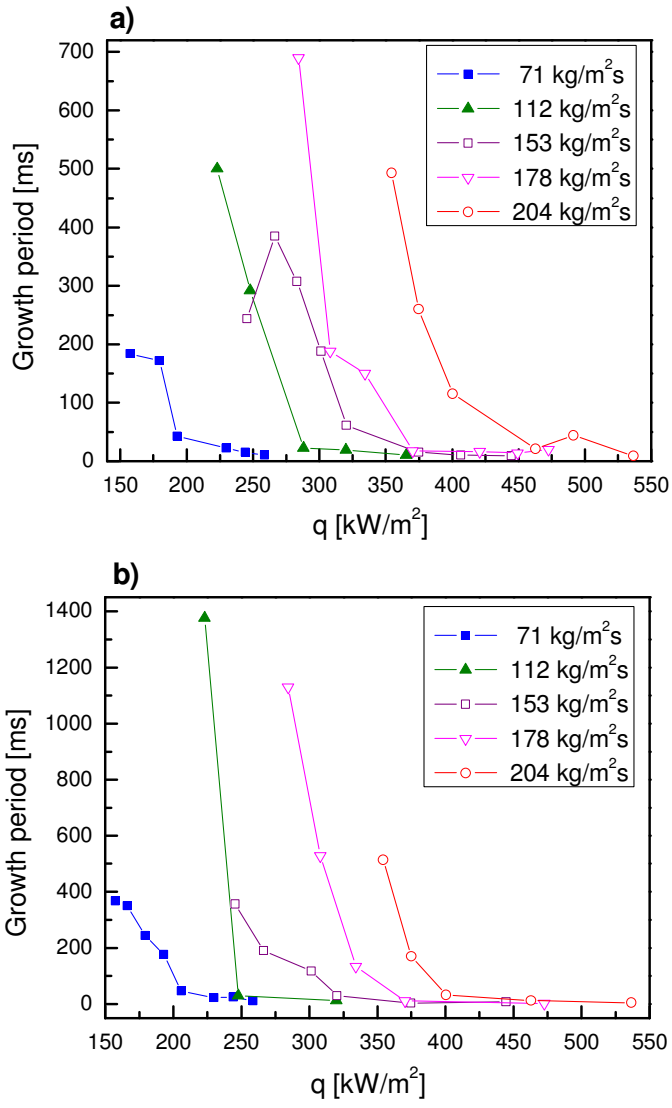

Figure 6.11 *The effect of heat flux on bubble growth period for (a) bottom wall bubbles and (b) side wall bubbles at different mass fluxes.*

bubble growth is strongly influenced by interactions between bubbles growing in the same channels, as well as the excessive flow from other channels due to flow instabilities. Figure 6.12 shows how reverse vapour flow after bubble explosion caused the other two bubbles in the channel to explode before they reached the size of channel width. An increase in heat flux leads to the intensification in bubble nucleation and flow instabilities with the reverse vapour flow, resulting in a significantly shorter growth period for saturated flow boiling as compared to

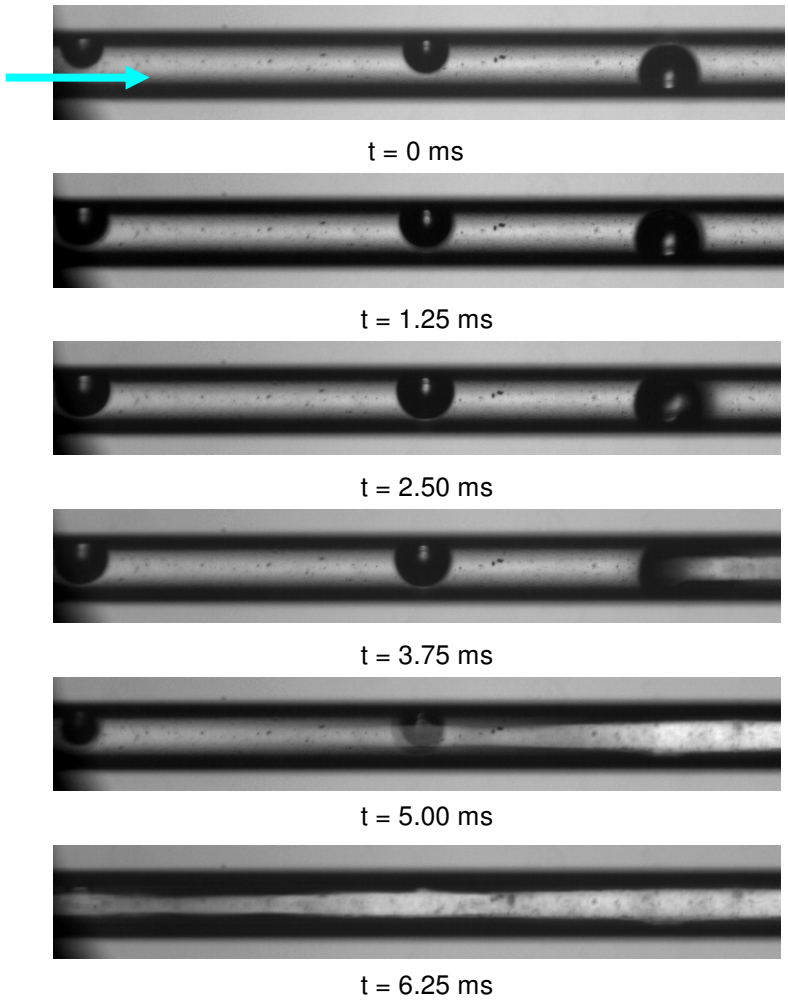

Figure 6.12 *Image sequences showing the effect of bubble explosion on growth period of the other bubbles, G = 71 kg/m^{2}s, q = 259 kW/m^2. Arrow shows direction of bulk flow.*

subcooled flow boiling. Bubbles in saturated flow boiling usually exploded before reaching the size of the channel width (150 µm).

Most of the bubbles observed at lower mass fluxes of 71 and 112 kg/m^{2}s grew and exploded while remaining attached to the heated wall. The dominant forces determining the bubble detachment from the nucleation site in a microchannel are the surface tension and the drag force. The surface tension tends to retain the bubble to the wall, while the drag force tends to detach the bubble from the wall. The number of bubbles departed from the nucleation site increased with an increase in the mass flux, as the drag force acting on the bubble interface increased. Figure 6.13a shows departure of the bottom wall bubble. The bubble appears to be distorted in the stream wise direction due to the drag force acting on the bubble interface. After departure the bubble was swept downstream by the bulk flow. It was observed that flow instabilities with reverse vapour flow can be a reason for bubble detachment as well, moving the bubble towards the upstream direction as shown in Figure 6.13b.

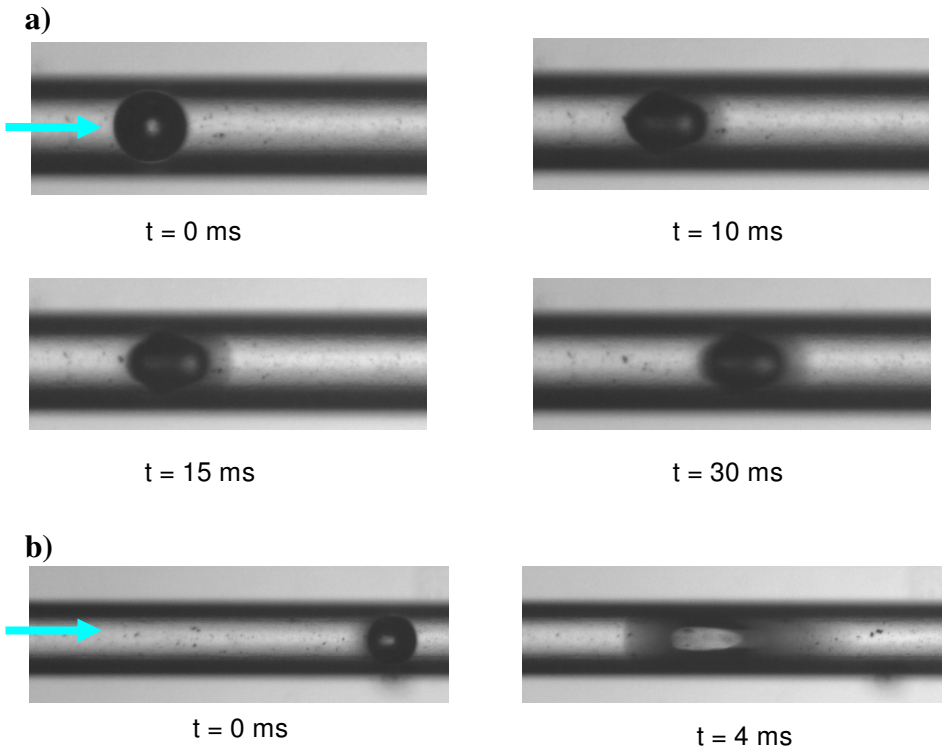

Figure 6.13 *(a) Bubble departure with downstream move, G = 153 kg/m^{2}s, q = 266 kW/m^2 and (b) bubble departure with upstream move, G = 153 kg/m^{2}s, q = 245 kW/m^2. Arrow shows direction of bulk flow.*

However, most of the bubbles detached from the wall were moved in the downstream direction.

Figure 6.14 shows the effect of heat flux on the departure bubble size for (a) bottom wall bubbles and (b) sidewall bubbles for different mass fluxes investigated in this study. In general, the bubble departure size decreased with an increase in heat flux. The departure bubble size is also influenced by the mass flux. The effect of mass flux on the departure bubble size is shown in Figure 6.15. In general, the

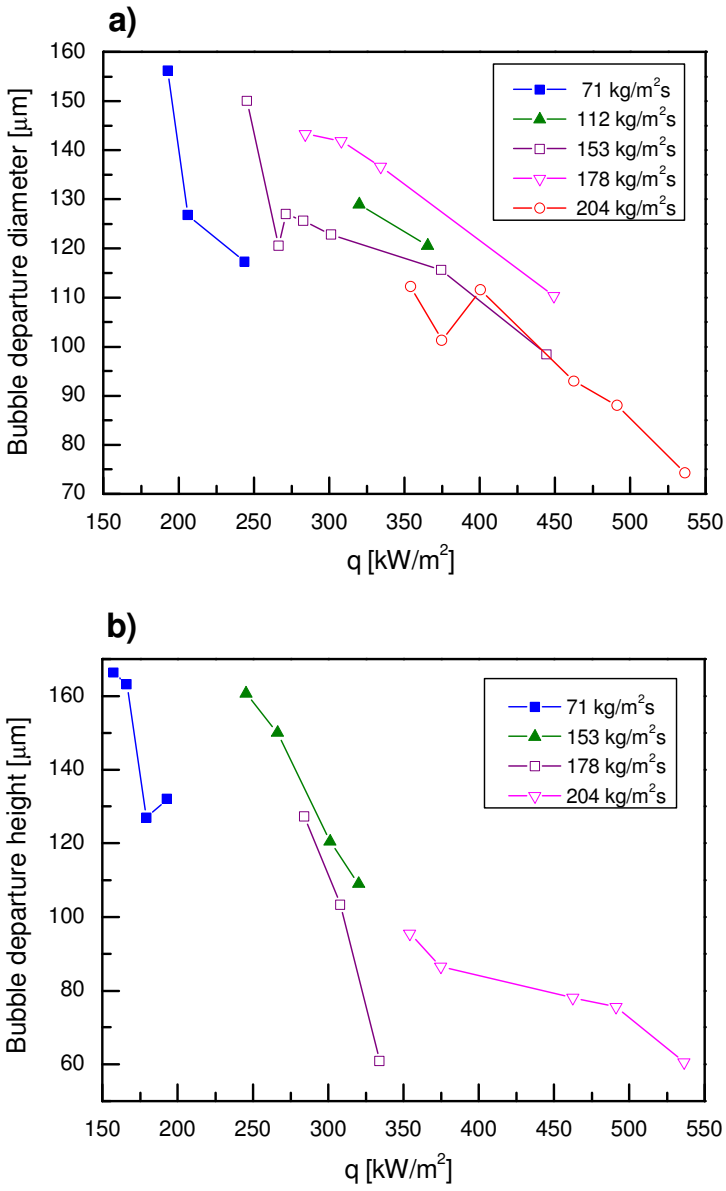

Figrue 6.14 *The effect of heat flux on (a) bottom wall departure diameter and (b) sidewall departure height.*

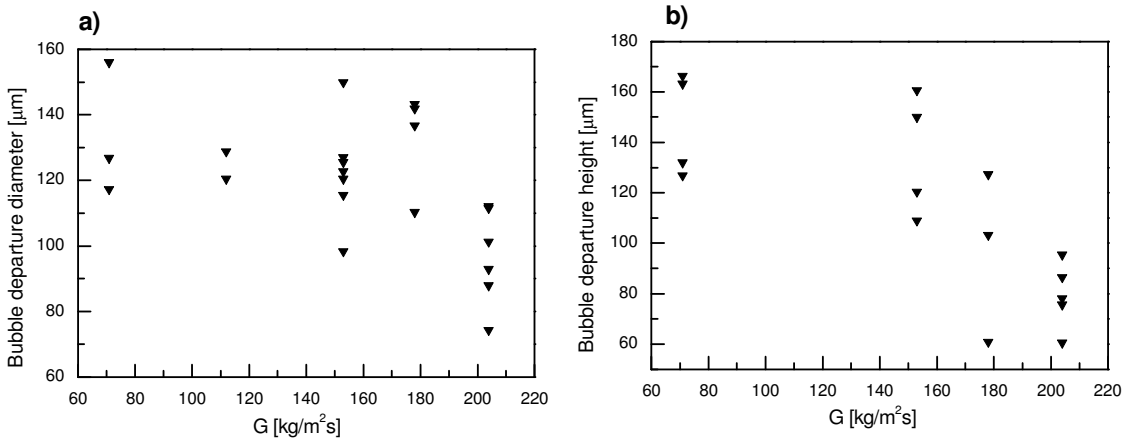

Figure 6.15 *The effect of mass flux on (a) bottom wall bubble departure diameter and (b) sidewall bubble departure height.*

departure bubble size decreased with increasing mass flux. An increase in the drag forces associated with increased mass flux caused the bubbles to depart at smaller diameters/heights.

When a bubble grows to the size of the microchannel, it will continue to grow in the axial direction forming a slug flow. It was observed that a confined bubble grew rapidly in both upstream and downstream directions as shown in Figure 6.16. The growth of the bubble length is mainly controlled by the evaporation of a thin liquid film around the bubble and pressure field around the bubble. While the evaporation of the thin liquid film has the promoting effect on the bubble growth, the pressure field around the bubble may limit the bubble growth. Figure 6.17 presents the growth of the bubble length ratio in time for different mass and heat fluxes. The bubble length ratio was determined as the ratio between the bubble axial length and the channel width (150 μm). There is no consistent trend in the bubble length ratio growth. For some cases the bubble length ratio grows in an exponential manner, while for another bubbles there is significant deviation from the exponential growth. Li et al. [6] reported a consistent exponential trend in the growth of bubble length in their investigation of bubble dynamics in two parallel microchannels. The authors concluded that the bubble length grows exponentially if the evaporation effect was dominant over pressure effect. The non-exponential growth of bubble length ratio indicates that the pressure field around the bubble had a significant influence on the bubble growth in slug flow with a diminishing effect on the evaporation of the thin

liquid film around the bubble. The reason for a higher pressure field effect on the bubble length growth observed in this study may be due to intensive flow boiling instabilities. The reverse vapour flow inside the channels with the bubble growing and excessive flows from other channels might cause a higher pressure field around the bubble that limited the bubble length growth in axial direction.

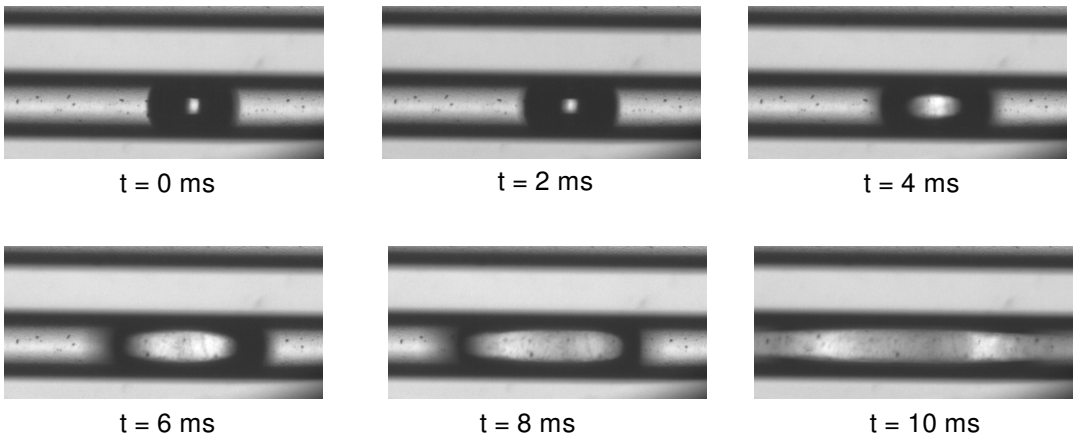

Figure 6.16 *The bubble growth in the axial direction, G = 71 kg/m^{2}s, q = 157 kW/m^2.*

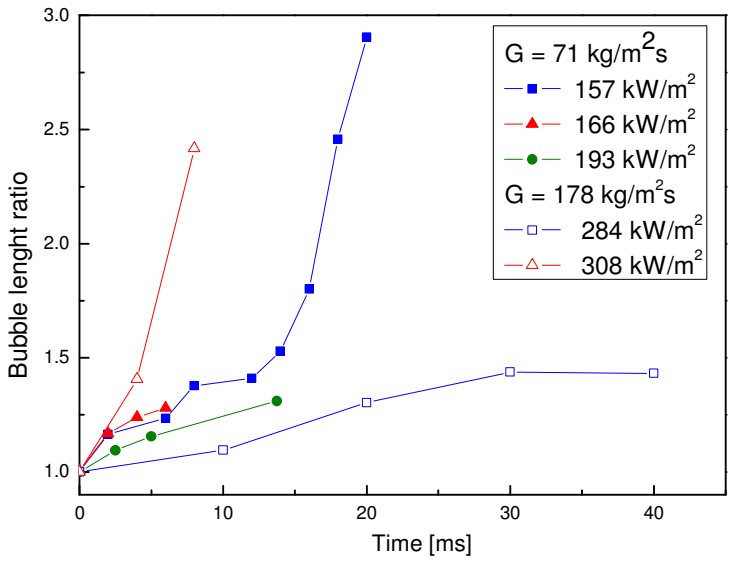

Figure 6.17 *Growth of the bubble length ratio in time.*

6.4.3 The effect of the bubble dynamics on the flow instabilities

A detailed description of the flow boiling instabilities encountered in the present experimental heat sink with microchannels is given in chapter 5. It was pointed out that appreciable fluctuations in pressure and temperature were caused by alternation between liquid, two-phase and vapour flow. In this chapter the effect of the bubble dynamics on the flow instabilities has been investigated. It was found that frequencies and amplitudes of the pressure and temperature fluctuations were related to the bubble size and growth period. The high amplitude/low frequency oscillations existed when the bubbles with long growth period were dominant, while the low amplitude/high frequency instabilities were associated with bubbles with short growth period. After the bubble reached the size of the microchannel, it continued growing in axial direction forming a bubble slug as shown in Figure 6.16. The bubble expansion in both downstream and upstream directions with subsequent condensation of the bubble vapour by the incoming subcooled liquid resulted in large amplitude fluctuation in temperature and pressure. As the bubble growth period decreased, the bubble usually exploded before reaching the size of the microchannel. A decrease in the bubble growth period resulted in a shorter period for one cycle of alternation between liquid, two-phase and vapour flow. Therefore, the bubble dynamics determined the frequency of alternation between phases, and consequently the frequency of the pressure and temperature oscillations.

Figure 6.18a shows the effect of heat flux on the frequency of alternation between liquid, two-phase and vapour flow in a microchannel located above the sensor T3. Frequency is the reciprocal of the period for one cycle of liquid, two-phase and vapour flow alternations. The average period of one cycle was calculated from the film taken using the high-speed camera as the ratio between the time and the number of successive liquid refills of the microchannel in that time. Figure 6.18b shows the effect of heat flux on the dominant frequency of temperature fluctuations measured by sensor T3 located beneath the observed channel. The dominant frequencies were identified by the magnitude of the amplitude of the

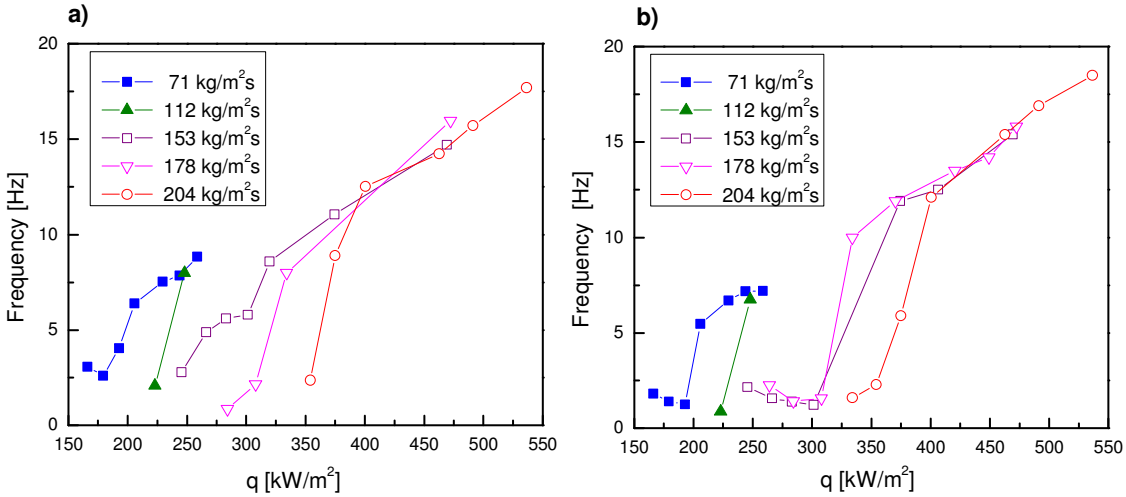

Figure 6.18 *The effect of heat flux on (a) frequency of phase alternations and (b) dominant frequency of temperature fluctuations.*

temperature signal presented in the frequency domain. In general, both the frequency of alternation between phases and the frequency of temperature fluctuations increased with increasing heat flux, except for low heat fluxes when the frequency of temperature had a decreasing trend. The same trend of decreasing frequency has been observed for the pressure drop fluctuations during the high amplitude/low frequency instabilities as it was reported in chapter 5. The effect of mass flux can be seen in Figure 6.18 as well. In general, an increase in mass flux resulted in higher frequencies, and the highest frequencies were found for the highest mass flux investigated.

Figure 6.19 shows a comparison between the frequencies of phase alternations and the dominant frequency of temperature fluctuations for the same conditions of the mass and heat flux. The largest deviation between two frequencies was found for smaller frequency values. It should be noted that the frequency of phase alternations represents fluctuations in only one observed microchannel located above the sensor T3, while the temperature frequency represents fluctuations in more microchannels. An increase in the frequency with increasing heat flux as shown in Figure 6.18 and a decrease in the bubble growth periods with increasing heat flux as shown in Figure 6.11 imply that shorter bubble growth period resulted in a higher frequency of

fluctuations during the flow boiling instabilities in microchannels. Bubbles with long growth period and slow growth rate resulted in a long two-phase period during the phase alternations, therefore lower frequency of fluctuations with high amplitudes in pressure and temperature.

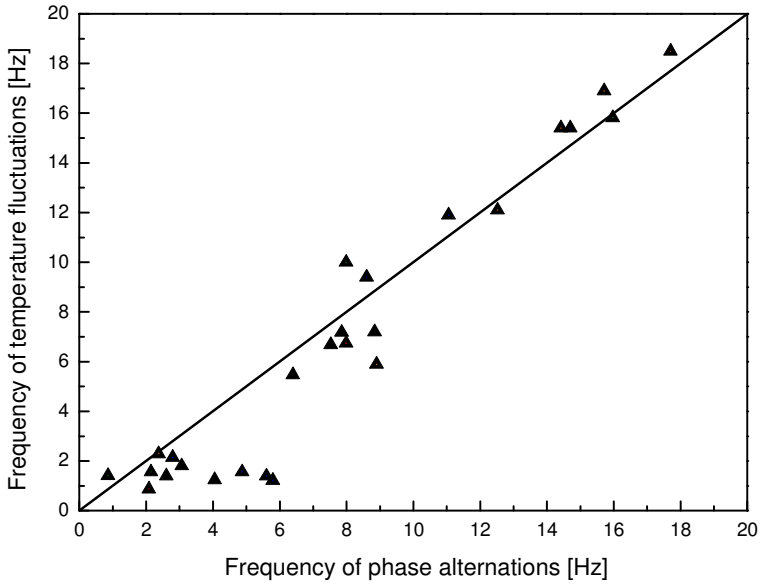

Figure 6.19 *Comparison between frequency of temperature fluctuations and frequency of phase alternations, line has a slope of 1.*

6.4.4 The effect of the bubble dynamics on the local heat transfer coefficient

The local heat transfer coefficients were calculated at locations of integrated temperature sensors T1, T3 and T5. Figure 6.20 shows the time averaged local heat transfer coefficient as a function of exit vapour quality at the axial location of (a) sensor T1, (b) sensor T3 and (c) sensor T5. The experiments were carried out for the exit vapour qualities less than 0.11. The non-uniform flow distribution among the channels for higher exit vapour qualities caused a local "dryout" in some parts of the microchannel assembly with possible damaging consequences for the heat sink.

The cooling water entered the microchannels under subcooled conditions and the wall temperature T1 at the microchannels inlet was below saturation temperature.

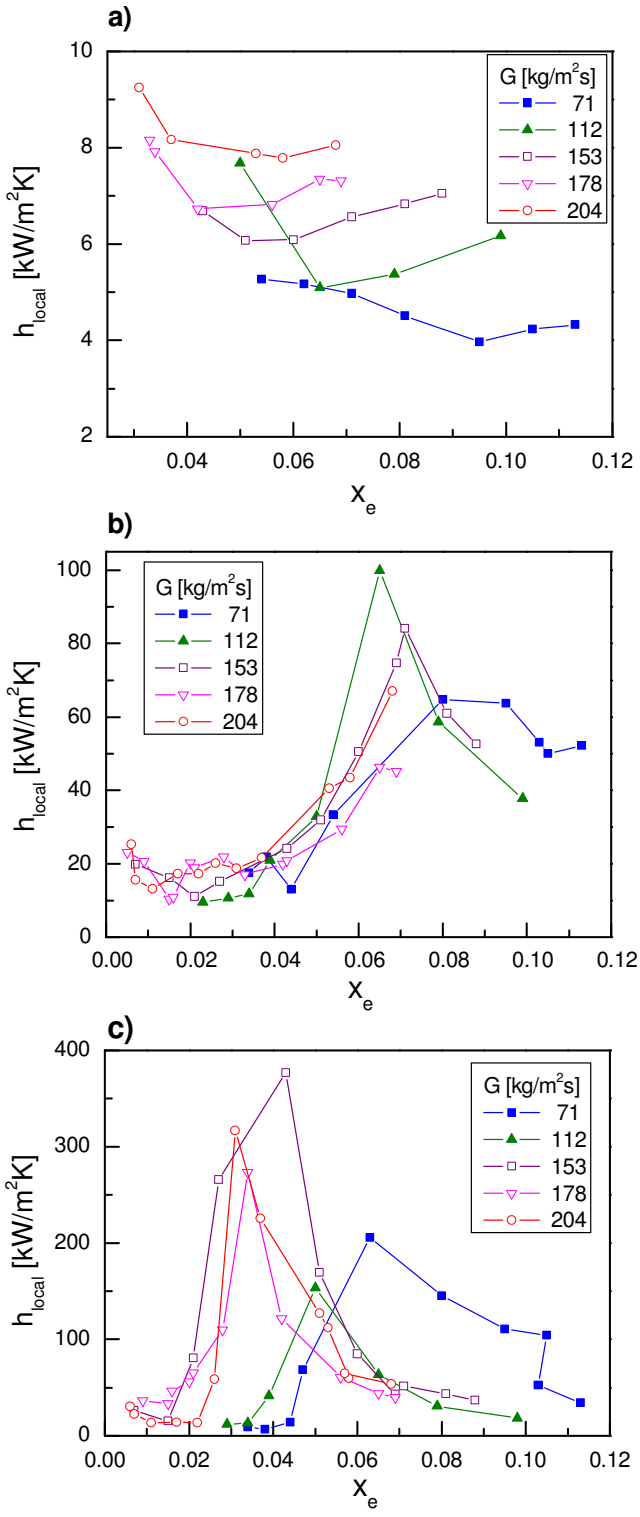

Figure 6.20 *Local heat transfer coefficient versus exit vapour quality at location of (a) temperature sensor T1, (b) temperature sensor T3, and (c) temperature sensor T5.*

The heat transfer coefficients showed in Figure 6.20a are fairly constant as compared to the other two local heat transfer coefficients at locations of T3 and T5 sensors. This implies that the single-phase heat transfer was the dominant mode of heat transfer at the location of sensor T1. Fluctuations in temperature T1 were driven by flow instabilities originating from boiling in downstream locations.

As indicated in Figures 6.20a and 6.20b, the heat transfer coefficient at location of sensors T3 and T5 increased with local vapour quality and then decreased at higher vapour quality. The local heat transfer coefficients at the location of T5 sensor reached the maximum value for lower exit vapour quality as compared to the local heat transfer coefficient at the location of sensor T3. The latter is due to the fact that saturated flow boiling at channels exit (sensor T5) occurred at lower exit vapour quality as compared to saturated flow boiling in the middle of channels assembly (sensor T3). The trend of increasing heat transfer coefficient with increasing vapour quality and then decreasing at higher vapour quality was similar to that reported by Chen and Garimella [7]. However this trend was different to those reported by Hetsroni et al. [8], Qu and Mudawar [9], as well as Wang et al. [10] who found that the heat transfer coefficient decreased with increasing vapour quality.

At low heat fluxes the bubble growth was slow with some bubbles growing to the size of the microchannel and forming vapour slugs. Figure 6.21 shows a vapour slug formed in the microchannel as a result of the coalescence of two bubbles. The vapour slug expanded both in upstream and downstream direction as a result of the evaporation of the liquid film around the bubble. An extensive evaporation turned the vapour slug flow into a vapour flow as shown in Figure 6.21 for t = 115 ms. The vapour flow was condensed by the incoming subcooled water. High speed camera imaging showed that both nucleation density and bubble growth rate were increased with increasing heat flux. A frequent bubbles interactions and coalescences were observed. This resulted in the liquid phase period being shorter during one cycle of phase alternation while the transient annular flow being the dominant flow pattern in microchannels.

Figure 6.22 presents the effect of exit vapour quality on the bubble growth period and trend is the same as that found for the effect of heat flux on the bubble

growth period. It is worth noting that for all mass fluxes investigated, local heat transfer coefficient at location of sensor T3 reached the maximum when the growth period of bubbles were shorter than 50 ms. This confirms that an increase in the bubble growth rate and decrease in the bubble growth period resulted in a higher heat transfer coefficients with the evaporation of the thin liquid film being the dominant heat transfer mechanism. Figure 6.23 shows a time evolution of the bubble with a short growth period and subsequent transient annular flow and "dryout" period captured using the high speed camera at 1000 fps. The bubble grew rapidly and before it reached the size of the microchannel it exploded at t = 10 ms. The bubble explosion was the result of vapour flow coming from the upstream direction as another bubble exploded in the same channel. After the bubble explosion the transient annular flow was formed at t = 11 ms in the observed channel. As the liquid film completely evaporated the temporary "dryout" period occurred at t = 52 ms with the successive channel refill at t = 60 ms. The liquid phase lasted for a short period turning into transient annular flow again. The transient annular flow was prevailing during the alternation between liquid, two-phase and vapour phase with the evaporation of the thin liquid film being a dominant mode of the heat transfer.

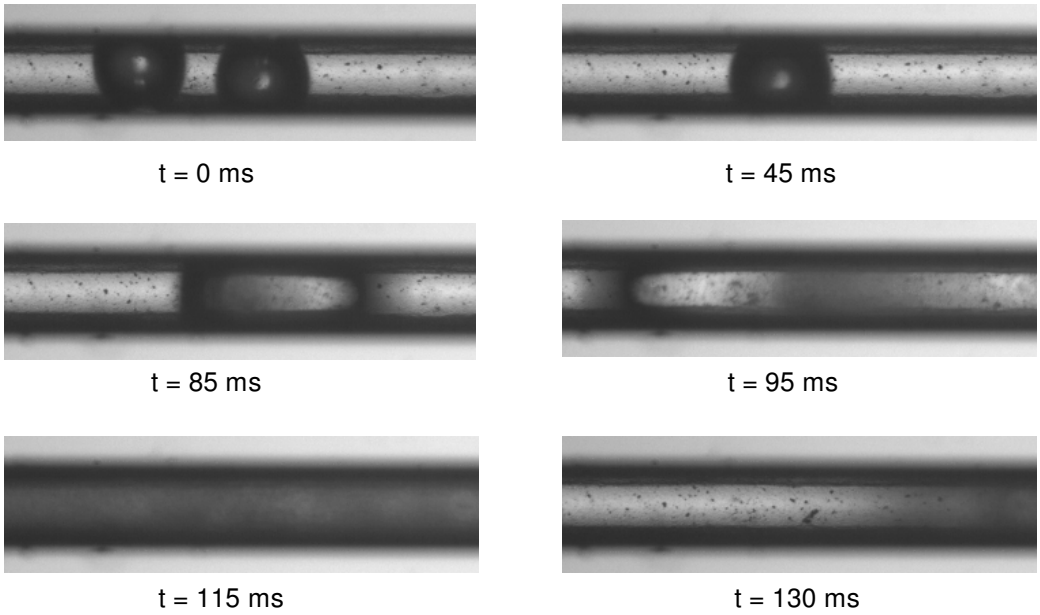

Figure 6.21 *Bubbles coalescence and vapour slug expansion, G = 153 kg/m^{2}s, q = 245 kW/m^2.*

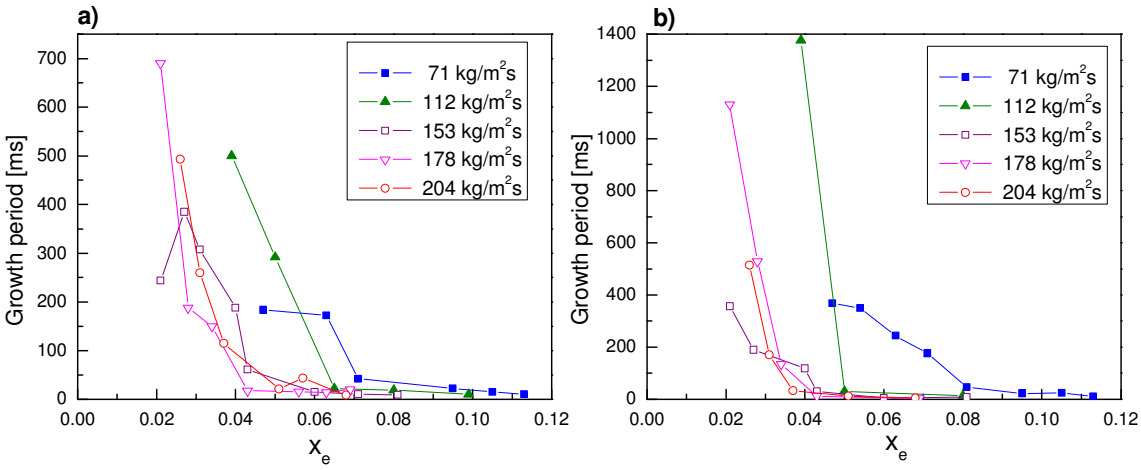

Figure 6.22 *The effect of exit vapour quality on bubble growth period for (a) bottom wall bubbles and (b) side wall bubbles at different mass fluxes.*

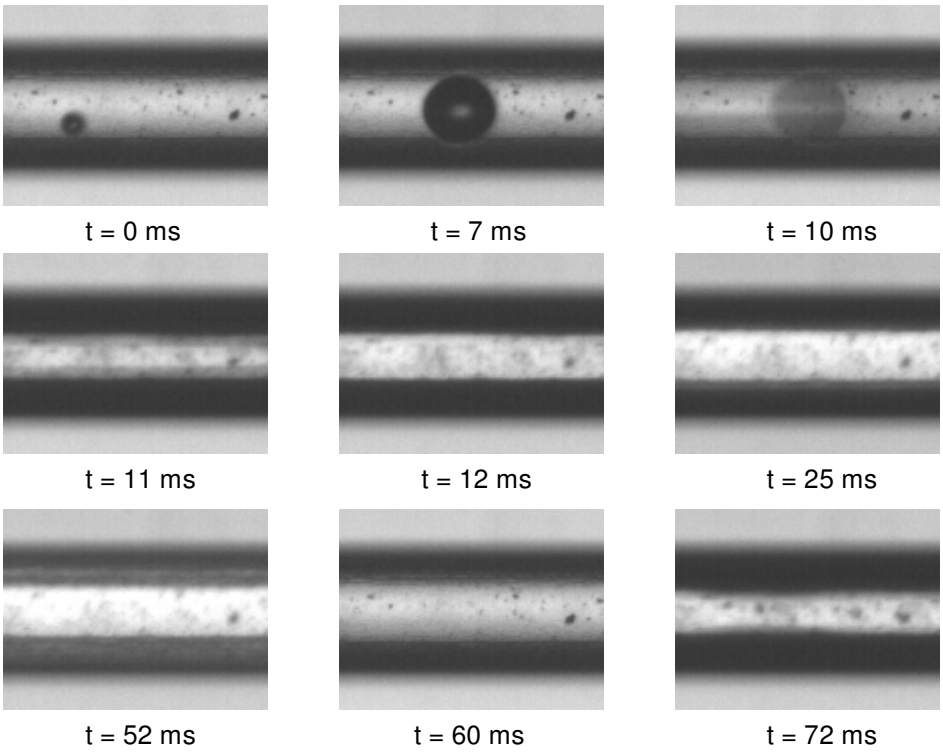

Figure 6.23 *Alternation between liquid, two-phase and vapour flow captured using high speed camera, G = 153 kg/m^{2}s, q = 469 kW/m^2.*

Further increase in exit vapour quality caused an increase in vapour phase period (temporary "dryout" period) during one cycle of phase alternation resulting in decreasing heat transfer coefficient.

Qu and Mudawar [11] and Jacobi and Thome [12] suggested the evaporation of a thin liquid film is the dominant heat transfer mechanism in flow boiling in microchannels. Hetsroni et al. [8] defined the "initial liquid film thickness" as the average thickness of liquid, evenly distributed during a period between successive events, τ, over the surface of a circular channel with a hydraulic diameter of the triangular channels used in their experiments. The authors assumed that during this period the liquid film entirely evaporated removing the heat from the wall surface required for the liquid film evaporation. Adopting this assumption, the average liquid thickness, δ, can be calculated from an energy balance applied to rectangular microchannels used in this study as follows:

$$2(D_{ch}+W_{ch})\delta\, L\rho_l = \frac{2(D_{ch}+W_{ch})Lq\tau}{h_{\mathrm{lg}}}. \tag{6.11}$$

Rearranging the above equation, the average liquid thickness can be calculated as:

$$\delta = \frac{q\tau}{\rho_l h_{\mathrm{lg}}} \tag{6.12}$$

The average period between successive events, τ, was determined from the sequence recorded using the high-speed camera as the ratio between the time and the number of successive liquid refills of the microchannel in that time. Figure 6.24 shows the effect of heat flux on the average period between successive events during the alternation of liquid, two-phase and vapour flow.

The average liquid thickness as a function of heat flux is presented in Figure 6.25 for three different mass fluxes. The high values of liquid film thickness were found for low heat fluxes when single-phase liquid prevailed during alternations between liquid, two-phase and vapour flow. In this case, single-phase heat transfer dominated over the heat transfer due to evaporation of the thin liquid film. Apart from these high values at the low heat fluxes, the liquid thickness decreased with increasing heat flux in the range from 25 to 13 μm for three mass fluxes investigated. Qu and Mudawar [11] developed an annular flow model to predict the saturated flow boiling

heat transfer coefficients in microchannels based on the evaporation of the liquid film. The authors calculated the film thickness in the range from 10 to 20 µm for two heat fluxes of 630 and 1290 kW/m^2 and a mass flux of 255 kg/m^{2}s. Hetsroni et al. [8] reported a decrease of the liquid film thickness from 8 to 2 µm in the range of q = 120 – 270 kW/m^2 and G = 95 kg/m^{2}s.

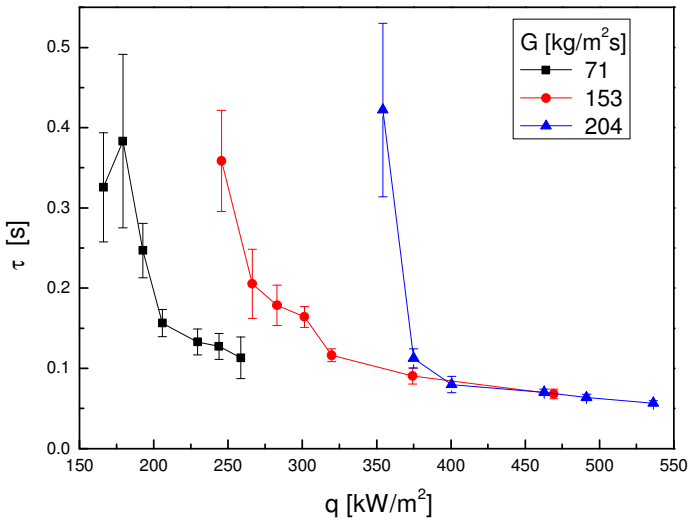

Figure 6.24 *The effect of heat flux on average period of successive events during the alternation of liquid, two-phase and vapour flow for different mass fluxes.*

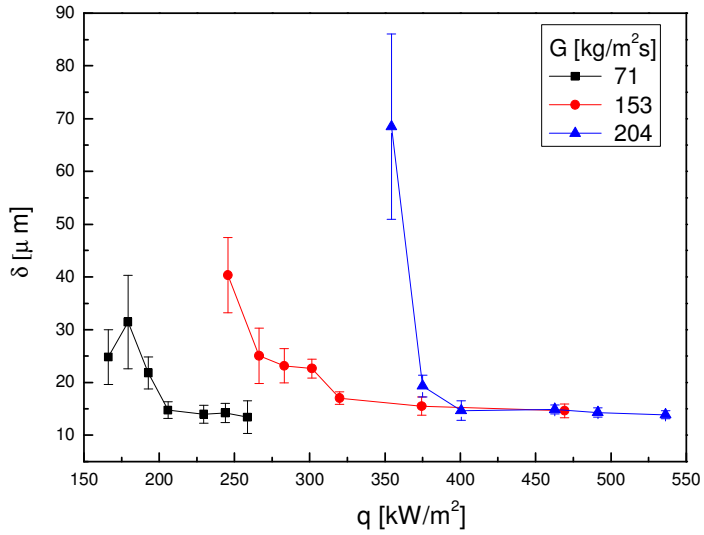

Figure 6.25 Variation of average liquid thickness with heat flux for different mass fluxes.

In order to generalise the trends for the variation of the average period and the liquid film thickness with heat and mass flux, dimensionless period, τ^*, and dimensionless liquid film thickness, δ^* were introduced, defined as follows:

$$\tau^* = \frac{\tau U}{D_h} \tag{6.13}$$

$$\delta^* = \frac{\delta U}{\nu} \ . \tag{6.14}$$

The results for the average period and the liquid thickness for the low heat fluxes were excluded from this analysis, as it was assumed that heat transfer mechanisms at low heat fluxes was a single-phase heat transfer dominantly.

Figure 6.26 shows the dimensionless average period as the function of the heat to mass flux ratio, q/G. The dimensionless average period decreased with an increase in the heat to mass flux ratio. An approximate expression for the dimensionless period as a function of the q/G ratio was obtained by the data fitting:

$$\tau^* = 399\left(\frac{q}{G}\right)^{-1.8} . \tag{6.15}$$

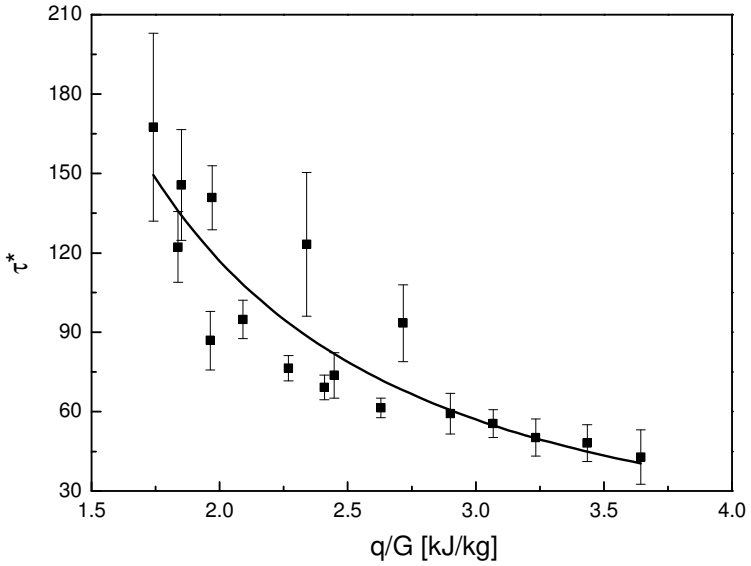

Figure 6.26 *Variation of dimensionless period between successive events with heat to mass flux ratio, line presents the best fit curve.*

Figure 6.27 presents the dependence of the dimensionless liquid thickness, δ^*, on the heat to mass flux ratio, q/G. The dimensionless liquid film thickness decreased with an increase in the heat to mass flux ratio. An approximate expression for the dimensionless liquid thickness as a function of the q/G ratio was derived by the data fitting and is given as follows:

$$\delta^* = 37\left(\frac{q}{G}\right)^{-1.7} . \tag{6.16}$$

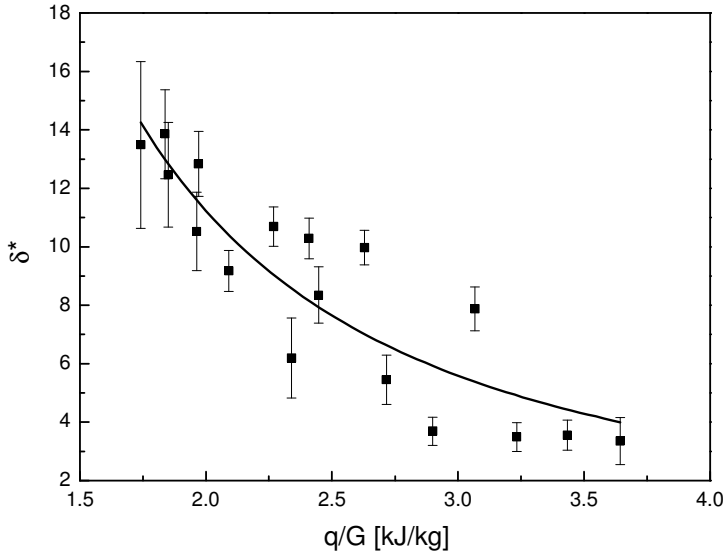

Figure 6.27 *Variation of dimensionless liquid film thickness with heat to mass flux ratio, line presents the best fit curve.*

The thickness of the thin liquid film determines the heat transfer coefficient and in general heat transfer coefficient should increase with liquid film thickness decreasing. However, the heat transfer coefficient is also determined by periodic behaviour of the flow patterns in microchannels. After the transient annular flow, as the liquid film evaporated, the temporary "dryout" period occurred resulting in an increase in the wall temperature. As the temporary "dryout" period increased with increasing vapour quality, the average heat flux decreased. Hetsroni et al. [13] reported the presence of a minimum initial film thickness during the "dryout" period. The minimum initial film thickness was assumed to be in the same order of

magnitude as the surface roughness. The authors reported a value of 3 μm for the minimum initial film thickness.

6.5 Conclusions

The bubble growth characteristics under subcooled and saturated flow boiling in parallel microchannels have been experimentally investigated. The effects of heat and mass flux on bubble growth, bubble growth period and departure diameter have been studied.

It was noted that bubble growth rates increased and the growth period reduced significantly with increasing heat flux. For a low wall temperature as the mass flux increased bubbles grew faster and the growth period was shorter. However, for a high wall temperature the effect of the mass flux on bubble growth diminished.

The bubble growth curves indicated three stages of the bubble growth in subcooled flow boiling. Although the first two stages are similar to the bubble growth observed in pool boiling or flow boiling in macroscale tubes, a third stage is quite unique for bubble growth in the microchannels. This stage was the result of bubble growth in a confined space when the bubble interface came closer to the channel walls. A highly superheated liquid layer near the wall enhanced the evaporation increasing the bubble growth rate. An acceleration in the bubble growth as it comes closer to the channels side walls was observed in saturated flow boiling as well. This implies that the superheated liquid layer near channel walls plays a significant role in bubble growth in subcooled and saturated flow boiling in microchannels.

Most of the bubbles observed at lower mass fluxes grew and exploded while remaining attached to the heated wall. The number of bubbles departed from the heated wall increased with increasing mass flux. In general, the bubble departure size decreased with an increase in heat flux. An increase in drag forces associated with increased mass flux caused bubbles to depart at smaller diameters/heights.

The non-exponential growth of bubbles in slug flow indicates that the pressure field around them had a significant influence on their growth with diminishing effect on the evaporation of the thin liquid film around. The reason for a higher pressure

field effect on the bubble growth in slug flow observed in this study may be due to intensive flow boiling instabilities.

In addition, the effects of the bubble dynamics on the flow boiling instabilities and the heat transfer coefficient have been investigated. The bubble dynamics determined the frequency of alternation between phases, and consequently the frequency of the pressure and temperature oscillations. It was found that shorter bubble growth period resulted in a higher frequency of fluctuations during the flow boiling instabilities in microchannels. On the other hand, bubbles with a long growth period and slow growth rate resulted in a long two-phase period during the phase alternations, therefore lower frequency of fluctuations with high amplitudes in pressure and temperature.

The averaged heat transfer coefficient at location of sensors T3 and T5 increased with local vapour quality and then decreased at higher vapour quality. An increase in the bubble growth rate and decrease in the bubble growth period resulted in an increase in heat transfer coefficients. The evaporation of the thin liquid film was the dominant heat transfer mechanism. The liquid thickness decreased with increasing heat flux in the range from 25 to 13 μm. A decrease in the liquid thickness led to an increase in vapour phase period (temporary “dryout” period) during one cycle of phase alternation, resulting in decreasing heat transfer coefficient.

References

1. Plesset, M.S. and S.A. Zwick, *The Growth of Vapor Bubbles in Superheated Liquids.* Journal of Applied Physics, 1954. 25(4) 493-500.
2. Forster, H.K. and N. Zuber, *Growth of a Vapor Bubble in a Superheated Liquid.* Journal of Applied Physics, 1954. 25(4) 474.
3. Kandlikar, S.G., Mizo, V.R., Cartwright, M.D, Ikenze, E. *Bubble Nucleation and Growth Characteristics in Subcooled Flow Boiling of Water* in *HTD-Vol. 342, ASME Proceedings of the 32nd National Heat Transfer Conference, vol. 4, pp. 11-18*. 1997.
4. The NIST Chemistry WebBook, http://webbook.nist.gov/
5. Kandlikar, S.G., *Fundamental Issues Related to Flow Boiling in Minichannels and Microchannels.* Experimental Thermal and Fluid Science, 2001. Vol. 26 387-407.
6. Li, H.Y., F.G. Tseng, C. Pan, *Bubble dynamics in microchannels. Part II: two parallel microchannels.* International Journal of Heat and Mass Transfer, 2004. 47(25) 5591-5601.
7. Chen, T. and S.V. Garimella, *Measurements and high-speed visualizations of flow boiling of a dielectric fluid in a silicon microchannel heat sink.* International Journal of Multiphase Flow, 2006. 32(8) 957-971.
8. Hetsroni, G., A. Mosyak, E. Pogrebnyak, Z. Segal, *Explosive boiling of water in parallel micro-channels.* International Journal of Multiphase Flow, 2005. 31(4) 371-392.
9. Qu, W. and I. Mudawar, *Flow boiling heat transfer in two-phase micro-channel heat sinks--I. Experimental investigation and assessment of correlation methods.* International Journal of Heat and Mass Transfer, 2003. 46(15) 2755-2771.
10. Wang, G., P. Cheng, A.E. Bergles, *Effects of inlet/outlet configurations on flow boiling instability in parallel microchannels.* International Journal of Heat and Mass Transfer, 2008. 51(9-10) 2267-2281.
11. Qu, W. and I. Mudawar, *Flow boiling heat transfer in two-phase micro-channel heat sinks--II. Annular two-phase flow model.* International Journal of Heat and Mass Transfer, 2003. 46(15) 2773-2784.
12. Jacobi, A.M. and J.R. Thome, *Heat Transfer Model for Evaporation of Elongated Bubble Flows in Microchannels.* Journal of Heat Transfer, 2002. 124(6) 1131-1136.
13. Hetsroni, G., A. Mosyak, E. Pogrebnyak, Z. Segal, *Periodic boiling in parallel micro-channels at low vapor quality.* International Journal of Multiphase Flow, 2006. 32(10-11) 1141-1159.

Chapter 7 Investigation of non-uniform heating effect on flow boiling instabilities

7.1 Introduction

If flow boiling is to be used as a thermal management method for high heat flux electronics it is necessary to understand the behaviour of a non-uniform heat distribution, which is typically the case observed in a real operating CPU. The work presented in this chapter is an experimental study of two-phase boiling in a multi-channel silicon heat sink with non-uniform heating, using water as a cooling liquid. Thin nickel film sensors, integrated on the back side of the heat sinks were used in order to gain insight related to temperature fluctuations caused by two-phase flow instabilities under non-uniform heating. The effect of various hotspot locations on the temperature profile and pressure drop has been investigated, with hotspots located in different positions along the heat sink. Two-phase flow instabilities, similar to those observed under uniform heating, have also been observed for non-uniform heating. It was observed that boiling inside microchannels with non-uniform heating leads to high temperature non-uniformity in the transverse direction.

7.2 Experimental setup and procedure

The experimental setup described in chapter 3 was also used in this experiment. The heater integrated on the back side of the heat sink with microchannels was designed to enable either uniform or non-uniform heating, the later being achieved by the independent operation of the upstream, middle or downstream heating elements. The microchannel heat sink, together with the locations of temperature sensors (T1-T5), the inlet/outlet hole and the upstream, middle and downstream hotspot are shown schematically in Figure 7.1.

The total heat flux applied to hotspot was calculated from $q_T = VI/A$, where V and I are the input voltage and current across the film heater, with A being the area of the hotspot (49.5 mm^2). The heat flux absorbed by the water, q was calculated from:

$$q = q_T - \frac{Q_{loss}}{A}, \tag{7.1}$$

where Q_{loss} represents the heat losses due to axial conduction through the silicon wafer and conduction through the bottom insulating plastic and the top pyrex glass cover. In order to estimate heat losses, a series of experiments were conducted using the heat sink completely drained of water. Power applied to the hotspot heater element was varied and sensor temperatures recorded. Approximately half an hour was allowed for the temperature to reach a steady state before measurements were recorded at each power magnitude applied to the hotspot. Once the sensor temperature reached a steady state, the heat supplied by the heater was equal to the conduction heat losses. Figure 7.2 shows experimentally measured heat losses with respect to the averaged sensor temperatures. The heat losses are nearly linear functions of temperature. Therefore, linear fitting was performed on each data set to derive functional expressions for the heat losses as a function of hotspot temperature (T1, T3 and T5 for upstream, middle and downstream hotspot respectively). The linear heat loss-temperature relationship indicates that the losses are mainly by

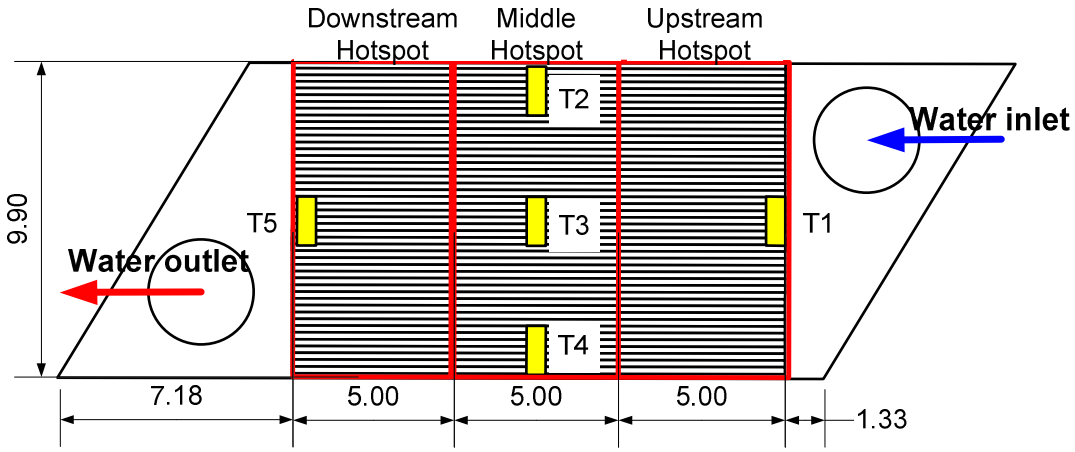

Figure 7.1 *Schematic of the microchannel based heat sink showing the location of the temperature sensors (T1-T5) and position of the upstream, middle and downstream hotspots. Units mm.*

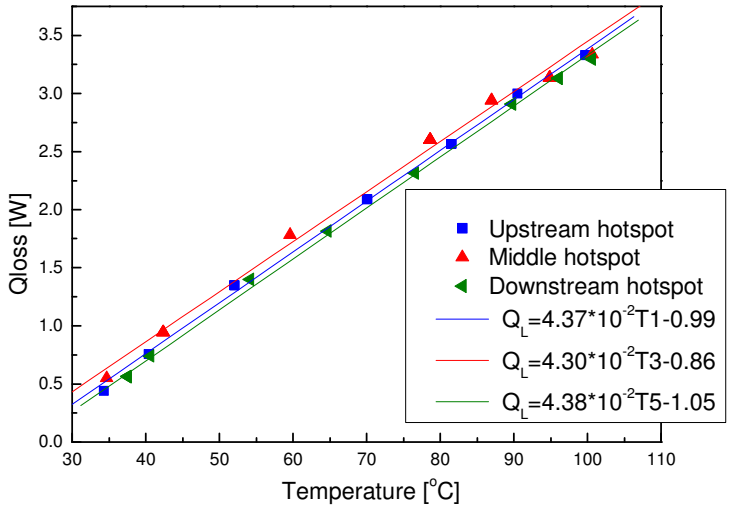

Figure 7.2 *Experimentally measured heat losses with respect to the sensor temperatures.*

conduction from the test section to the ambient. It is worth noting that the procedure of calculating the heat losses was similar to that used by Chen and Garimella [1] and Lee and Garimella [2]. Prior to carrying out the experiments, deionised water in the reservoir was degassed by vigorous boiling it for approximately one hour. Afterwards, the flow rate and the inlet water temperature were adjusted to the desired

values. Experiments were conducted for water mass flow rates of 10 and 17 g/min (102 and 173 kg/m^{2}s respectively) with a water inlet temperature of 71 ˚C. For each of the mass flow rates one heater element (hotspot) was varied over a range of power while the other two heater elements were powered at a constant power of 10 W each. A power magnitude of 10 W was experimentally found optimal for investigation of flow boiling under non-uniform heating for given mass fluxes. Power magnitudes less than 10W required very high power levels to be applied to hotspot with possible damaging consequences for heater elements. Power magnitudes higher than 10 W caused boiling to commence first at microchannels located out of hotspot region for a relatively small power magnitude applied to the hotspot.

7.3 Results and discussion

7.3.1 Flow boiling instabilities

Two-phase flow instabilities were observed during flow boiling in the microchannels heat sink with non-uniform heating. Figure 7.3 shows temporal measurements of the temperature recorded on the five integrated sensors for the cases of: an upstream hotspot (a), a middle hotspot (b) and a downstream hotspot (c), for a mass flux of 173 kg/m^{2}s, inlet water temperature of 71 ˚C and two different heat fluxes applied to the hotspot. Two types of instabilities with appreciable oscillations in pressure and temperature were observed, similar in frequency to those observed under uniform heating. The first type of instability was observed when lower heat flux was applied to the hotspot. Pressures and temperatures oscillated with higher amplitude similar to those observed at high amplitude/low frequency instabilities under uniform heating with the dominant frequency being around 2 Hz. Another type of instabilities was observed when a higher heat flux was applied to the hotspot. Pressure and temperatures oscillated with lower amplitude than in the case of first type of instabilities. Frequency analysis identified a broad range of frequencies, similar to those observed with low amplitude/high frequency instabilities under uniform heating.

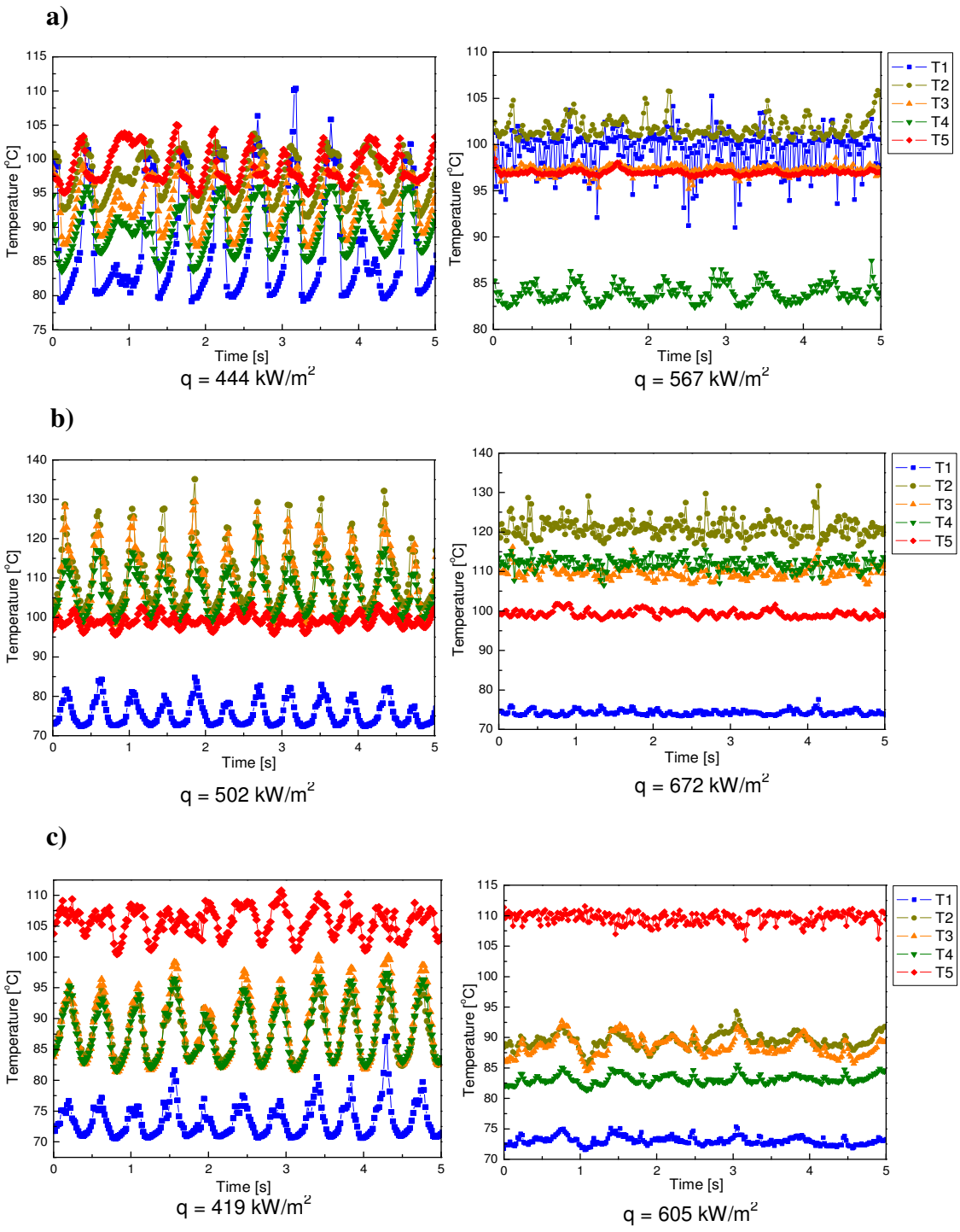

Figure 7.3 *Temporal measurements of the temperature recorded on the five integrated sensors. (a) upstream hotspot, (b) middle hotspot, (c) downstream hotspot.*

Large amplitude fluctuations in T1 (Figure 7.3a, q = 444 kW/m^2) indicates intermittent boiling at an upstream hotspot. Oscillations of T2 temperature were normally below the saturation temperature (~100 ˚C) while T3 and T4 temperatures were always below the saturation temperature, thus bubbles coming from upstream condensed in region of the middle hotspot. Oscillations of T5 temperature with maxima between 102 and 105 ˚C indicate more established boiling downstream.

In the case of a middle hotspot (Figure 7.3b, q = 502 kW/m^2) the temperature T1 was always subcooled indicating a fluctuation in single phase liquid cooling, driven by the flow instabilities originating from middle hotspot boiling. Temperatures T2, T3 and T4 had the same minimum of 100 ˚C, indicating saturated boiling in middle hotspot region. The temperature T5 fluctuated between 95 ˚C and 105 ˚C at a somewhat higher frequency then the other sensors due to combination of local boiling and flow disturbances driven by middle hotspot boiling.

Figure 7.3c (q = 419 kW/m^2) shows dominant subcooled conditions at upstream and middle locations (temperatures T1-T4). Cooling on the first two heaters was a single phase liquid, since there was no superheat to drive evaporative cooling. The large amplitude fluctuations of temperature T5 are in phase with the fluctuations at T1-T4 but there were some additional smaller amplitude fluctuations. This suggests that the main activity was downstream hotspot boiling with bubble confinement occurring at low frequency and driving the fluctuations observed elsewhere.

An increase in applied heat flux led to a higher oscillation frequency with smaller amplitudes in temperatures, as shown in Figure 7.3 for the higher heat flux level. In the case of an upstream hotspot with a heat flux of 567 kW/m^2 there was a large difference between temperatures measured in the transverse direction (T2, T3 and T4, Figure 7.3a, q = 567 kW/m^2) indicating a non-uniform liquid distribution within the channels. Temperature T4 shows high subcooling conditions inside the channels located above the sensor T4, with fluctuations being completely different from fluctuations in temperatures measured by the other sensors. This suggest that there was boiling activity over at least half the width of the channel assembly from T2 to T3 and T5 that diverted single phase liquid flow towards the T4 side of the assembly.

There was a difference in temperatures along transverse direction (T2, T3 and T4) in the case of middle hotspot with a heat flux of 672 kW/m^2. However, boiling was observed over the total width of the channel assembly from the T2 to T4 sensor. The latter is confirmed by temperatures of T2, T3 and T4 being higher than the saturation temperature.

A higher heat flux of 605 kW/m^2 applied on the downstream hotspot settled down the temperature fluctuations observed at lower heat flux as it can be seen in Figure 7.3c. Boiling was restricted to downstream hotspots as only the T5 sensor recorded temperatures above the saturation temperature. However, all the other temperatures measurements exhibited irregular fluctuations. These fluctuations were driven by downstream hotspot boiling and were closely correlated in time.

Figure 7.4 shows temporal measurements of pressure drop and temperatures simultaneously recorded during high amplitude oscillations for upstream (a), middle (b) and downstream (c) hotspots. The fluctuation of the pressure drop and temperatures were correlated in time indicating that temperature oscillations were driven by the difference between spatial average pressures at the inlet and outlet manifolds. The pressure drop and temperatures oscillated with a similar frequency and nearly in phase, except for the T5 temperature, which oscillated at a somewhat higher frequency due to more developed boiling in the region of the downstream hotspot.

Discrete Fourier transformation (DFT) was used to analyse the pressure drop oscillations. A fast Fourier transformation algorithm and Origin software were used to solve DFT and obtain the frequency distribution for the pressure drop data. Amplitudes of the frequency domain were derived from the square root of the sum of the squares of the real and imaginary parts of the frequency domain. The dominant frequencies were identified by the magnitude of the amplitude. Figure 7.5 shows the pressure drop data shown in Figure 7.4 presented in the frequency domain for different hotspot locations. The dominant frequency was in order of 2 Hz, similar to the frequency observed under uniform heat flux and similar mass flux conditions. The frequency was found to slightly decrease with an increase in hotspot heat flux.

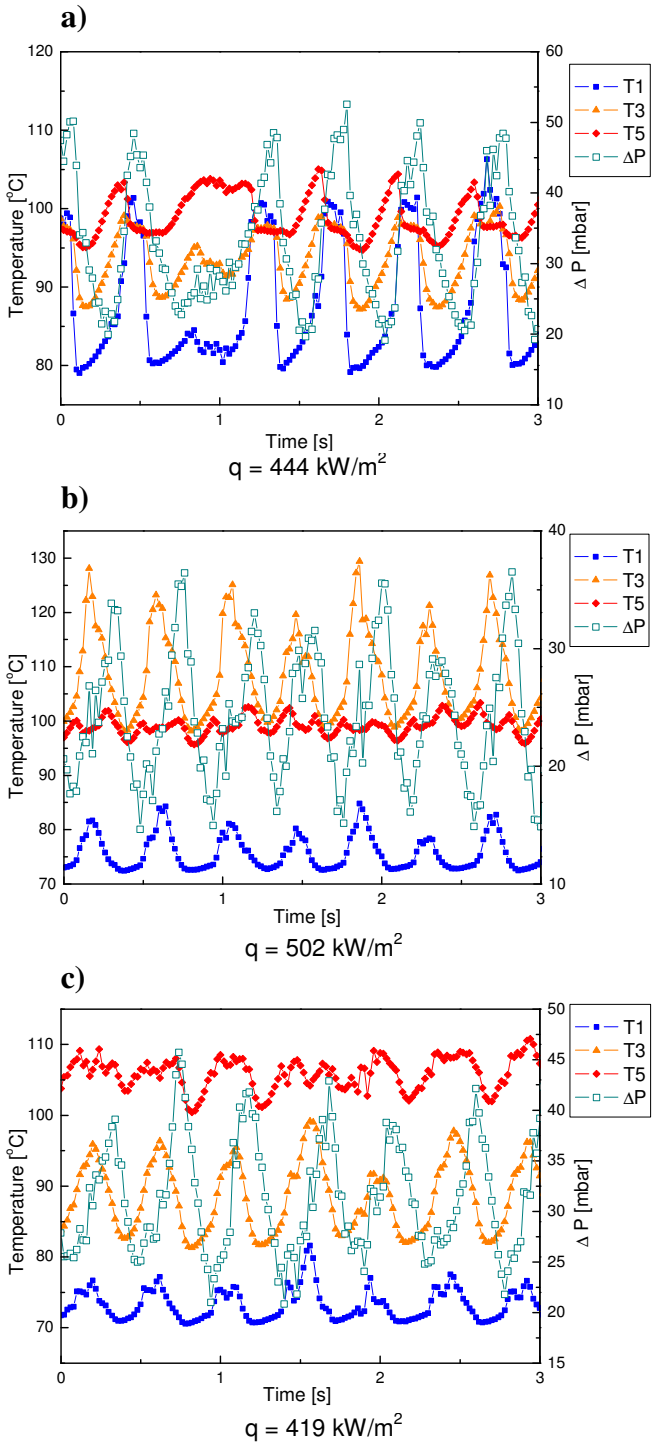

Figure 7.4 *Temporal measurements of pressure drop and temperatures simultaneously recorded during high amplitude oscillations for upstream (a), middle (b) and downstream (c) hotspot.*

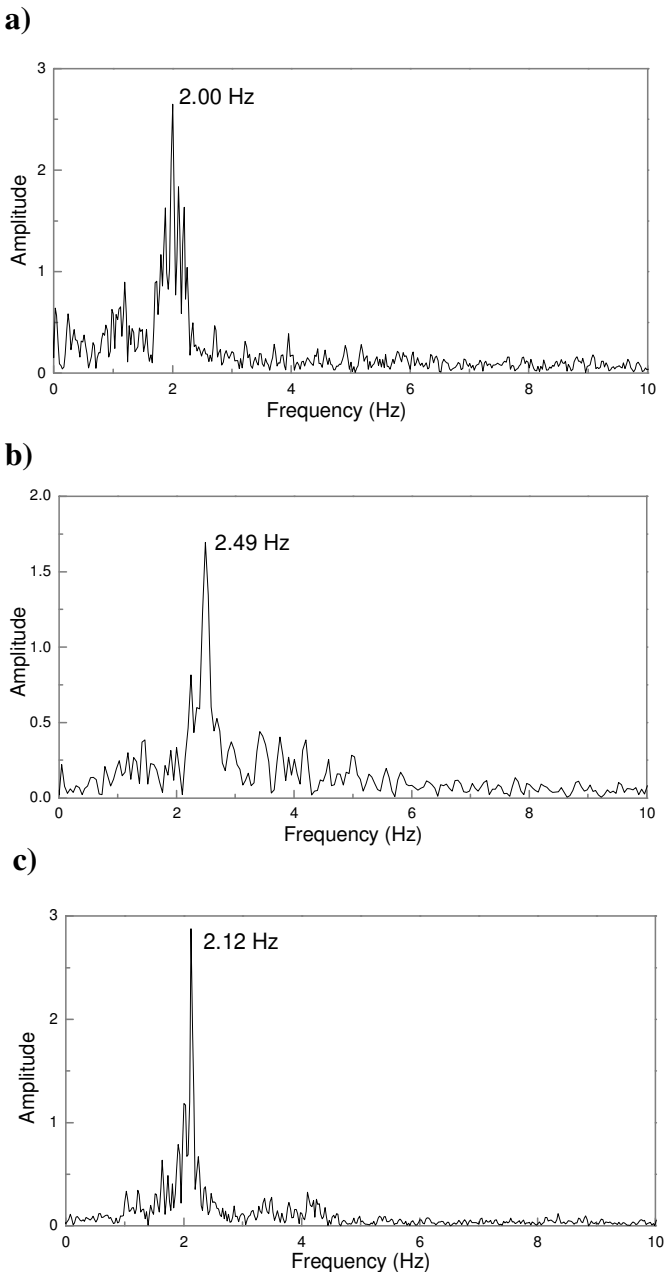

Figure 7.5 *Pressure drop data shown in Figure 7.4 presented in frequency domain for upstream (a), middle (b) and downstream (c) hotspot.*

The same trend was observed under a uniform heat flux for high amplitude/low frequency oscillations. However, the range of frequencies observed for non-uniform heating was smaller than for uniform heating. The frequencies observed for the case of high amplitude/low frequency and an upstream hotspot decreased from 2.25 to 1.78 Hz, for a downstream hotspot from 2.37 to 1.90 Hz, and for a middle hotspot from 2.49 to 2.14 Hz. The frequencies observed for the same type instabilities and similar mass flux rate under uniform heating were in the range from 1.24 to 2.27 Hz. Two-phase flow is present in a larger length of the microchannel for uniform heating as compared to non-uniform heating causing the difference in observed range of frequency for high amplitude oscillations.

Figure 7.6 shows temporal measurements of pressure drop and temperatures simultaneously recorded when low amplitude oscillations existed with heat flux applied on upstream (a), middle (b) and downstream hotspots (c). The fluctuations of pressure drop and temperatures are not correlated in time, as was the case when a lower heat flux was applied on hotspots (Figure 7.4). Frequency analysis of the pressure drop data showed a broad range of frequencies for all hotspot locations investigated, with frequencies higher than in the case of high amplitude oscillations. Amplitudes of the frequency domain are lower than in the case of high amplitude oscillations. Figure 7.7 shows the pressure drop data presented in the frequency domain for different hotspot locations. A broad range of frequencies indicates non-uniform flow distributions among channels and dissimilar boiling activities in different microchannels. The total pressure drop fluctuations correspond to the effects caused by each channel, and therefore the signal analysis of the pressure drop fluctuations present a wide range of frequencies.

Simultaneously high speed camera imaging showed that oscillations are caused by the flow alternating between liquid, two-phase and vapour. To illustrate these oscillations, Figure 7.8 shows selected images recorded at a rate of 500 fps for 502 kW/m^2 and the middle hotspot, at a mass flux of 173 kg/m^2s and water inlet temperature of 71 ˚C. The image recorded at t = 0 ms, shows bubble nucleation inside the microchannels above the middle hotspot. The arrow in the first image

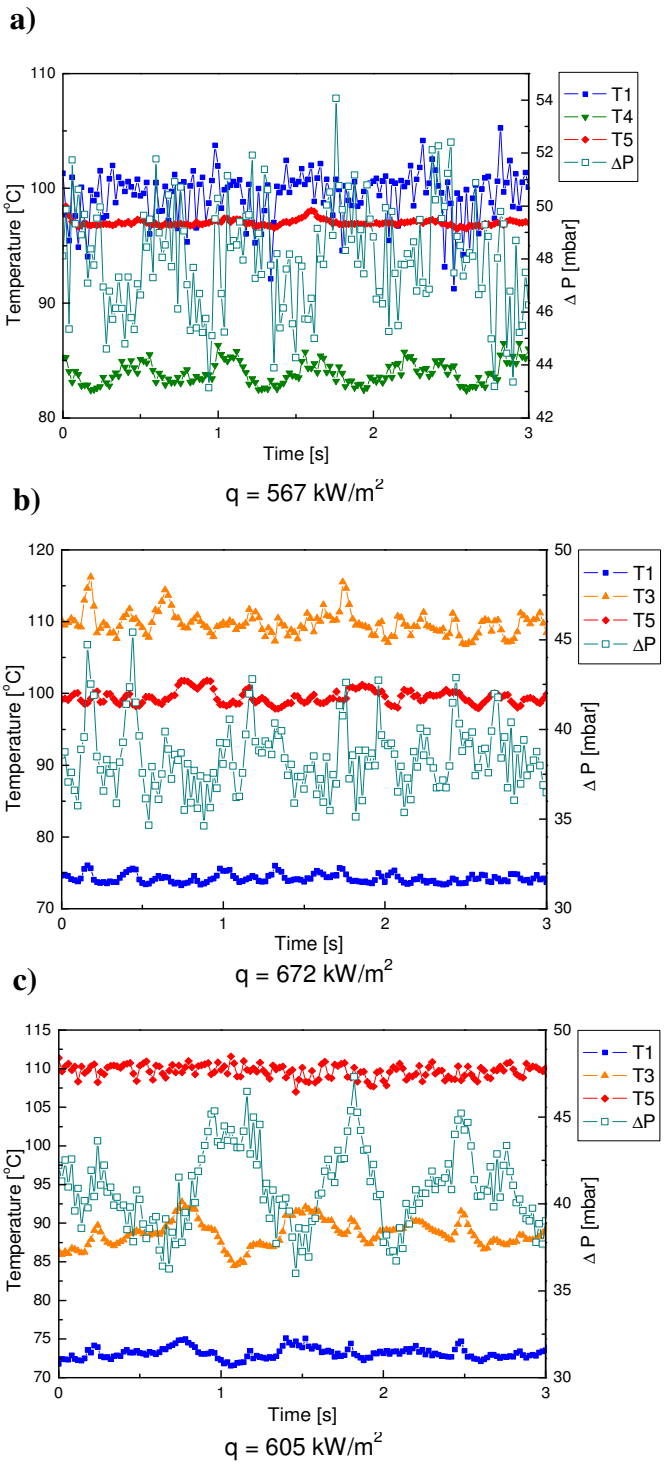

Figure 7.6 *Temporal measurements of pressure drop and temperatures simultaneously recorded when low amplitude oscillations existed for upstream (a), middle (b) and downstream hotspot (c).*

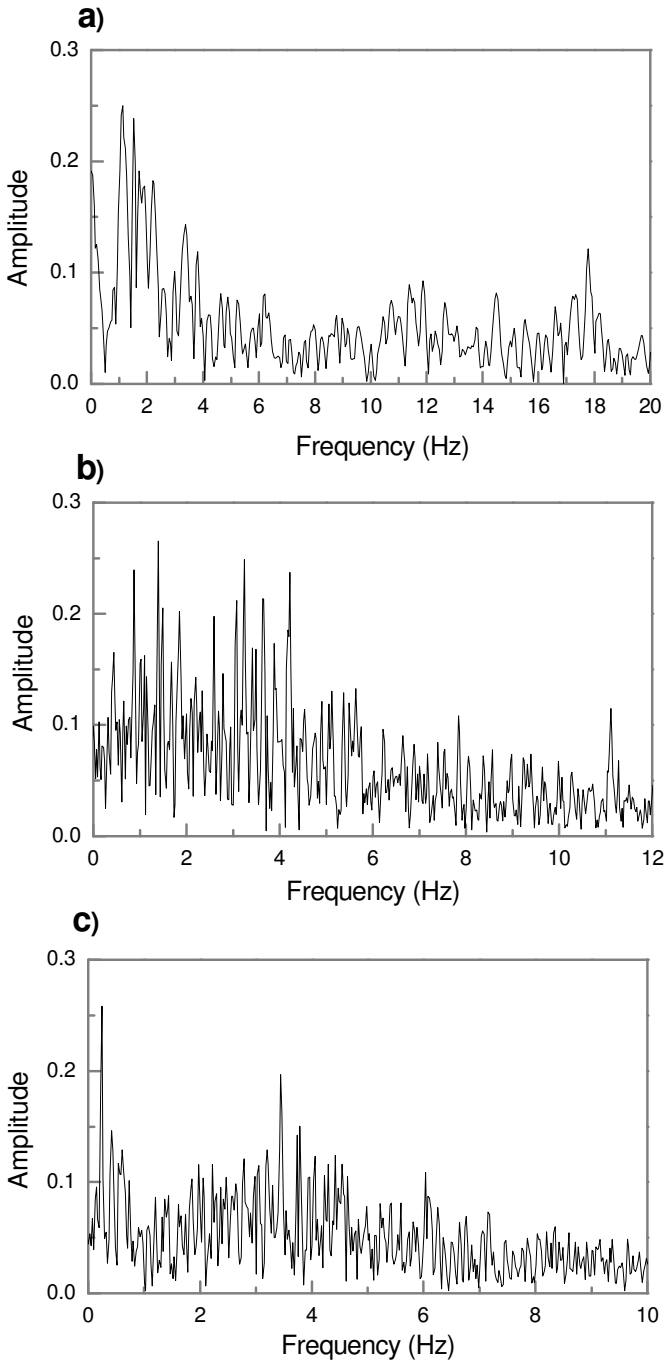

Figure 7.7 *Pressure drop data shown in Figure 7.6 presented in frequency domain for upstream (a), middle (b) and downstream (c) hotspot.*

shows the direction of the water flow and the circle marks the nucleation site. Initially, the bubble grew and remained at the place of nucleation. At t = 98 ms bubble detached from nucleation site and moved downstream. This stage was followed by bubble axial growth causing the bubbles to expand both upstream and downstream coalescing with other bubbles growing at the same nucleation site. After bubbles coalescence, transient annular flow results (t = 138 ms). A thin liquid film evaporation led to a temporal "dry out" period in the observed channel with the nucleation site as shown in the image captured at t = 286 ms. Vapour is condensed by incoming subcooled liquid and a new cycle starts again with bubble nucleation occurring when the subcooled liquid refills the channel downstream of the nucleation site (t = 388 ms). Similar as it was observed under uniform heating, there were short periods when the liquid phase exists inside all the microchannels and this was captured using a high speed camera using a 2300 μm diameter field of view, covering about nine channels. This period corresponds to minima in the temperature and the pressure drop measurements during the long amplitude oscillations.

Further increase in heat flux applied to hotspot led to the intensification of bubble nucleation along the channel assembly. Bubble frequency increased and the bubble growth period became shorter resulting in a decrease in the period between two successive events during cycling through liquid/two-phase/vapour flow. For the nucleation site observed in Figure 7.8, the bubble frequency was found to increase from 5.5 Hz to 17.8 Hz with an increase in heat flux from 502 to 672 kW/m^2. Frequency is the reciprocal of the sum of waiting and bubble growth time. Intensification of bubble nucleation led to a higher oscillation frequency with smaller amplitudes in temperatures, as shown in Figure 7.3 for higher heat flux magnitudes. Alternations between liquid, two-phase and vapour were not synchronized in channels leading to non-uniform flow distribution. This was more transparent in the case of low amplitude oscillations than in the case of high amplitude oscillations.

Figure 7.9 shows selected images captured using a high speed camera when a heat flux of 394 kW/m^2 was applied to the downstream heater element. The images show the inlet and outlet zone of the same channels. The bulk flow is from left to right and the reverse vapour flow is indicated by a red arrow. As it can be seen from

Figure 7.9 for the inlet zone, subcooled water was prevailing with intermittent bubble nucleation and growth. The reverse vapour flow was not intense and was observed only sporadically in channels. At the outlet zone of the same channels, intense bubbles nucleation was present with dominant two-phase flow and severe reverse vapour flow.

In the case of upstream hotspots, vigorous boiling was observed at the inlet as well as in outlet zone of the microchannel's assembly, as is shown in Figure 7.10 for

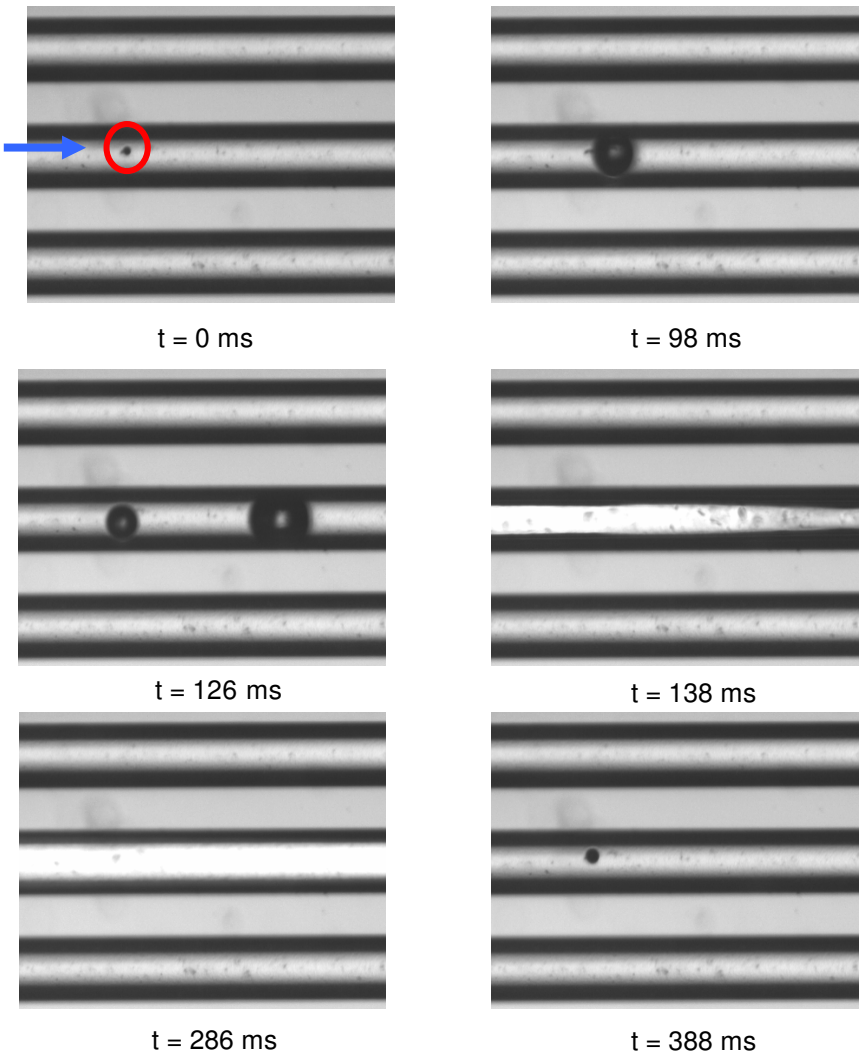

Figure 7.8 *Images recorded using high speed camera at a rate of 500 fps for a heat flux of 502 kW/m^2 and middle hotspot, arrow shows direction of the bulk flow.*

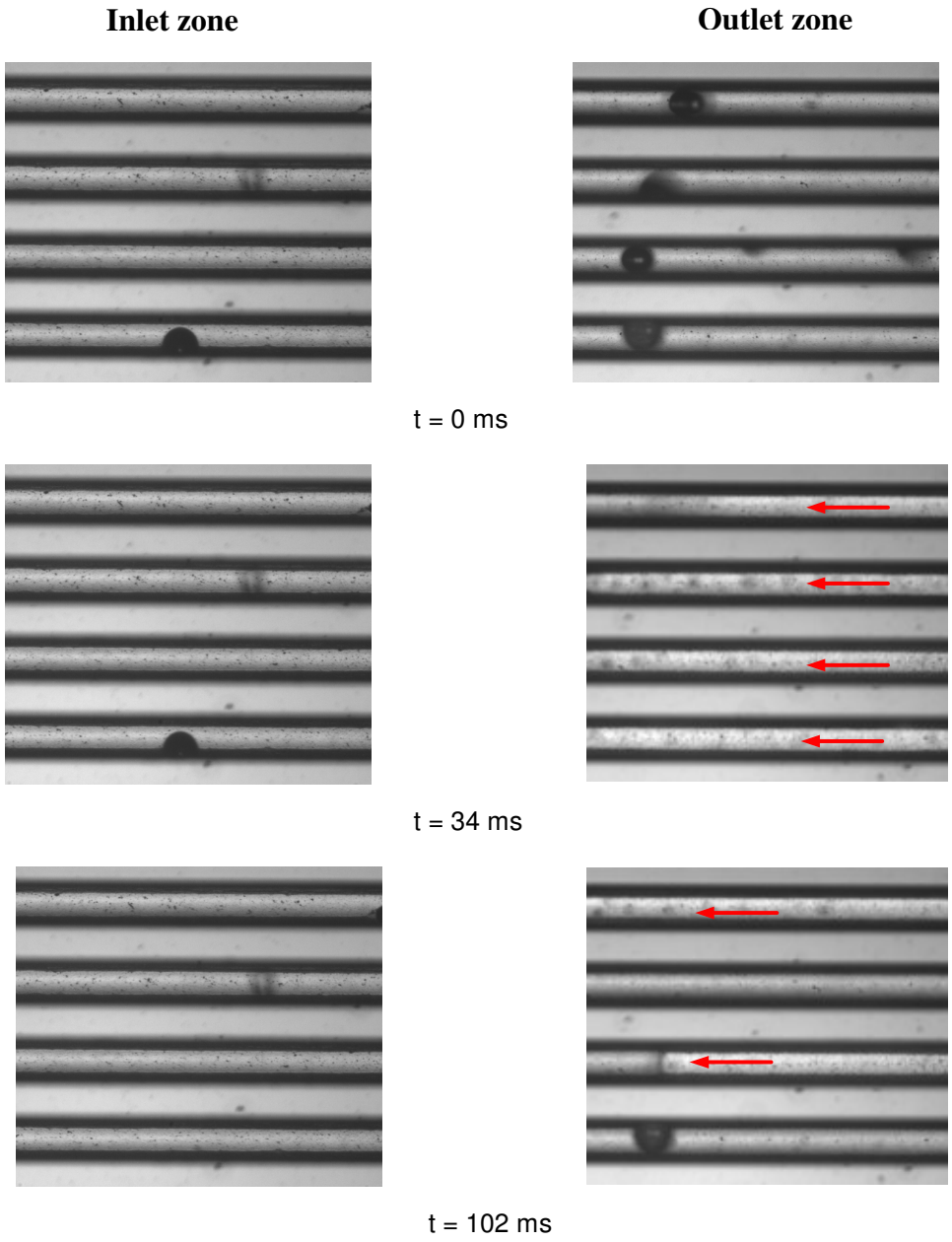

Figure 7.9 *Images captured using high speed camera, showing inlet and outlet zone of microchannels for a heat flux of 394 kW/m^2 and downstream hotspot, arrows show direction of the reverse vapour flow.*

a heat flux of 406 kW/m^2. Intense bubbles nucleation and reverse vapour flow exists in both the inlet and outlet zones of the observed microchannels. Figure 7.9 and Figure 7.10 indicate that two-phase was present in a longer length of microchannel

for upstream hotspots compared with downstream hotspots for similar values of heat flux.

In the case of hotspots midway along channel, vigorous boiling was observed in the midpoint and downstream parts of the channel assembly with reverse flow of vapour inside the inlet zone. However, less vapour was present in the inlet and outlet manifolds of the heat sink when compared the upstream and downstream hotspots.

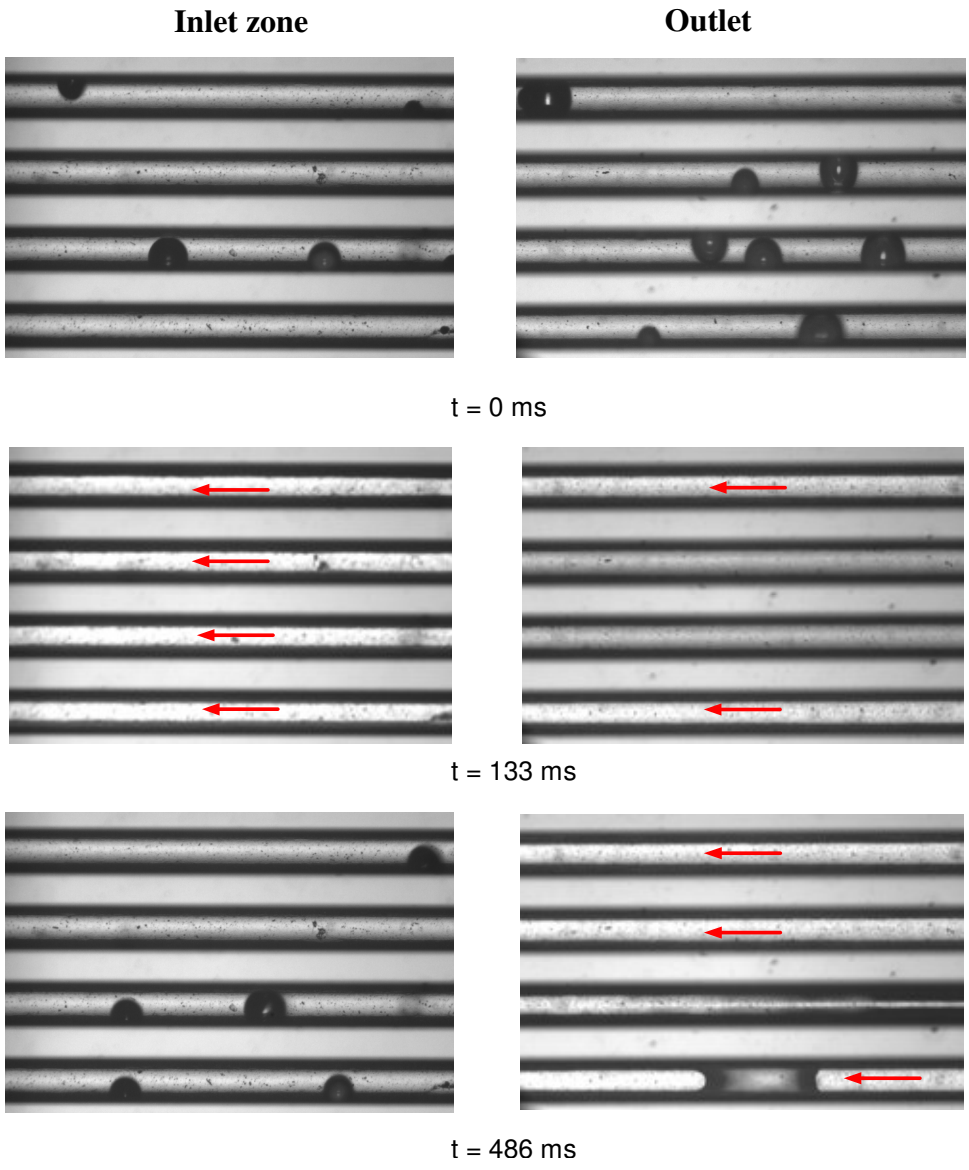

Figure 7.10 *Images captured using high speed camera, showing inlet and outlet zone of microchannels for a heat flux of 406 kW/m^2 and upstream hotspot, arrows show direction of the reverse vapour flow.*

7.3.2 Temperature and pressure drop analysis

Figure 7.11 and Figure 7.12 show the temperature distribution with respect to the heat flux applied to upstream (a), middle (b) and downstream hotspots (c) , for two water mass flux rates of 102 and 173 kg/m^{2}s respectively with a water inlet temperature of 71 ˚C. Each point on the graphs is the average value from one experimental data set. The vertical line (labeled as OFI in graphs) shows the threshold of two-phase flow instabilities when appreciable fluctuations in temperature and inlet/outlet pressure were observed. The magnitude of the pressure drop was used as criterion for the onset of flow instabilities (OFI) when the high amplitude fluctuations in pressure and temperature were observed for the first time with increasing heat flux. The magnitude of the pressure drop at OFI was 20 mbar or higher.

The vertical bars in the graphs present the magnitudes (minima and maxima values) of temperature on hotspot (T1 for upstream, T3 for middle and T5 for downstream hotspots). The highest temperature amplitudes were recorded by the upstream (T1) and middle (T2, T3 and T4) sensors when located below operating hotspots. However, in the case of downstream hotspot the highest temperatures were observed at upstream locations. This was observed for both mass flux rates (102 and 173 kg/m^{2}s) investigated.

The onset of flow instabilities was usually observed at the beginning of boiling inside the microchannels, resulting in the change of slope shown in Figures 7.11 and 7.12. The change in slope is more pronounced for the higher mass flux rate of 173 kg/m^{2}s. For upstream hotspots, boiling inside microchannels caused increased temperatures T1 measured at the inlet of the microchannels. On the outlet side of the channel temperature T5 decreased. A similar effect was observed in the case of a midpoint hotspot when an increase in the power was applied to the hotspot, during the boiling inside the microchannels. This resulted in a decrease in temperature T5 at microchannels outlet. Once boiling occurred inside the microchannels with hotspot located downstream, the slope related to the temperature T5 in Figure 7.11c and

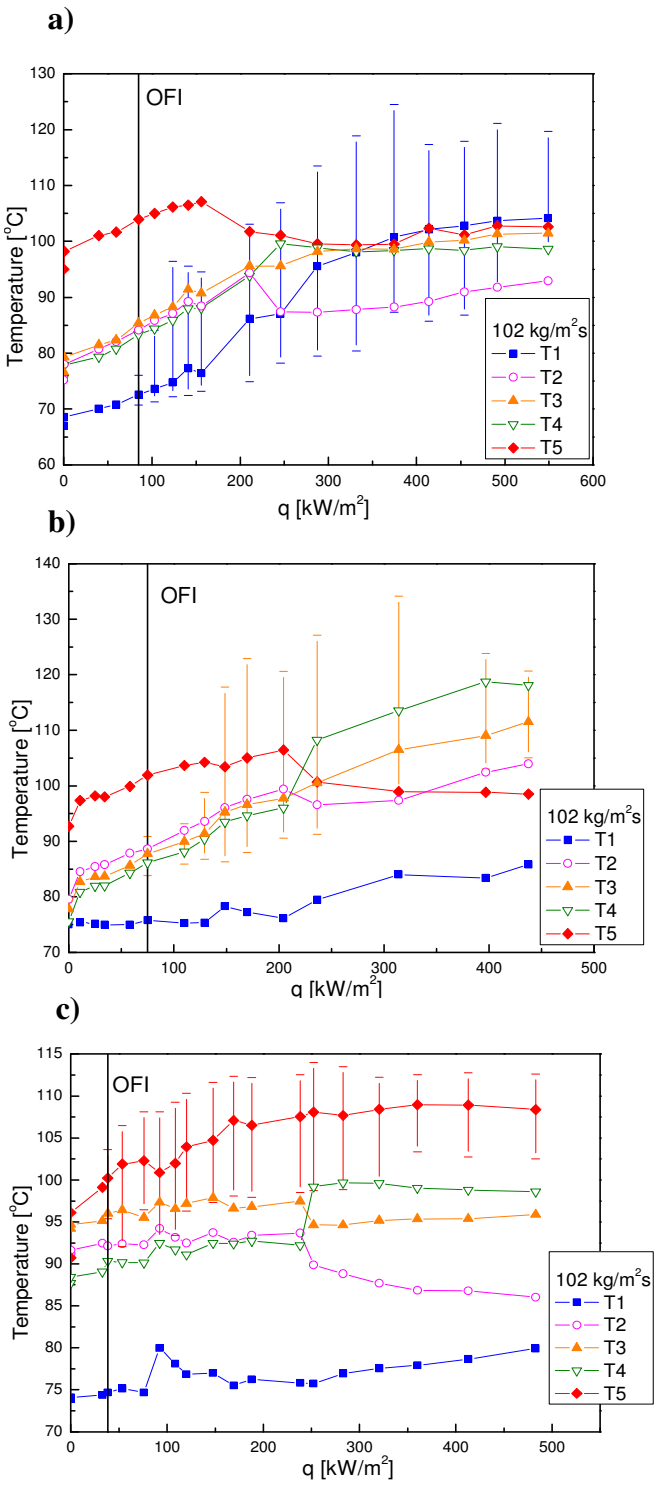

Figure 7.11 *Temperature distribution with respect to heat flux, G = 102 kg/m²s (a) upstream hotspot, (b) middle hotspot, (c) downstream hotspot. Vertical bars present the magnitudes of temperature (a) T1, (b) T3, (c) T5, OFI is onset of flow instabilities.*

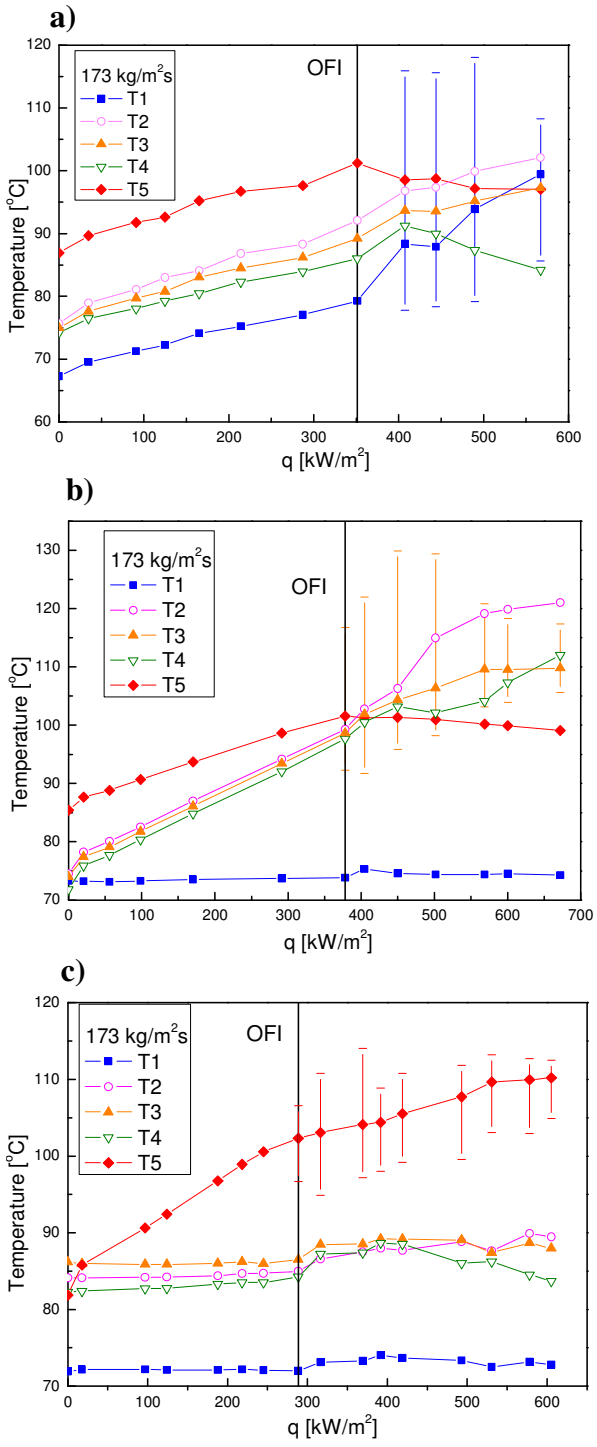

Figure 7.12 *Temperature distribution with respect to heat flux, G = 173 kg/m^{2}s (a) upstream hotspot, (b) middle hotspot, (c) downstream hotspot. Vertical bars present the magnitudes of temperature (a) T1, (b) T3, (c) T5, OFI is onset of flow instabilities.*

Figure 7.12c decreases. After the onset of flow instabilities, further increases of the power applied at the downstream hotspot did not significantly affect mean values of temperatures at upstream locations (T1, T2, T3 and T4). The prevailing single phase flow was observed in upstream location and good lateral flow distribution was indicated by temperatures T2 and T4 being very similar. However, high power applied to downstream hotspot, breaks up the temperature uniformity in the transverse direction as the boiling propagates towards the inlet of the heat sink.

Figure 7.13 depicts the temperature distribution in the axial (a) and transverse direction (b) for different hotspot locations, with similar magnitudes of heat flux and a mass flux rate of 173 kg/m^{2}s. The axial temperature distribution is presented with averaged temperatures measured by sensors T1, T3 and T5 located at 0.367, 7.500 and 14.632 mm respectively from the channels inlet. The transverse temperature distribution is presented with averaged temperatures measurements from sensors T2, T3 and T4 located at 1.005, 5.000 and 8.995 mm respectively from the edge of the channel assembly. Figure 7.13a shows that a hotspot located upstream yielded a more uniform temperature along the microchannel assembly compared with the middle and downstream hotspots. The smallest temperature difference along axial direction occurred with upstream located hotspot. For the hotspot located downstream the difference between temperatures along the transverse direction was smaller than the other two hotspot locations (Figure 7.13b). This implies that a hotspot located downstream resulted in better temperature uniformity in the transverse direction than the upstream and middle hotspot locations. A long subcooled inlet region and single-phase flow prevailing at the inlet zone (Figure 7.9) enabled a better fluid distribution within the channels, compared with upstream and middle hotspots, together with a suppressed reverse flow originating at the outlet zone of microchannels.

The temperature non-uniformity in transverse direction increases with the increasing hotspot heat flux. Again, temperature non-uniformity was more pronounced for the middle and upstream hotspots than the downstream hotspot. The temperature distribution in the transverse direction strongly depends on mass flow distribution within the microchannels. It was observed that boiling was not uniformly

established in transverse directions. The pressure drop due to boiling established on one side of the channel assembly diverted single phase liquid flow towards another side of the microchannels heat sink. This caused a difference between the average values of the temperatures in transverse direction and inconsistency in their oscillation amplitude and frequency.

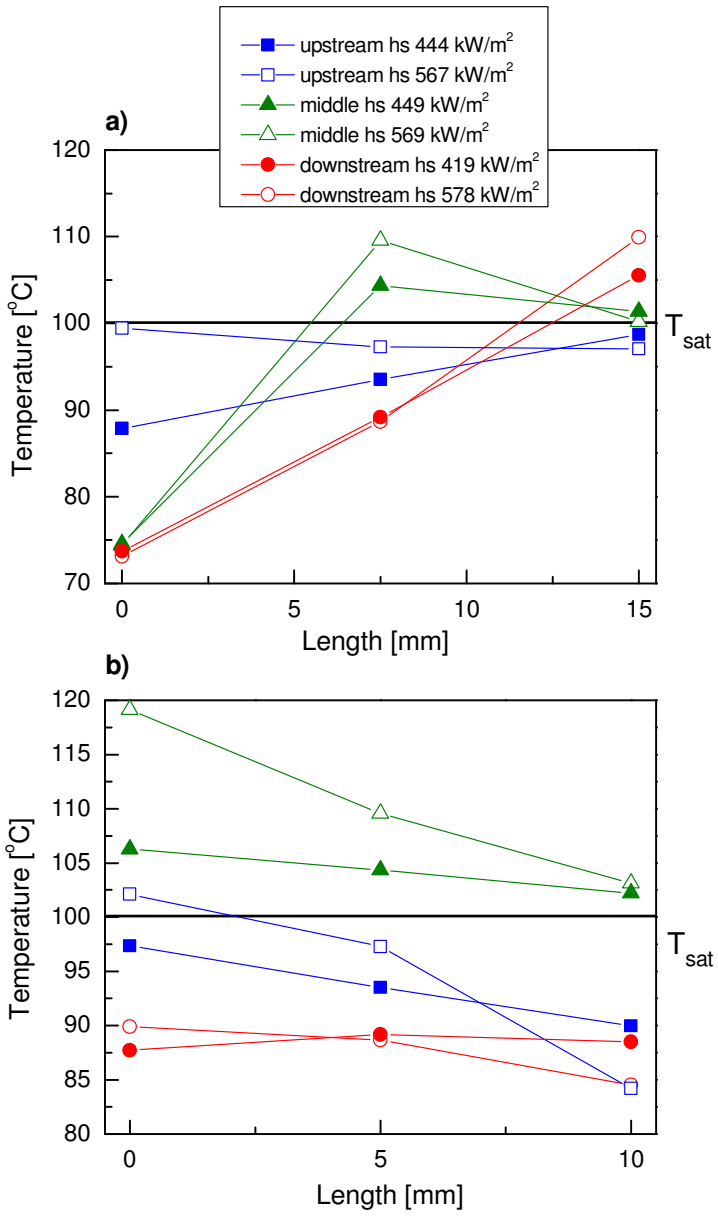

Figure 7.13 *Temperature distribution in axial direction (a) and transverse direction (b) for two heat fluxes and upstream, middle and downstream hotspots.*

Figure 7.14 shows the pressure drop with respect to the heat flux applied to the upstream, middle and downstream hotspots for mass flux rates of 173 and 102 kg/m^{2}s. Each point on the graphs is an average value from one experimental data set. The heat flux was varied over a set range, while the other two heater elements were both maintained at a constant power of 10 W (q = 202 kW/m^2). It was found for both mass flow rates that a centrally located hotspot resulted in the lowest pressure drop once boiling occurred inside the heat sink. Boiling at the inlet and outlet manifold observed for upstream and downstream hotspots due to axial heat conduction led to a higher pressure drop compared with hotspots located at the midpoint along the channel length.

The highest pressure drop was recorded for upstream hotspot at higher rates of heat flux. Two-phase flow was present in a longer length of the microchannel for upstream hotspots compared with downstream hotspots, leading to a higher pressure drop.

Pressure drop analysis showed that the magnitude of pressure drop oscillations (difference between the maximum and minimum value from one experimental data set) was higher for upstream hotspots than for middle and downstream located hotspots. This can be seen from the data presented in Table 7.1 for a mass flux of 173 kg/m^{2}s. Similar results were observed for both mass flux rates (102 and 173 kg/m^{2}s) investigated. It is suggested that higher magnitudes of pressure drop are due to the interaction between vapour generated in the upstream region and the compressible volume of the two-phase mixture in the inlet manifold. A long subcooled inlet region, particularly in the case of downstream hotspots, suppressed flow reversals originating at the downstream end of the channels, by partially condensing reversing bubbles. This resulted in smaller magnitudes of the pressure drop oscillations for downstream located hotspots.

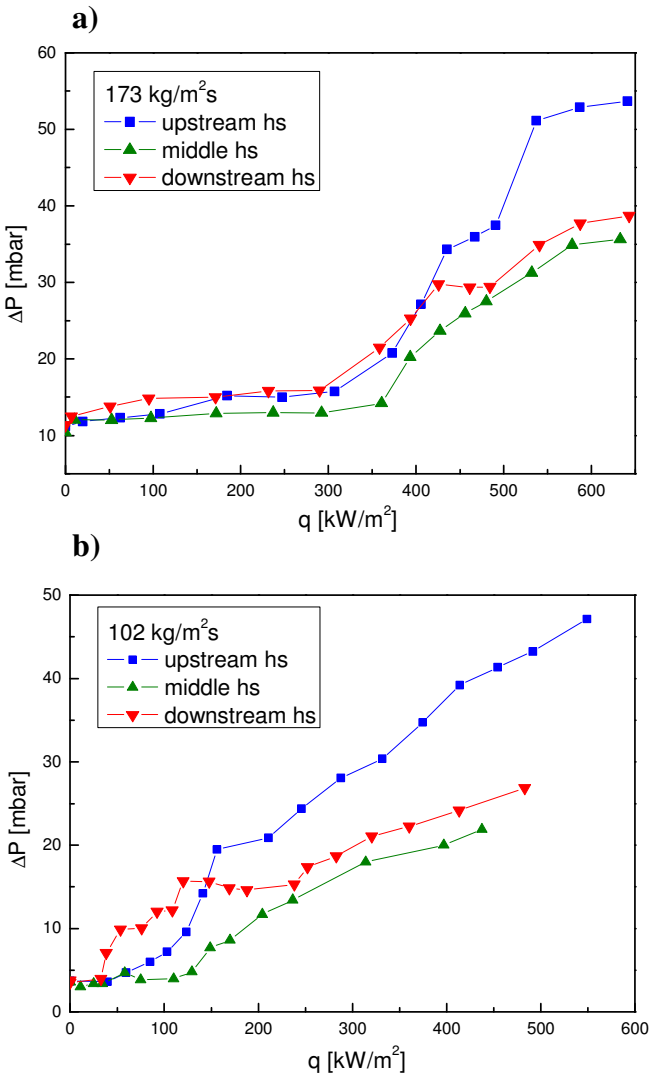

Figure 7.14 *Pressure drop with respect to heat flux and upstream, middle and downstream hotspot for mass fluxes of (a) 173 and (b) 102 kg/m^{2}s.*

7.4 Conclusions

A series of experiments has been carried out to investigate the performance of a silicon microchannels based heat sink under non-uniform heating conditions. Two mass flux rates of 102 and 173 kg/m^{2}s were used and the effect of non-uniform heating on temperature distribution and pressure drop has been assessed, with hotspots located upstream, in the middle and downstream along the heat sink. Two-

Table 7.1 *Pressure drop magnitudes with respect to heat flux for upstream, middle and downstream hotspot.*

Mass flux, G [kg/m^{2}s]	Upstream hotspot heat flux, q [kW/m^2]	Pressure drop magnitude [mbar]	Middle hotspot heat flux, q [kW/m^2]	Pressure drop magnitude [mbar]	Downstream hotspot heat flux, q [kW/m^2]	Pressure drop magnitude [mbar]
173	**373**	29	**361**	23	**358**	26
	406	39	**393**	21	**394**	26
	435	33	**427**	17	**426**	23
	467	42	**456**	21	**461**	21
	491	40	**480**	19	**484**	24
	537	32	**532**	22	**541**	22
	587	17	**578**	18	**587**	20
	641	19	**633**	17	**643**	16

phase flow instabilities have been observed, with a characteristic oscillation in temperature and pressure. Two types of two-phase flow instabilities were observed, one with high amplitude oscillations and another with low amplitude oscillations in temperatures and pressures. Frequencies were similar to those observed under uniform heating.

The highest amplitude of temperature oscillations were recorded by the sensors located below the upstream and middle hotspots, while in the case of downstream located hotspot the highest amplitudes were observed at upstream locations. It was also observed that boiling inside microchannels with non-uniform heating led to high temperature non-uniformity in the transverse direction caused by the diversion of single phase liquid flow towards one side of the heat sink assembly. For a higher mass flux of 173 kg/m^{2}s, a downstream hotspot resulted in better temperature uniformity than upstream and middle hotspots. On the other hand, a hotspot located upstream provided better axial temperature distribution.

Boiling inside the inlet and outlet manifold observed for upstream and downstream hotspots led to a higher pressure drop compared with middle hotspots. Two-phase flow was present in a longer length of microchannel for upstream hotspot

compared with downstream hotspot causing the highest pressure drop at higher heat fluxes. Pressure drop analysis showed that the magnitude of pressure drop oscillations was higher for upstream hotspot than for middle and downstream located hotspot. Higher magnitudes of pressure drop are due to the interaction between the vapour generated at the upstream region and the compressible volume of the fluid in the inlet manifold.

References

1. Chen, T. and S.V. Garimella, *Measurements and high-speed visualizations of flow boiling of a dielectric fluid in a silicon microchannel heat sink.* International Journal of Multiphase Flow, 2006. 32(8) 957-971.
2. Lee, P.-S. and S.V. Garimella, *Saturated flow boiling heat transfer and pressure drop in silicon microchannel arrays.* International Journal of Heat and Mass Transfer, 2008. 51(3-4) 789-806.

Chapter 8 Conclusions

8.1 General conclusions

Flow boiling of water in a silicon microchannels heat sink under uniform and non-uniform heating has been investigated with particular attention to flow boiling instabilities. An experimental system was designed and constructed to carry out the experimental investigations. The experimental heat sink consisting of forty parallel rectangular microchannels with 194 μm hydraulic diameter together with integrated inlet and outlet manifold was fabricated on a silicon wafer using inductive coupled plasma dry etching, in conjunction with photolithographic techniques. Five temperature sensors made from a thin nickel film, and an aluminium heater track were integrated on the back side of the device with the sensors located between the heater and the microchannels. This design allows local temperature measurements with a much faster response time and smaller thermal resistance as compared to temperature measurements using thermocouples. The integrated heater was designed to enable either uniform or non-uniform heating (hotspot investigation) with a low thermal resistance between the heater and the channels.

Numerical simulations for single phase flow in adiabatic conditions were used to assist the design of manifold geometry in the microchannel heat sinks. An approximate model was used to evaluate the effect of manifold geometry on the flow

distribution and the results were compared with CFD simulation based on the finite element method. For low Reynolds numbers good agreement was found between results of the approximate model and those evaluated by CFD. The approximate model was used to calculate dimensions of the manifolds with non-constant linear cross-section. The CFD simulation results indicated that inlet and outlet holes inside the manifolds make the fluid more uniformly distributed than holes outside, while minimizing the area of manifolds. Experiments carried out with the microchannel heat sink indicate good flow distribution within the channels in the case of the single-phase flow. However, it was found that boiling significantly affects flow distribution in the present heat sink due to flow instabilities, causing the significant temperature non-uniformity in transverse direction.

Flow boiling instabilities with appreciable fluctuations in pressure and temperature have been observed in the present heat sink. Two types of two-phase instabilities with flow reversal were identified and classified into flow stability maps for the two inlet water temperatures of 25 ˚C and 71 ˚C. The criterion of classification was the frequency and amplitude of the pressure drop oscillations. It was found that the flow regime and type of two-phase flow instabilities depended on the heat flux, mass flux and inlet subcooling condition. High amplitude/low frequency instabilities existed for $2.62 \cdot G < q < 2.92 \cdot G + 52.7$ at an inlet water temperature of 25 ˚C and $0.99 \cdot G < q < 1.15 \cdot G + 89.9$ at an inlet water temperature of 71 ˚C. Characteristic frequencies of the pressure drop oscillations were in the range of 0.9-2.7 Hz with amplitudes higher than 25 mbar. Low amplitude/high frequency instabilities existed for the cases when $q > 2.92 \cdot G + 52.7$ at an inlet water temperature of 25 ˚C and $q > 1.15 \cdot G + 89.9$ at an inlet water temperature of 71 ˚C. Frequency analysis for LAHF instabilities showed a wide range of frequencies higher than those found for HALF instabilities with amplitudes of the pressure drop ranged between 10 and 25 mbar. It was found that inlet water temperature affects the magnitudes of temperature oscillations during two-phase flow instabilities. Lower inlet water temperature leads to higher magnitudes of temperature oscillations.

Flow boiling instabilities with flow reversal lead to non-uniform flow distribution within microchannels and simultaneous existence of different flow

boiling patterns along the transverse direction. This resulted in a significant difference between temperatures measured on the sensors located in the transverse direction. The temperature non-uniformity in transverse direction increases with increasing heat flux as the boiling propagates towards channels inlet. A higher inlet temperature of coolant gives better temperature uniformity along the direction of the flow stream and the transverse direction, indicating better flow distribution than in the case of lower inlet water temperature.

High speed camera imaging, performed simultaneously with pressure and temperature measurements, showed that inlet/outlet pressure and temperature fluctuations existed due to alternation between liquid/two-phase/vapour flows. Pure flow patterns have not been observed due to the oscillatory nature of flow instabilities. Alternation between isolated bubble, confined bubble (plug/slug flow), annular flow and mist flow existed during flow boiling instabilities. The bubble dynamics determined the frequency of alternation between phases, and consequently the frequency of the pressure and temperature oscillations. A decrease in the bubble growth period resulted in a shorter period for one cycle of alternation between liquid, two-phase and vapour flow. The high amplitude/low frequency oscillation existed when the bubbles with long growth period were dominant, while the low amplitude/high frequency instabilities were associated with the bubbles with short growth period. The bubble growth rates increased and the growth period reduced significantly with increasing heat flux. For a low wall temperature as the mass flux increased, bubbles grew faster and the growth period was shorter. However, for a high wall temperature the effect of the mass flux on the bubble growth diminished. In general, the bubble departure size decreased with an increase in heat flux. An increase in the drag forces associated with increased mass flux caused the bubbles to depart at smaller diameters/heights.

The bubble growth characteristics observed in subcooled and saturated flow boiling indicate an acceleration in the bubble growth as it comes closer to the channels side walls. This implies that a superheated liquid layer near channel walls plays a significant role in bubble growth in microchannels. The period associated

with acceleration in the bubble growth is unique for the bubble growth in the microchannels and it is the result of bubble growth in confined space.

Two-phase heat transfer coefficient is dictated by periodic behaviour of the flow patterns in microchannels. Two-phase heat transfer coefficient was found to first increase with increasing exit vapour quality and then decreased at higher vapour quality. At low heat flux and exit vapour quality the dominant heat transfer mechanisms were bubbly flow with nucleate boiling mechanism and evaporation of the thin liquid film around the bubble associated with slug flow. At high heat flux and vapour quality the dominant heat transfer mechanism was convective evaporation of the thin liquid film in annular flow. The liquid thickness decreased with increasing heat flux in the range from 25 to 13 μm. A decrease in the liquid thickness led to an increase in vapour phase period (temporary "dryout" period) during one cycle of phase alternation, resulting in decreasing heat transfer coefficient.

Two-phase flow boiling instabilities with characteristic fluctuations in pressure and temperature were observed under non-uniform heating. Two types of two-phase flow instabilities were observed with fluctuation frequencies being similar to those observed under uniform heating. It was also observed that boiling inside microchannels with non-uniform heating led to high temperature non-uniformity in the transverse direction caused by the diversion of single phase liquid flow towards one side of the heat sink assembly. Single-phase liquid was present in a longer length of the microchannel for a downstream hotspot compared with upstream and middle hotspots resulting in a better flow distribution within channels and better temperature uniformity in transverse direction. A long subcooled inlet region, particularly in the case of downstream hotspots, suppressed flow reversals originating at the downstream end of the channels, by partially condensing reversing bubbles. This resulted in smaller magnitudes of the pressure drop oscillations for downstream located hotspots. Particularly high magnitudes of pressure drop were noted for upstream located hotspot due to the interaction between the vapour generated at the upstream region and the compressible volume of the fluid in the inlet manifold.

Boiling inside the inlet and outlet manifold observed for upstream and downstream hotspots led to a higher pressure drop compared with middle hotspots.

The following is a summary of general conclusions:

1. The previous studies on flow boiling in microchannels indicate that still many controversies about flow regimes, flow instabilities and mechanisms of heat transfer exist.
2. In this work an experimental system that utilised integrated temperature sensors that allow local measurements, integrated heater and high-speed imaging has been used, in order to gain further insight into flow boiling in microscale.
3. An approximate model was proven to be an effective tool for the design of manifold geometry for nearly uniform flow distribution in the microchannel heat sinks with single phase flow.
4. Two types of two-phase instabilities with flow reversal and significant temperature and pressure fluctuations were identified and classified into flow stability maps. Lower inlet water temperature leads to higher magnitudes of temperature fluctuations. Flow boiling lead to non-uniform flow distribution within microchannels and simultaneous existence of different flow boiling patterns along the transverse direction. A higher inlet temperature of coolant gives better temperature uniformity in transverse direction indicating better flow distribution than in the case of lower inlet water temperature.
5. It was found that a superheated liquid layer near channel walls plays a significant role in bubble dynamics during boiling in microchannels. This resulted in acceleration in the bubble growth as it comes closer to the channels side walls. The bubble dynamics determined the frequency of alternation between phases, and consequently the frequency of the pressure and temperature oscillations. This had an impact on two-phase heat transfer mechanism which was dictated by periodic behaviour of the flow patterns in microchannels. Two-phase heat transfer coefficient was found to first increase with increasing exit vapour quality and then decreased at higher vapour quality.
6. Position and magnitude of hotspot, during flow boiling under non-uniform heating, had an effect on magnitudes of the pressure drop and temperature

oscillations, overall pressure drop and flow distribution among the channels. A long subcooled inlet region, particularly in the case of downstream hotspots, suppressed flow reversals originating at the downstream end of the channels, by partially condensing reversing bubbles resulting in a better flow distribution within channels and smaller magnitudes of the pressure drop oscillations for downstream located hotspots.

8.2 Future studies

Flow boiling instabilities under uniform and non-uniform heating have been investigated in this study. The flow boiling instabilities were classified into flow stability maps. It has been shown that the type of instabilities depends on the bubble dynamics in microchannels. Maximum heat transfer was found when the transient annular flow dominated during phase alternation. The future work in this area should be geared to elimination of flow boiling instabilities using orifices installed at microchannels inlet. Properly designed orifices should suppress flow instabilities with flow reversal while keeping the pressure drop reasonably low. The cavitation in the single-phase flow created by the inlet orifices can promote bubble nucleation and decrease a large amount of superheat usually associated with flow boiling in microchannels.

Another problem related to microchannel heat sinks with flow boiling is non-uniform flow distribution among the channels. Cross-linking of microchannels can be a promising solution for achieving better flow distribution within microchannels, hence improved temperature uniformity in transverse direction. Preliminary results obtained in this study showed that cross-linking of microchannels enhanced the lateral mixing in the microchannels providing better flow distribution within microchanenls. The results are presented in appendix F. However, cross-linking of microchannels might amplify the flow instabilities and the pressure drop oscillations due to the compressibility of the two-phase mixture in adjacent channels. If cross-linking of microchannels is to be used in microchannel heat sink design, it would be

necessary to install orifices after each cross-linked channel along the microchannnel heat sink.

More experiments with different cooling liquids should be conducted in order to assess the effect of different surface tensions on the bubble dynamic, flow instabilities and heat transfer characteristics of a microchannel heat sink with flow boiling. If flow boiling is to be used as thermal management method for CPUs it is likely that cooling liquids such as refrigerants and fluorocarbon coolants will be utilised. Safe and efficient operation of CPUs requires a junction temperature below 85 ˚C, therefore a cooling liquid with a saturation temperature close to a junction temperature should be considered. A cooling liquid with high dielectric constant is preferable as it will not damage electronic equipment in the event of a leak or other failure.

Appendix A A drawing of the assembly of the experimental setup

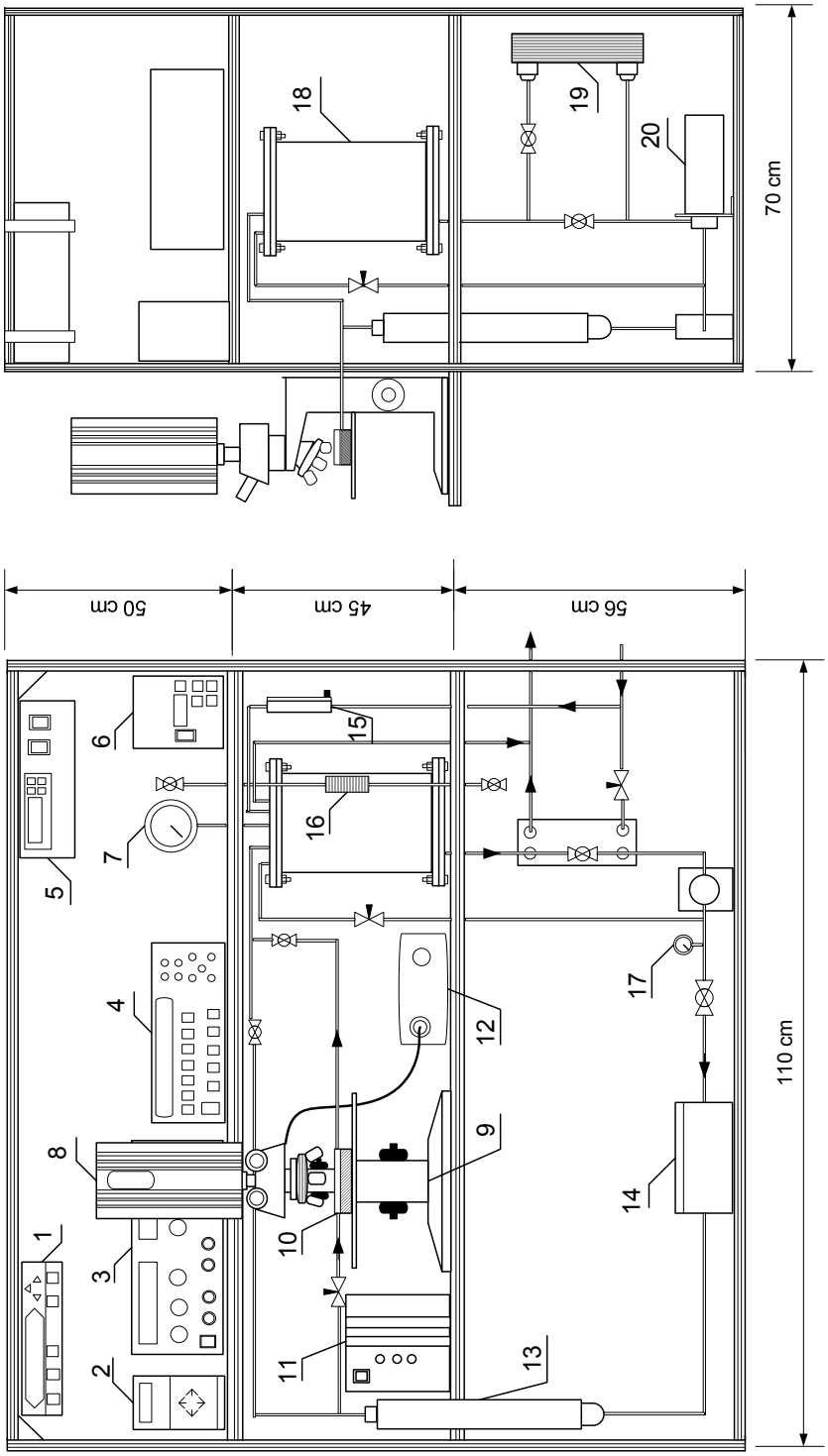

No	Name	No	Name
1	PID controller for circulation heater	11	DAQ device
2	Mass flow meter console	12	Light illuminator with fiber optic conductor
3	DC power supply	13	Circulation heater
4	Ammeter	14	Mass flow meter
5	PI controller for reservoir heaters	15	Rotameter
6	Pump console	16	Level indicator
7	Pressure gauge	17	Pressure gauge
8	High speed camera	18	Reservoir
9	Microscope	19	Plate heat exchanger
10	Test module	20	Gear pump

Appendix B Test module top and bottom frame dimensions

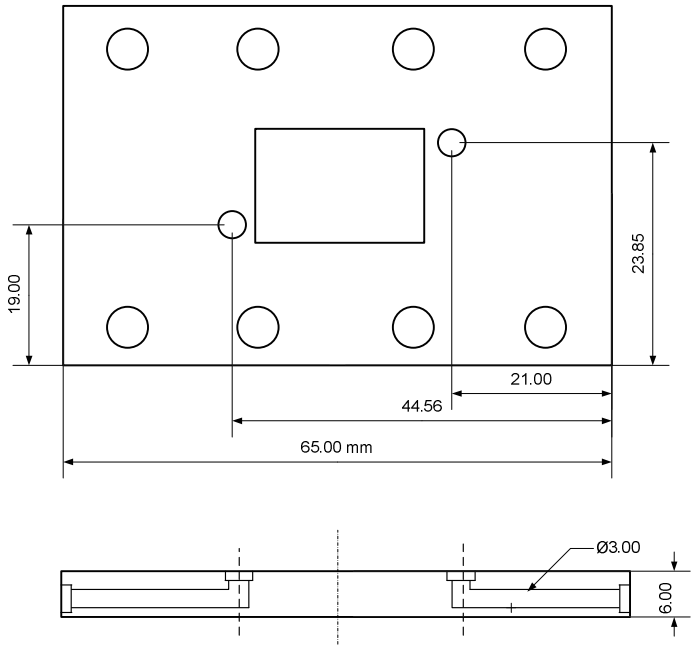

Top frame

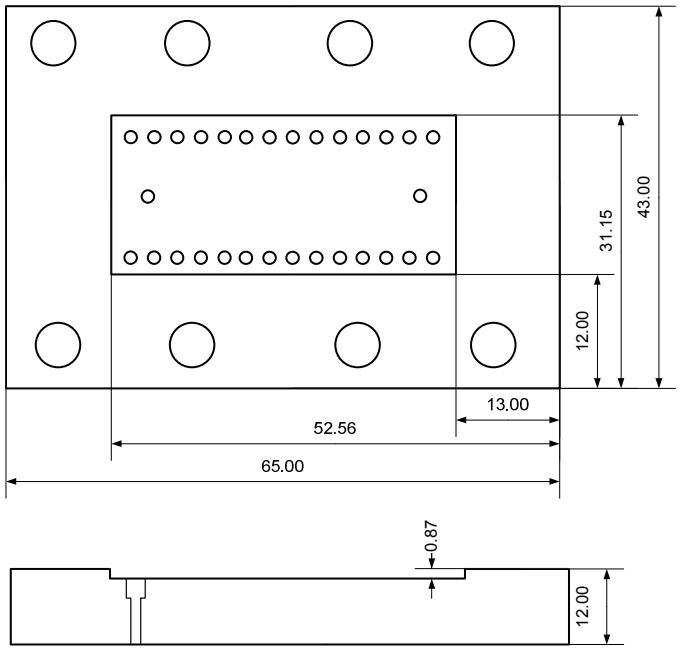

Bottom frame

Appendix C LabView software interface and block diagram

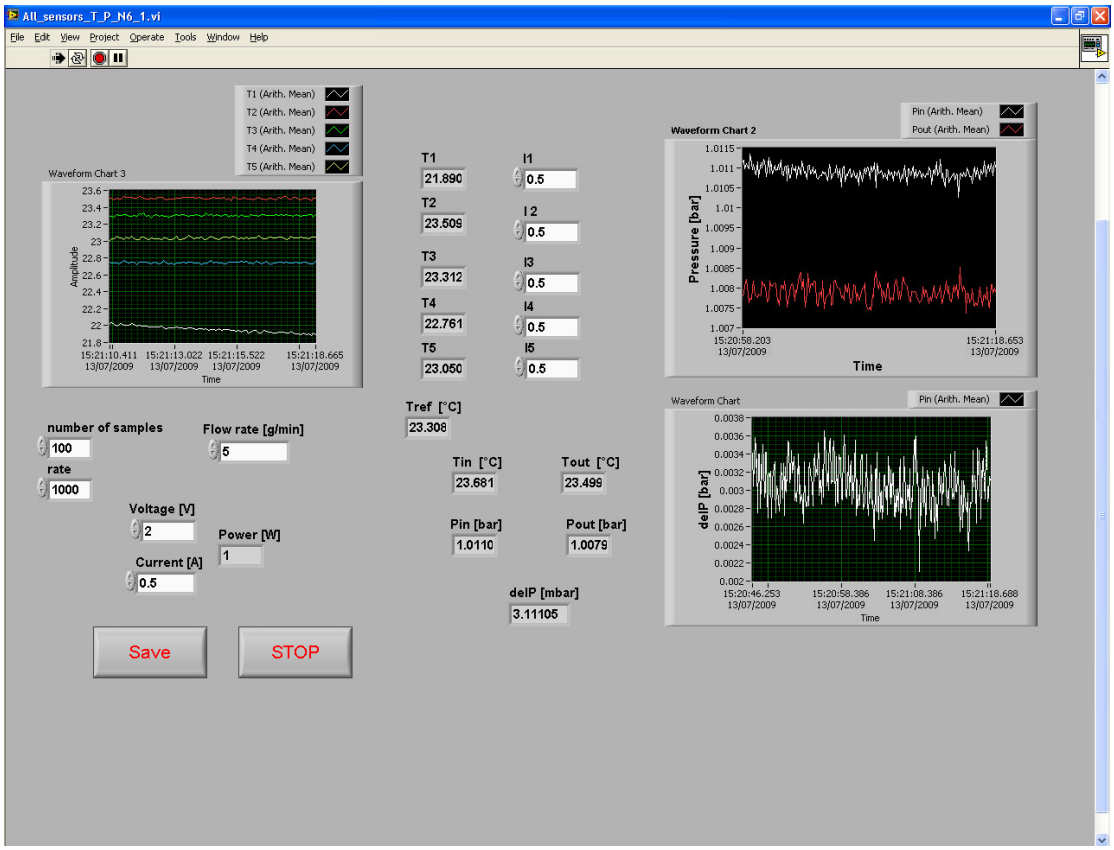

LabView software interface

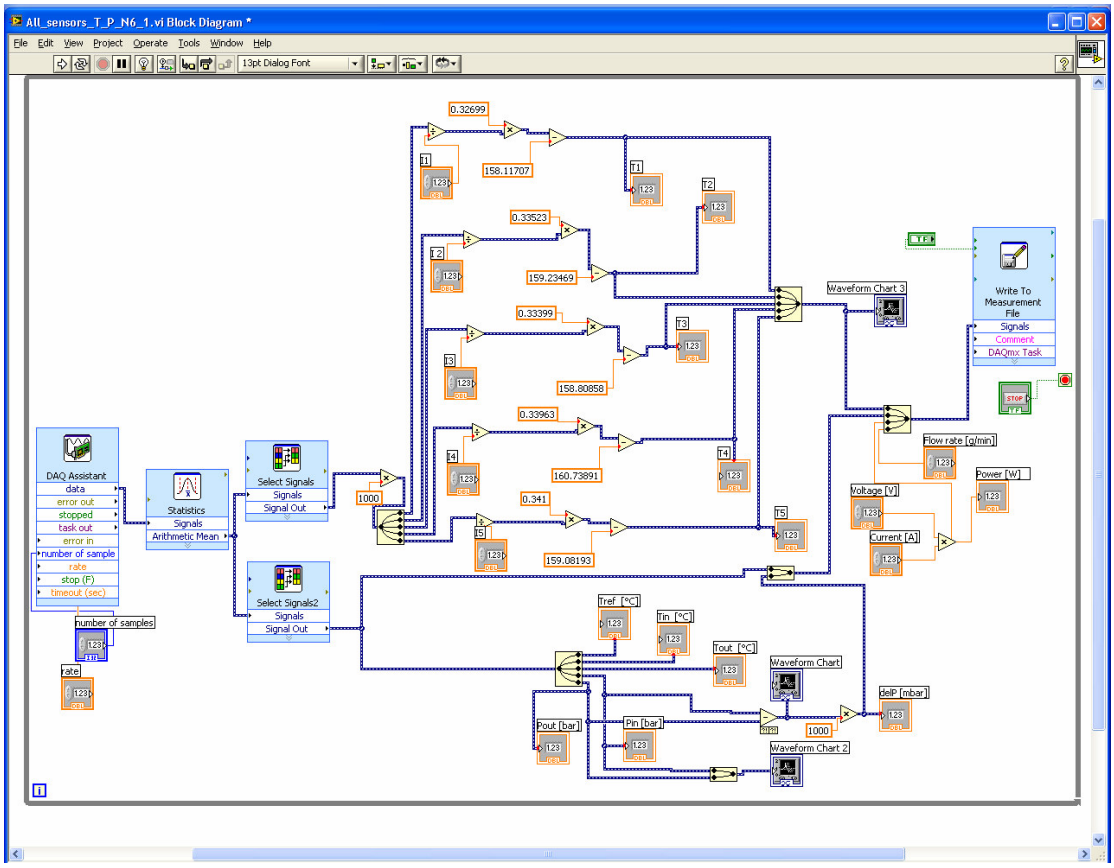

LabView block diagram

Appendix D The effect of heat flux on bubble growth in subcooled and saturated flow boiling

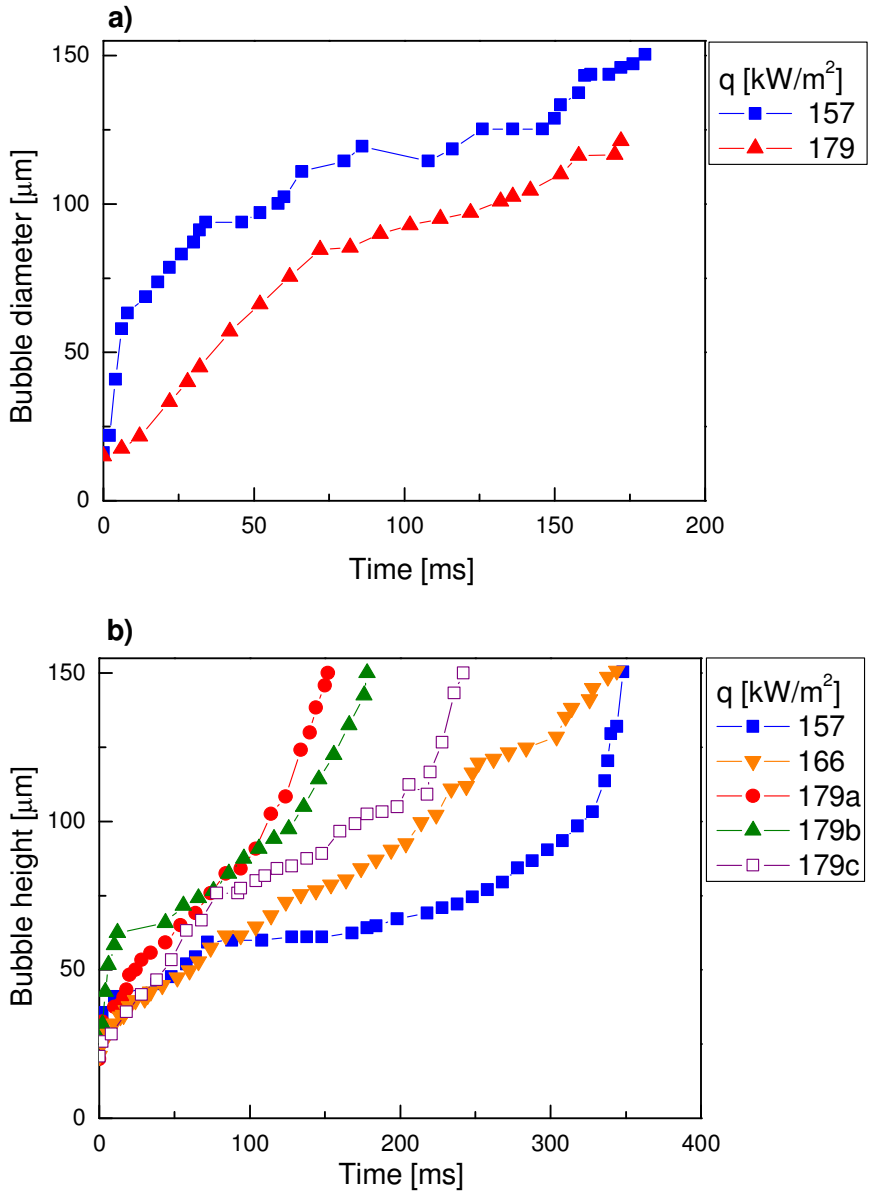

Figure 1. *Subcooled flow boiling, G = 71 kg/m²s, (a) Bottom wall bubbles growth and (b) side wall bubbles growth.*

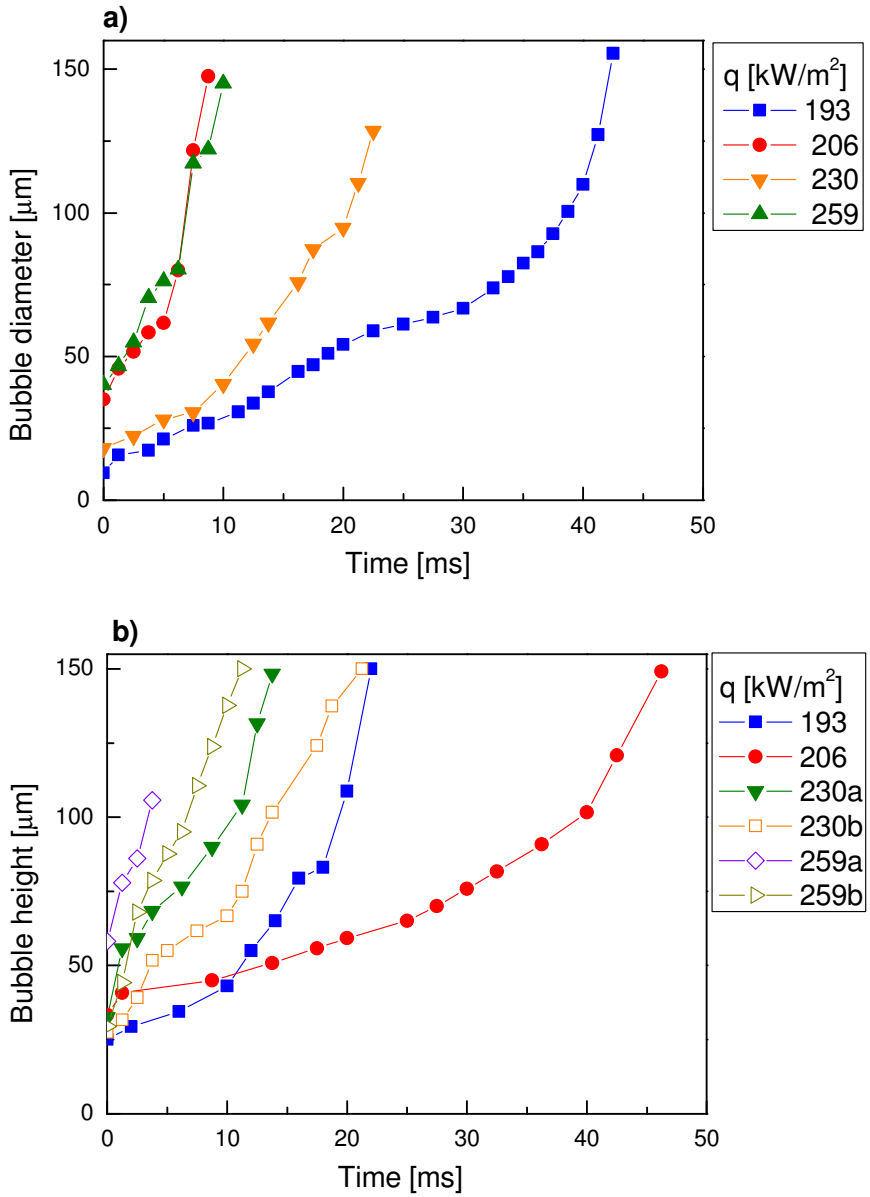

Figure 2. *Saturated flow boiling, G = 71 kg/m²s, (a) Bottom wall bubbles growth and (b) side wall bubbles growth.*

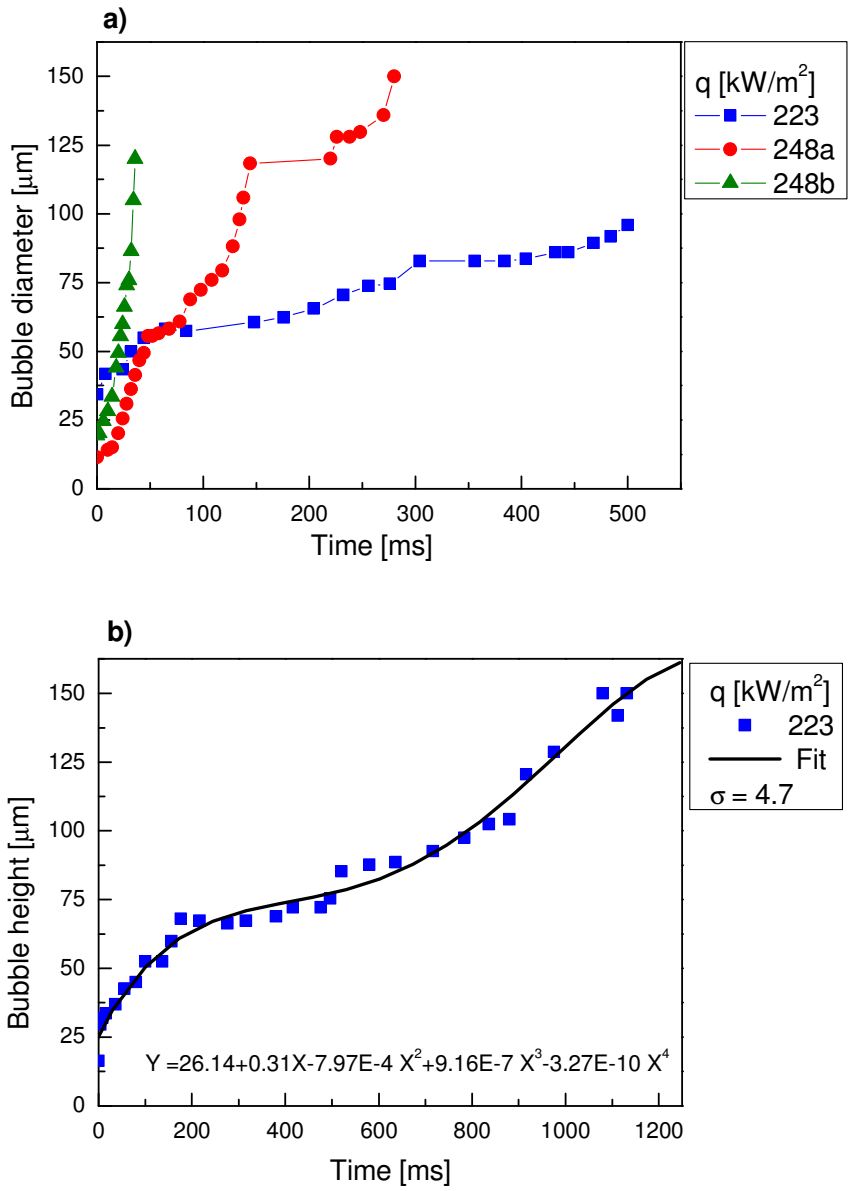

Figure 3. *Subcooled flow boiling, G = 112 kg/m^{2}s, (a) Bottom wall bubbles growth and (b) side wall bubbles growth.*

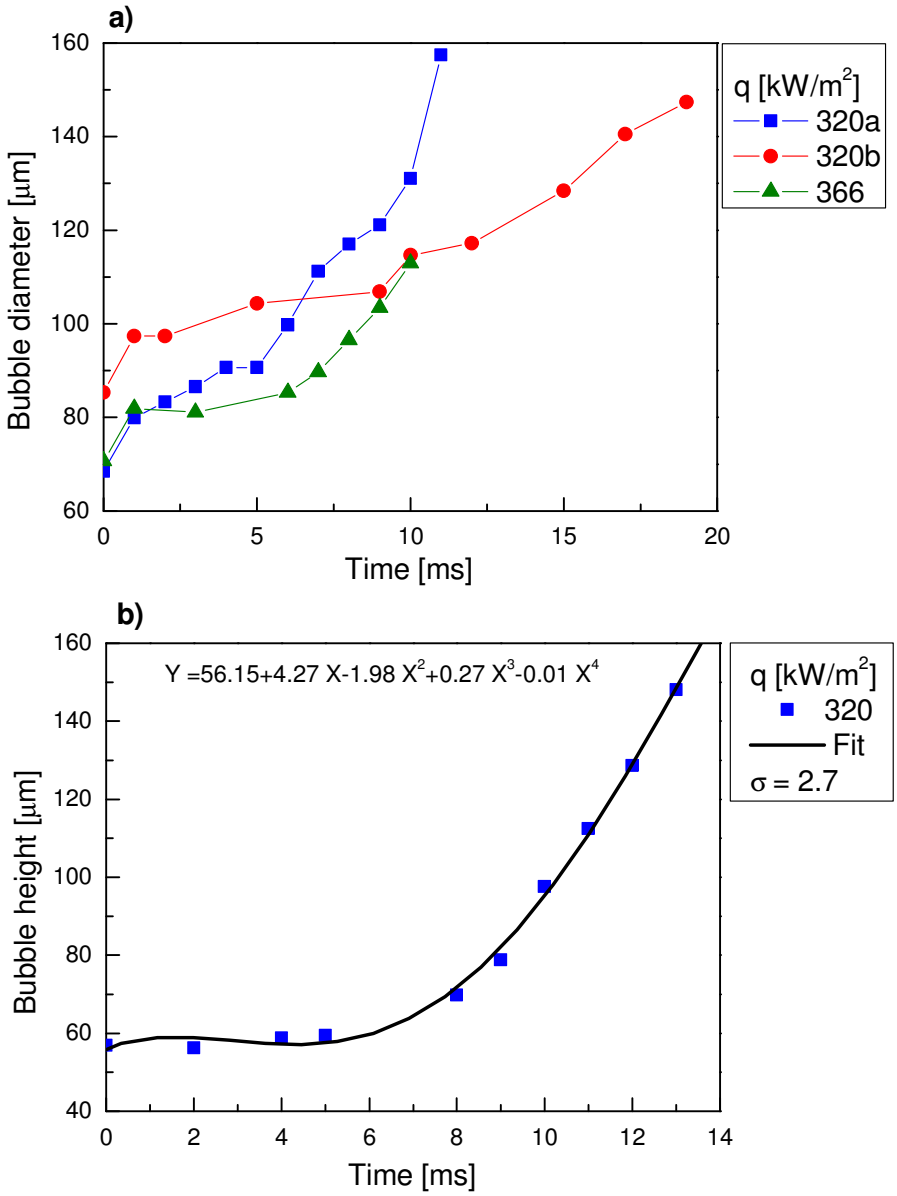

Figure 4. *Saturated flow boiling, G = 112 kg/m²s, (a) Bottom wall bubbles growth and (b) side wall bubbles growth.*

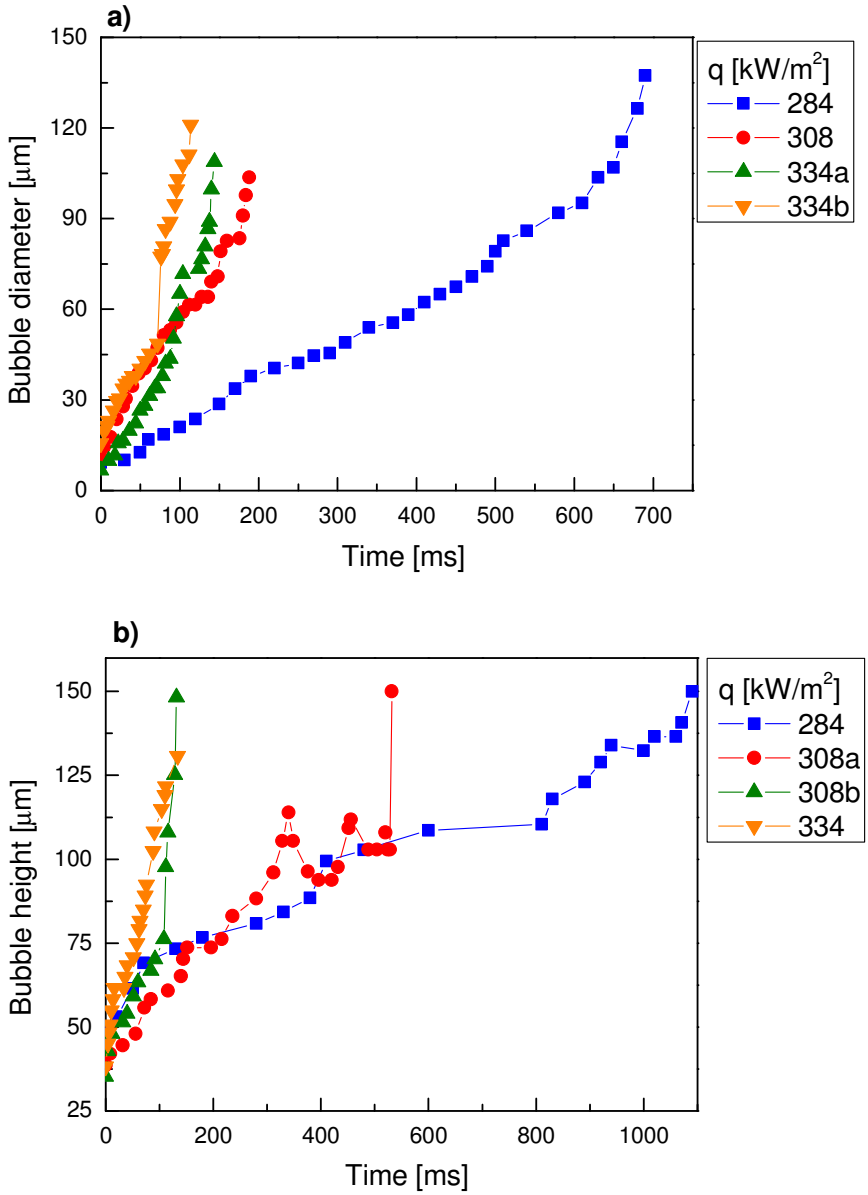

Figure 5. *Subcooled flow boiling, G = 178 kg/m^{2}s, (a) Bottom wall bubbles growth and (b) side wall bubbles growth.*

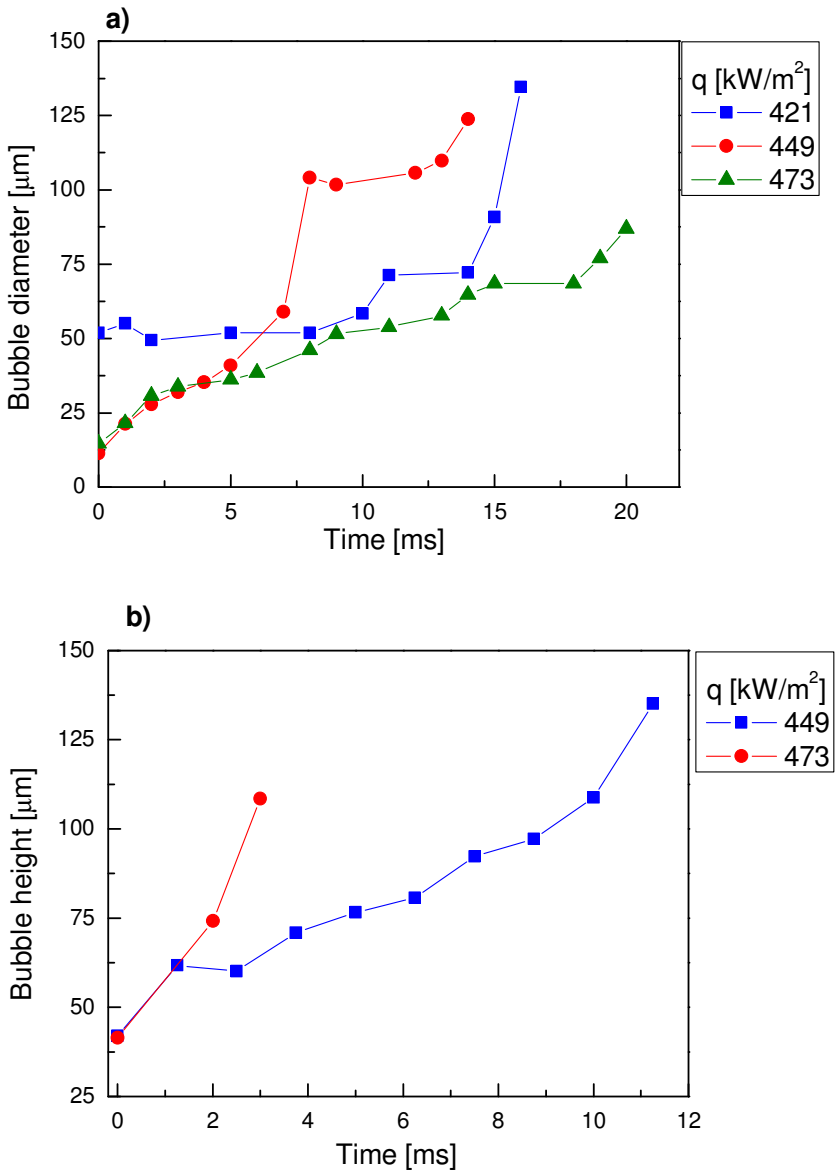

Figure 6. *Saturated flow boiling, G = 178 kg/m^{2}s, (a) Bottom wall bubbles growth and (b) side wall bubbles growth.*

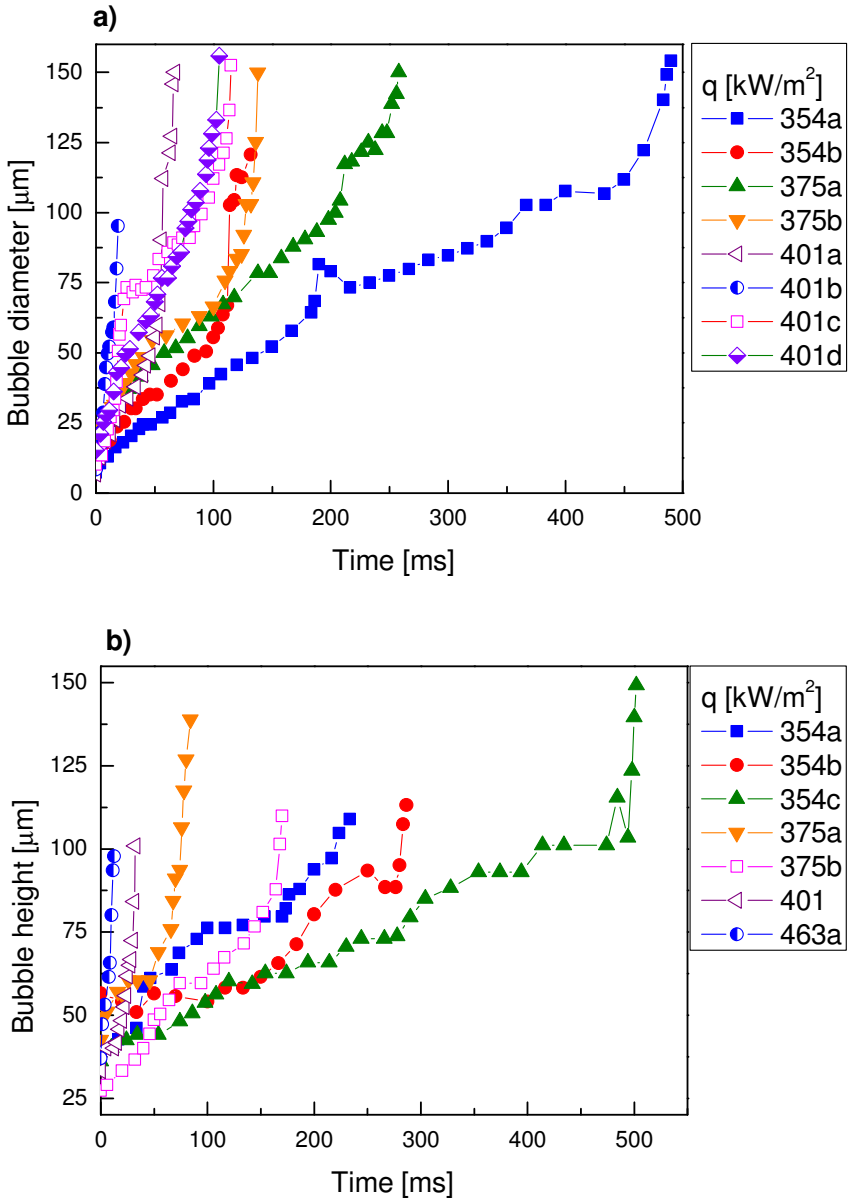

Figure 7. *Subcooled flow boiling, G = 204 kg/m²s, (a) Bottom wall bubbles growth and (b) side wall bubbles growth.*

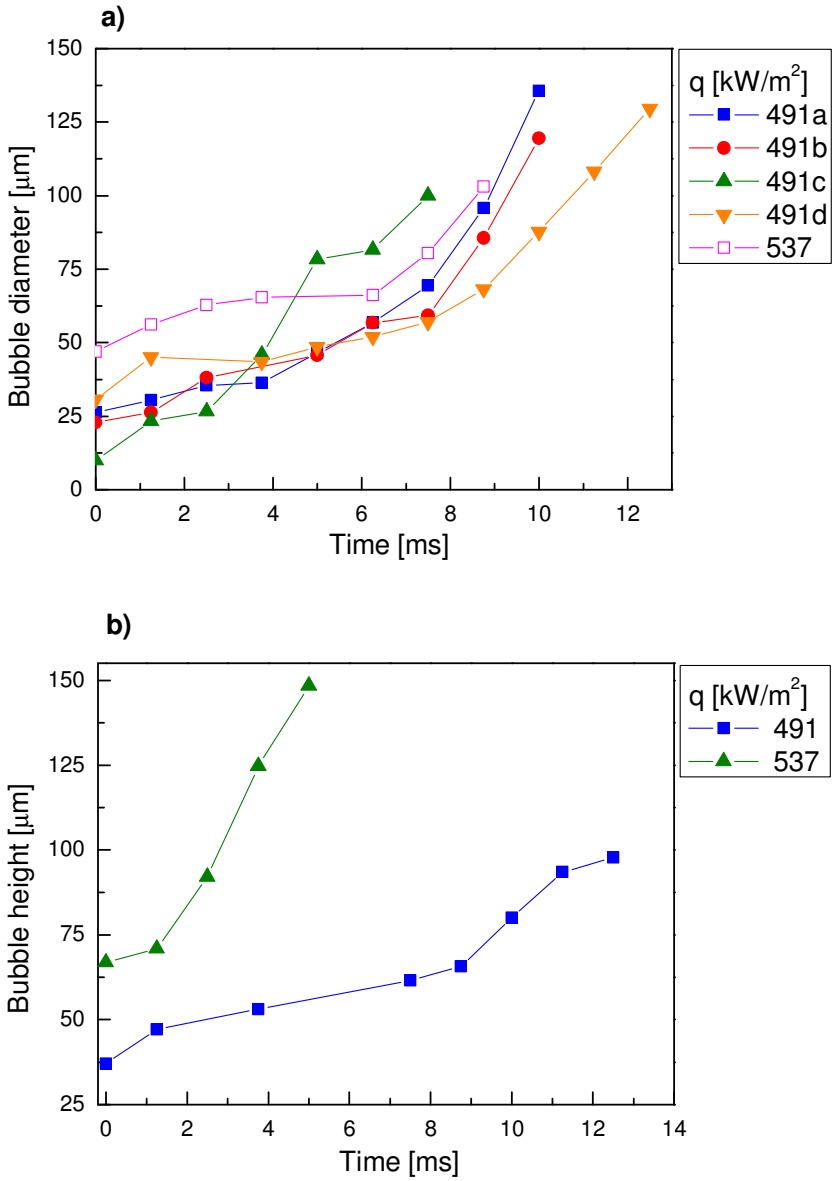

Figure 8. *Saturated flow boiling, G = 204 kg/m^{2}s, (a) Bottom wall bubbles growth and (b) side wall bubbles growth.*

Appendix E The effect of heat flux on normalised bubble growth curves in subcooled and saturated flow boiling

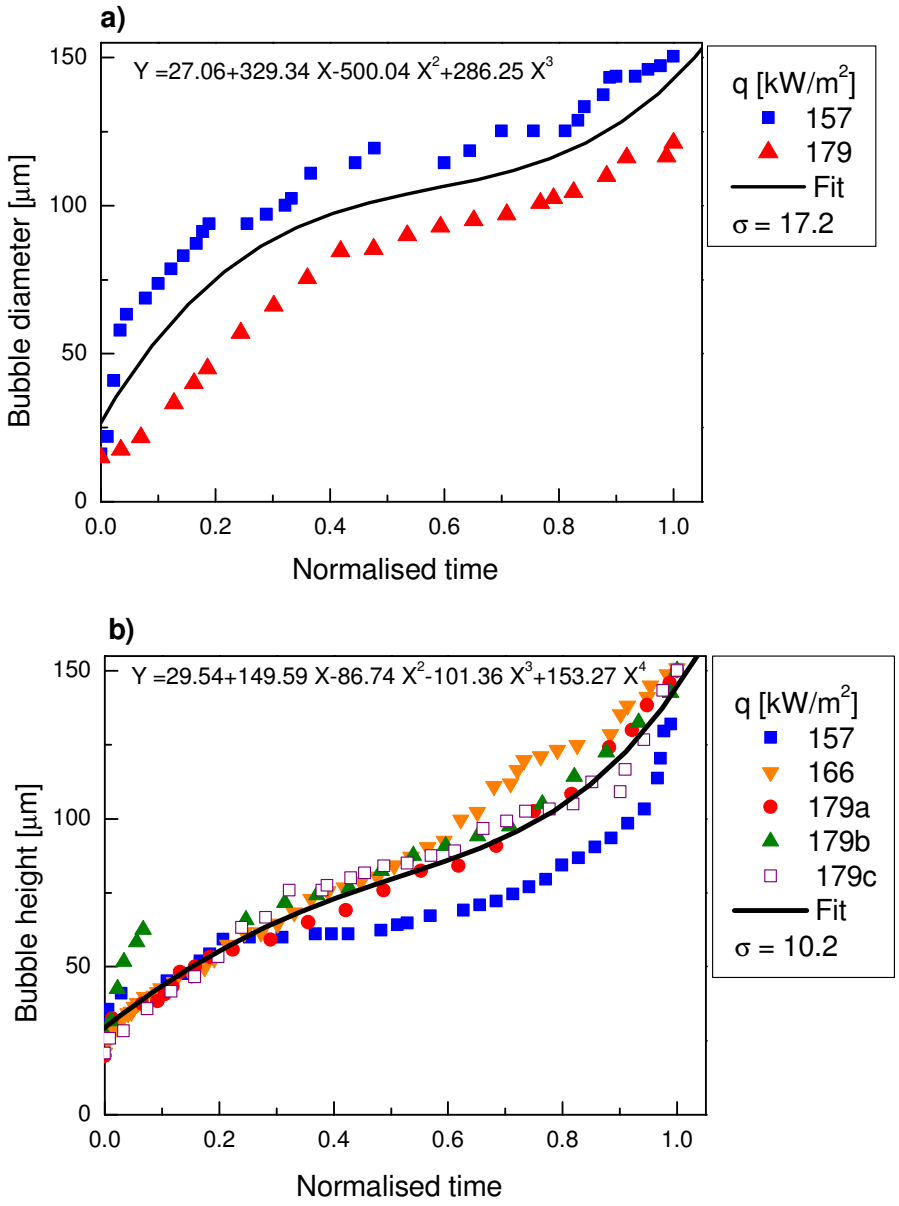

Figure 1. *Subcooled flow boiling, G = 71 kg/m²s, (a) Bottom wall bubbles growth and (b) side wall bubbles growth.*

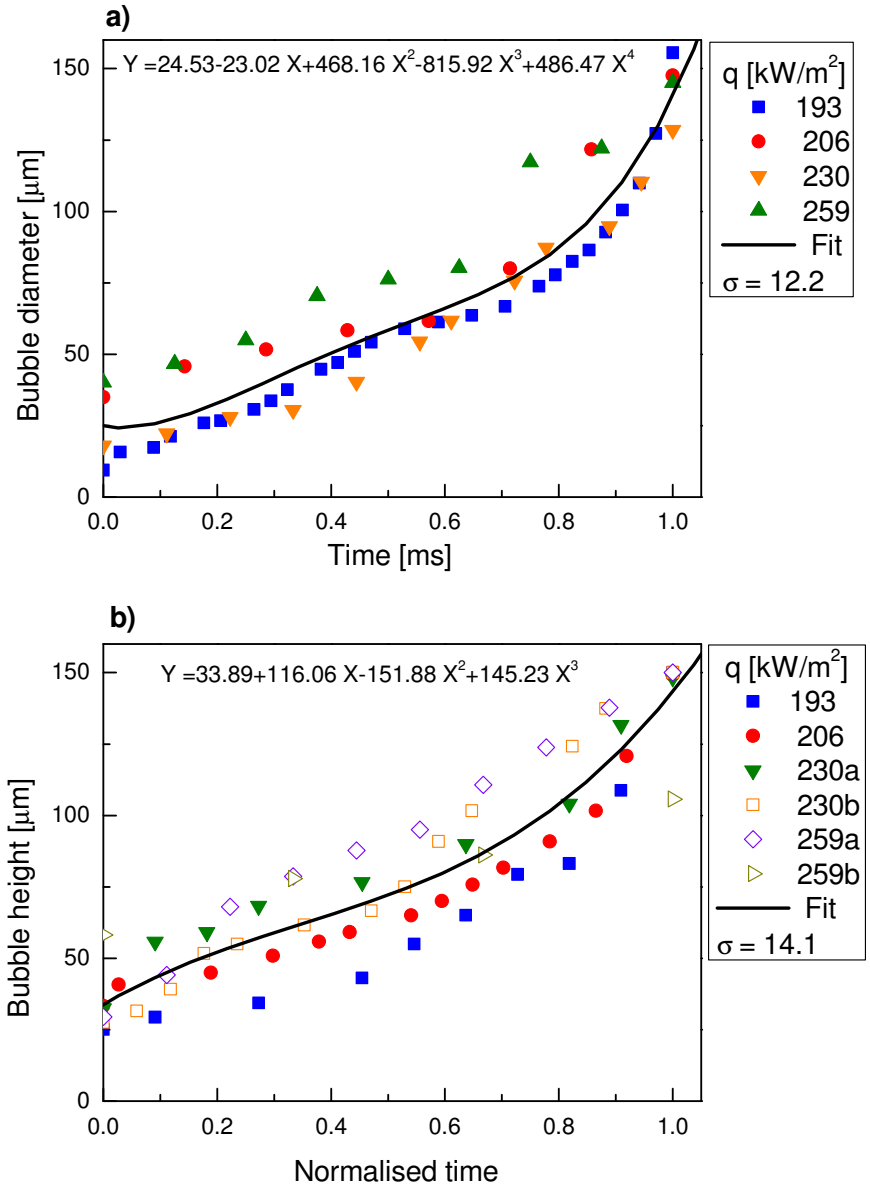

Figure 2. *Saturated flow boiling, G = 71 kg/m²s, (a) Bottom wall bubbles growth and (b) side wall bubbles growth.*

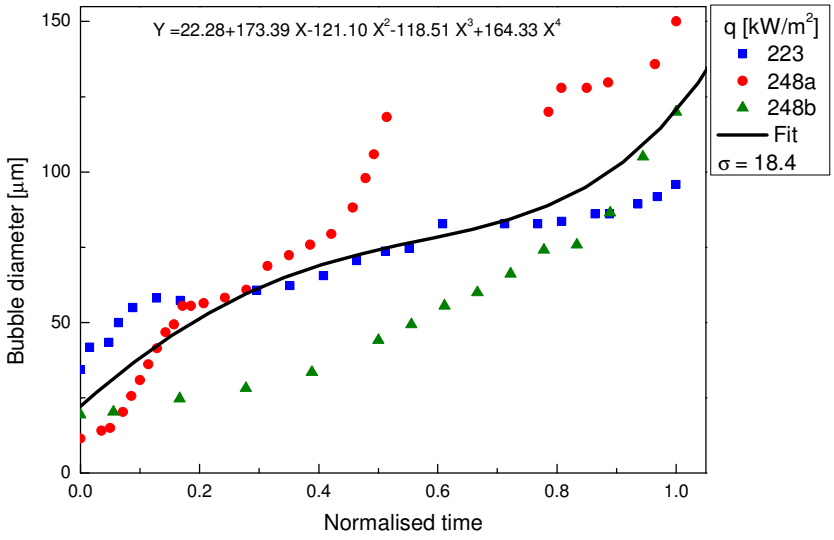

Figure 3. *Subcooled flow boiling, G = 112 kg/m²s, bottom wall bubbles growth.*

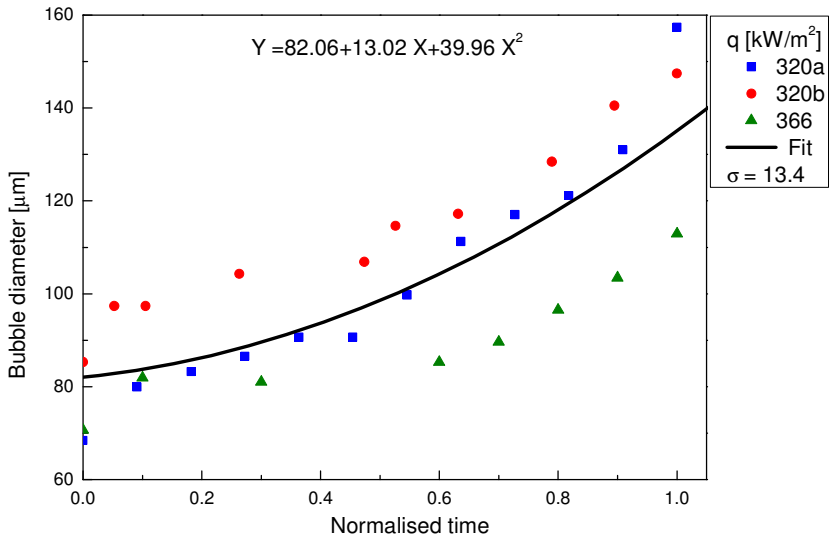

Figure 4. *Saturated flow boiling, G = 112 kg/m²s, bottom wall bubbles growth.*

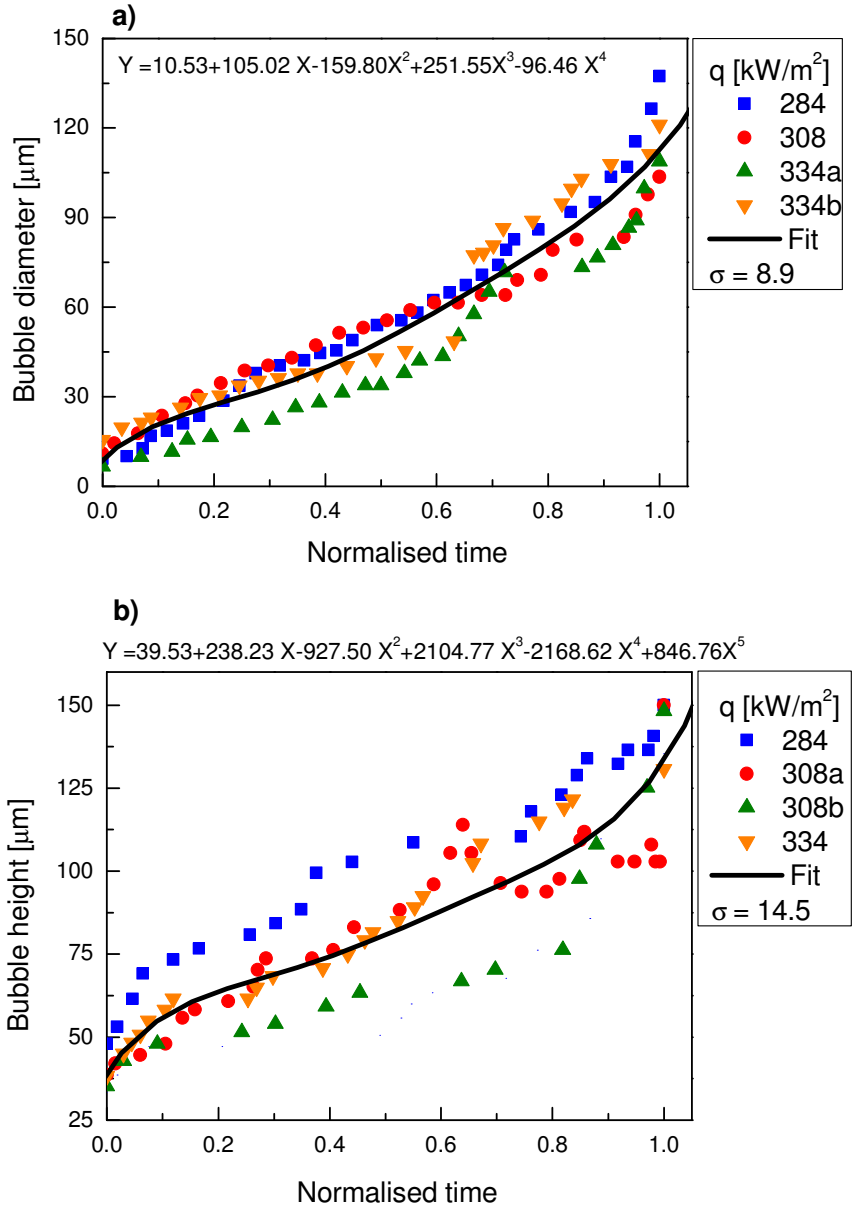

Figure 5. *Subcooled flow boiling, G = 178 kg/m^{2}s, (a) Bottom wall bubbles growth and (b) side wall bubbles growth.*

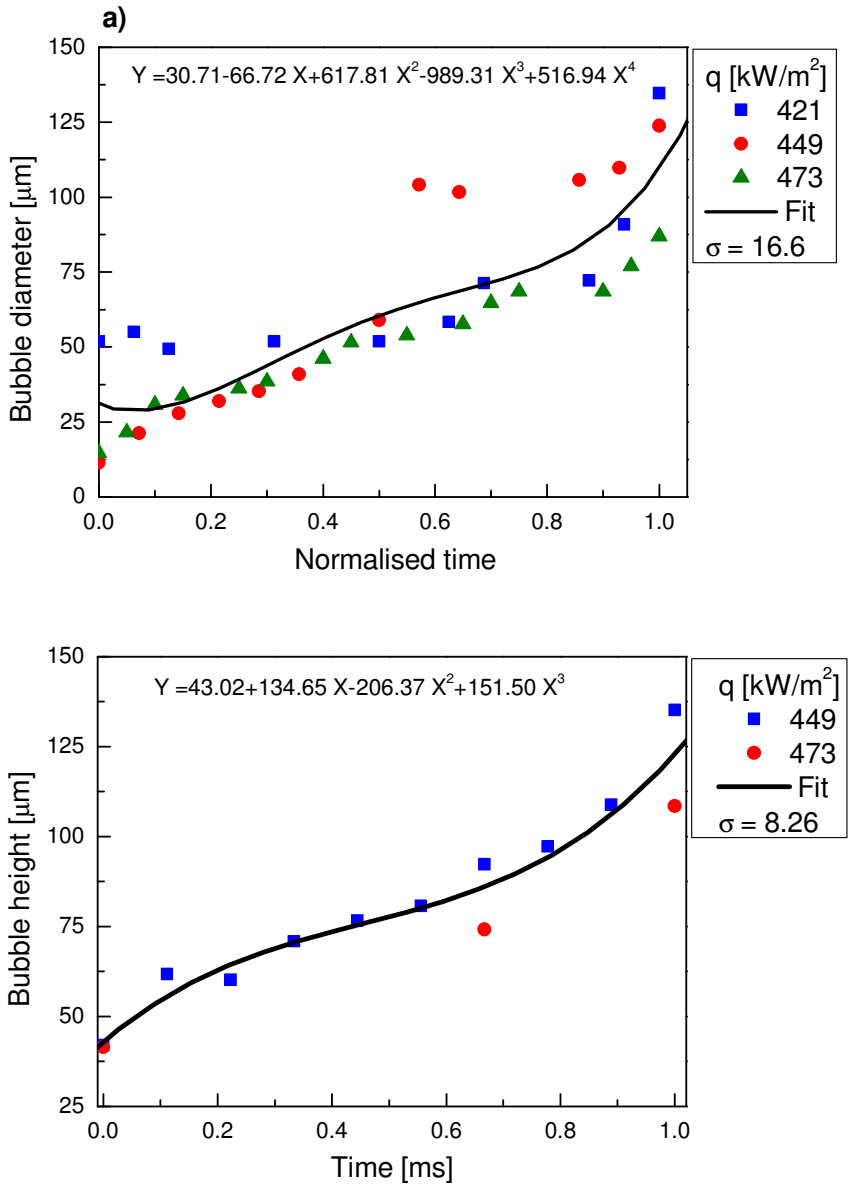

Figure 6. *Saturated flow boiling, G = 178 kg/m²s, (a) Bottom wall bubbles growth and (b) side wall bubbles growth.*

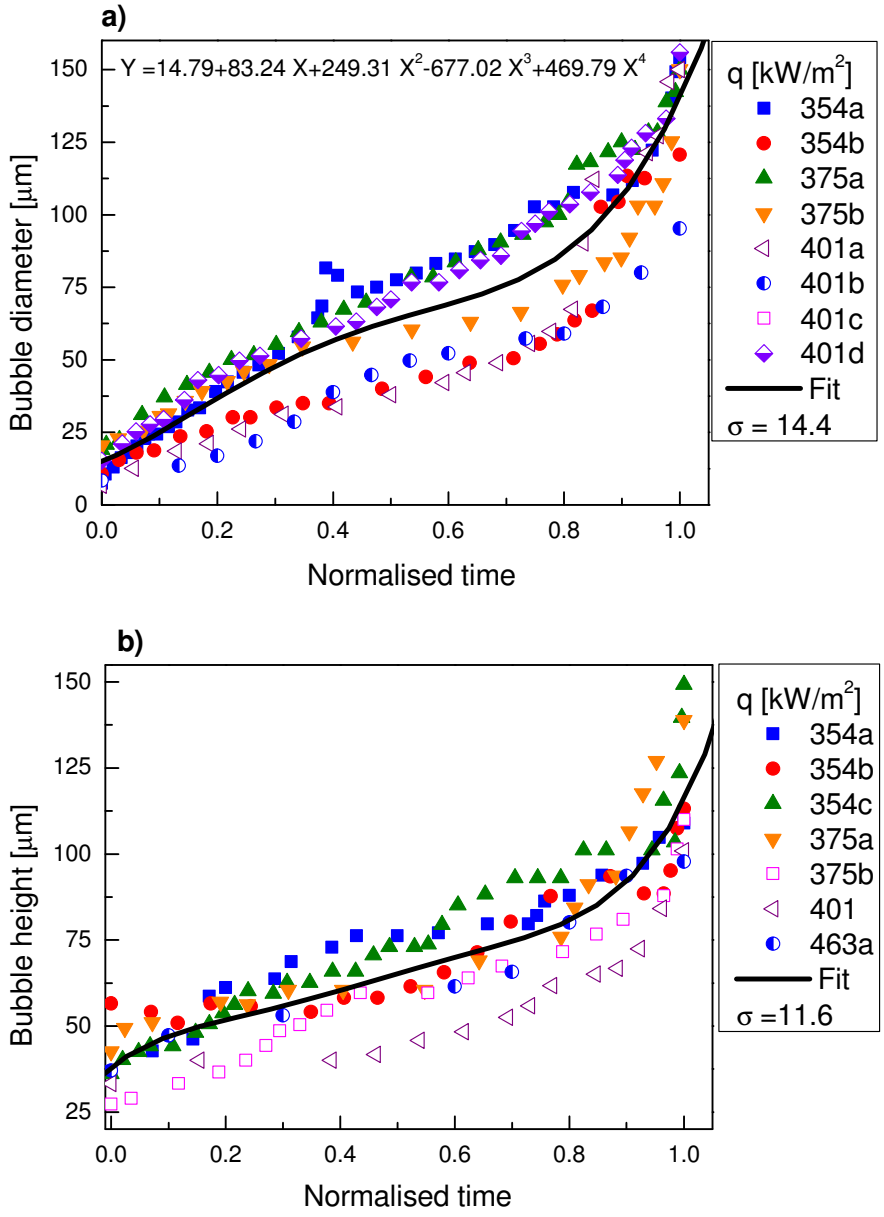

Figure 7. *Subcooled flow boiling, G = 204 kg/m^{2}s, (a) Bottom wall bubbles growth and (b) side wall bubbles growth.*

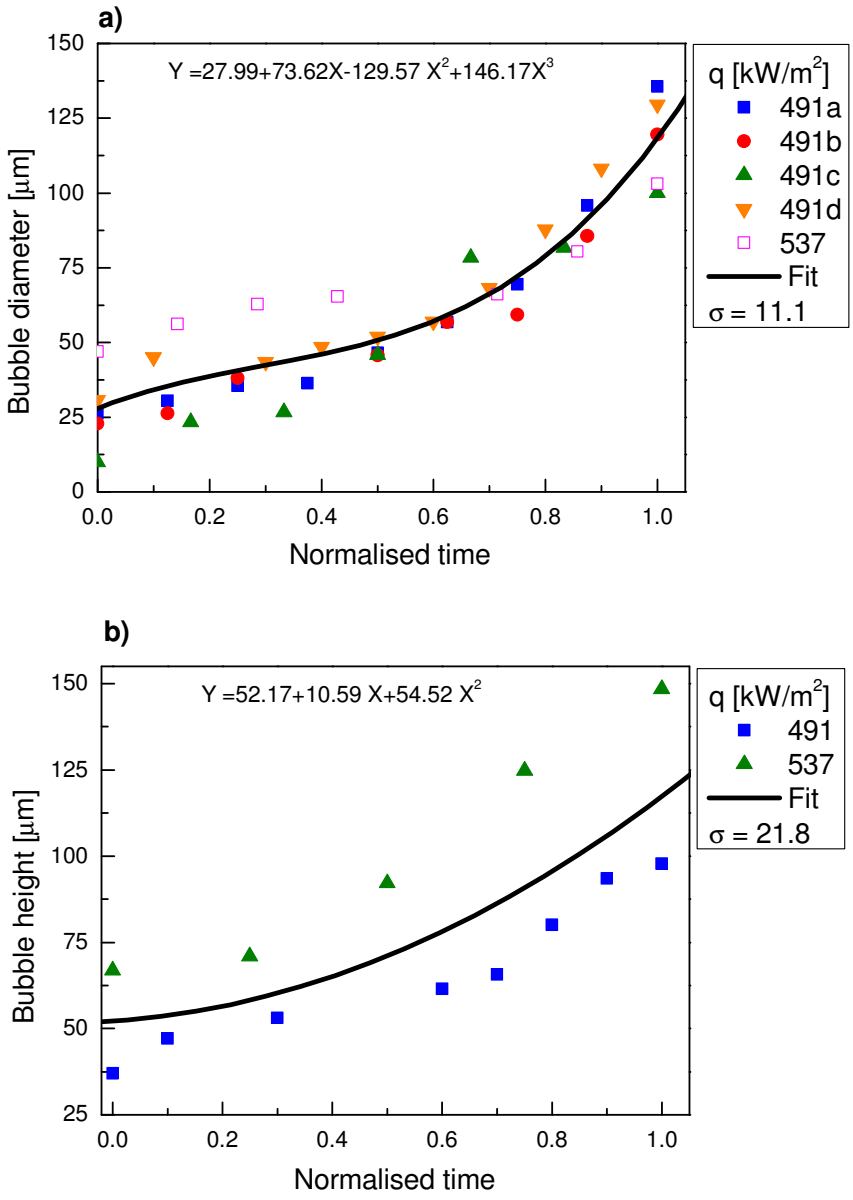

Figure 8. *Saturated flow boiling, G = 204 kg/m²s, (a) Bottom wall bubbles growth and (b) side wall bubbles growth.*

Appendix F Results for cross-linked microchannel heat sink

The heat sink consist of 40 channels with a hydraulic diameter of 194 μm and integrated inlet/outlet manifolds. There are four cross linked channels to enhance lateral mixing in the microchannels providing better flow distribution.

Figure 1a shows image sequences captured using a high speed camera for a mass flow rate of 24.7 g/min, a heat flux of 35 W/cm^2 and an inlet temperature of 71 ˚C. Figure 1b shows simultaneously recorded inlet and outlet pressure. The image recorded at t = 0 ms shows a bubble growing in the cross-linking channel and single-phase flow in all microchannels. After the bubble collapsed, an annular flow set up in all microchannels followed with a temporary "dryout" period at t = 148 ms and water refill at t = 258 ms. It is clear from the images that alternations between liquid, two-phase and vapour flows were synchronized in channels indicating uniform flow distribution.

Figure 2a shows image sequences for a heat flux of 65 W/cm^2 and the same mass flow rate of 24.7 g/min. Figure 2b shows simultaneously recorded inlet and outlet pressure. Again, alternations between phases were synchronized in observed channels due to lateral mixing and fluid transport through cross-linking channels. The images recorded at t = 0 ms and t = 54 ms show mist flow, while the images recorded at t = 26 ms and t = 76 ms show transient annular flow present in observed channels.

a)

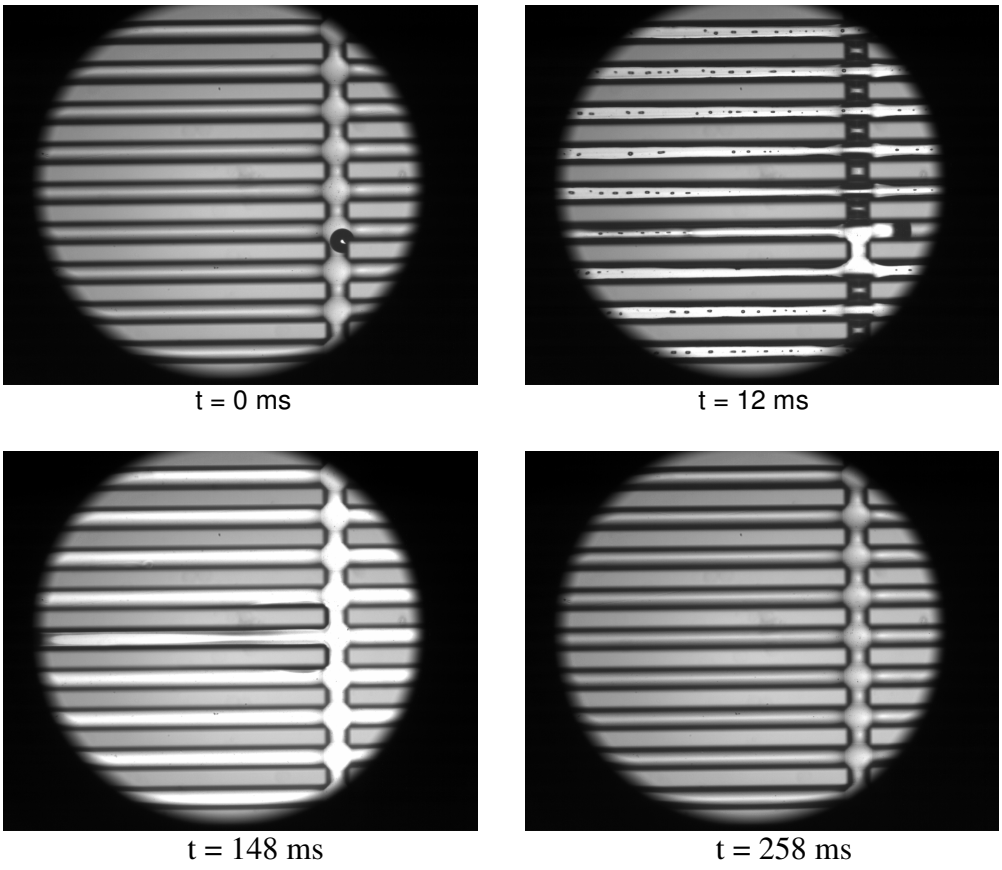

b)

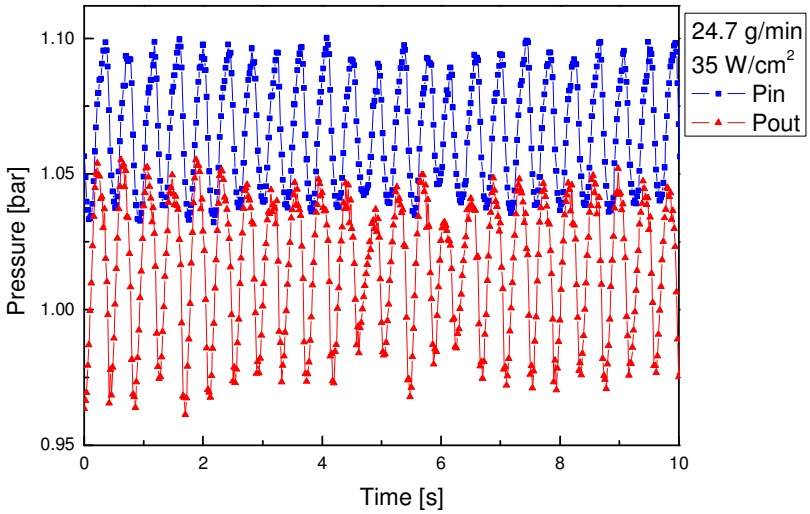

Figure 1. *(a) Images recorded using high speed camera at a rate of 500 fps for a heat flux of 35 W/cm^2 and cross-linked microchannel heat sink, (b) simultaneously recoded inlet and outlet pressure.*

a)

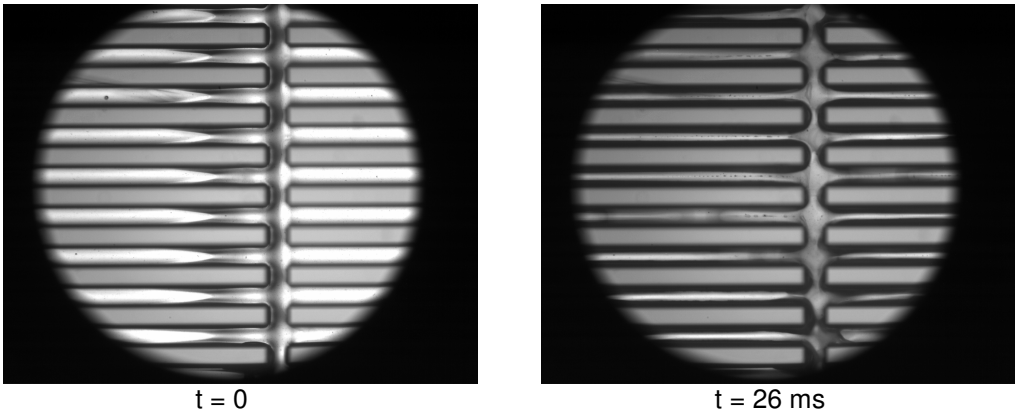

b)

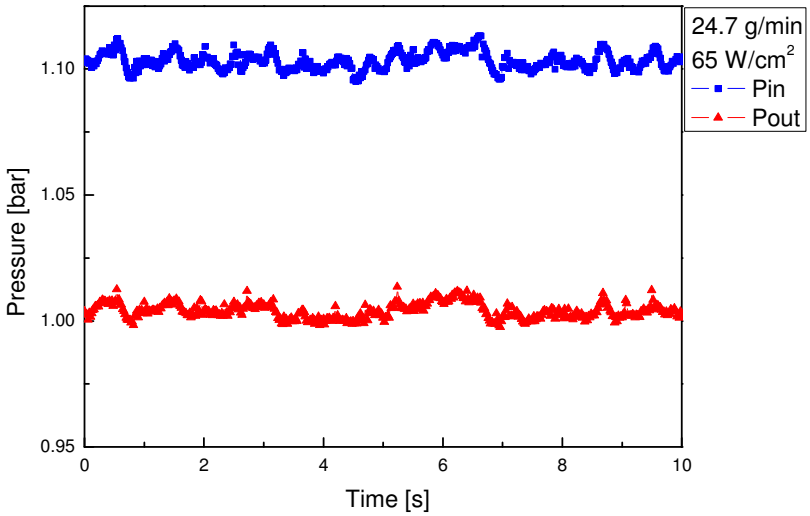

Figure 2. *(a) Images recorded using high speed camera at a rate of 500 fps for a heat flux of 65 W/cm^2 and cross-linked microchannel heat sink, (b) simultaneously recoded inlet and outlet pressure.*

Publications and presentations

The following publications and presentation have been made during the course of the present investigation:

- **Refereed journal publications**

D. Bogojevic, K. Sefiane, A.J. Walton, J. R. E. Christy, G. Cummins, H. Lin; *"Investigation of flow distribution in microchannels heat sinks"*, Heat Transfer Engineering, Volume 30 (13), Nov 2009, Pages 1049-1057

D. Bogojevic, K. Sefiane, A.J. Walton, H. Lin, G. Cummins; *"Two-phase flow instabilities in a silicon microchannels heat sink"*, International Journal of Heat and Fluid Flow, Volume 30, Issue 5, Oct 2009, Pages 854-867.

- **Conference publications and presentations**

D. Bogojevic, K. Sefiane, A. J. Walton, H. Lin, G. Cummins, D.B.R. Kenning, T.G. Karayiannis; *"Experimental investigation of non-uniform heating on flow boiling instabilities in a microchannels based heat sink",* accepted for publication in Proceedings of the 7th International ASME Conference on Nanochannels, Microchannels and Minichannels, June 22-24, 2009, Pohang, South Korea.

D. Bogojevic, K. Sefiane, A.J. Walton, H. Lin, G. Cummins; *"Two-phase flow instabilities in microchannels"*, ECI International Conference on Heat Transfer and Fluid Flow in Microscale, Whistler, Canada, 21-26 September 2008.

D. Bogojevic, K. Sefiane, A.J. Walton, J. Christy, G. Cummins, H. Lin; *"Investigation of flow distribution in microchannels heat sinks"*, The 10th UK National Heat Transfer Conference, Edinburgh, UK, 10-11 September 2007.

G. Cummins, D. Bogojevic, A.J. Walton, K. Sefiane; *"Investigation into the Effect of Non Uniform Temperature"*, Micro and Nanoscale Flows, Advancing the Engineering Science and Design, Glasgow, UK, 7-8 December 2006.